DOCTOR OF PHILOSOPHY

# Shift-Free Wide-Angle Metamaterial Narrowband Filters for Anti-Laser Striking Applications

Monks, James

*Award date:*
2020

*Awarding institution:*
Bangor University

DOCTOR OF PHILOSOPHY

# Shift-Free Wide-Angle Metamaterial Narrowband Filters for Anti-Laser Striking Applications

Monks, James

*Award date:*
2020

QIOPTIQ
Photonics for Innovation
An Excelitas Technologies Company

# *Shift-Free Wide-Angle Metamaterial Narrowband Filters for Anti-Laser Striking Applications*


PRIFYSGOL
BANGOR
UNIVERSITY

**James Norman Monks**

School of Computer Science & Electronic Engineering

Bangor University

A thesis submitted in partial fulfilment for the degree of

*Doctor of Philosophy*

Optoelectronics & Nanophotonics

January 2020

"If you want to find the secrets of the universe,
Think in terms of energy, frequency and vibrations."
- *Nikola Tesla*

Ymroddedig I’r Dyn Gorau I Mi Erioed Ei Adnabod -

*Dedicated to the Greatest Man I Ever Knew* -

# Norman Jones

(1929-2018)

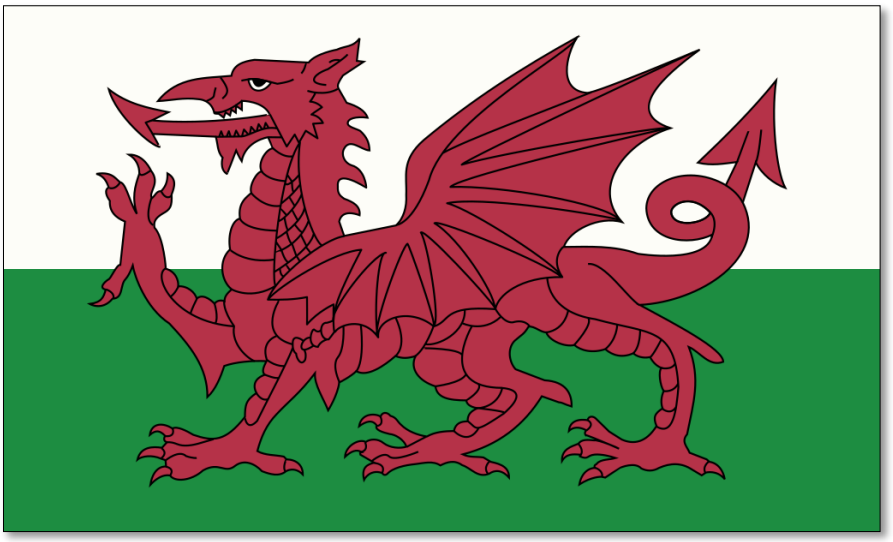

# ABSTRACT

In recent years, the threat to pilots and other transport vehicles has increased through laser striking. This is due to the ease of accessibility and the low cost of ownership for handheld portable lasers. The reports from the Civil Aviation Authority (CAA) and their American counterpart, the Federal Aviation Administration (FAA), have outlined that visible green laser attacks consist of 83-91% of all incidents. This can lead to temporary impairment to the human eye, with consequences increasing with exposure time resulting in retinal and photo-chemical eye damage. Additionally, the magnitude of severity is increased and could lead to fatal collisions. Current efforts for laser protection devices consist of traditional thin film filters. This technology is well-established, but it has disadvantages related to the angular intolerance, where the transmission spectrum of the protection filter undergoes a continuous blue shift to shorter wavelengths as angle of the incident beam increases. The optical and transport industry, as well as government defence agencies, have a desired interest in developing a truly wide-angle (up to 60 degree) and shift-free laser protection system, which is the main drive behind this research. Furthermore, optical narrowband filters with wide-angle operation are highly sought after in other applications including Raman spectroscopy, multi-photon microscopy, and life science.

The research presented in this doctoral thesis employs a new theoretical approach to the problem and presents laser protection designs that can effectively block out any desired wavelength within the visible region through merging plasmonic physics with thin film interference theory. This allows for high transmission filters with a single rejection band at the plasmonic resonant wavelength. Filter designs can be established in quick succession with a specifically developed inverse design software tool that supplements industry standard optical thin film filter design software by integrating an effective Drude-Lorentz model to describe a ‘metafilm’, or supplements a full-wave electromagnetic simulator by incorporating the meta-atom design. The metafilm methodology provides reliable results when compared to the design of a full metamaterial model through a full-wave electromagnetic simulation software.

Attributing minimal parameters to the metamaterial allows for an inverse full metamaterial model to be designed through isotropic plasmonic particles. The functional responses of the designed filters can achieve optical densities (OD) within the range of 1OD to 4OD for all polarisation states over a wide range of angles up to 85+ degrees. The use of thin film interference theory enables wavelengths outside the plasmonic resonance to obtain high overall

transmission allowing for a high integrated visual photopic response. Due to the narrowband, typically full-wave half-maximum below 50 nm, the filter colouration can be near-neutral.

The discussion for the applications of metafilms can also be applied to traditional thin film filters in order to create a combination filter. This work presents combination filters which provide a boost and enhancement to the optical density, and advanced angular sensitivity performance. Traditional thin films are still an integral part for optical systems, so allowing a gradual introduction to metamaterial filters is a functional starting point to convince the industry that the future of wide-angle shift-free bandstop filter lies with optical metamaterials. Furthermore, the advances for manufacturing optical metamaterials are not yet advanced enough for a direct and solo metamaterial filter. Nevertheless, with current fabrication techniques, a combinational filter is a plausible route.

The device's active blocking layer structure is based on a three-dimensional plasmonic nanocomposite metamaterial, with a base element of aluminium/silver/gold nanoparticles arranged in a crystallographic primitive hexagonal Bravais lattice planar array, surrounded in a host dielectric medium. The active component is sandwiched between a transparent substrate and an anti-reflection coating. The lattice arrangement enables polarisation insensitivity, with a three-dimensional array density catering for an increased attenuation.

The full metamaterial wide-angle operating optical filters have to feature uniform structural sub-wavelength features, which is a highly difficult process over large areas with conventional lithographic techniques. Prototype filters have been fabricated with a shift-free wide-angle notch that is capable of filtering out blue light. The fabrication process takes advantage of self-assembled diblock copolymers (BCP) with metallic nanoparticle inclusions through selective impregnation. The BCP layers (PS-b-PEO) were annealed within a solvent vapour atmosphere (SVA) to induce a phase separation that forms a pentagonal periodic nanostructure of ~20 nm features with ~40 nm separation distance. Blue light filters were used for a proof of concept and provide a step towards desired blocking at any chosen wavelength.

The research undertaken within this Doctor of Philosophy programme provides a robust metamaterial filter design process with a method for developing and fabricating the devices as a proof-of-concept. The designed filters can be placed onto a number of devices ranging from personnel goggles to aircraft windows. This work can lead to the realisation for the next generation of laser protection devices that are currently in high demand.

# ACKNOWLEDGEMENTS

A PhD is no easy task. The idea of conducting high quality research with a 'significant – albeit modest – contribution' is a daunting endeavour. An effort that cannot be achieved without supporting characters. While I cannot hope to name all the individuals that contributed support and guidance; I can highlight a few key players, that without their efforts, this journey would be vastly different.

Firstly; I would like to give credit to my academic supervisory team, Dr. Zengbo Wang and Dr. Liyang Yue. A truly inspiring academic, Dr. Wang has provided me with every opportunity to become the best I can be over the course of the PhD and throughout my undergraduate studies. His encouragement, enrichment and guidance has been second to none. The immense knowledge that he has installed within me has been inspirational. Pun aside, the field of photonics is a brighter one with Dr. Wang in it. My co-supervisor, Dr. Yue, has provided emotional and academic support at any and all times. He has shown encouragement and pushed me to develop my skills. The years I have spent with these two academics have been life changing. For their support and guidance, I am forever grateful. I am sure that our relationship will continue for years to come.

Secondly; Mr. Andrew Hurst and Co. at Qioptiq. My industrial supervisor, Andy, has been an excellent source of knowledge and applications. His direction and reassurance throughout this programme has been motivating and stimulating. Andy, as director of advanced process and coatings, has put me in touch with some inspiring and knowledgeable people that have aided me at every opportunity and provided me with knowledge that books cannot teach. Thus, a special thanks must be gifted to Mr. Jonathan Williams, Mr. Barrie Aldred and Dr. Andy Wood.

Thirdly; my sincere thanks also go to Dr. Parvaneh Mokarian and her team at Trinity College Dublin who provided me an opportunity to join their research group over the summer, and gave me access to the laboratories, research facilities and key knowledge in block copolymer chemistry.

Fourthly; to my friends and family. Although it has been hard for friends and family to understand the process that has been undertaken over the last few years, they have provided endless support and enjoyment. The leading appreciation goes to my mother, Lilian Mary Monks, as for without her none of this would be possible. She has been the most inspirational person throughout my life with endless amounts of encouragement, teaching and love. Thanks to my Nain for all her support, reassurance and joyful company. To my sister and brother in-law for feeding me, and my nephews who have entertained and exhausted me. My friendship

group, who cannot be individually named, have shown me that having fun and a good time remains possible in this world of research chaos. A further distinct thank you message to Ffion Haf Jones, who has put up with me during my PhD, provided me with a roof over my head and food in my belly; with almost no complaining. She manages to make me laugh and smile everyday whilst showering me in love.

Lastly, I would like to personally thank my fellow PhD's and other academics who have helped out along the ways. Jake Shearwood, Shaun Preston and William Taplin for providing their ears for boundless rants, occasional sensible discussions and distractions when needed. Aeron Jones for being an outstanding photographic model and providing entertainment. Dr. Bing Yan, Dr. Rakesh Dhama and Dr. Noel Bristow for academic support. Cameron Grey for always making himself available when needed, not only for computer support but also as a great friend. Tudur David for the 4pm physics discussion tea breaks. The computer science lunch time crew for providing entertaining discussions and company. Mr Ben Assinder, school technician, for continuously putting up with me. And Finally, Dr. Iestyn Pierce, Dr. Mohammad Mabrook, Dr Jeffrey Kettle, Dr. Paul Sayers and Prof. Jonathan Roberts who have each provided me with support on a number of issues.

Supplementary thanks go to the funding body of this PhD, KESS II.

Ysgoloriaethau Sgiliau Economi Gwybodaeth
Knowledge Economy Skills Scholarships

# JOURNAL PUBLICATIONS

## THESIS RELATED

1. **J. Monks**, L. Yue, B. Yan, B. Aldred, A. Hurst and Z. Wang, "Wide-angle Shift-free Metamaterial Filter Design for Anti-laser Striking Applications", *Optics Communications*, vol. 429, pp. 53-59, 2018.
2. **J. Monks**, L. Yue and Z. Wang, "Effective Permittivity of Plasmonic Nanoparticle Composites Based on an Effective Drude-Lorentz Approximation Model", (*Being prepared for submission*).
3. **J. Monks**, J. Williams, L. Yue, A. Hurst and Z. Wang, "Combinational filters: Enhancing thin film interference coating designs with metamaterials", (*Awaiting Patent approval*).
4. **J. Monks**, S. Mir, S. Baxter, O. Armstrong, L. Yue, P. John Thomas, J. Williams, B. Aldred, A. Hurst, P. Mokarian and Z. Wang, "Wide-Angle Blue Light-Blocking Optical Metamaterial Filer via Block Copolymer Self-Assembly", (*Being prepared for submission*).

## NON-THESIS RELATED

5. **J. Monks**, B. Yan, N. Hawkins, F. Vollrath and Z. Wang, "Spider Silk: Mother Nature's Bio-Superlens", *Nano Letters*, vol. 16, no. 9, pp. 5842-5845, 2016.
6. B. Yan, Z. Wang, A. Parker, Y. Lai, J. Thomas, L. Yue and **J. Monks**, "Superlensing Microscope Objective Lens", *Applied Optics*, vol. 56, no. 11, p. 3142, 2017.
7. L. Yue, B. Yan, **J. Monks**, Z. Wang, H. Hguyen, D, Vu, O. Minin and I. Minin, "Production of photonic nanojets by using pupil-masked 3D dielectric cuboid", *Journal of Physics D: Applied Physics*, vol. 50, no. 17, p. 175102, 2017.
8. L. Yue, **J. Monks**, B. Yan and Z. Wang, "Large area formation of microsphere arrays by using laser surface texturing technology", *Applied Physics A: Materials Science & Processing*, vol. 123, no. 5, 2017.
9. L. Yue, Z. Wang, **J. Monks**, O. Minin, A. Shalin, I. Minin, "Photonic hook: A curved super-resolution light beam", *Optics Letters*, vol. 43, no. 4, pp. 771-774, 2018.
10. L. Yue, B. Yan, **J. Monks**, R. Dhama, Z. Wang, O. Minin and I. Minin, "Intensity-Enhanced Apodization Effect on an Axially Illuminated Circular-Column Particle-Lens", *Annalen der Physik*, p. 17000384, 2017.
11. L. Yue, B. Yan, **J. Monks**, R. Dhama, Z. Wang, O. Minin and I. Minin, "A Millimetre-Wave Cuboid Solid Immersion Lens with Intensity-Enhanced Amplitude Mask Apodization", *Journal of Infrared, Millimeter, and Terahertz Waves*, vol. 39, no. 6, pp. 546-552, 2018.
12. L. Yue, B. Yan, **J. Monks**, R. Dhama, Z. Wang, O. Minin and I. Minin, "Photonic jet by a near-unity-refractive-index sphere on a dielectric substrate with high index contrast", *Annalen der Physik*, vol. 530, no.6, p.1800032, 2018.
13. Z. Wang, B. Luk'yanchuk, L. Yue, B. Yan, **J. Monks**, R. Dhama, O. Minin, I. Minin, S. Huang and A. Fedyanin, "High order Fano resonances and giant magnetic fields in dielectric microspheres", *Scientific Reports*, vol. 9, no. 1, 2019
14. L. Yue, B. Yan, **J. Monks**, R. Dhama, C. Jiang, O. Minin, I. Minin and Z. Wang, "Full three-dimensional Poynting vector flow analysis of great field-intensity enhancement in specifically sized spherical-partciles", *Scientific Reports*, vol. 9, no.1, 2019.
15. B. Yan, L. Yue, **J. Monks**, X. Yang, D. Xiong, C. Jiang and Z. Wang, "Superlensing Plano-Convex-Microsphere (PCM) lens for direct laser nano marking and beyond", *Optical Letters*, 2020.

# CONFERENCES PROCEEDINGS

## THESIS RELATED

16. **J. Monks**, B. Yan, R. Dhama, L. Yue and Z. Wang, "Conjectural PT Symmetry Breaking for Switchable Lasing Anti-lasing of a Two Dimensional Arrayed Nanoparticle System", in *Progress in Electromagnetics Research Symposium*, Toyama, Japan, 2018.
17. **J. Monks**, L. Yue, B. Yan, A. Hurst and Z. Wang, "Shift-Free Wide-Angle Optical Thin film Metamaterial Notch Filter for Visible Laser Protection Systems", in *UK Defence and Security Doctoral Symposium*, Swindon, United Kingdom, 2018.
18. **J. Monks**, S. Mir, B. Jennings, L. Yue, B. Yan, R. Dhama, A. Hurst, P. Mokarian-Tabari and Z. Wang, "Direct Self-Assembled Optical Metamaterial Bandstop Filters with a Wide-Angle Shift-Free Operation, in *Nanometa 2019 7th International Topical Meeting on Nanophotonics and Metamaterials*, Seefeld, Austria, 2019.
19. **J. Monks**, B. Yan, R. Dhama, L. Yue, A. Hurst and Z. Wang, "Alternative Plasmonic Materials for Tailoring Optical Metamaterials Filters", in *Nanometa 2019 7th International Topical Meeting on Nanophotonics and Metamaterials*, Seefeld, Austria, 2019.

## NON-THESIS RELATED

20. Z. Wang, B. Yan, L. Yue and **J. Monks**, "Superlenses based on Loss-free Dielectric Materials", in *8th International Workshop on Advanced Materials Science and Nanotechnology*, Ha Long City, Vietnam, 2016.
21. **J. Monks**, B. Yan, N. Hawkins, F. Vollrath, F. Conradi, C. Mullineaux and Z. Wang, "Spider Silk helps create microscope superlens for nano-imaging and fabrication", *The Silk Road Symposium – Past and Present: Confucius Institute*, Bangor, United Kingdom, 2017.
22. **J. Monks**, B. Yan, N. Hawkins, F. Vollrath, F. Conradi, C. Mullineaux and Z. Wang, "Biomining for Mother Nature's Superlenses", in *Conference on Lasers and Electro-Optics/Europe and the European Quantum Electronics Conference*, Munich, Germany, 2017.
23. Z. Wang, B. Yan, **J. Monks** and L. Yue, "All-dielectric metamaterial superlenses: A new route to near-perfect lenses", in *Conference on Lasers and Electro-Optics/Europe and the European Quantum Electronics Conference*, Munich, Germany, 2017.
24. B. Yan, L. Yue, **J. Monks** and Z. Wang, "Near-field Focusing of Dielectric Microspheres: Super-resolution and Field-invariant Parameter Scaling", in *Progress in Electromagnetics Research Symposium*, St Petersburg, Russia, 2017.
25. L. Yue, B. Yan, **J. Monks** and Z. Wang, "Loss Impact on Super-resolution Photonic Jet Produced by a Teflon Sphere", in *Progress in Electromagnetics Research Symposium*, St Petersburg, Russia, 2017.
26. B. Yan, L. Yue, **J. Monks**, O. Guy, P. Nithiarasu, F. Jiang and Z. Wang, "A Novel Optofludic Lab-on-Chip Device with Integrated Super-resolution Imaging System", in *Progress in Electromagnetics Research Symposium*, Toyama, Japan, 2018.
27. Z. Wang, L. Yue, B. Luk'yanchuk, B. Yan and **J. Monks**, "Super resonance in microspheres", in *Nanometa 2019 7th International Topical Meeting on Nanophotonics and Metamaterials*, Seefeld, Austria, 2019.

# ABBREVIATIONS

| Abbreviation | Meaning | Abbreviation | Meaning |
|---|---|---|---|
| 2D | Two-dimensional | $\varepsilon''$ | Permittivity (imaginary component) |
| 3D | Three-dimensional | $\varepsilon_\infty$ | Permittivity constant offset |
| a | Particle radius | $\varepsilon_{eff}$ | Effective permittivity |
| $A$ | Additional matching layer | $\varepsilon_{ib}$ | Interband permittivity |
| A | Absorption | $\varepsilon_0$ | Permittivity of free space |
| AAO | Anodic Aluminium Oxide | Eq. | Equation |
| AB | Active blocking layer | $Er^{3+}$ | Erbium |
| AEI | Average effective index | $F$ | Lorentz force |
| AFM | Atomic force microscopy | FAA | Federal Aviation Administration |
| Ag | Silver | FEM | Finite element method |
| $AgNO_3$ | Silver Nitrate salt | FSS | Frequency surface structure |
| AI | Aluminium | FWHM | Full wave half maximum |
| $Al_2O_3$ | Aluminium oxide | $G$ | Dampening constant |
| AOI | Angle of Incident | $\Gamma$ | Dampening frequency |
| AR | Anti-Reflection | $\gamma$ | Dampening frequency |
| ASAP | Adjoint sensitivity analysis procedure | GPS | Global Positioning System |
| Au | Gold | GUI | Graphical user interface |
| $B$ | Magnetic field vector | $H$ | Magnetising field |
| $BaTiO_3$ | Barium titanate | $h$ | Planck's constant |
| BCP | Block copolymer | H | High index material |
| BM | Bound mode | $HfO_2$ | Hafnium dioxide |
| C | Restoring force | HW | Half wave |
| $c$ | Speed of light | $i$ | Imaginary unit |
| CAA | Civil Aviation Authority | IMS | Industrial methylated Spirits |
| $Ce^{3+}$ | Cerium | IR | Infrared |
| $\chi$ | Lorentz depolarisation factor | IVPT | Integrated visual photopic transmission |
| $\chi_e$ | Electric susceptibility | IVST | Integrated visual scotopic transmission |
| $\chi_m$ | Magnetic susceptibility | $\vec{J}$ | Current density |
| CMOS | Complementary metal oxide semiconductor | $k$ | Extinction coefficient |
| CPA | Coherent perfect absorber | $k_0$ | Wavevector |
| CW | Continuous wave | KTP | Potassium titanyl phosphate |
| $D$ | Displacement field | $l$ | Electron free mean path |
| DPSS | Diode-pumped solid-state | L | Low index material |
| DSTL | Defence science tech. labs | $\lambda$ | Wavelength |
| $E$ | Electric field vector | $\lambda_0$ | Reference wavelength |
| E-beam | Electron beam | LSPR | Localised surface plasmon resonance |
| $\varepsilon'$ | Permittivity (real component) | $\vec{M}$ | magnetisation |

| | |
|---|---|
| m | Mass |
| $M$ | Metamaterial layer |
| MDE | Maximum dazzle exposure |
| Metafilm | Thin film metamaterial equivalent layer |
| $MgF_2$ | Magnesium fluoride |
| MGT | Maxwell-Garnett theory |
| MM | Metamaterial |
| MPE | Maximum permissible exposure |
| MTI | Metamaterial Technology Inc. |
| $\mu_0$ | Permeability of free space |
| $n$ | Refractive index |
| $\tilde{n}$ | Complex refractive index |
| $n_{eff}$ | Effective refractive index |
| $n_i$ | Refractive index of incident medium |
| $n_t$ | Refractive index of transmitted medium |
| $Na_3AlF_6$ | Sodium hexafluoroaluminate |
| Nd:YAG | Neodymium doped yttrium aluminium garnet |
| NP | Nanoparticle |
| OD | Optical density |
| $\omega$ | Angular frequency |
| $\omega_p$ | Plasma frequency |
| $\omega_0$ | Resonant frequency |
| $\vec{P}$ | Polarisation |
| p | Dipole moment |
| P | Dipole density |
| PDMS | Polydimethylsiloxane |
| PNJ | Photonic nanojet |
| PS-b-PEO | Polystyrere-*block*-polyethylene oxide |
| PS-b-PMMA | Polystyrere-*block*-polymethyl methacrylate |
| $PT$ | Parity-Time symmetry |
| p-type | Transverse magnetic |
| PVP | Polyvinylpyrrolidone |
| $q$ | Electron charge |
| $Q_{abs}$ | CS absorption efficiency |
| $Q_{ext}$ | CS extinction efficiency |
| $Q_{scatt}$ | CS scattering efficiency |
| QBM | Quasi-bound mode |
| QW | Quarter wave |
| $R$ | Distance between two charges |
| $r$ | Electron displacement |
| R | Reflection |
| $r_\perp$ | Reflection coefficient (TE) |
| $r_\parallel$ | Reflection coefficient (TM) |
| RGB | Red Green Blue |
| $\rho$ | Density |
| RLC | Resistor inductor capacitor network |
| RM | Radiative mode |
| $S$ | Poynting vector |
| SCFT | Self-consistent field theory |
| $\sigma_{abs}$ | Cross-section (CS) absorption |
| $\sigma_{ext}$ | Cross-section (CS) extinction |
| $\sigma_{scatt}$ | Cross-section (CS) scattering |
| $SiO_2$ | Silicon dioxide |
| SP | Surface plasmon |
| SPP | Surface plasmon polaritons |
| s-type | Transverse electric |
| SVA | Solvent vapour atmosphere |
| T | Transmission |
| $t_\perp$ | Transmission coefficient (TE) |
| $t_\parallel$ | Transmission coefficient (TM) |
| $Ta_2O_5$ | Tantalum pentoxide |
| TE | Transverse electric |
| TEM | Transverse electromagnetic |
| $\theta$ | Angle of incident |
| $TiO_2$ | Titanium dioxide |
| TM | Transverse magnetic |
| TMM | Transfer Matrix Method |
| UV | Ultraviolet |
| $v$ | |
| $v_F$ | Fermi velocity |
| Vis | Visible |
| $Y_2O_3$ | Yttrium oxide |
| ZnS | Zinc Sulphide |
| $ZrO_2$ | Zirconium dioxide |

# CONTENTS

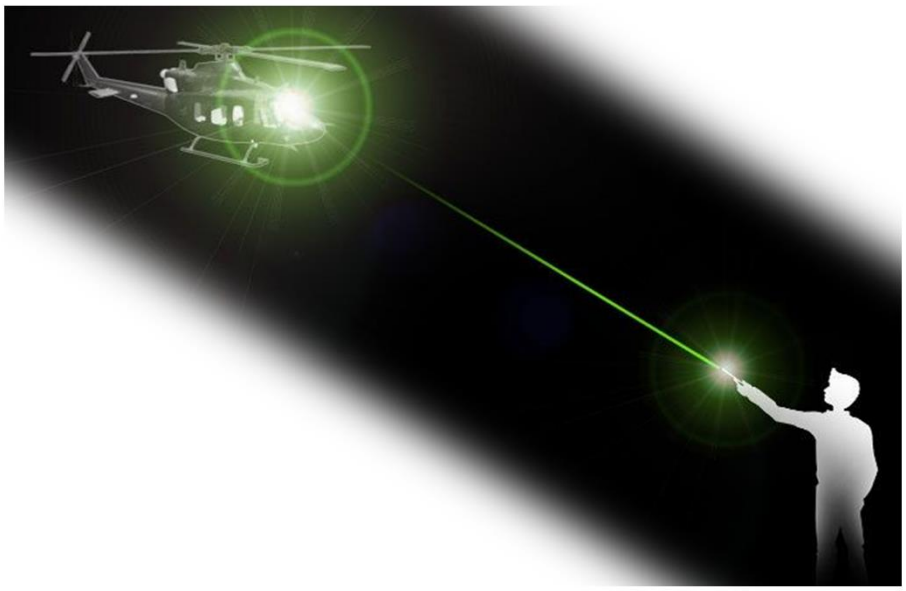

# CHAPTER I. INTRODUCTION

## 1.1 **Motivation**

Over the past decade, visible lasers have become as serious risk to aircraft, other transportation vehicles, and military and non-military personnel due to the ease of accessibility and low cost of ownership. Recent reports from the British Civil Aviation Authority (CAA) and their American counterparts, the Federal Aviation Administration (FAA), have illustrated that visible laser attacks from green lasers make up 83-91% of all reported incidents [1,2], with the CAA reporting that there were 941 laser illumination incidents on pilots within the U.K in 2018 [3]. The resulting damage caused from these attacks are mainly associated with laser eye dazzle [4,5] due to the distance of attacks, which describes the temporary impairment to the human eye caused from lasing light within the visible wavelengths. However, exposure for even a short time at the visible radiation range can produce retinal and photo-chemical damage to the human eye, and even cause thermal damage to the skin [6].

Reports in 2018 highlighted laser attacks by military to military personnel, with the US claiming that China have been using lasers to interfere with US military aircraft at, and near, military bases [7]. The activity resulted in minor eye injuries of two US military pilots but could have led to a much more serious outcome. Clearly the concern for both military and non-military personnel is on the increase, but particularly when concerning military action as laser weapons are forbidden under the Geneva Convention Protocol IV, the Protocol on Blinding Laser Weapons, of the 1980 Convention on Certain Conventional Weapons [8]. The protocol on blinding laser weapons prohibits the use of laser weapons specifically designed to cause permanent blindness and unnecessary suffering. Evidently, with more efficient weapon systems being designed and tested worldwide, violations to the Geneva Convention will inevitably be tested.

The alarming concern relating to laser attacks is that the lasing light could be incident from any angle. Traditional thin film optics, most commonly used Rugate notch filters, are the current staple for protection against lasers [9-11] and comprise of interference band filters organised as multiple thin coating layers of high and low refractive index dielectric films on a desired substrate [12]. This technology can provide high optical density, typically 4OD+ to 8OD+ [13], and allows for the blocking wavelength to be tailored according to the requirements [14]. Although Rugate filters are now the most commonly used laser protection systems, figure 1.1 shows the current technology available in fixed line protection.

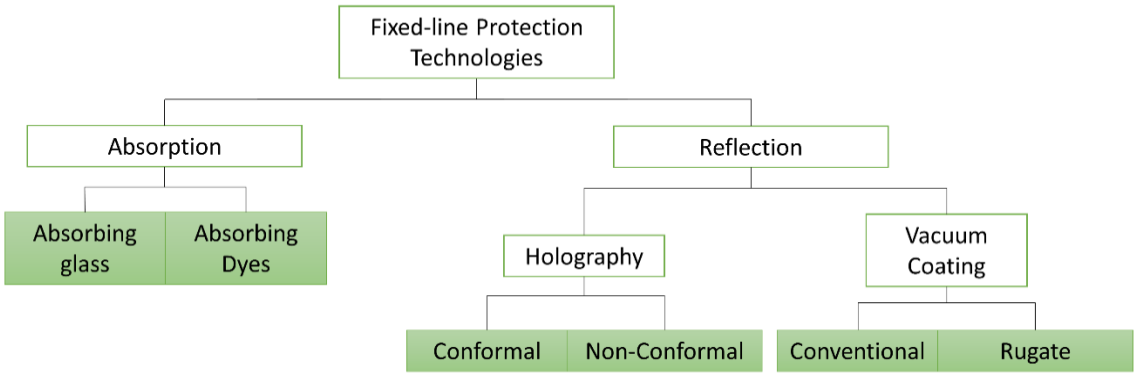


**Figure 1.1.** Current fixed-line technology for laser protection filters.

However, despite the technologies being well established, they have disadvantages, especially with angular intolerance [14]. The spectral characteristics of interference filters all shift to shorter wavelengths, blue shift, as the angle at which light is incident on the filter increases [15]. The angular sensitivity, rate at which the transmission and reflection characteristics shifts, depends on the design of the filter, specifically it depends on the refractive index values in the filters dielectric layers. The precise design of the filter and selection of materials will influence the angular sensitivity. With Holography, it is largely determined by the depth of refractive index modulation, where material and processing become a main issue. The spectral shift is also highly polarisation sensitive, more sensitive for *p-type* (TM) polarised light than for *s-type* (TE). Fixed-line absorption technology does not blue shift with angle but present a whole other issue with transparency and colouration.

Since the reflection peak blue shifts with angle of incidence, the filter's characteristics must be extended to the long wavelength sides if it is to continue to cover the specific laser wavelengths at increased angles. There is a direct relationship between the spectral bandwidth and the angular bandwidth, and consequently between the integrated visual transmission (the transmission from the human eye perspective) and the angular bandwidth. In layman's terms, to compensate for the angular intolerance, the filter must block off a larger portion of the spectrum towards the red wavelengths, so that when the beam incidence angle is greater than 0°, the blue shifted spectrum still covers the laser wavelength. However, by blocking off a larger portion of the transmission spectrum, the visual transmission from the human eyes' perspective decreases. Furthermore, blocking of the visible spectrum also leads to high colouration in the filters; for example, blocking a portion of the green band in the visible region will lead to a magenta colourised filter, and subsequently, giving the perception of removing the colour vision of the human eye.

A promising method to overcome the problems associated with traditional thin film filters could be the introduction of optical metamaterials (MMs). MMs are man-made materials that are not found in nature and are able to gain electromagnetic (EM) characteristics due to the structural arrangement of meta-atoms [16,17]. Meta-atoms, or unit-cells, are at the subwavelength scale and can achieve exotic EM properties when arranged in a pseudo-lattice pattern, which consists of one or more material composite that has shape, geometry, orientation and arrangement.

## 1.2 **Aims and Objectives**

The optical and transport industries, as well as government defence agencies, have a desired interest in developing a truly shift-free wide-angle (up to 60 degrees angle of incidence) laser protection system, which is the main drive behind this research. This research has been supported by Qioptiq's Defence & Aerospace division, who have provided the fundamental objectives to this project. The project aims to establish and design a shift-free wide-angle bandstop filter for laser protection device using theoretical and computational physics. Where possible, the theory will be supported by experimental analysis to provide clarity and test the key aspects of the underlying concepts. Therefore, the main overall intent of the research is to develop a simple optical metamaterial filter design that is practically achievable.

The specific project objectives are;

- Propose a method that can inversely design a metamaterial filter to block a desired wavelength. The ideal aim is for the user to select an arbitrary wavelength and the design to be established around that chosen wavelength of interest. The design must include structure and material considerations. [*Chapters 3 & 4*].
- Develop a job specific inverse optical metamaterial design tool from the principles set out in *Chapters 3 & 4.* [*Appendix A*]
- Design a laser protection device that blocks wavelengths in the visible part of the spectrum through the established inverse design method. The key wavelength of interest is a green 532 nm laser as this is the closest operational lasing wavelength to the human eye's peak photopic response of 555 nm and is the most commonly used wavelength during laser attacks. Furthermore, establishing alternative designs for visible band will also be put forward for discussion. [*Chapters 5, & 6*].
- Potential large area nano fabrication processes will be investigated, and design alterations will be customary in order to cater for the available methods. Any underlying key concepts will be fabricated as a proof of principle. [*Chapter 7*].

## 1.3 **Industrial Application**

Laser protection eyewear is set to be worth £260mil in 2021 [18] and the metamaterial market is set to be worth £3,728mil in 2025 [19]. Further development for the research carried out within this thesis could provide immense potential for future commercialisation. This is due to the unique angular performance features outlined, which have the impending ability to overcome the shortfalls of tradition thin film laser protection filters.

The prospective market expands from eyewear and could be introduced in the fields of Raman spectroscopy, confocal or multi-photon microscopy, laser-based fluorescence instrumentations and other life science applications.

With the development of large area nanoscale fabrication, the metamaterial filters could further expand to aircraft, trains and car windows. With the threat of laser attacks increasing, it is not too farfetched to imagine the aviation industry making a permanent safety feature to install laser protection on every aircraft window, (commercial, private and military). With this becoming a possible essential safety feature, the market demand and worth will greatly increase.

## 1.4 **Novelty of Thesis**

The novelties of this doctoral research are as follows;

1. Development of a new design route for optical bandstop filters with the use of metamaterials.
2. Consideration of design complexity vs. design practicality for manufacturability.
3. Construction of a flexible metamaterial design tool that can be used as a standalone software tool or supplement for industry design tools.

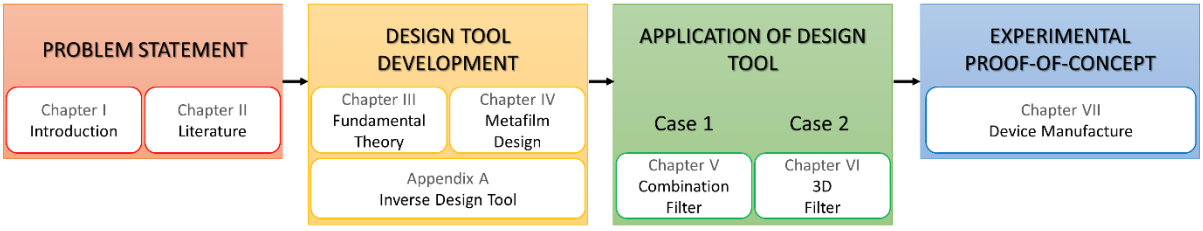


**Figure 1.2.** Thesis roadmap.

Figure 1.2 shows the roadmap of this thesis starting with the problem statement of current notch filter technology, and progresses through the design principles to develop two application solutions for visible band laser protection devices. The first case combines current technology with a metamaterial to consider the introduction of metamaterials into industry. The second application case demonstrates a full metamaterial notch filter. An innovative fabrication process has been outlined as an experimental proof of concept.

## 1.5 **Contribution to Field**

The main contributions within this thesis are as follows:

**Contribution 1 – Design principles for metafilm coatings**

Metafilm coatings are homogenised metamaterial layers that can be incorporated into many different designs, arrangements and organisations. Utilising the design principle of thin film optics, plasmonics and effective medium approximations, a metafilm can be designed to target any desired wavelength within the optical frequencies. This empowers optical designers to tune, adjust and design, single or multi fixed line notch filters within standard optical design software and without the need for intensive full wave electromagnetic solvers. The developed principles have been packaged into an inverse design software to define the properties of a metamaterial.

**Contribution 2 – Combination filters**

The addition of a metafilm layer to a standard thin film interference layer structure to create a combination filter, highlights the ability to enhance the optical performances comparing to a solo thin film filter. The combination filter provides a boost to the optical density of a given system as well as improving the blue shift behaviour of the dielectric thin film stack. Additionally, the presence of the metafilm layer supplies the filter with a baseline protection across all angle of incidences.

**Contribution 3 – Three-dimensional metamaterial filter**

The three-dimensional metamaterial filter provides a full wave simulation solution to better understand the plasmonic contribution of the metallic nanoparticles arranged within the metamaterial layers. The designed filter centres on a 532 nm fixed line filter and provides an in-depth optical analysis.

**Contribution 4 – Large area self-assembled nano-fabrication method**

Large area nano patterning that is required for optical metamaterials is a very difficult, costly and lengthy process with conventional lithographic methods. The employment of a self-assembled method has enabled experimental validation for metafilms. The metafilm has been designed to provide an optical notch filter at a blue laser wavelength. The method utilises diblock copolymers to form a thin nano patterned layer allowing for selective impregnation of metallic nanoparticles.

## 1.6 **Thesis Outline**

Chapter two outlines the basic theory and literature associated with the fundamental behaviour of light with consideration to laser light and its use as a weapon system with the associated consequences and hazards. This chapter will present modern day, and next generation, laser protection devices and systems, and a review of metamaterials with a focus on electromagnetic filters.

Chapter three will focus on the design aspects for inversely tailoring a metamaterial design. Deriving from plasmonic resonances, Mie theory will be investigated as an analytical method for inversely designing a filter's notch position by reviewing the extinction cross section for different size and shaped particles, as well as exploring the effects of alternative surround refractive indices. The progressive development towards an isotropic design will be drawn and a mathematical analysis for tailoring the notch response via plasmonic resonances will be outlined.

> **Publication**: J. Monks, B. Yan, R. Dhama, L. Yue, A. Hurst and Z. Wang, "Alternative Plasmonic Materials for Tailoring Optical Metamaterial Filters", in *Nanometa 2019 7$^{th}$ International Topical Meeting on Nanophotonics and Metamaterials*, Seefeld, Austria, 2019.

Chapter four follows on from the finding of *Chapter three* and institutes a method of design for shift-free wide-angle optical notch filter's through metamaterial assisted optical films. This draws on the well-established theories of optical thin film design techniques, and utilising these theories to assist the design of a full filter device by mixing together traditional optical thin films with embedded metamaterials to achieve a high transmission filter with a tailorable rejection wavelength.

> **Publication**: J. Monks, L. Yue and Z. Wang, "Effective Permittivity of Plasmonic Nanoparticle Composites Based on an Effective Drude-Lorentz Approximation Model", (Being prepared for submission).
>
> **Technical Company Report**: J. Monks, "Optical Thin film Equivalent Modelling for Metamaterials", Qioptiq Ltd., St. Asaph, United Kingdom, 2018.

Chapter five investigates the enhancing properties of metafilms when combined with traditional thin film interference filters. This chapter discusses design principles of thin film notch filters and introduces the design principles for a combinational filter. The results for the combination

filter highlight optical density and angular sensitivity improvements. The designs centre on laser wavelengths within the visible region.

**Patent**: J. Monks, J. Williams, L. Yue, A. Hurst and Z. Wang, "Combinational Filters: Enhancing Thin Film Interference Coating Designs with Metamaterials", [*Preparing Patent application*].

Chapter six implements the design principles, discussed in *Chapter four*, for a three-dimensional optical metamaterial notch filter for visible laser protection applications exploiting plasmonic resonances as the main blocking component. A comprehensive discussion on the design requirements and process will be put forward. The results will be analysed, reviewing the optical performance of the filter and its ability to block out laser light at chosen and known operational laser wavelengths.

**Publication**: J. Monks, L. Yue, B. Yan, B. Aldred, A. Hurst and Z. Wang, "A wide-angle shift-free metamaterial filter design for anti-laser striking applications", *Optics Communications*, vol. 429, pp. 53-59, 2018.

J. Monks, L. Yue, B. Yan, A. Hurst and Z. Wang, "Shift-Free Wide-Angle Optical Thin film Metamaterial Notch Filter for Visible Laser Protection Systems", in *UK Defence and Security Doctoral Symposium*, Swindon, United Kingdom, 2018.

Chapter seven reviews the theory and limitations of large area nano fabrication and manufacturing processes and presents a novel method to solve for the associated problem. This chapter analyses the promising field of block copolymers and provides theoretical and experimental results as a proof of concept and evaluation process for the theory outlined in previous chapters. The results highlight the shift-free wide-angle behaviour of plasmonic metamaterials.

**Publication**: J. Monks, S. Mir, B. Jennings, L. Yue, B. Yan, R. Dhama, A. Hurst, P. Mokarian-Tabari and Z. Wang, "Direct Self-Assembled Optical Metamaterial Bandstop Filters with a Wide-Angle Shift-Free Operation", in *Nanometa 2019 7$^{th}$ International Topical Meeting on Nanophotonics and Metamaterials*, Seefeld, Austria, 2019.

J. Monks, S. Mir, S. Baxter, O. Armstrong, L. Yue, P. John Thomas, J. Williams, B. Aldred, A. Hurst, P. Mokarian and Z. Wang, "Wide-Angle Blue Light-Blocking Optical Metamaterial Filer via Block Copolymer Self-Assembly", (Being prepared for submission).

Chapter eight concludes the results presented in this thesis, discusses the success of the project and highlights an outlook on the future work within the discipline of optical metamaterials for laser protection.

**Publication**: J. Monks, B. Yan, R. Dhama, L. Yue and Z. Wang, "Conjectural *PT* Symmetry Breaking for Switchable Lasing Anti-lasing of a Two-Dimensional Arrayed Nanoparticle System", in *Progress in Electromagnetics Research Symposium*, Toyama, Japan, 2018.

## 1.7 **References**


[1] UK Civil Aviation Authority, "Laser Incidents reported to the UK CAA 2016", Civil Aviation Authority, 2019.

[2] Federal Aviation Administration, "Reported Laser Incidents for 2016", Federal Aviation Administration, 2016.

[3] UK Civil Aviation Authority, "Laser Incidents reported to the UK CAA 2018", UK Civil Aviation Authority, 2019.

[4] C. Williamson and L. McLin, "Laser eye dazzle safety framework", International Laser Safety Conference, 2017. Available: 10.2351/1.5056871.

[5] J. Coelho, J. Freitas and C. Williamson, "Optical eye simulator for laser dazzle events", Applied Optics, vol. 55, no. 9, p. 2240, 2016. Available: 10.1364/ao.55.002240.

[6] J. Birtel, W. Harmening, T. Krohne, F. Holz, P. Charbel Issa and P. Herrmann, "Retinal Injury Following Laser Pointer Exposure", Deutsches Aerzteblatt Online, 2017. Available: 10.3238/arztebl.2017.0831.

[7] A. France-Presse, "China is shining military-grade lasers at US pilots flying out of Djibouti base", The National, 2018. [Online]. Available: https://www.thenational.ae/world/asia/china-is-shining-military-grade-lasers-at-us-pilots-flying-out-of-djibouti-base-1.727233.

[8] "Treaties, States parties, and Commentaries - CCW Protocol (IV) on Blinding Laser Weapons, 1995", Ihl-databases.icrc.org, 1995. [Online]. Available: https://ihl-databases.icrc.org/ihl/INTRO/570.

[9] M. Chen, C. Li, M. Xu, W. Wang, S. Ma and Y. Xia, "Eye-protection glasses against YAG laser injury based on the band gap reflection of one-dimensional photonic crystal", Optics & Laser Technology, vol. 39, no. 1, pp. 214-218, 2007. Available: 10.1016/j.optlastec.2005.02.005.

[10] A. Richter, "Characteristic features of laser-produced plasmas for thin film deposition", Thin Solid Films, vol. 188, no. 2, pp. 275-292, 1990. Available: 10.1016/0040-6090(90)90290-t

[11] F. Aguayo-Rios, F. Villa-Villa and J. Gaspar-Armenta, "Dichroic rugate filters", *Applied Optics*, vol. 45, no. 3, p. 495, 2006. Available: 10/1364/ao.45.000495.

[12] L. Epstein, "The Design of Optical Filters", *Journal of the Optical Society of America*, vol. 42, no. 11, p. 806, 1952. Available: 10.1364/josa.42.000806.

[13] "Coated filters", uvex Laservision, 2019. [Online]. Available: https://www.uvex-laservision.de/en/laser-safety-eyewear/laser-safety-filter/coated-filters/.

[14] P. Baumeister, *Optical coating technology*. Bellingham, WA.: SPIE Optical Engineering Press, 2004.

[15] F. Shan et al., "Blueshift of near band edge emission in Mg doped ZnO thin films and aging", Journal of Applied Physics, vol. 95, no. 9, pp. 4772-4776, 2004. Available: 10.1063/1.1690091.

[16] G. Eleftheriades and N. Engheta, "Metamaterials: Fundamentals and Applications in the Microwave and Optical Regimes [Scanning the Issue]", Proceedings of the IEEE, vol. 99, no. 10, pp. 1618-1621, 2011. Available: 10.1109/jproc.2011.2161808.

[17] W. Cai and V. Šalaev, *Optical metamaterials*. New York, NY: Springer, 2010.

[18] TechNavio, "Global Laser Protection Eyewear Market 2017-2021", technavio.com, 2017.

[19] Markets and Markets, “Metamaterial Market by Material Type (Electromagnetic, Terahertz, Photonic, Tunable, and FSS), Application (Communication Antenna, Windscreen, Solar Panel, Sensing, Display, and Medical Imaging), Vertical and Geographical – Global Forecast to 2025”, marketandmarket.com, 2017.

# CHAPTER II. LITERATURE REVIEW: THEORETICAL FOUNDATIONS AND PRELIMINARY WORK

This chapter outlines the background and importance of this study by investigating the key concepts and underpinning theories through exploring electromagnetic radiation and the damage effects of high-power visible light. Furthermore, a review of the current laser protection systems available and future systems is given. This section also provides an overview of metamaterials which is the foundation of the research presented in this thesis.

## 2.1 **Electromagnetic Theory, Visible Light and Plasmonics**

The electromagnetic spectrum is a range of frequencies describing electromagnetic radiation and associated wavelengths, figure 2.1. The electromagnetic spectrum covers wavelengths of thousands of kilometres, radio frequencies, down to a fraction of the size of an atomic nucleus, gamma rays. The spectrum is broken down into bands with each band having different characteristics. I.e. how they are produced, how they interact with matter, and their applications.

The interest of the electromagnetic spectrum for this thesis lies at the near-UV, optical and near-IR frequencies. Visible light is the portion of the spectrum that the human eye responds to and is made up of fundamental colours. Additionally, this region has many active laser wavelengths; thus, making the human eye susceptible to the laser wavelengths.

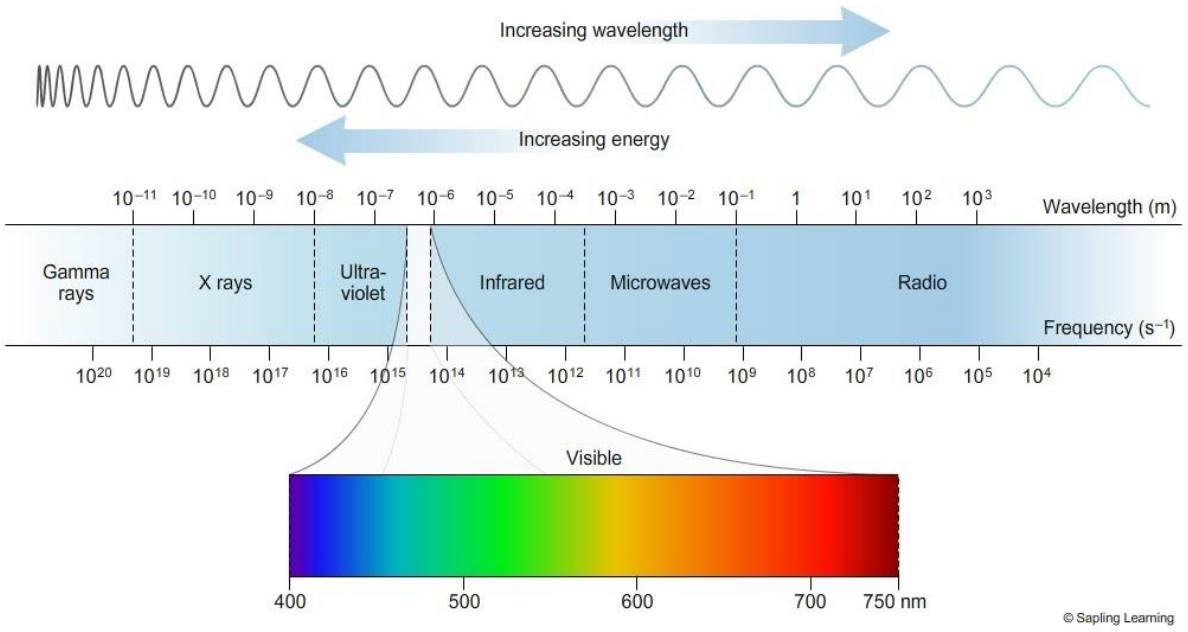


**Figure 2.1.** The electromagnetic spectrum [1].

### 2.1.1 Maxwell's Equations

The electromagnetic field is a vector field and is described by two vectors; the electric field vector ($E$) and the magnetic induction vector ($B$). It is considered for a general case that the two vectors are a function of time ($t$) with spatial coordinates ($R$). With the absence of the time function, the fields become static fields. With the removal of *R*, or non-dependence of the coordinates, the field can be considered homogeneous. The electric and magnetic vectors satisfy the four Maxwell's equations, table 2.1 (Eq.2.1.1a – Eq.2.1.1d) and were first formulated in 1861 by Scottish physicist James Clerk Maxwell [2]. Along with the electric and magnetic vectors, Maxwell's equation often includes the displacement field ($D$) and the magnetising field ($H$) which are related to the electric and magnetic fields together with the bound charges and currents through the constituent equations. Within the constituent equations the permittivity ($\varepsilon_0$) and permeability ($\mu_0$) of free space are introduced in Maxwell's equations.

**Table 2.1.** Maxwell's equations

| | **Differential Form** | **Integral Form** | |
|---|---|---|---|
| Faraday's law | $\vec{\nabla} \times E = -\frac{\partial B}{\partial t}$ | $\oint_C E \cdot d\vec{l} = -\frac{d}{dt}\int_S B \cdot \hat{n}\, da$ | (2.1.1a) |
| Ampere-Maxwell law | $\vec{\nabla} \times H = \vec{J} + \frac{\partial D}{\partial t}$ | $\oint_C H \cdot d\vec{l} = I_{enc} + \frac{d}{dt}\int_S D \cdot \hat{n}\, da$ | (2.1.1b) |
| Gauss's law for electric field | $\vec{\nabla} \cdot D = \rho$ | $\oint_S D \cdot \hat{n}\, da = q_{enc}$ | (2.1.1c) |
| Gauss's law for magnetic fields | $\vec{\nabla} \cdot B = 0$ | $\oint_S B \cdot \hat{n}\, da = 0$ | (2.1.1d) |
| | **Electric Field** | **Magnetic Field** | |
| Material equations | $D = \varepsilon_0 E + \vec{P}$ | $B = \mu_0 H + \vec{M}$ | (2.1.1e) |
| Wave Equations | $\nabla^2 E = \varepsilon_0 \mu_0 \frac{\partial^2 E}{\partial t^2}$ | $\nabla^2 B = \varepsilon_0 \mu_0 \frac{\partial^2 B}{\partial t^2}$ | (2.1.1f) |

Faraday's law states that the source of electric field rotor is equal to a magnetic induction alternating with time. Ampere-Maxwell law is defined by Ampere's circuital law which states that the source of magnetic induction rotary is electrical current described by the density ($\vec{J}$) and the alternating electric field that varies with time. Gauss's law for electric field states that the source of electric field is electrical charge described by density ($\rho$). The final is Gauss's law for magnetic fields and states that for magnetic induction, there is zero magnetic charges in nature.

The electromagnetic field properties can describe the situation that if a particle is present in an electromagnetic field, there will be a force acting on that particle. This force is known as the Lorentz force which contains information from the electric and magnetic fields.

$$F = qE + qv \times B \tag{2.1.2}$$

With $v$ defining the velocity of the particle.

An electromagnetic field also has the property to transfer energy. The flux of the energy is given by the Poynting vector (Eq. 2.1.3). The Poynting vector describes the amount of energy crossing a unit area per unit time.

$$S = \frac{1}{\mu_0} E \times B \tag{2.1.3}$$

Maxwell's equations can have some interesting effects, particularly for describing the interactions of the electromagnetic fields with a medium. For simple explanations, considering a neutral particle consisting of a positively charged nucleus and a negatively charged cloud of electrons surrounding the nucleus, figure 2.2a. *The electron cloud model* [3] *differs from the Bohr model* [4] *which explains the behaviour of electron orbits for quantum mechanics. The electron cloud model states that one cannot know exactly where an electron is at any given time but provides probability that an electron is more likely to be in a specific area.* If an electric field is applied to the particle, the electron cloud will shift with respect to the nucleus. This presents two charges, a negative charge on one side of the particle and a positive charge on the opposite side. This is known as an electric dipole, figure 2.2b, and the phenomenon is called polarisation which also occurs on the macroscopic scale.

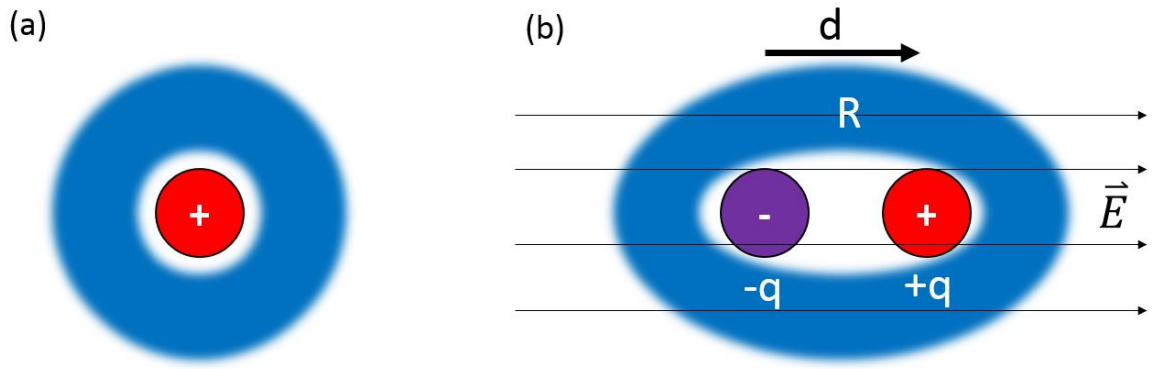


**Figure 2.2.** (a) Neutral particle without an external electric field. (b) Particle displaying dipole properties due to the external electric field.

The electric dipole of a system is given by (Eq. 2.1.4).

$$d = \sum_i r_i q_i \rightarrow d = Rq \tag{2.1.4}$$

Where $R$ is the distance between the two charges and $q$ is the charge of the system.

### 2.1.2 Permittivity and Permeability

Polarisation and magnetisation describe the density of the electric and magnetic dipole moments that have been induced by an external field. Thus, polarisation is a function of electric field and magnetisation is a function of the magnetic field.

$$\vec{P}(E) = \vec{P}_0 + \chi_e E + \chi_e^2 E^2 + \cdots \tag{2.1.5a}$$

$$\vec{M}(H) = \vec{M}_0 + \chi_m H + \chi_m^2 H^2 + \cdots \tag{2.1.5b}$$

Where $\vec{P}_0$ is the constant polarisation, usually zero with the exception for pyroelectric materials, $\chi_e E$ is a linear term that contains the electric susceptibility and the electric field vector. The last term is a non-linear term in the form of a quadratic function and is proportional to the second power of electric field. Similarly, this applies to the magnetisation equation. However, at optical frequencies the constant polarisation and the linear terms are infinitesimal, therefore can be neglected [5]. Some exemptions can be applied when considering modern day optics such as metamaterials [6] and high index all-dielectric structures [7].

The permittivity and permeability are material properties that interact with the electromagnetic fields and can be simply generalised by the following formula which can provide a complex solution. Considering that for general optics, the magnetisation is approximately zero, discussions of the permittivity need only apply. The complex function of the permittivity allows the real part to describe the polarisation of the material and the imaginary part to be responsible for the loss in the material.

$$\varepsilon = 1 + \chi_e \tag{2.1.6a}$$

$$\mu = 1 + \chi_m \tag{2.1.6b}$$

Table 2.2 provides a simplistic summary of the permittivity for different materials at optical frequencies where $\varepsilon'$ defines the real part of the permittivity and $\varepsilon''$ defines the imaginary part of the permittivity.

**Table 2.2.** Permittivity of materials

| | Visible Region | Infrared Region |
|---|---|---|
| **Metals (Au, Ag, Cu, Al …)** | $\varepsilon' < 0$<br>$\varepsilon'' \approx 1$ | $\varepsilon' \ll -1$<br>$\varepsilon'' \gg 1$ |
| **Semiconductors (GaAs, Si …)** | $\varepsilon' \approx 11 - 16$<br>$\varepsilon'' \approx 0 - 2$ | $\varepsilon' \approx 11 - 16$<br>$\varepsilon'' \approx 0$ |
| **Glasses** | $\varepsilon' \approx 2.0 - 2.3$<br>$\varepsilon'' \approx 0$ | $\varepsilon' \approx 2.0 - 2.3$<br>$\varepsilon'' \approx 0$ |

### Optical Material Properties

The oscillation frequency of a nanoparticle can be quantitatively described by the materials complex dispersive, frequency dependant, permittivity ($\varepsilon$) or refractive index ($n$) and extinction coefficient ($k$). This dispersive nature is significant to many optical effects.

$$\tilde{n}^2 = (n^2 - k^2) + 2ink \equiv \tilde{\varepsilon} = \varepsilon_r + i\varepsilon_i \tag{2.1.7}$$

### The Drude-Lorentz Model

The Drude-Lorentz model can describe the dispersive permittivity of many materials. The model applies a time-varying electric field on the bound electrons within a material, considering the material as a bulk medium [8]. The net force on an electron that is bound to its ion core for a given material is described by (Eq. 2.1.8).

$$m\frac{\partial^2 r}{\partial t^2} = qE - G\frac{\partial r}{\partial t} - Cr \tag{2.1.8}$$

Where, $m$ is the mass and $q$ is the charge of an electron, r describes the electron's displacement from an equilibrium state, E is the electric field, $G$ is the dampening constant and $C$ is the restoring force. The three terms on the right-hand side of (Eq. 2.1.8) each have their individual role to play in describing the net force. The first term denotes the force experienced by the electron with an applied field, the second term signifies the dampening force resulting from electron scattering and the third term represents the electrons attraction to the ion core. By allowing the electron to assume a harmonic oscillation at the same frequency as the electric field, $r = r_0 e^{i\omega t}$ and $E = E_0 e^{i\omega t}$ can be substituted.

$$-\omega^2 mr = qE + i\omega Gr - Cr \tag{2.1.9}$$

Adapting (Eq. 2.1.9) to make the driving term the subject, the equation of motion becomes more evident.

$$qE = Cr - i\omega Gr - \omega^2 mr \tag{2.1.10}$$

By allowing the driving term to be the subject, three terms become distinguishable, as does the description of their roles in the system. The three terms available now define low frequencies, high frequencies and during resonant conditions.

At low frequencies (Eq. 2.1.11), the restoring force is maintained by the force applied from the electric field. Thus, the terms that include $\omega$ become negligible.

$$qE = Cr \tag{2.1.11}$$

At high frequencies (Eq. 2.1.12), the electron effectively becomes a free particle where there is no force acting to restore equilibrium or dampen the motion. This is a result of the dominating $\omega^2$ term.

$$qE = -\omega^2 mr \tag{2.1.12}$$

During the resonance period (Eq. 2.1.13), the dampening term directs the result and actions a limitation to the velocity, causing the displacement of the electrons that lags the electric field.

$$qE = -\omega Gr \tag{2.1.13}$$

Following the analytical breakdown of the terms found in (Eq. 2.1.9), that equation can be rewritten to give the following:

$$r = \frac{qE}{-i\omega G + C - \omega^2 m} = \frac{\left(\frac{qE}{m}\right)}{-i\omega\frac{G}{m} + \frac{C}{m} - \omega^2} \tag{2.1.14}$$

Grouping certain components together, namely $\gamma = G/m$ and $\omega_0 = \sqrt{C/m}$, where $\omega_0$ is the resonant frequency, the subsequent equation can be obtained:

$$r = \frac{\left(\frac{qE}{m}\right)}{-i\omega\gamma + \omega_0^2 - \omega^2} \tag{2.1.15}$$

The significance of (Eq. 2.1.15) shows that the position of the electron, as a function of time, is directed by the dampening term when under resonance.

To obtain the frequency dispersive permittivity, $\varepsilon_r$, for a given material, the polarisation can be expressed as a density of discrete dipole moments, with the electric susceptibility represented as a relation to the materials permittivity, $\chi_e = \varepsilon_r - 1$ .

$$P = np = nqr = \varepsilon_0\chi_e E = \varepsilon_0(\varepsilon_r - 1)E \tag{2.1.16}$$

Where $P$ is the dipole density and $p$ is the dipole moment that is a product of displacing an electron with charge $q$ at a distance of $\boldsymbol{r}$ from the position of equilibrium.

The expression for the relative permittivity of a material can be derived by substituting (Eq. 2.1.15) into (Eq. 2.1.16).

$$\varepsilon_r = 1 + \frac{\left(\frac{nq^2}{m}\right)}{\varepsilon_0(-i\omega\gamma + \omega_0^2 - \omega^2)} \tag{2.1.17}$$

The common form for expressing the permittivity is found in (Eq. 2.1.18), with notation of the plasma frequency, $\omega_p = \sqrt{\frac{nq^2}{\varepsilon_0 m}}$, included.

$$\varepsilon_r = 1 - \frac{\omega_p^2}{\omega^2 - \omega_0^2 + i\omega\gamma} \tag{2.1.18}$$

An example of a hypothetical material can be found in figure 2.3. The figure shows the real and imaginary parts of the Drude-Lorentz permittivity as a function of frequency. The imaginary component peaks at $\omega_0$, which in turn, induces the real component to cross the origin.

The Drude-Lorentz model can be used to describe dielectrics due to the electrons being tightly bound to the atoms.

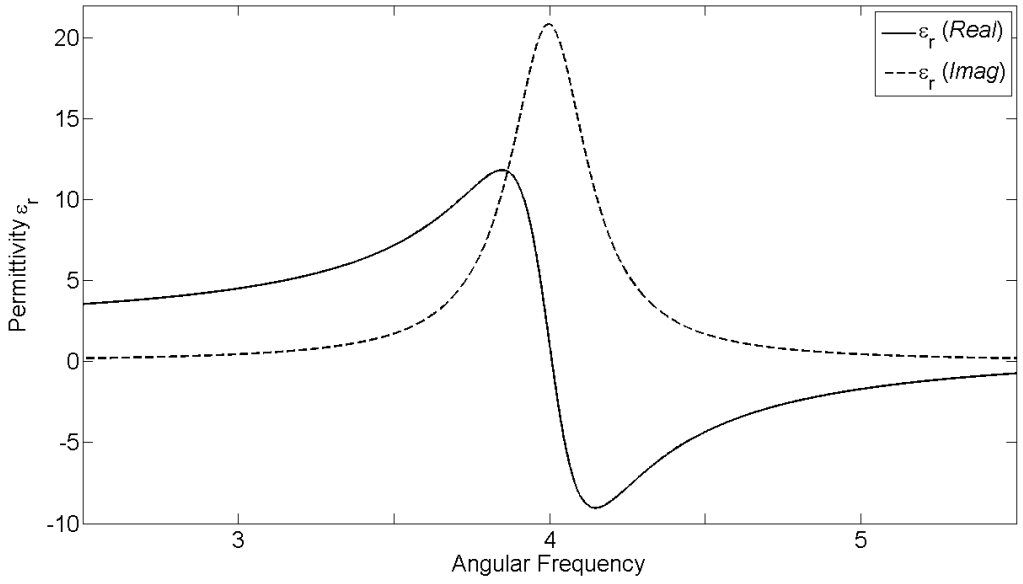


**Figure 2.3.** The Drude-Lorentz permittivity for a conjectural material with $\omega_0 = 4, \omega_p = 5, and\ \gamma = 0.3$.

**The Drude Model**

Similar to the Drude-Lorentz model, most metals ascribe to frequency-dependent permittivity [9]. The electromagnetic relations with metals are dictated by the collection of free electron movement within a metal crystalline structure. This introduces a special case of the Drude-Lorentz model, namely the Drude model, where the restoring force or spring constant is removed from the model due to the Coulomb's interaction between the electrons and the ion cores (i.e $\omega_0 = 0$) [10]. The Drude model is useful for describing metallic mediums as the model describes only the free electrons [11]. Neglecting the restoring force is possible considering that the applied electric field interacts strongly with the conducting electrons.

The Drude equation (Eq. 2.1.19) response can be seen in figure 2.4 for a given hypothetical material.

$$\varepsilon_r = 1 - \frac{\omega_p^2}{\omega^2 + i\omega\gamma} \tag{2.1.19}$$

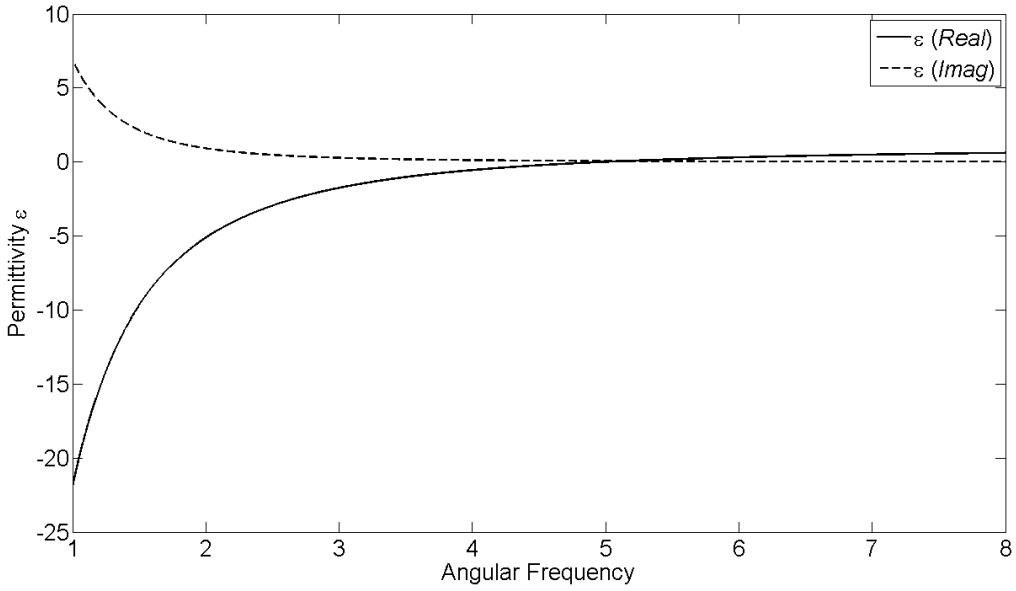


**Figure 2.4.** The Drude permittivity for a conjectural material with $\omega_p = 5, and\ \Gamma = 0.3$. The plasmas frequency is the point at which the real part switches from negative to positive.

An important aspect to the Drude model is defined by the real part of the permittivity becoming negative below the plasma frequency $\omega_p$. At frequencies below $\omega_p$, the material becomes metallic in response due to the electrons at the surface of the material responding to the incident field. This gives an antiphase where the electrons out-of-phase oscillations act to produce a reflected field [12], hence why a yellowish colour is seen with gold for example.

The Drude model accounts for the free electrons within a material but does not describe the electrons that are bound to the atoms for the given material. Although the behaviour of some metals is predominately due to the free electrons' response (sample selection found in table 2.3), the involvement of the bound electrons should also be considered when subjected to high frequencies, including optical regions. The Drude model clearly describes the outer atomic orbiting electrons, specifically the 4s, 5s and 6s states for Copper, Silver and Gold, respectively [13]. Interband transitions occur in metals when the bound electrons are excited by light waves, for example, the interband transition from the 4d state to the 5s state for Silver.

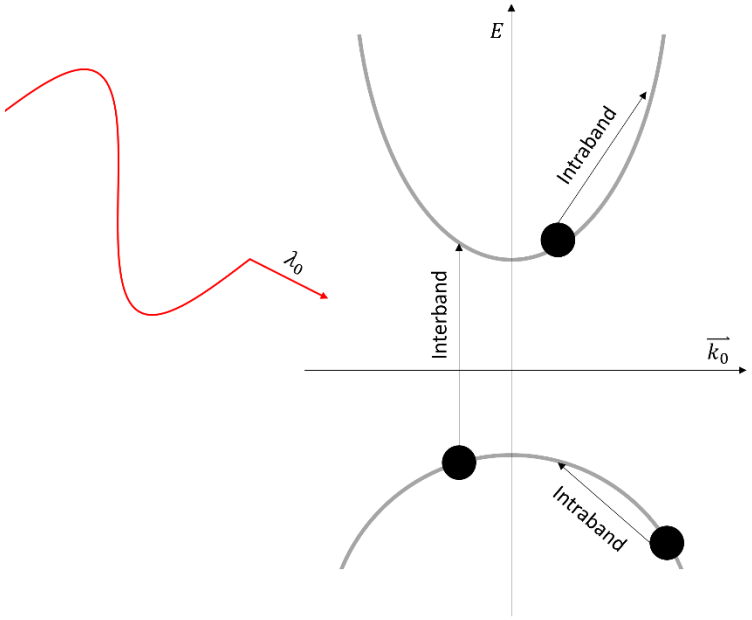


**Figure 2.5.** A diagram to represent interband transitions vs intraband transitions.

The influence of the interband transitions of bound electrons can be described in a standard Drude-Lorentz form (Eq. 2.1.20) and contributes to the permittivity of metals.

$$\varepsilon_{ib} = 1 + \frac{\omega_1^2}{\omega_0^2 - \omega^2 - i\omega\gamma} \tag{2.1.20}$$

Where $\omega_0$ signifies the bound electrons oscillation frequency when an electric potential is applied, and $\omega_1$ and $\gamma$ relate to the density and damping force of the bound electrons, respectively.

The complete permittivity function of metals contains both the Drude term to describe the free electrons and the Lorentz term to describe the bound electrons. The impact of the interband on the permittivity is noticeable at wavelengths much longer than the resonant wavelengths. Thus, when working at longer wavelength, away from resonance, the frequency dependent $\varepsilon_{ib}$ can be

replaced by a constant offset denoted $\varepsilon_\infty$. Due to the complicated band structure of bound electrons, there are often multiple interband transitions, particularly in the UV spectrum for metals [14]. To obtain the constant offset, an integration of all pertinent transitions must be taken into account. $v_F$ denotes the Fermi velocity which is the velocity associated to the Fermi energy.

$$\varepsilon = \varepsilon_{ib} + 1 - \frac{\omega_p^2}{\omega^2 + i\omega\Gamma} = \varepsilon_\infty - \frac{\omega_p^2}{\omega^2 + i\omega\Gamma} \tag{2.1.21}$$

**Table 2.3.** Optical properties for noble metals.

| **Metal** | $\boldsymbol{\varepsilon_\infty}$ | $\boldsymbol{\omega_p(10^{15}s^{-1})}$ | $\boldsymbol{\Gamma(10^{15}s^{-1})}$ | $\boldsymbol{v_F(10^6 ms^{-1})}$ |
|---|---|---|---|---|
| Silver | 4 | 14.0 | 0.032 | 1.4 |
| Gold | 9.5 | 13.8 | 0.11 | 1.4 |
| Copper | 8.8 | 13.4 | 0.14 | 1.6 |
| Aluminium | 15.1 | 22.9 | 0.92 | 2 |

Although Drude's model is approximate and measured experimental data should be preferable for the permittivity values, the Drude model does give a physical insight into the behaviour of conduction electrons that have been excited by a time-harmonic incident field.

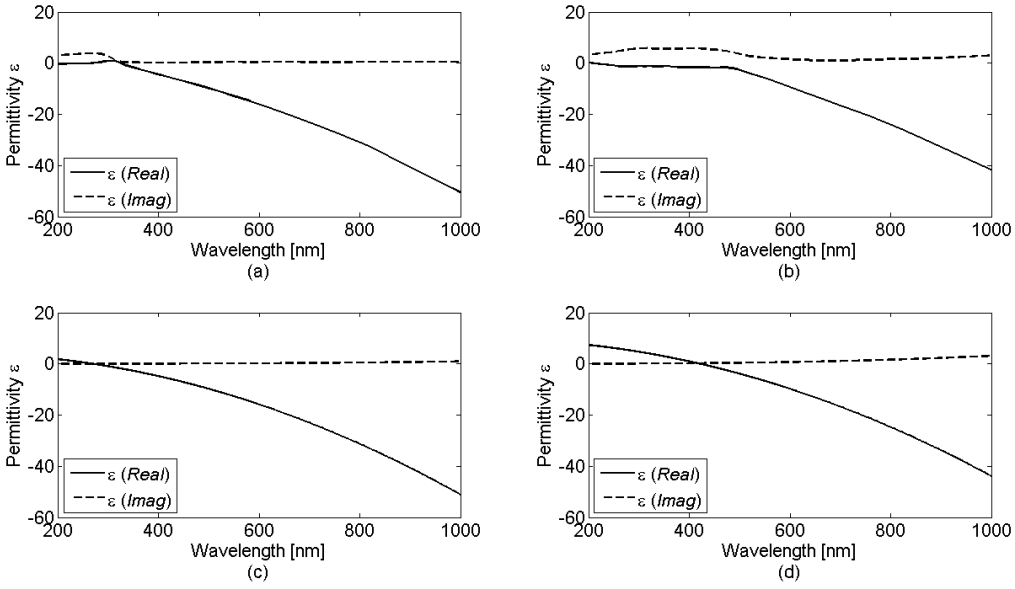


**Figure 2.6.** Permittivity values, real and imaginary, for (a) Ag from Johnson & Christy, (b) Au from Johnson & Christy, (c) Ag from Drude formula and (d) Au from Drude formula.

Experimental data that is commonly used was measured by Johnson and Christy and describes many metals at optical frequencies, including Silver and Gold [15]. Figure 2.6 shows the closely matched behaviour for theory (Drude model) and experimental results (Johnson & Christy).

**Particle Size Correction for Drude's Model**

When studying the interaction of light-matter on the nanoscale, the properties of the materials need to be further modified due to the size effect [16]. A fixed dampening value, $\Gamma$, becomes insufficient when the geometric size of the material goes below the skin depth. For noble metals, the skin depth at the visible region is around 50 nm. The dampening constant, $\Gamma$, is related to the Fermi velocity, $v_F$, and the electrons mean free path, $l$. As the geometric length of a continuous metallic section of the metamaterial unit structure approaches or surpasses the movement of free electrons, the geometric metamaterial becomes the physical boundary for the effective mean free path.

$$\Gamma_{Adjusted} = \frac{v_F}{l} + \frac{v_F}{\left(\frac{4a}{3}\right)} = \Gamma + \Gamma_{Particle} \tag{2.1.22}$$

The adjusted dampening constant has an additional term added to the bulk dampening constant, which takes into consideration the particle radius, $a$. As such, when the particle radius decreases, the free electrons exhibit more collisions resulting in an increased dampening frequency.

$$\varepsilon = \varepsilon_\infty - \frac{\omega_p^2}{\omega^2 + \Gamma_{Adjusted}^2} + i\frac{\omega_p^2\,\Gamma_{Adjusted}}{\omega\left(\omega^2 + \Gamma_{Adjusted}^2\right)} \tag{2.1.23}$$

When evaluating the adjusted particle size Drude model, it is evident that the modified dampening constant is only marginally related to the real part but is proportionally related to the imaginary part. As a result, the real function of the permittivity varies very little when considering size effects compared to bulk. However, the imaginary part vastly alters for nanostructured metals below the free mean path of the electron. The effect can be found in figure 2.7, which shows the permittivity's imaginary component increase in magnitude as the radius of a spherical silver particle decreases. The deviation of magnitude is larger as the wavelength increases.

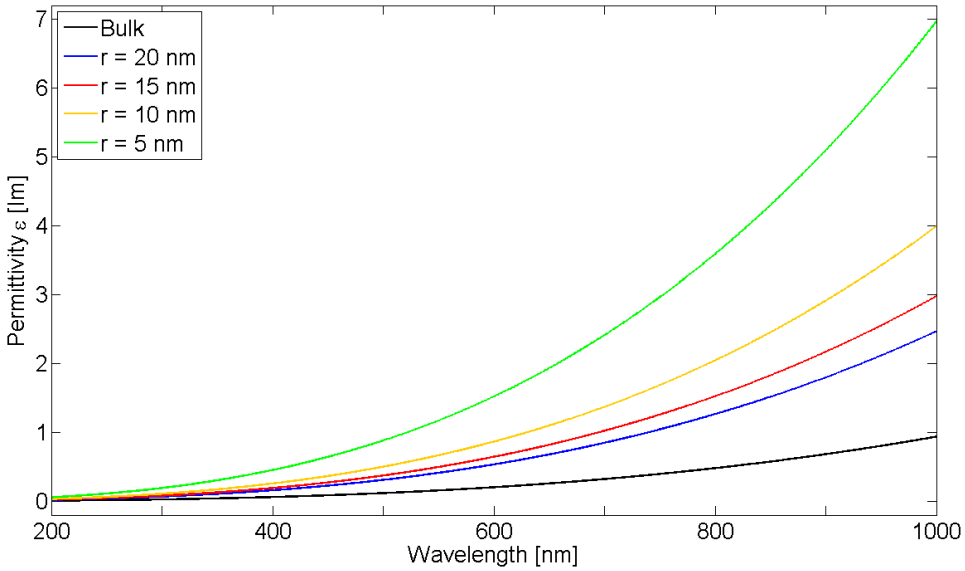


**Figure 2.7.** The imaginary part of the permittivity of silver with consideration to spherical particle size.

### 2.1.3 Fresnel Equations

Fresnel equations [8] define the transmission and reflection of electromagnetic radiation when incident on an interface from another medium, *example – Air to Glass.* The equations assume that the interface between the two mediums are flat, with the mediums being isotropic and homogeneous. Even for non-flat surfaces, the equations can hold true by assuming an effective index [17]. It is also assumed that the incident light is a plane wave. This is satisfactory to solve any given optical problem since any incident light field can be resolved into plane waves and polarisation.

Polarisation can be grouped into two sections; Transverse electric (TE or s-) and transverse magnetic (TM or p-). The s-polarisation describes the electric field being perpendicular to the plane of the incident light, with p-polarisation describing the magnetic field being perpendicular to the plane of the incident light. A visual diagram is shown in figure 5.8 for light-matter interactions according to the incident polarisation light and reflected light.

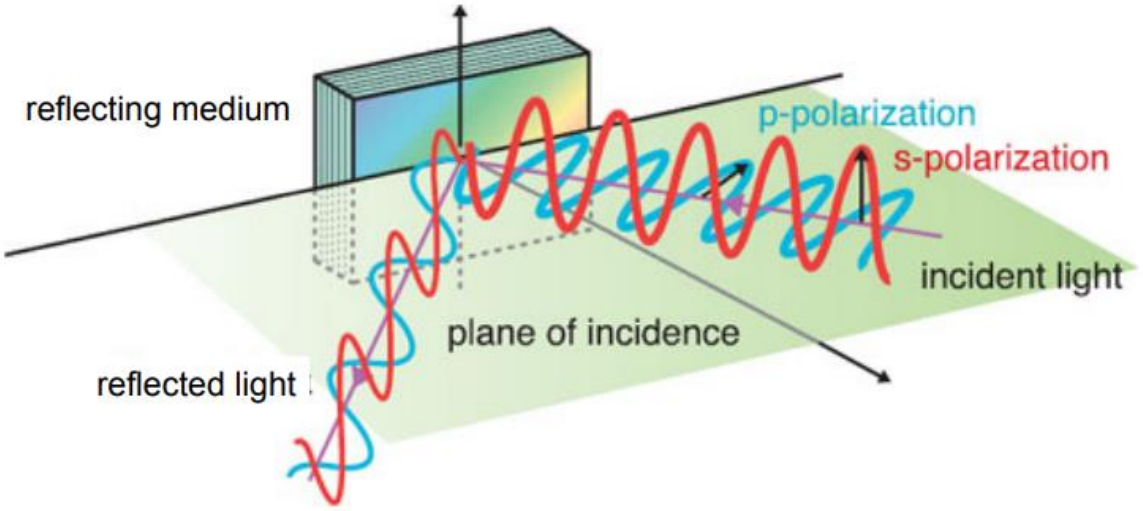


**Figure 2.8.** Diagram showing the visual effects of polarisation. [18].

Fresnel's equations are defined in table 2.4 and describe the transmission (*t*) and reflection (*r*) coefficients. Where $n_i$ is the incident refractive index, $n_t$ is the transmitted refractive index and $\theta$ are the associated angles.

**Table 2.4.** Fresnel's equations for transmission and reflection coefficients.

| | **Transmission Co.** | **Reflection Co.** | |
|---|---|---|---|
| s- polarisation | $t_{\perp} = \frac{2n_i \cos(\theta_i)}{n_i \cos(\theta_i) + n_t \cos(\theta_t)}$ | $r_{\perp} = \frac{n_i \cos(\theta_i) - n_t \cos(\theta_t)}{n_i \cos(\theta_i) + n_t \cos(\theta_t)}$ | (2.1.24a) |
| p- polarisation | $t_{\parallel} = \frac{2n_i \cos(\theta_i)}{n_i \cos(\theta_t) + n_t \cos(\theta_i)}$ | $r_{\parallel} = \frac{n_i \cos(\theta_t) - n_t \cos(\theta_i)}{n_i \cos(\theta_t) + n_t \cos(\theta_i)}$ | (2.1.24b) |

The transmittance (*T*) and reflectance (*R*) are given by squaring the absolute values of the coefficients.

$$T = \frac{n_2 \cos\theta_t}{n_1 \cos\theta_i}|t|^2 \text{ and } R = |r|^2 \qquad (2.1.25)$$

Figure 2.9 shows the angular dependence of the reflectance. In figure 2.9a, the wave is incident from air to dielectric medium, and in figure 2.9b the wave is incident from dielectric medium to air. At normal incidence the polarisation cannot be distinguished; however, this is not the case for the rest of the angles beside 90°. For the case of the wave incident from air to the dielectric, the reflectance is equal to zero at some angles. This is known as the Brewster angle. The case is also true when the wave is incident from the dielectric to air. Yet, for the second case, there is the presence of perfect reflectance starting from some angle. This is called the critical angle and is the phenomenon of total internal reflection.

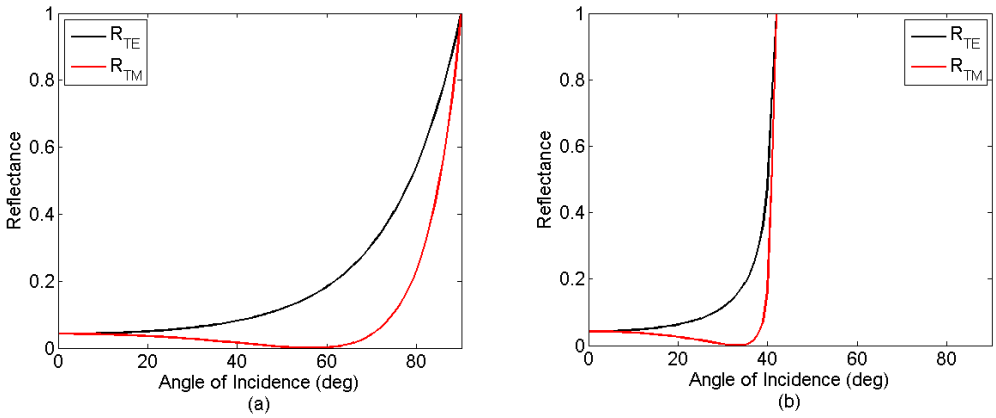


**Figure 2.9.** (a) Brewster angle and (b) critical angle for $n_i = 1$ and $n_t = 1.52$.

Absorption (*A*) is not present if the refractive index is purely real. However, for a complex refractive index the imaginary component induces loss into the material in the form of absorption. The imaginary term of the refractive index is often called the extinction coefficient.

$$A = 1 - R - T \tag{2.1.26}$$

### 2.1.4 **Plasmons**

When an external electric field is applied to a metallic particle, the electron in the outer shell becomes free to move and does so in the opposing direction to the field. This results in a net negative charge accumulation on one side of the particle, leaving a net positive charge remaining on the mirrored side of that particle. This phenomenon is known as a dipole. Due to the net separation of charges, the negative charges are attracted to the positive charges. The attraction force acts as a restoring force on the electrons associated with that particle, much like the common analogy of a mass on a spring, causing a resonant condition, providing that a time-varying electric field is applied.

Deriving from Newton's second law of motion [19]; initially, the external field may be ignored and the restoring force, $F_r$, is the subject of the displaced charges from equilibrium. Where *m* is the mass of the particle in motion and ***r*** is the particle's position.

$$F_r(t) = m\frac{d^2r}{dt^2} \tag{2.1.27}$$

Providing the harmonic solution of $r = r_0 e^{i\omega t}$ and $F_r = F_{r0} e^{i\omega t}$, the restoring force scales linearly with respect to the displacement.

$$k_0 r = \omega^2 m r \tag{2.1.28}$$

Thus, the oscillation frequency is;

$$\omega = \sqrt{\frac{k_0}{m}} \tag{2.1.29}$$

This example is generalised; however, it does determine the existence of a restoring force under a static condition and provides a method to calculate the natural oscillation frequency of a particle's electron. This type of electron oscillation referencing to a nanoparticle is known as localised surface plasmon resonance, LSPR [20]. For metallic nanoparticles, the natural resonances occur at the optical region of the electromagnetic spectrum, resulting in the nanoparticles strongly scattering and absorbing light at these wavelengths.

**Plasmonic Resonances**

The presence of free electrons in metals is very important in the field of plasmonics. Plasmonics deals with the interactions between light and metallic structures [21]. The dispersion of metals at optical frequencies allows for surface waves to exist, known as surface plasmon polaritons (SPP). The SPP wavelengths are very short compared to the excitation wavelength due to the dispersion relation of SPP, figure 2.10. The property of shorter wavelengths is the key to plasmonics because it allows light to be confined to volumes much smaller than the wavelength of light [22].

Surface waves propagating in a medium assume distinct behaviours below and above the plasma frequencies, $\omega_p$. Therefore, SPPs can be described by different modes [21]. Bound modes (BM) occur for all $\omega \leq \omega_{sp}$. BMs define SPs that occur at the interface with the spectral band denoted as the 'plasmonic band'. The Quasi-bound mode (QBM), lies in the region $\omega_{sp} < \omega < \omega_p$. This region is called the 'forbidden band' as it is the frequency gap region with a purely imaginary $k_x$, therefore forbidding the propagation of SPs, where the wave decays exponentially with distance inside the metal. The third mode, Radiative mode (RM), where $\omega > \omega_{sp}$, is transparent to the incident electromagnetic wave due to the SP wave propagating through the metal without decaying. This mode is named the 'transparent band'.

$$k_x = k_{sp} = \frac{\omega}{c}\sqrt{\left(\frac{\varepsilon_r \varepsilon_d}{\varepsilon_r + \varepsilon_d}\right)} \tag{2.1.30}$$

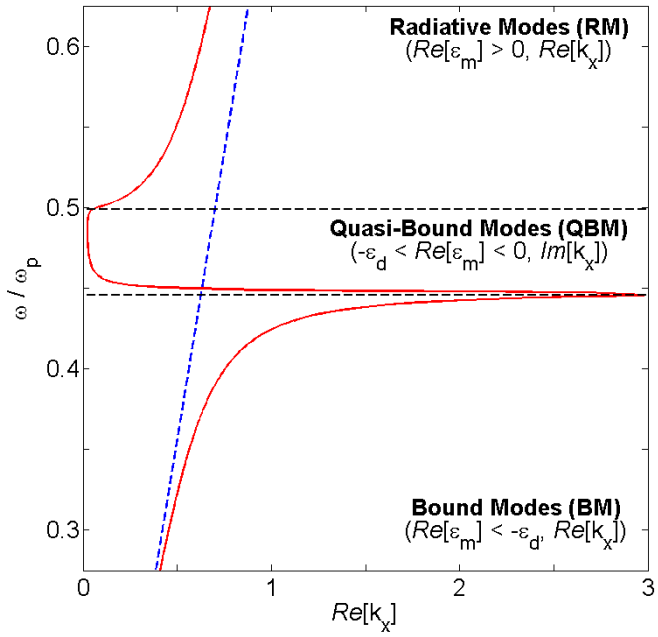


**Figure 2.10.** Dispersion relation of surface plasmons for Drude model and the different modes. The dotted blue line represents the 'light line', $\omega = c\, k_x$.

Previous references to localised surface plasmon resonance (LSPRs) are a special case to the SPP and are a result of the SPs being confined to a nanoparticle. LSPRs display some important and useful effects; electric field enhancement and optical absorption at the plasmon resonant frequency [23]. When the particle's plasmons are excited by the incident light at a specific frequency, the particle harvests the light by the optical cross-section and will be confined to a volume comparable to the particle's geometric volume [24].

For sub-wavelength particles, plasmons can enable a resonance wavelength much smaller than the size of that particle because the oscillating electric field acts on the charges within the particles. This polarisability can be described by the Clausius-Mossotti equation [25], where $a$ is the particle size, $\varepsilon_r$ is the permittivity of the particle, $\varepsilon_d$ is the permittivity of the surrounding dielectric and $\chi$ is a relation to the Lorentz depolarisation factor determined by the shape and orientation of the particle. For spherical particles $\chi = 2$ and is discussed further in *Chapter IV*.

$$\alpha = 4\pi a^3 \left( \frac{\varepsilon_r - \varepsilon_d}{\varepsilon_r + \chi \varepsilon_d} \right) \tag{2.1.31}$$

The resonant condition is provided by the equality condition of $\varepsilon_r = -2\varepsilon_d$ and when $\varepsilon_d > 0$ [26]. The real part to $\varepsilon_r$ must be negative to establish a resonance. This transpires at specific wavelengths for a given particle material, with the particle radius having a very limiting effects to this resonant wavelength.

## Applications of Plasmonic Nanoparticles

Since the discovery of plasmons in 1952 by David Pines and David Bohm [27], scientists have been searching for routes to exploit the advantages that they hold. In the last couple of decades, scientific publications have increased year-on-year, figure 2.11. The more recent research into the production and optical characteristics of metal nanoparticles that diverge in shape, size, structure and tunability over the optical frequencies, have opened new possibilities for application research.

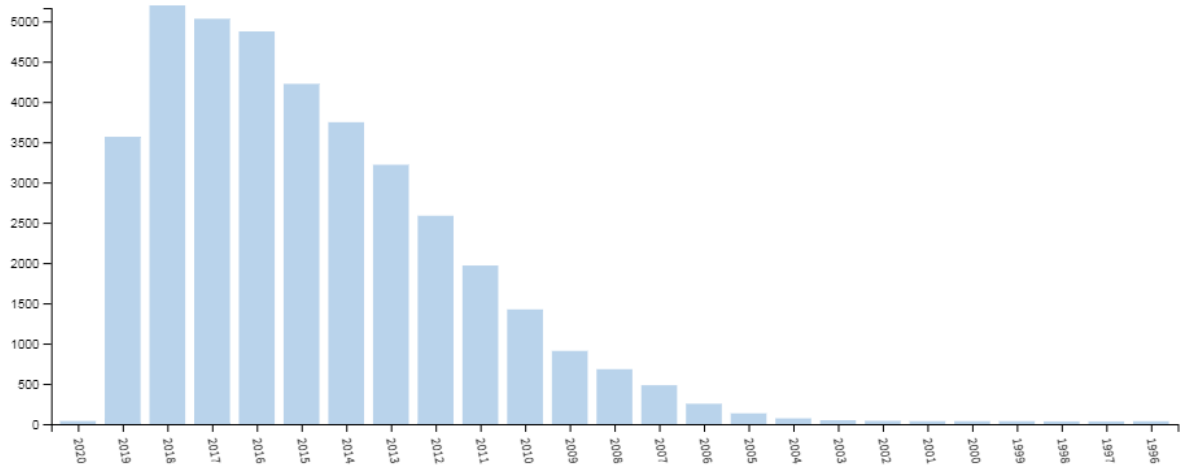


**Figure 2.11.** Number of publications on plasmonics according to Web of Science [28].

Research into plasmonics has provided much growth in areas of colour engineering [29], biomedical science [30], solar cells [31], spectroscopy [32], thin films [33] and many others [34].

Colour engineering has been made possible due to the unique optical properties of metallic nanoparticles, described by dimensions within the size range of 1-100 nm. Customised nanoparticles (material, shape, size and composite) are designed for the purpose of absorbing and scattering at specific wavelengths. This highly efficient absorption and scattering property is what generates a colour.

**Figure 2.12.** Colloidal metallic nanoparticles generating colour through their plasmonic resonance [35].

The existence of colloidal metallic nanoparticles was first acknowledged by Faraday in 1857 [36], with Mie providing a quantitative explanation of their colour in 1908 [37]. However, during the medieval age, metallic nanoparticles were exploited to generate and decorate cathedral windows, stained glass [38]. The optical properties of noble metallic nanoparticles (silver, gold, platinum) ascends from the resonant oscillation of their free electron, LSPR.

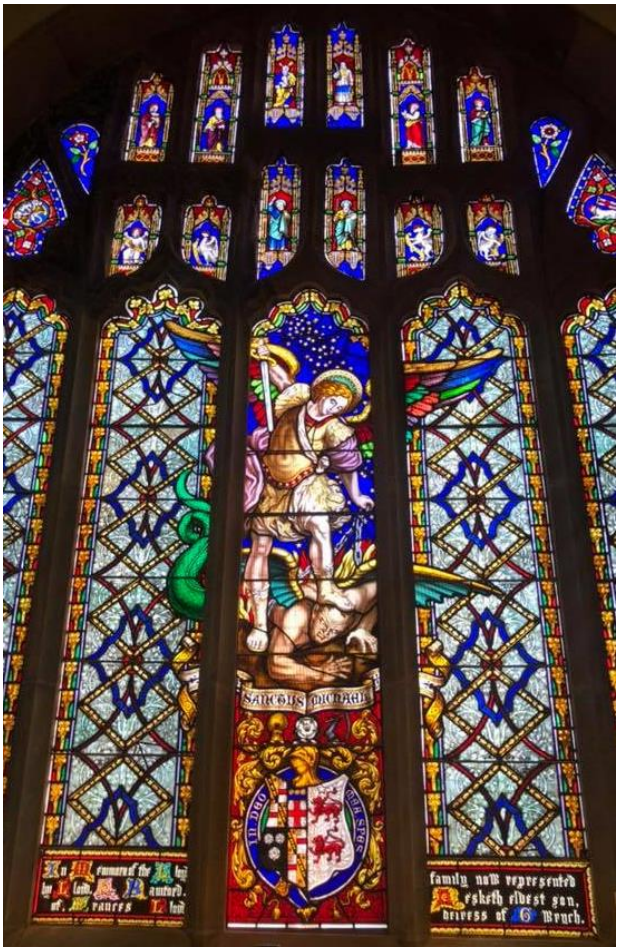

**Figure 2.13.** Colourful stained-glass windows found in Gwrych Castle, Abergele, North Wales, erected between 1819-1825.

Alternative to metallic nanoparticles, dyes and pigments colouration derives from the chemical formula and must be modified in order to tune the colour [39]. This presents a problem with tunability and makes subtle alterations of colour very difficult. Dyes and pigments also tend to either scatter or absorb light and rarely manage to do both. Additionally, they have wide applications for optical longpass filters but do not offer a solution to other types of filters [40].

The colloidal metallic nanoparticles are an important aspect to achieve bandstop filters because they are able to absorb, scatter, or both absorb and scatter simultaneously at discrete wavelengths. The arrangement, orientation and number of layers could enhance this property further, paving the way for a plasmonic nanoparticle optical narrowband metamaterial filter.

## 2.2 **Laser Attacks, Consequences and Prevention**

Lasers are incredible tools that have fundamentally changed our world. The technology provides many unique characteristics that have been exploited for a variety of applications. The theoretical foundations for lasers was first established by Albert Einstein in 1917 [41], which highlighted the concepts for absorption, spontaneous emission and stimulated emission of electromagnetic radiation. It wasn't until the 1960s that the first functional laser was experimentally operated [42]. The unique behaviour of laser light provides spatial and temporal coherence, monochromicity, unidirectional and high radiation intensity.

Lasers have advanced many industries including scientific, military [43], medical [44], and industrial and commercial, from applications in spectroscopy [45], nuclear fusion [46], soft tissue surgery [44], photolithography [47] and much more. Lasers in a military environment are often used in direct energy weapons, defence countermeasures and firearms. The cost effectiveness and accessibility of lasers has enabled devices to enter into the leisure and entertainment market, particularly with the development of the small handheld laser pointer. As a result, laser attacks have been the subject of many incidents involving airplanes, helicopters, vehicles, trains, athletes and ordinary citizens [48]. The rapid deployment of portable consumer lasers has resulted in a lag in development for protection systems.

### 2.2.1 **Laser Fundamentals**

Laser light, like other light sources, generates photons and follows the basic physical process of a change in the energy state of a body that acts as the source. However, unlike other (incoherent) light sources where energy transitions are spontaneous, (coherent) laser sources utilise stimulation for energy transitions. This leads to the unique properties of laser light. The

name laser originates from an acronym, “Light Amplification by Stimulated Emission of Radiation”; thus, a laser, as defined by the acronym, is essentially a photon amplifier.

The emission of photons from stimulated emission is a consequence of the conservation of energy and the wavelengths are well defined by quantum theory. As an electron transitions from a higher energy level to a lower energy level, the difference in energy between the two transition energy levels is released to conserve the energy of the system. The energy difference between the two levels regulate the emitted wavelength [49]. The relationship is defined by;

$$E_2 - E_1 = \Delta E = hf \tag{2.2.1}$$

Where $\Delta E$ is the energy difference, $h$ is Planck constant and $f$ is the frequency of light, determined by $f = c/\lambda$, with $c$ indicating the speed of light and $\lambda$ signifying the wavelength.

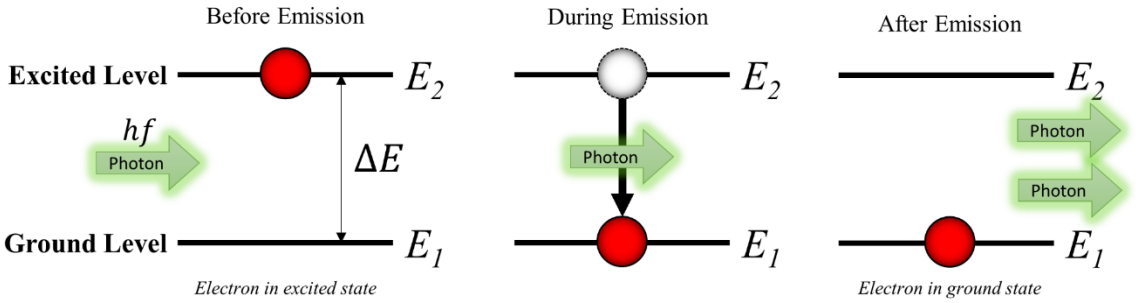


**Figure 2.14.** Process of photon emission from electron transitioning confined in a gain medium.

To enable the distinct properties of a laser, the action of stimulated emission must result from precise mechanisms within a resonator, other known as laser cavity. The laser cavity consists of at least two mirrors (Fabry-Perot) with a gain medium placed between them, as shown in figure 2.15. These mirrors enable the photons to pass back and forth, and in doing so, as the photon travels through the cavity, the number of photons increase leading to an intensification in optical power. The mirror configuration typically consists of one highly reflective mirror and the other partly transparent, permitting a small fraction of resonated photons to be emitted forming the laser beam.

Stimulated emission ascends when an atom, molecule or ion (laser specie) absorbs a photon when in an excited state and emits an identical photon reverting the laser specie to its ground state. The absorbed photon and identical photon are both emitted simultaneously.

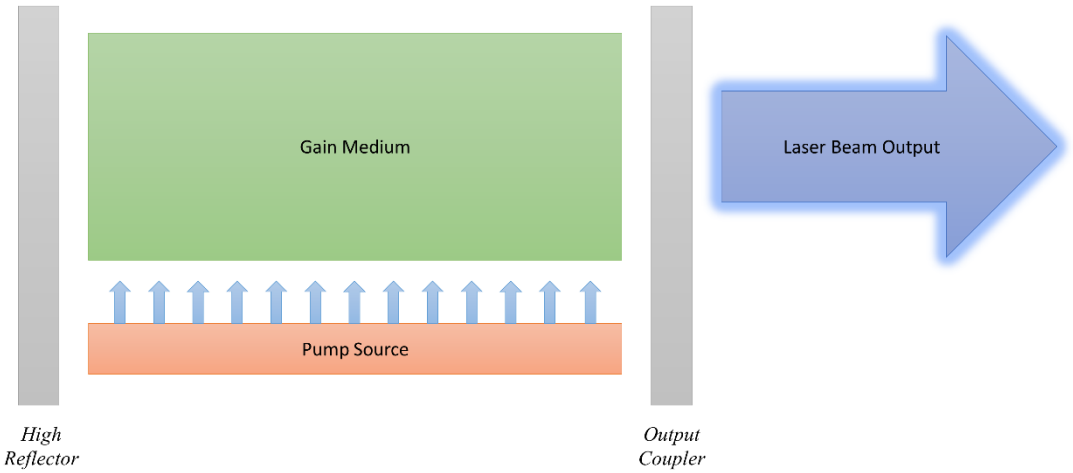


**Figure 2.15.** Basic Laser Schematic.

Population inversion, where the laser specie are in an excited state instead of ground state, involves techniques that enable energy absorption known as pumping. The pumping state takes the laser specie from ground state to an excited state and is a prerequisite for stimulated emission. The most common techniques to invoke the pumping mechanism involve:

- Absorption of photons from another source.
- Chemical reactions.
- Forward biasing of semiconductor. *This displaces the electrons and holes within the semiconductor junction.*

Figure 2.14 highlights the principle of photon emission but in reality, the system would exhibit multiple energy levels. The complexities of a laser transition rely on a variety of probabilistic statistics relating to the laser specie behaviour, i.e. time spent in a particular state. The first operational ruby laser in the 1960's took advantage of a three-level system [42]. However, this displays some disadvantages when dealing with non-radiative transfers by increasing the population of the lower energy state through internal thermal effects. The difficulty of maintaining population inversion becomes progressive as laser action continues. A four-level system offers a solution, subjugated by neodymium ions [49]. The addition of another energy level depopulates $E_1$ and increases population inversion, as seen in figure 2.16.

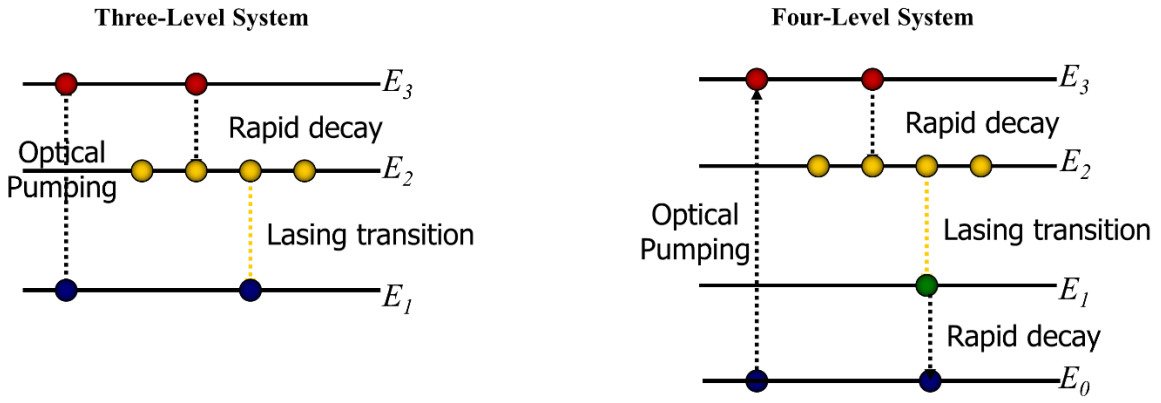


**Figure 2.16.** Three- and Four-level energy systems.

Lasers display transverse and longitudinal modes which are based on oscillations determined by the dimensions of the resonant cavity where the laser action takes place [49]. These resonant oscillations influence the beam quality of emission and determine the spatial characteristics and absolute frequency (bandwidth) of the emission. The subscribed modes are denoting the number of interacting modes in orthogonal directions to the cavity's propagation axis. The lowest order mode, $TEM_{00}$, can be well defined without ambiguity (Eq. 2.2.2). However, there are many modes that laser operation can display. Some examples of lower order modes can be found in figure 2.17.

$$D \approx \omega_0^2 \left\{ 1 + \left( \frac{4\lambda R}{\pi \omega_0^2} \right)^2 \right\} \tag{2.2.2}$$

The diameter ($D$) of a $TEM_{00}$ beam with wavelength ($\lambda$), varying distance ($R$) and beam waist radius ($\omega_0$).

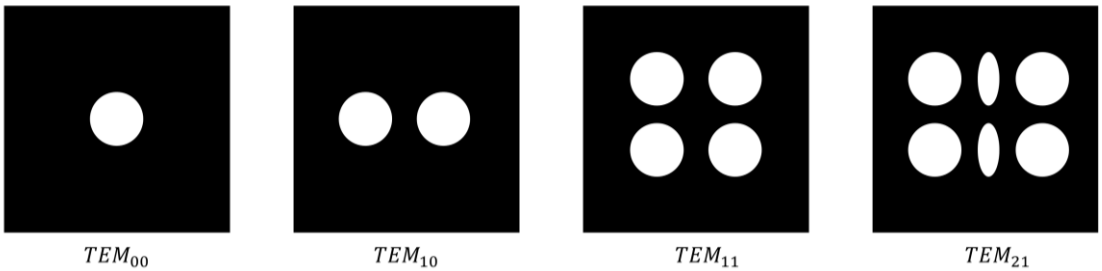


**Figure 2.17.** Example of low order transverse laser modes.

### Near- and far-field

Observing (Eq. 2.2.2) shown in figure 2.18, analysis shows that for a significant distance from the laser source, the beam divergence is fundamentally invariant, and the spot size increases a considerably.

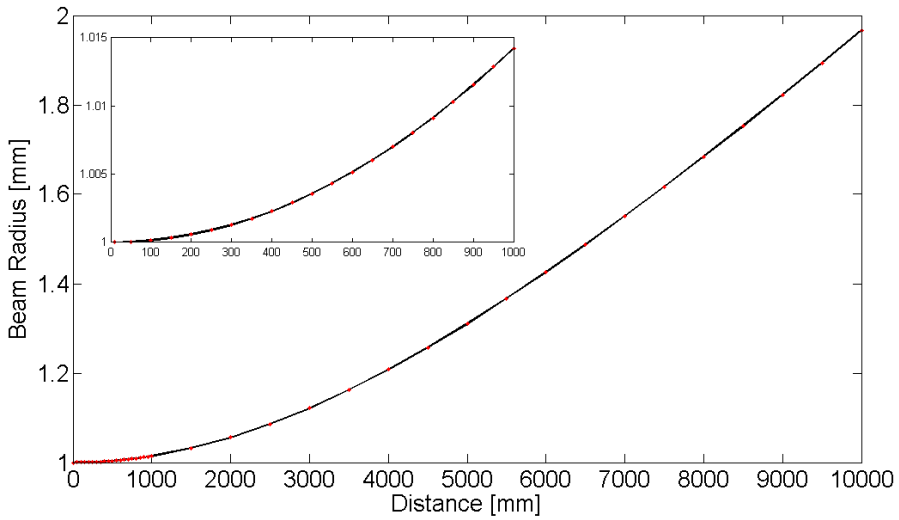


**Figure 2.18.** Example of increasing beam radius with varying distance to the laser source. Insert shows the variation across the first 1m distance. $\lambda = 532nm$ and $\omega_0 = 1mm$.

Near-field is often described in terms of the Rayleigh range [43] (Eq. 2.2.3) and is defined by the distance along the propagation direction of a beam from the waist position, to the position where the cross-section area is doubled.

$$R_{Rayleigh} = \frac{\pi \omega_0^2}{\lambda} \tag{2.2.3}$$

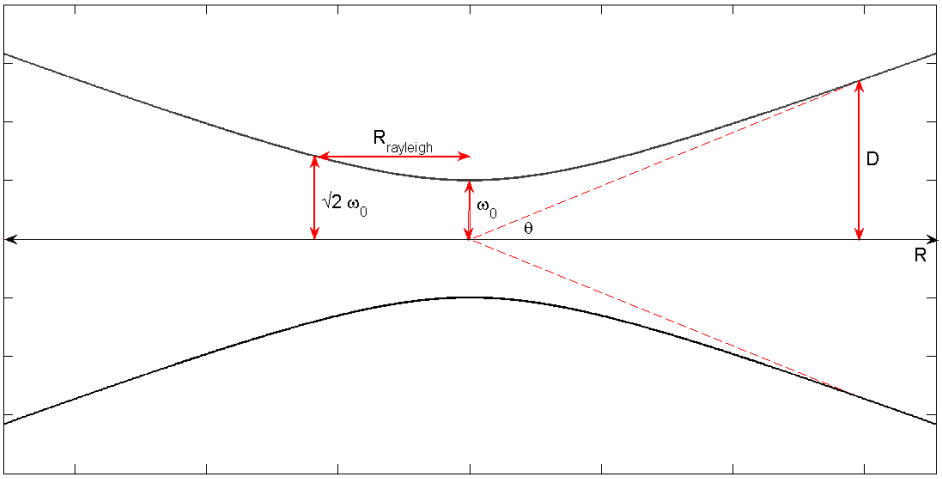


**Figure 2.19.** Gaussian beam width ($D$) as a function of axial distance ($R$) with $\lambda = 532nm$ and $\omega_0 = 1mm$.

Far-field dictates the state of play when the beam begins to diverge with the spot size diameter showing an angular dependency and is often defined on laser data sheets labelled "beam divergence ($\theta$)". Similarly, to the near-field, the far field can be described in terms of the Rayleigh range.

$$near - field < \frac{\pi\omega_0^2}{\lambda} \tag{2.2.4}$$

$$far - field > \frac{\pi\omega_0^2}{\lambda} \tag{2.2.5}$$

As the laser source increases with distance, the spot size also increases in diameter ($2r$). Consequently, the power density also decreases with distance.

$$Power\ Density\ \left(\frac{W}{cm^2}\right) = \frac{Power(W)}{\pi r^2} \tag{2.2.6}$$

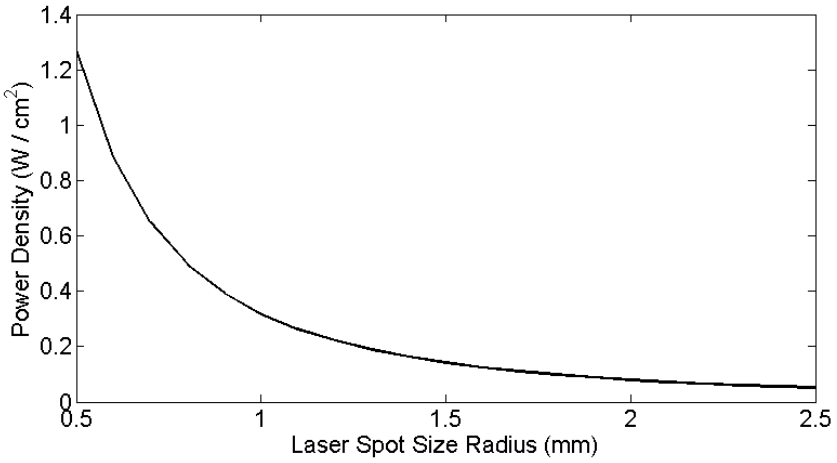


**Figure 2.20.** Power density vs laser spot size radius for 10mW laser.

**Wavelength generation**

The wavelength is produced from a transition determined by the difference in the energy gaps that are involved in the process of stimulated emission [43].

$$\lambda = \frac{h\,c}{\Delta E_g} = \frac{1{,}239(eV \cdot nm)}{\Delta E_g} \tag{2.2.7}$$

Where $\lambda$ is the wavelength, $h = 6.626e - 34\ J/s$, $c = 3e8\,m/s$ and $\Delta E_g$ being the change in energy. $h$ defines Planck's constant and $c$ states the speed of light.

The gain medium is the material that determines the energy gap, thus determines the emission wavelength. Yet some wavelengths have to be generated through indirect generation [50]. This is a nonlinear optical process, namely $\chi^2$ process. Generally, the revised wavelength emission

bands are directed by a nonlinear crystal. For example, a DPSSL, diode-pumped solid-state laser, uses a neodymium-doped yttrium aluminium garnet (Nd:YAG) crystal to produce a wavelength of 1064 nm. A transition of the neodymium ion, with the use of a nonlinear optical process in a potassium titanyl phosphate (KTP) crystal, frequency doubles the 1064 nm to produce a 532 nm green light [51].

Figure 2.21 highlights the range of common wavelengths available, for handheld laser pointers, in the visible spectrum from violet to red.

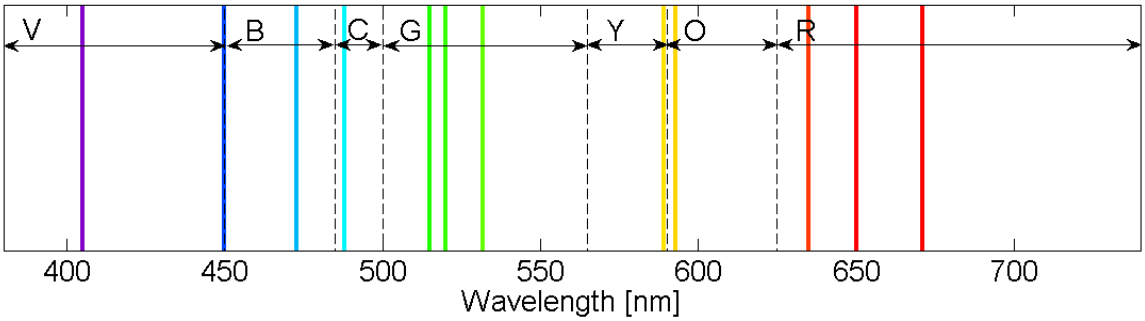


**Figure 2.21.** Common wavelengths for handheld laser pointers, represented by their associated colour.

### Laser Hazard Classifications

Lasers sold in the United Kingdom have to be classified in agreement with the British standards on laser safety [52]. The document sets out the specified requirements for laser products to safeguard against accidental exposures through engineering control and product labelling. Lasers are categorised into four classifications based on hazards and power. The classifications are derived from the medical maximum permissible exposure (MPE) levels, measured in watts per square meter ($Wm^{-2}$) and can also be called irradiance, which specify the amount of danger for the eye or the skin with respect to the laser radiation.

$$Irradiance\ (Wm^{-2}) = \frac{Radiant\ Power\ (W)}{Area\ (m^2)} \tag{2.2.8}$$

**Table 2.5.** Laser Classifications (*Adapted from* [53]).

| Laser Class | Description | Sub-Division | Power |
|---|---|---|---|
| 1 | Emitted power generally safe, even with optical instruments. | Very low power laser. Embedded laser. | Blue: 40 µW Red: 400 µW |
| 1M | Laser is eye safe but may present hazards with optical elements. | Collimated/Divergent laser beam. | Same as Class 1. |
| 2 | Laser is eye safe as a result of normal human aversion responses. | Low power laser. Laser pointer. | CW: <1 mW (400-700 nm) |
| 2M | Laser has the same power as class 2 beam but the divergence or beam diameter may cause the laser to be unsafe. | Collimated/Divergent laser beam. | CW: < 1 mW (400-700 nm) |
| 3R | Accident exposure not usually hazardous but possible eye injury with direct intra-beam viewing. | | CW: < 5 mW (400-700 nm) |
| 3B | The view into the laser is dangerous to the eyes. The diffused reflected beam as not considered the same classification. | Medium power. | CW: < 500 mW Pulsed: < 30 mJ (300 nm-far IR) |
| 4 | Laser is inherently unsafe, including scattered radiation. Danger of fire, skin and serious damage to eye. | High power. | Not limited. |

### 2.2.2 Laser Attacks

Laser strikes on the transport industry and military personnel have drastically increased worldwide. Visible laser pointers have become a serious risk due to the ease of accessibility and low cost of ownership. Reports on the number of laser attacks that occur to trains, road vehicles and civilians are absent, so to deduce the number of attacks within these areas is hugely difficult. However, one area that maintains a suitable and continuous standard for recording laser attack incidents is the aviation industry.

**Figure 2.22.** Federal Aviation Administration image showing the effects of a laser pointer aimed at an airline cockpit [54].

Since the year 2004, pilots and aviation staff from eight countries have reported sightings or direct illumination by laser light of almost 75,000 times up to the year 2018. Figure 2.23 presents the cumulative annual data from laser strikes on aircraft.

The countries that make up these statistics are:

- United Kingdom
- United States of America
- Australia
- Canada
- Italy
- Sweden
- New Zealand
- Japan

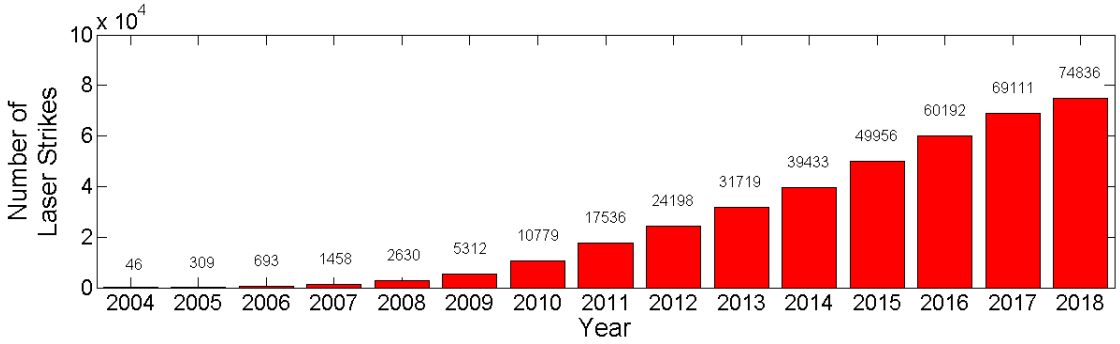


**Figure 2.23.** Worldwide cumulative and annual data on laser strikes on aircrafts [55].

As of 2019, there have been zero documented or proven reports of permanent eye injuries to pilots. However, approximately 0.5% of incidents have resulted in some temporary injuries [55].

### United Kingdom

The number of incidents in the United Kingdom have decreased over the last couple of years. This may be due to stricter laws, more policing and better education on the subject matter. However, the number is still significant and the overseas incidents of UK operators remain at similar levels year on year. The peak number of reported incidents was in 2011, with a total number of events in excess of 2250 attacks. 2017 saw a ~46% reduction, compared to the peak in 2011, in laser attacks according to the civil aviator authority (CAA).

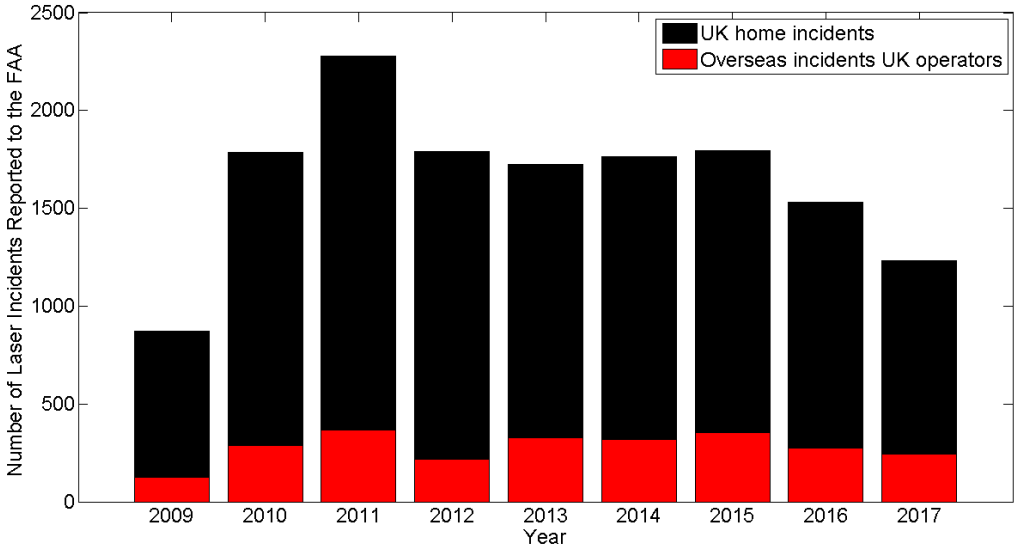


**Figure 2.24.** Laser incidents reported to the UK CAA [56].

Furthermore, the events reported in 2016 highlights that green lasers were the most common choice of laser wavelength to use during these events.

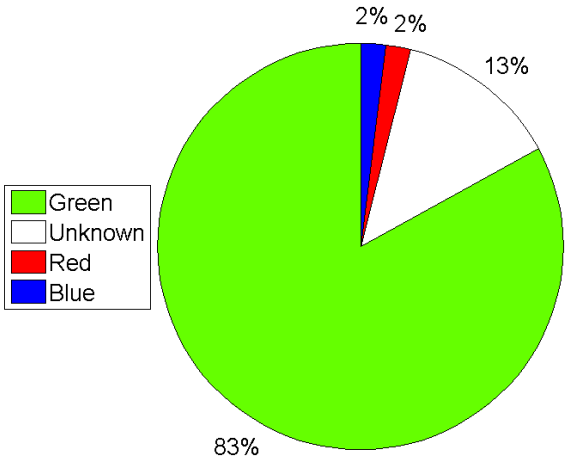


**Figure 2.25.** Laser illumination events by laser colour reported to the UK CAA in 2016 [57].

According to CAA, 55% of pilots experienced laser illumination in the 12 months following September 2015 [58]. Police helicopters are also a target, with one police aircraft in 2015 conceding nearly 100 events [59]. In 2017, the UK government published a document records from the British Transport Police that stated between 2011 and 2016, there was a total of 466 laser incidents targeting trains [60], and a further 112 incidents in 2017 [61].

### United States of America

Similar to the UK, the United States have also experienced problems with laser attacks on aircraft, but on a much larger scale. Reports from the U.S. Federal Aviation Administration (FAA), show a significant increase in laser attacks from 2014 to 2015, with the record events

decreasing in 2018. Though the number of incidents is still nearing the 6000 mark. A further worrying concern is that in 2017, there is circumstantial evidence to suggest some pilots have stopped reporting each laser incident and are now only reporting the serious incidents [62]. These number of events are considerably disquieting and are inevitably waiting for a true disaster to happen as handheld lasers become more powerful and cheaper.

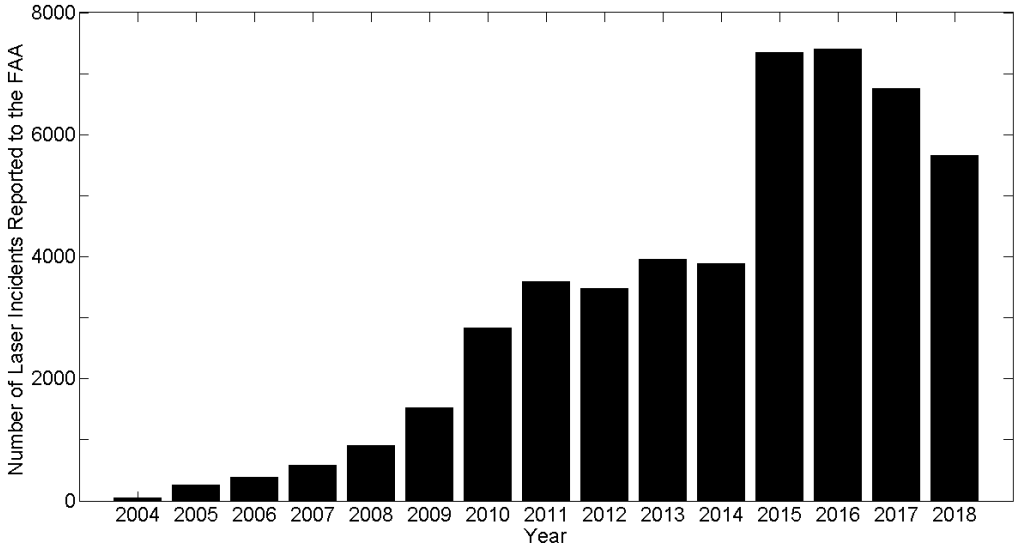


**Figure 2.26.** Laser incidents reported to the USA FAA [63].

The FAA reported similar percentage levels with the UK on the colour of lasers used in the attacks. The extent of the levels reported in 2018 are similar to that in 2016 and 2017, with an increased use of blue lasers from 2.9% in 2016 to 5.4% in 2018.

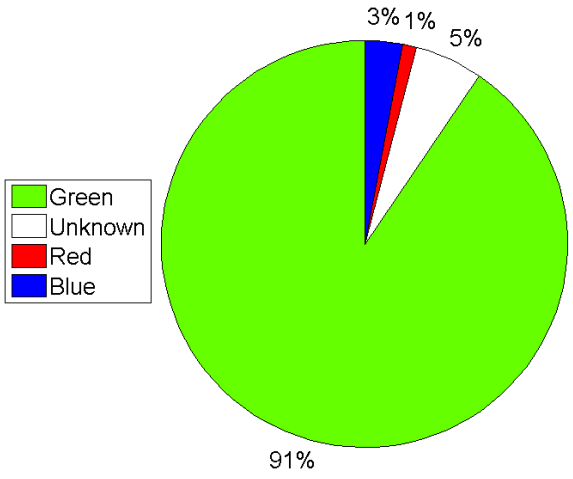


**Figure 2.27.** Laser illumination events by laser colour reported to the USA FAA in 2016 [64].

### 2.2.3 Human Eye and Laser Damage

The human eye is one of the most valuable and the most sensitive sense organ. It is a natural optical instrument that aids the conversion of visible light into information. Exposure of the eye to high intensity lights, such as lasers, can cause serious damage. Exposure of laser light to the eye can change in severity depending on the power of the beam, divergence, distance, wavelength, time of exposure, incident location on the eye (central vision vs. peripheral vision) and whether the laser was pulsed or continuous wave.

#### Human Eye Anatomy

The cornea located at the front of the eye is covered by a transparent spherical membrane. Located behind the cornea sits the iris, a pigmented or non-pigmented muscular diaphragm that is responsible for controlling the amount of light entering the eye. The light enters the pupil, centred in the middle of the iris, and is black in colour because no light is reflected from it. The iris regulates the amount of incoming light by adjusting the pupils' diameter. When a bright or intense light is incident on the eye, the iris contracts the pupil to decrease the amount of light entering. The eye lens is a proteinaceous material with a convex shape and is held in place by ciliary muscles. The ciliary muscles job is to help adapt the shape and therefore focal length of the eye lens. At the back location of the eyeball sits the retina, a light sensitive semi-transparent membrane. The light sensitive receptors found located in the retina are called rods and cones. The rods and cones convert the light into electrical signals which are sent through the optical nerve to the brain. Between the lens and the retina is a fluid called vitreous humour. Within the retina sits the macula and fovea. The macula is the functional centre of the retina and is important for providing "20/20" and colour vision. The fovea is a small centre feature composed of closely packed cones and is responsible for sharp central vision. [65].

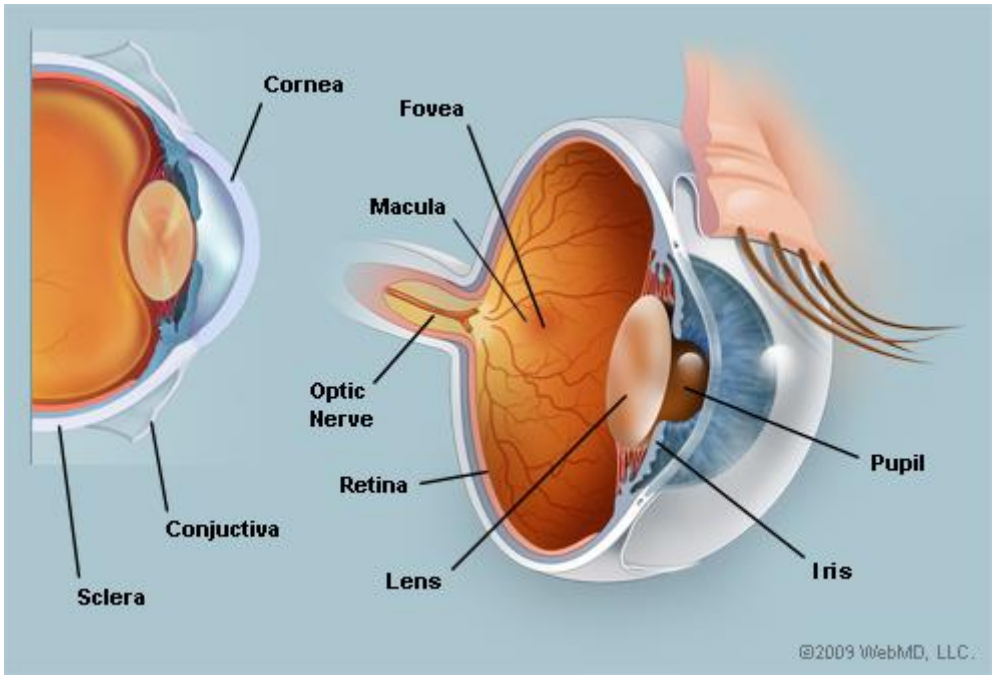


**Figure 2.28.** The human eye anatomy [66].

### Photopic and Scotopic Vision

The rod-shaped photoreceptors are used in the detection of low intensity light, play little role in colour vision and are entirely responsible for the night vision. The cone cells are responsible for reacting to different colours of light (wavelengths of light), in control of colour vision and function well in bright light. There are three types of cones (L, M, S) and they respond to long, medium and short wavelengths, red, green and blue respectively [67]. Interestingly, the cones are responsible for tricking our minds into seeing the colour pink which does not exist in the visible spectrum.

Photopic vision describes the human vision under well illuminated conditions (levels 10 to $10^8$ cd/m$^2$) and enables the colour vision. The photopic vision peaks in sensitivity at around 555 nm, green light. The scotopic vision on the other hand operates in low level light conditions and is most sensitivity near 507 nm. Additionally there is a third vision, mesopic vision that acts as a transition vision between the photopic and scotopic vision. Mesopic is a combination of the two visions and is active is luminescent levels of around 0.001 to 3 cd/m$^2$. [67].

The photopic and scotopic vision may also play a vital role on humans' psychological attraction towards laser light, particularly green.

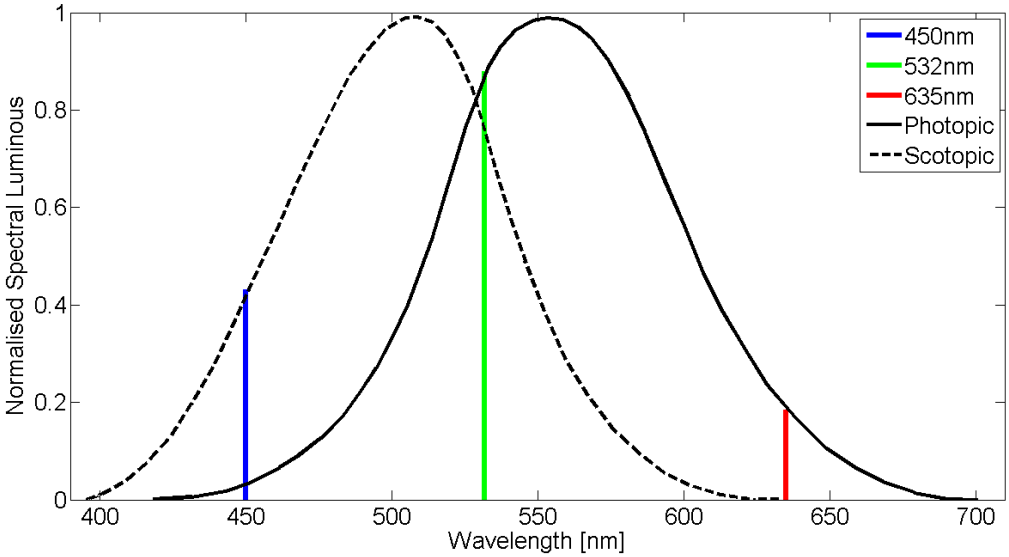


**Figure 2.29.** The photonic and scotopic spectrum with added visuals locating the laser wavelengths. *Adapted from* [67].

### Integrated Visual Transmission

The IVPT is the function associated with the average spectral sensitivity of the filter in accordance to the typical human visual perception, given by (Eq. 2.2.9). The importance of this is to understand how the human eye will interact visually with the filter.

$$IVPT = \frac{\int_0^\infty I(\lambda)\, V(\lambda)\, T(\lambda)\, d\lambda}{\int_0^\infty I(\lambda)\, V(\lambda)\, d\lambda} \tag{2.2.9}$$

Where $I(\lambda)$ is the spectrum illumination CIE-D65 (daylight), $V(\lambda)$ is the photopic response of the human eye and $T(\lambda)$ is the transmission spectrum of the filter ($0 \leq T \leq 1$).

The photopic response and the spectrum illumination can be replaced to find the integrated visual scotopic transmission.

### Damaging Effects via Lasers

*Potential Hazards.* There are three main biological damage mechanisms of human tissue as a direct results of laser interactions [43].

1. Photo-thermal
2. Photo-acoustic
3. Photo-chemical

The photo-thermal effect is the most likely interaction that results in acute injury. This happens when some of the photo energy is absorbed by the underlying tissues. The result causes a temperature increase to the tissues leading to tissue damage, burns. This type of effect depends

on the power of the laser and can vary dependent on the amount of water and pigment in the tissue. Permanent damage to the cells occurs with temperatures at and exceeding 60°C.

The photo-acoustic effect is a result of high-energy pulsed lasers and results in rapid tissue expansion that causes shock waves that produce mechanical reactions in the cell structure.

The photo-chemical effect occurs when the laser flux, energy per unit time, is insufficient to cause thermal effects. The absorbed radiation can result in a modification of certain mechanisms on the tissues and cells. For example, tanning of the skin. The chemical changes are reversible over time, though recurrent exposure can lead to permanent damage. This process is photon-energy dependent and shorter wavelengths, such as blue and ultraviolet, are more damaging.

*Eye Hazards.* Figure 2.30 highlights some of the potential outcomes of laser interactions with eye tissues. The damage is highly dependent on power and wavelength.

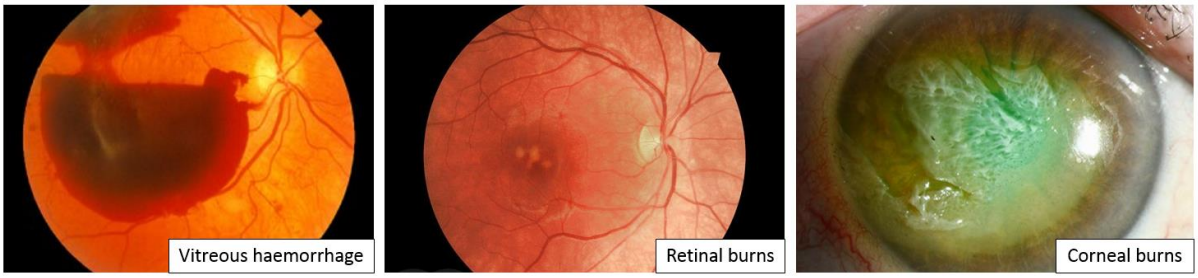


**Figure 2.30.** Laser induced bio effects [68-70].

Laser threats to the human eye can come in direct or indirect forms. Direct exposure often leads to retinal or corneal burns depending on the incident wavelength. Indirect exposure has comparable outcomes but displays an increased chance of cumulative damage formation, such as cataracts.

The human eye consists of many complex parts, figure 2.28 (*human eye*), that differ in optical transparencies. Thus, the potential hazards are wavelength dependent. Figure 2.31 presents a schematic illustration of the optical transparency with dependence on electromagnetic subcategories. The UV and IR (above 1400 nm) radiation can cause damage to the cornea, and the visible band and some near-IR wavelengths will damage the retina.

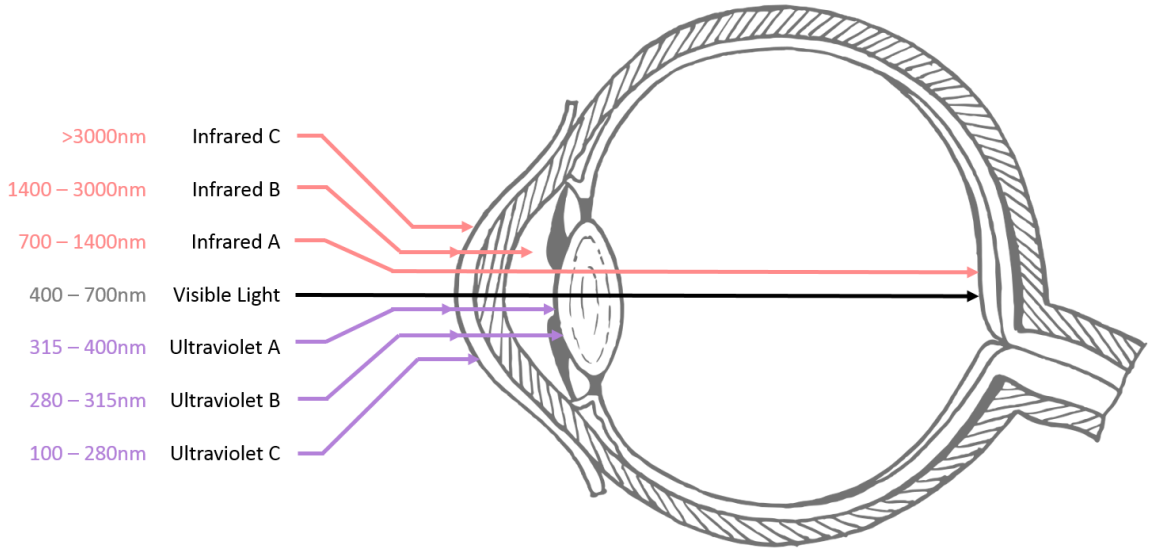


**Figure 2.31.** Schematic illustration of the wavelength transparency of the eye.

A summary of laser radiation hazards to the human eye resulting from exposure of high-power lasers are presented in table 2.6.

**Table 2.6.** Summary of laser radiation hazards to the eyes.

| Wavelength Band (nm) | Radiation Range | Hazard |
|---|---|---|
| 180 – 400 | Ultraviolet | Photo-chemical change and thermal damage. |
| 400 – 700 | Visible | Retinal damage. |
| 400 – 600 | Visible | Photo-chemical damage. |
| 700 – 1400 | Infrared band A | Retinal damage. |
| 1400 – 2600 | Infrared band B | Thermal damage. |
| 2600 – 1mil | Infrared band C | Thermal damage. |

*Skin Hazards.* Skin hazards are often overlooked due to the severity of the potential hazards to the eyes. However, laser exposure to the skin can result in burns from direct or indirect laser beam exposure. The exposure of UV light presents further problems that mimic ‘sunburn’. This includes increase pigmentation, accelerated skin aging and onset of cancer [71]. Additionally, some medication side effects can lead to photo-sensitive reactions that can occur for any waveband.

Figure 2.32 presents a schematic cross-section of the human skin arrangement and the penetration depth of various wavebands. The upper skin layers are a few micrometres in thickness whilst the lower layers are millimetres thick [72].

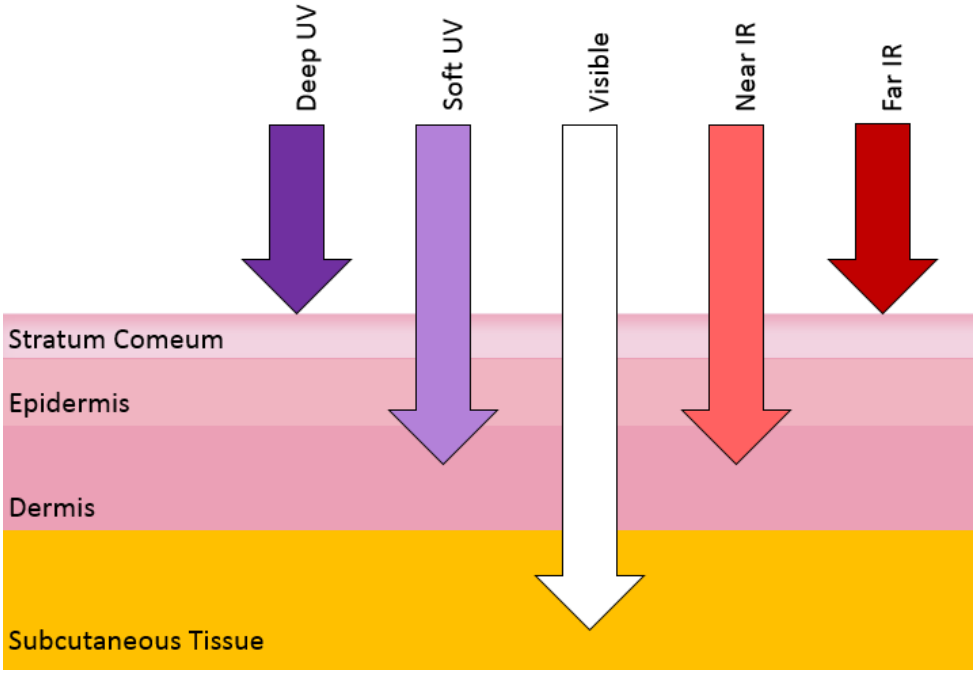


**Figure 2.32.** Schematic illustration of the wavelength dependence of human skin.

A summary of laser radiation hazards to skin tissue resulting from exposure of high-power lasers are presented in table 2.7.

**Table 2.7.** Summary of laser radiation hazards to skin.

| Wavelength Band (nm) | Radiation Range | Hazard |
|---|---|---|
| 180 – 400 | Ultraviolet | Erythema. |
| 400 – 700 | Visible | Thermal damage. |
| 700 – 1400 | Infrared band A | Thermal damage. |
| 1400 – 1mil | Infrared band B and C | Thermal damage. |

### Laser Dazzle and Glare

Dr Craig Williamson from the Defence Science and Technology Laboratory (DSTL) in the United Kingdom and Dr Leon McLin from the 711$^{th}$ Human Performance Wing United States Air Force, have done extensive research of how laser light affects and blocks human vision, by defining the parameters of visible-light laser interference with vision [73].

The key areas highlighted by Dr Williamson and Dr McLin are;

1. Determining to what effect the laser spot size can block vision, namely laser dazzle.
2. Determining the laser parameters that cause interfering vision blockage (wavelength, power, divergence and distance).

Laser eye dazzle describes the temporary impairment to the human eye caused from lasing light within the visible wavelengths. Williamson and McLin have published a series of tests and scientific publications of the concepts of laser dazzle, including the maximum dazzle exposure (MDE).

"The MDE is the threshold laser irradiance at the eye below which a given target can be detected. It can also be used as a measure of the minimum laser irradiance required to obscure a given target" [74].

The research presented a method for measuring dazzle as a degree that blocks the human vision. They selected four "dazzle levels" as significant, figure 2.33. The effect to whether laser dazzle occurs is also dependent on the ambient light. Figure 2.34 shows that the power and ambient light are factors that can greatly influence laser dazzle.

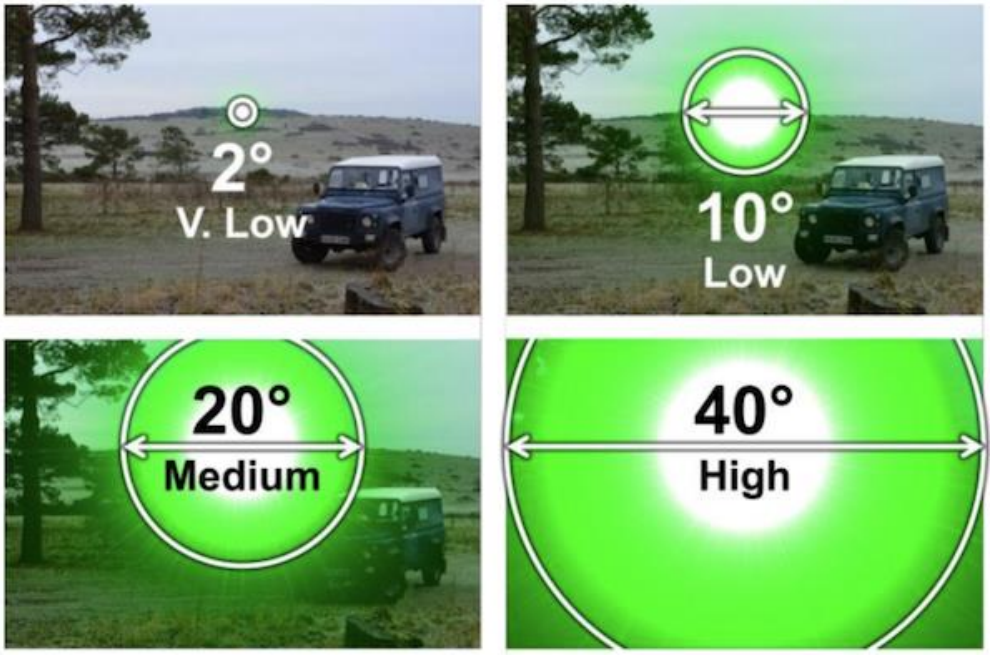


**Figure 2.33.** A simulation showing the extent of the four dazzle levels [75].

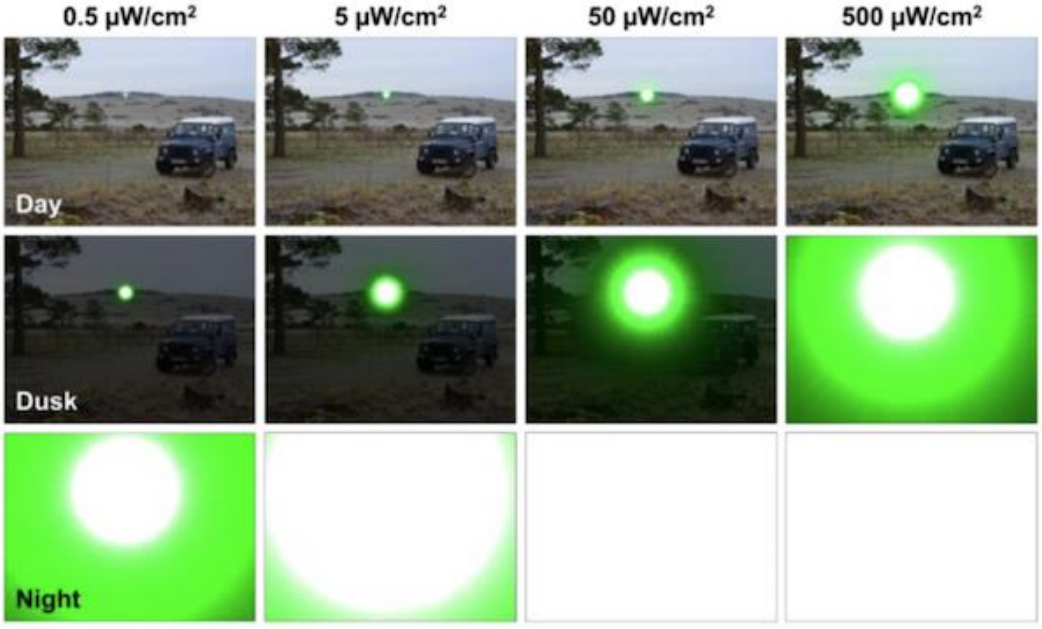


**Figure 2.34.** Visual dazzle from a green 532 nm laser from low to high laser irradiances at day (1000 cd/m$^2$), dusk/dawn (10 cd/m$^2$) and night (0.1 cd/m$^2$) ambient light levels [75].

As previously discussed, the human eye is most sensitive to green light, photopic ~555 nm and scotopic ~507 nm. As a function of the photopic and scotopic sensitivity profiles, light outside the green band appears less intense. Consequently, green laser light will always result in more dazzle than other lasers with the same power and divergence.


**Figure 2.35.** Visual dazzle resulting from difference laser wavelengths of equal irradiance at dusk/dawn conditions [75].

Williamson and McLin also demonstrated that eye colour and age also play a role in the susceptibility to laser dazzle. Together they developed a complex formula (Eq. 2.2.10) for calculating the maximum dazzle exposure (MDE) level, not to be confused with the maximum permissible exposure (MPE), which depends on the laser's irradiance for a specified time. Differing to the MPE, the MDE requires a complex analysis of many influences.

- Ambient light
- Laser divergence
- Obscuration extent
- Laser power
- Laser wavelength
- Target size
- Atmospheric visibility
- Target contrast
- Age of the viewer
- Eye pigment

$$MDE = \frac{\left(\frac{L_b C_{orig}}{\Omega \mathrm{AF}} - L_b\right)}{f_{eye} 683 V_\lambda} \tag{2.2.10}$$

Where $L_b$ is the background luminance, $C_{orig}$ target contrast, $\Omega$ describes other factors associated to the background luminance, AF denotes the age adjustment factors, $f_{eye}$ signifies the eye scattering function (eye pigment is a factor here), and $V_\lambda$ is the visual correction factor. *A more detailed discussion can be found in reference* [76].

### 2.2.4 Thin Film Laser Protection: Modern Day Prevention

Modern day laser protection is essential for personnel that work with, or could come into contact with, lasers. Laser protection is the last line of defence. The direct and indirect viewing of a class 3B and Class 4 beam must be avoided at all costs. Laser protection equipment are designed to block the wavelengths emitted by a laser and provide adequate optical density at the specific laser wavelength, as well as ergonomic comfort for the user. However, due to the core design principles of laser protection, they often provide inadequate protection with low integrated visual transmission and high colouration. This all stems from a single problem, blue shift.

#### Constructive and Destructive Interference

Interference is the fundamental physical mechanism for thin films, allowing for anti-reflection coatings and thin film filters to exist. Interference happens when two or more waveforms interact to form a resultant wave that is either reinforced (constructive) or cancelled (destructive) [49]. This is highly dependent on the position of the peaks and troughs of the waves. Figure 2.36 provides an example of the combination of two waves and its resultant.

$$A + B = C\ (Construstive) \tag{2.2.12}$$

$$D + E = F\ (Destructive) \tag{2.2.13}$$

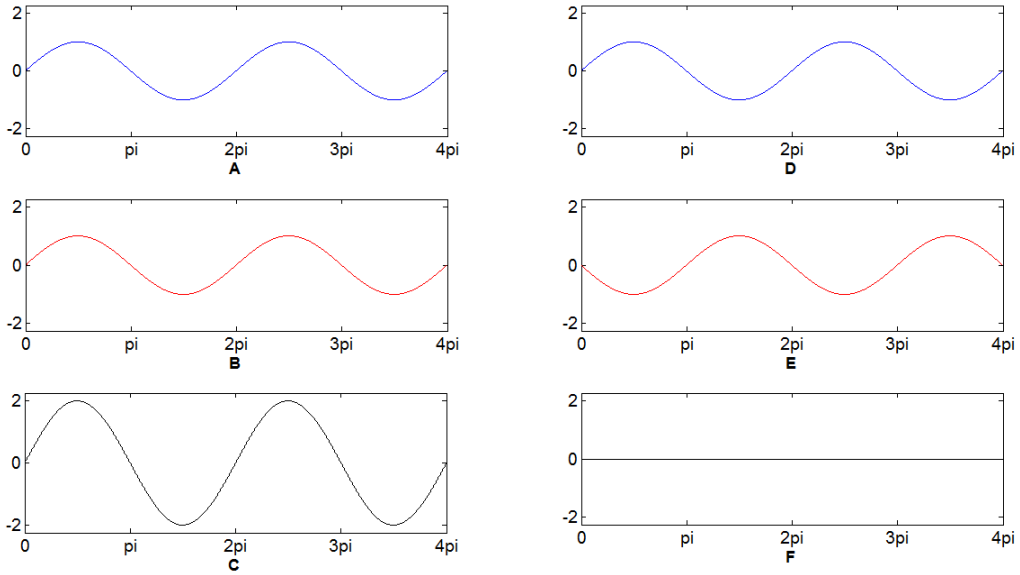


**Figure 2.36.** Demonstration of constructive and destructive interference.

Constructive interference occurs when the combined waves are in phase with one another and the resulting amplitude is increased. For the example provided in figure 2.36, the two waves (A+B) have equal amplitudes interfering that results in wave C displaying an amplitude twice that of the individual waves. For 50 constructively interfering waves, the resulting amplitude

will be 50 times greater than the amplitude of the individual waves. With a greater number of in phase interfering waves, a significant increase in amplitude can be obtained.

On the other hand, destructive interference occurs when two waves combine in such a way that they completely cancel each other out. The example provided in figure 2.36 demonstrates that the waves (D+E) are out of phase by $\pi\ radians\ or$ 180°, the peaks and troughs do not match up and consequently cancel each other out. When more than two waves come together, the result is more complicated. However, the net result allows them all to combine in such a way that produces a zero-amplitude resultant. In general, whenever a number of waves combine, the interference will rarely be completely constructive or completely destructive, and is often a multiple-path interference.

Thin film interference is most dominant when the path length difference for the two or more perpendicular incidence waves are a quarter-integral or half-integral wavelength for constructive and destructive, respectively. The thin film interference is highly reliant on the film thickness, the wavelength of light, and the refractive indices of the film.

*Constructive interference*.

$$t_c = \frac{\lambda}{4n_2}, \frac{3\lambda}{4n_2}, \frac{5\lambda}{4n_2}, \ldots \tag{2.2.12}$$

*Destructive interference.*

$$t_d = \frac{\lambda}{2n_2}, \frac{2\lambda}{2n_2}, \frac{3\lambda}{2n_2}, \ldots \tag{2.2.13}$$

For thin films analysis, considering a soap bubble is an interesting route as it provides an example of a single layer where either side of that layer is air; thus $n_1 = n_3 = 1.00$, and $n_2 = 1.33$ for a soap bubble. It is possible to calculate the thicknesses of the layer where constructive and destructive interference would take place, with an example reference wavelength of 650 nm.

**Table 2.8.** The three smallest thicknesses of a soap bubble that produce constructive and destructive interference.

| **Constructive** | **Destructive** |
|---|---|
| $t_{c,1} = \frac{\lambda}{4\ (1.33)} = \ 122nm$ | $t_{d,1} = \frac{\lambda}{2\ (1.33)} = 244nm$ |
| $t_{c,2} = \frac{3\lambda}{4\ (1.33)} = 366nm$ | $t_{d,2} = \frac{2\lambda}{2\ (1.33)} = 488nm$ |
| $t_{c,3} = \frac{5\lambda}{4\ (1.33)} = 610nm$ | $t_{d,3} = \frac{3\lambda}{2\ (1.33)} = 733nm$ |

As the thin film construction gains more and more layers, the many reflections combine with constructive interference and the layers act as a high-quality reflector. The regulated thickness can be contained by selecting a reference wavelength and the bandwidth of the reflected wavelengths depend on the chosen refractive indices.

### Anti-Reflection Coatings

Anti-reflection (AR) coatings are a category of thin film optical coatings that are applied to the surface of an optical substrate to reduce reflection. The AR coating works by creating destructive interference of the reflected light [77]. Considering $1 = T + R$, as the destructive reflected waves increases, the transmission must additionally increase. Fresnel's equations are regularly used for the design process of AR films.

AR coatings can exist in a number of forms (figure 2.37) that include single-layer, multi-layer, index-matching and moth eye. The thickness of the layer or layers is easily determinable from (Eq. 2.2.13). The single layer is the simplest form and consists of a single thin layer of transparent dielectric material. The multi-layer AR is much more complex and can enable a near perfect transmission. Additionally, design dependant, multi-layer AR coatings can achieve a broader transmission and improved performance over a single layer. Index-matching AR coatings are often used for more complex filter designs where the two layers of significantly different refractive indices require a layer between them so that the step in index from one layer to another if not as large. Moth eye AR structures [78], unlike the other listed types, are a nanostructured surface film. The structure design is based on a moth's eye which naturally eliminates reflection so that it does not give away its location to predators. The moth eye design works because light sees the surface as a continuous refractive index gradient when the structures are sub-wavelength and can be considered as an example of a metamaterial.

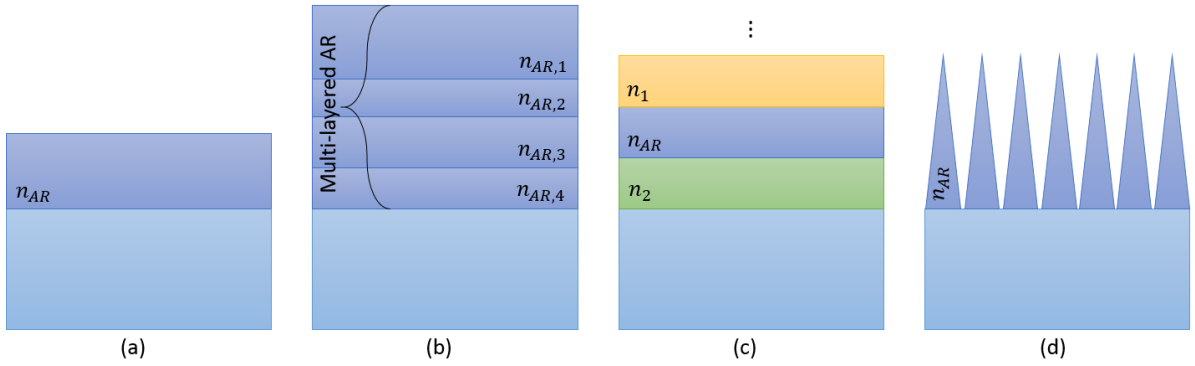


**Figure 2.37.** Sub-categories of anti-reflection coatings. (a) Single-layer, (b) Multi-layer, (c) Index-matching, and (d) Moth eye layer.

Figure 2.38a demonstrates an example comparing a single layer with multilayer AR coating, and figure 2.38b validates the index-matching layer by comparing the reflection with and without the required layer. The reference wavelength is 510 nm. The single-layer coating consists of an $MgF_2$ layer with a refractive index of 1.38 and thickness of 92.39 nm, on a glass substrate with a refractive index of 1.52. The multilayer consists of a four-layer AR coating ($MgF_2$ [92.66 nm] – $ZrO_2$ [131.72 nm] – $MgF_2$ [30.31 nm] – $ZrO_2$ [16.54 nm]) on a glass substrate.

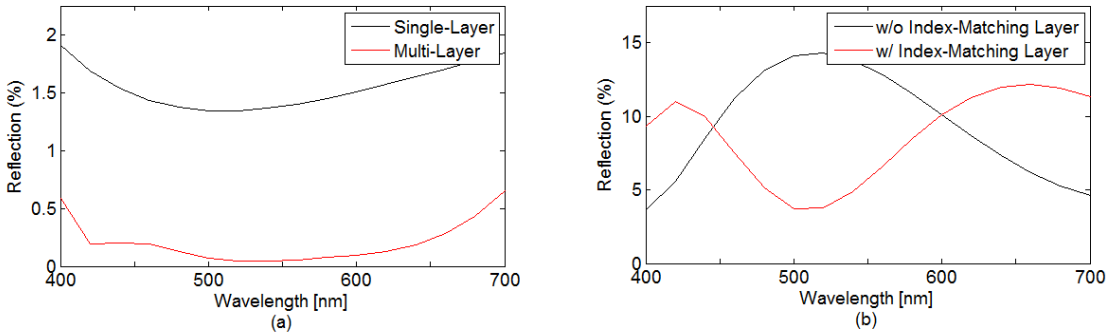


**Figure 2.38.** Comparison of different types of AR coatings.

### Fixed Line Laser Protection

Fixed-line laser protection filters are widely used in many applications including defence, medical, manufacturing and research fields. They are notch (bandstop) filters that are specifically designed to protect against laser wavelengths and often have a small bandwidth. The notch filter is a combination of a longwave pass and shortwave pass filter. The general design follows alternating layers of high- and low- index materials, each at a thickness of a quarter wavelength to create partially reflected waves at each interface [77]. The reflections recombine through constructive interference, and fashion a high-quality reflector. There are several types of different approaches to achieve the alternating high- low- index layers.

Notch filters can achieve high reflection within the rejection band and offer high transmission outside the rejection band. However, the inherent design results in the presence of harmonic rejection bands.

The difference in refractive index between the high- and low- layers will determine the bandwidth of the filter. An approximate bandwidth can be given by (Eq. 2.2.15).

$$2g = \frac{2}{\pi}\sin^{-1}\left(\frac{n_H - n_L}{n_H + n_L}\right) \tag{2.2.15}$$

Where $g$ is half the bandwidth as a percentage, and $n_H$ and $n_L$ is the refractive index of the high and low indices, respectively.

*Step Index.*

The step index form provides an abrupt change in dielectric material to achieve the alternating layers of high- low- index mediums. Figure 2.39 shows a schematic example of the step index film. An increasing number of layers will provide greater transmission attenuation.

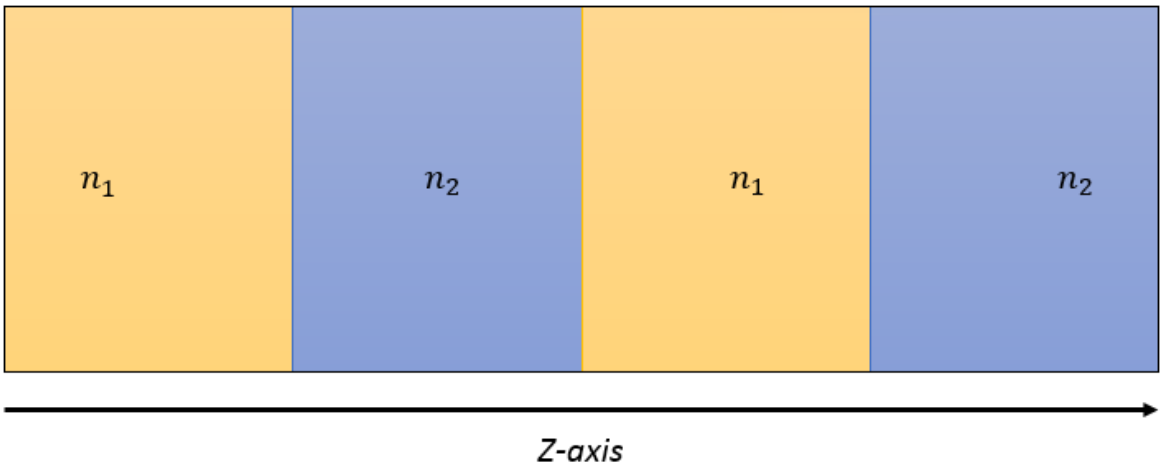


**Figure 2.39.** Schematic example of step index filter through film.

The refractive index, figure 2.40, demonstrates the immediate binary change as the layers switch between materials as the position progresses through the stack.

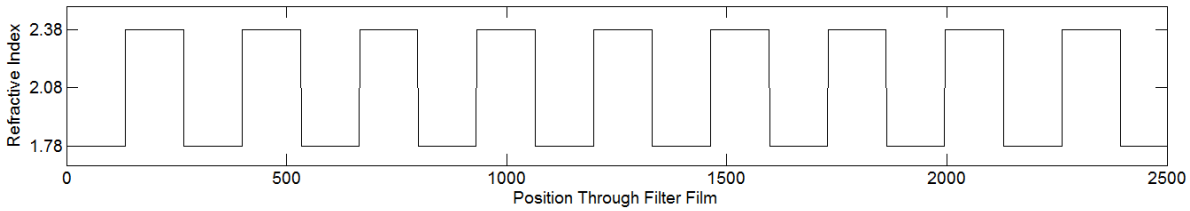


**Figure 2.40.** Schematic representation of the refractive index changes though the step index film.

*Rugate.*

The Rugate filter is probably now the most used notch filter [79]. It provides greater efficiency than that compared to the step index design. The Rugate design is particularly attractive for narrow spectral bandwidths by combining the best aspects of step index and holographic technology. Essentially, this design provides a pseudo-continuous refractive index. The gradual transition of the refractive index is achieved by dividing conventional step index quarter wave layers into multiple thinner layers, which have refractive index values that progressively vary between the minimum and maximum indices.

The intermediate index values are attained by co-evaporating the two coating materials such that the deposition rate of each material varies for each sub-layer; thus, controlling the

deposition so that a pseudo-continuous index is obtained. Figure 2.41 delivers an example of the gradual change between two materials.

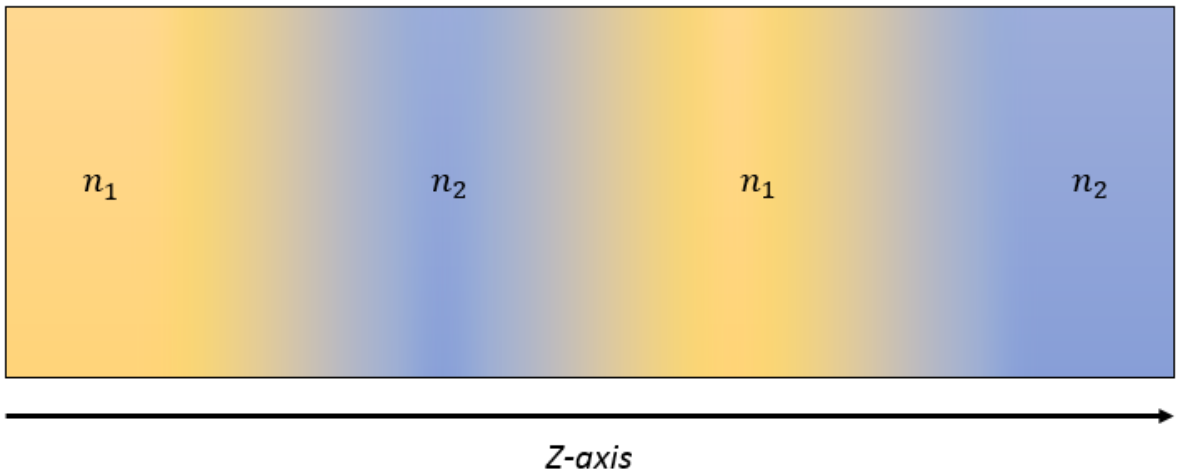


**Figure 2.41.** Schematic example of Rugate filter through film.

A non-apodized, absence of a window function, can be described by (Eq. 2.2.16) with an example of the pseudo-continuous refractive index provided in figure 2.42.

$$n(z) = n_0 + \frac{\Delta n}{2} \sin\left(\frac{4\pi}{\lambda_p} z\right) \tag{2.2.16}$$

Where $n(z)$ is the new refractive index depending on the position through $z$, $n_0$ is the average index of the two materials, $\Delta n$ is the difference in index, and $\lambda_p$ is the wavelength reflection peak.

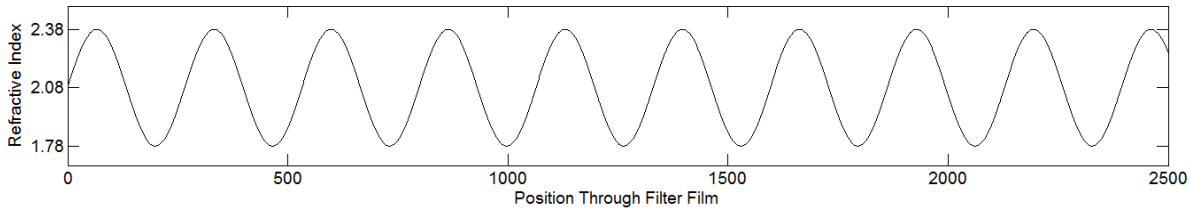


**Figure 2.42.** Schematic representation of the refractive index changes though the Rugate film.

*Holographic.*

Unlike the step index and Rugate design, holographic filters only require a single 'photorefractive' material [80]. Photorefraction is a photo-induced change to the refractive index of a material. That material can be a crystal or polymer that possesses photoconductive properties and exhibit an electro-optic effect.

- Photoconductive exhibits charge transport enabling a space-charge distribution under inhomogeneous illumination [81].
- Electro-optic effect transforms the internal electric fields induced by the inhomogeneous space-charges into refractive index modulation [81].

The modulated refractive index schematic is presented in figure 2.43, where $n_1$ describes the standard unmodulated refractive index and $n_{1\pm}$ describes the photo-induced change to $n_1$. This subtle change in index provides a similar effect to the Rugate design with less control over the material selection, and consequently, less control over the change in index through the film. Modulation can vary depending on the illumination wavelength.

Holographic notch filters are often much thicker than the counter designs offered [82]. The filters offer a deep rejection band and high transmission. Often high transmission is more available, particularly with photorefractive polymers where the unmodulated refractive index is reasonably low, on the order of ~1.5. This type of filter does not present a harmonic rejection bands. Furthermore, due to the manufacturing process the holographic filters can be fabricated on complex non-conformal shapes, and depending on the illumination interference pattern, they can offer nano/meso structures within the film itself [83].

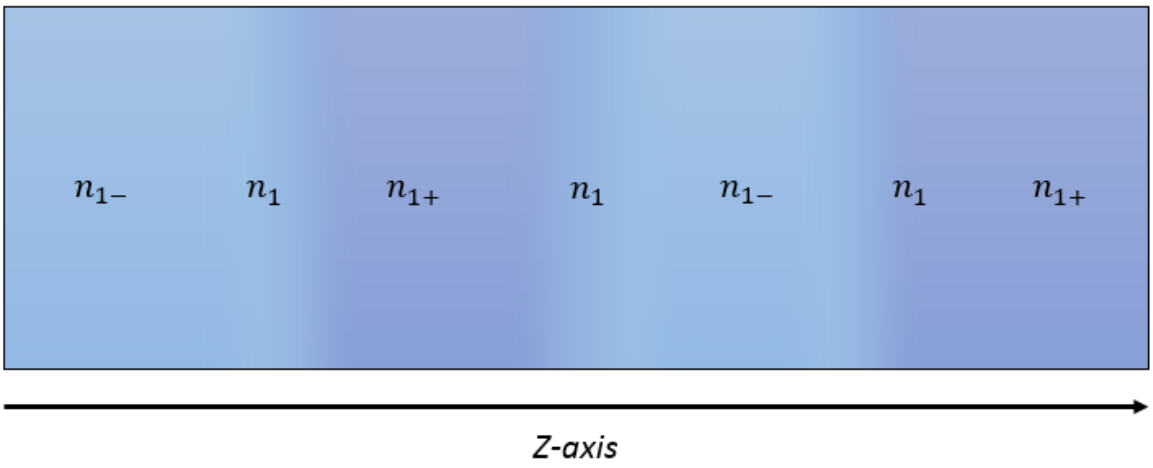


**Figure 2.43.** Schematic example of holographic filter through film.

The refractive index can be similarly described by (Eq. 2.2.15); however, the change in index is very small ($\Delta n \approx 0.01$).

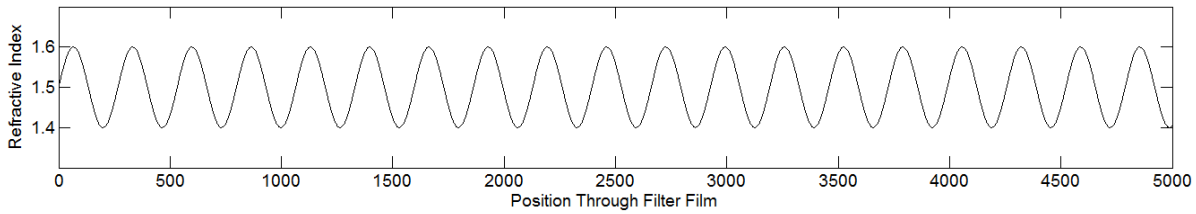


**Figure 2.44.** Schematic representation of the refractive index changes though the holographic film.

### Optical Colouration

All optical notch filters will experience a degree of functional visual impairment. The visual impact of an optical filter is related to the loss of transmission (IVPT) and the colouration. For the colour analysis of the metamaterial filter, the standard colour map (CIE 1931 *Standard Observer*) will be used. Due to individual variation of the human eye, the distribution of cones in the eye results in the tristimulus values being dependent on the observer's field of view [84]. The CIE 1931 colour map represents a chromatic response for the average human within 2° arc inside the fovea centralis, a region of closely packed cones in the eye; thus, providing the user confidence of the colouration response [85]. The transmission and reflective cases can be established from the following equations;

$$X = \int_0^\infty I(\lambda)\, T(\lambda)\, \overline{x}(\lambda)\, d\lambda \tag{2.2.17a}$$

$$Y = \int_0^\infty I(\lambda)\, T(\lambda)\, \overline{y}(\lambda)\, d\lambda \tag{2.2.17b}$$

$$Z = \int_0^\infty I(\lambda)\, T(\lambda)\, \overline{z}(\lambda)\, d\lambda \tag{2.2.17c}$$

Where $I(\lambda)$ and $T(\lambda)$ are the same as Eq. 2.2.9, and $\overline{x}(\lambda)$, $\overline{y}(\lambda)$ and $\overline{z}(\lambda)$ are colour matching functions that numerically describe the chromatic responses of the observer, figure 2.45.

The translation to the *x*-*y* coordinates on the colour map are described by;

$$x = \frac{X}{X + Y + Z} \tag{2.2.18a}$$

$$y = \frac{Y}{X + Y + Z} \tag{2.2.18b}$$

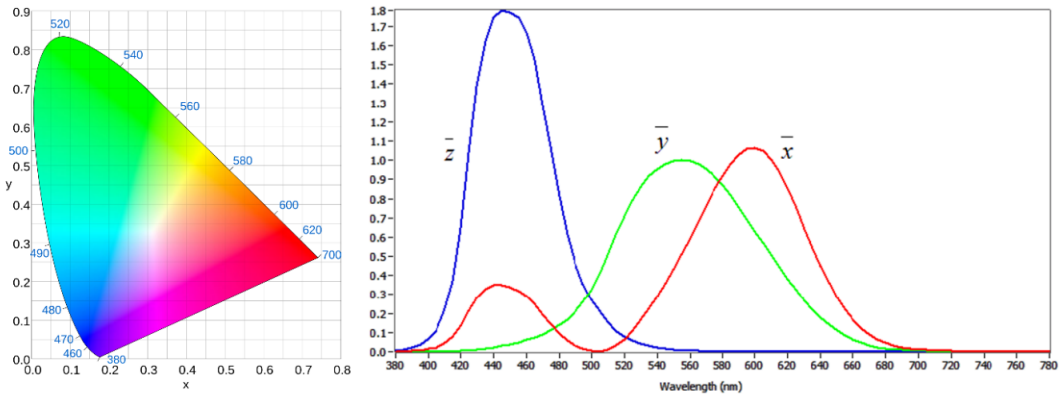


**Figure 2.45.** CIE 1931 [*Left*] and the CIE 1931 colour matching functions [*Right*]. (*Adapted from* [85]).

**Blue Shift**

Although the existing thin film technology has been the staple for laser protection systems for many years and have considerable advantages, they also have some concerning and underlying problems.

The main issue with thin films is the angular intolerance. As the angle of incidence (AOI) increases, the transmission spectrum of the filter experiences a continuous blue shifting to shorter wavelengths [86]. This results in the failure of the device to operate at the desired blocking wavelength. To circumvent this issue, the thin film filter is designed with an increased bandwidth, to allow coverage over the desired wavelength as blue shifting occurs. This in turn creates further problems through reduced visibility (transmission decrease) and high colouration. Furthermore, in order to achieve the correct optical density at non-zero angle of incidence, the thin films require additional layers to attenuate the transmission effectively. By default, the additional layers increase the overall thickness, further increasing the probability of delamination, particularly on high stressed surfaces such as fighter jet visors.

The amount of blue shift is inversely proportional to the effective average refractive index of the thin film stack, figure 2.46.

$$\lambda_\theta = \lambda_0 \sqrt{1 - \frac{\sin^2 \theta}{n_{eff}^2}} \tag{2.2.19}$$

Where $\lambda_\theta$ is the central shifted wavelength, $\lambda_0$ is the reference wavelength at normal AOI, $\theta$ is the AOI and $n_{eff}$ is the effective average refractive index.

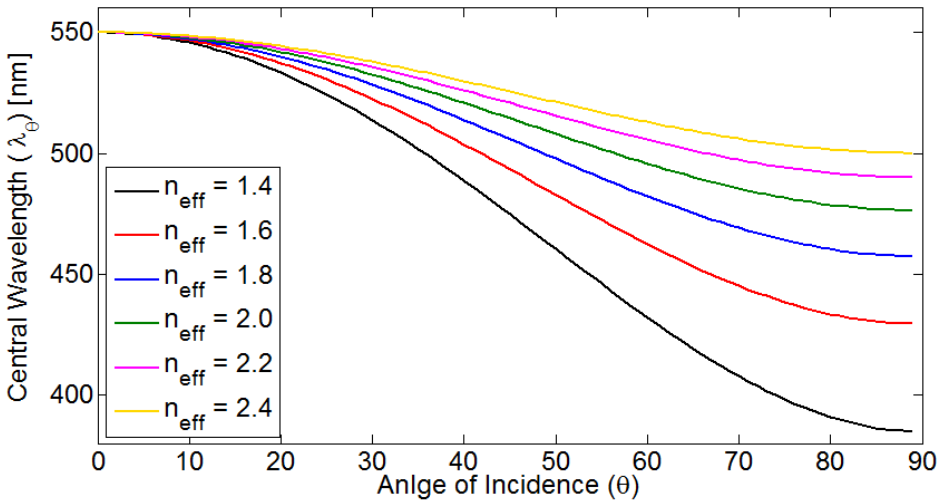


**Figure 2.46.** Blue shift rate versus the effective average refractive index with $\lambda_0 = 550\,nm$.

Figure 2.47 presents the mean transmission spectrum of a Rugate filter that blocks 53 2nm. As the angle of incidence increases, it is evident that blue shift occurs. Moreover, the addition of the "shelves", present at around 50% transmission for non-zero incidence angles, demonstrates that the thin film filters are also polarisation sensitive meaning they favour one polarisation over the other. The insert of the picture highlights the colouration of the filter according to the CIE 1931 chart. By restricting a section of the visible spectrum, a colour imbalance is produced that is inversely related to the colour blocked. For example, by limiting the transmission of blue light, the filter with display a yellowish tint.

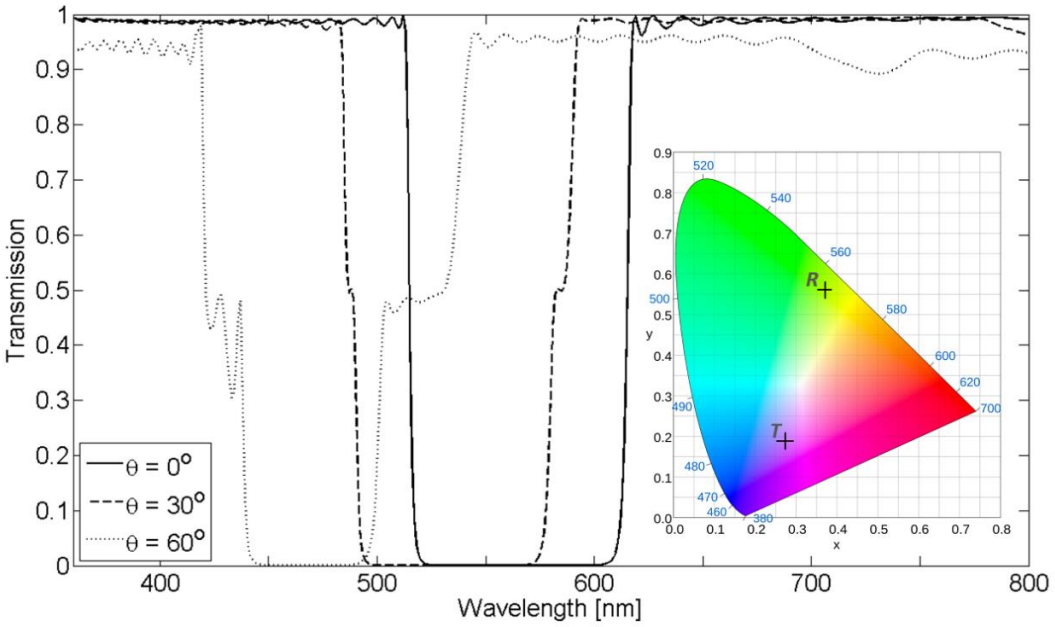


**Figure 2.47.** Example of Rugate filter transmission as different angle of incidents.

### 2.2.5 Next Generation Protection, Prevention and Beyond

The next generation of protection and prevention must not only protect personnel but also enable law enforcement to locate and prosecute the perpetrator. However, additional resources are required to protect personnel at large angles of incidence. For this, some novel solutions need to be developed.

#### Legislation

In 2018 new legislation was passed for the offences of shining or directing a laser beam towards a vehicle or air traffic [87]. The legislation is titled the "Laser Misuse (Vehicles) Act 2018" could lead to up to a five-year prison sentence, an unlimited fine or both. Police have also been given additional powers to catch anyone responsible for the misuse of lasers. Police officers, alongside their powers of arrest and the ability to conduct a personnel search, no longer need to establish proof of intent to endanger. This makes it much easier to prosecute.

**DSTL Detecting Lasers via Mobile Apps**

DSTL's Dr Craig Williamson developed an application for smart phones to record live laser events. The app was created in 2013 and is called "LERapp", Live Event Recorder [88]. This app has never been made available publicly. The app is designed so that when a laser is detected via a smartphone camera, the application becomes live and records the event, creating a digital footprint of the incident. This footprint provides a picture of the event, the GPS location, time and date, and the laser parameters (colour and estimated irradiance). The app will not directly locate the coordinates of the laser attack. Instead, it will photograph the event including the geographic region allowing law enforcement to locate the area of incidents through landmarks and street patterns. The future versions of the app are to include notification to other nearby aircraft and a solution for triangulating the location of the source.


**Figure 2.48.** Digital footprint of a laser event from the 2013 version of the LERapp [88].

**Laser Location detective device**

A student from George Mason University developed a prototype laser illumination detector to determine the estimated location of a green laser source [89]. The equipment is a self-contained system that is designed to be installed within the cockpit of an aircraft without interfering within any other aircraft instruments. The device contains a GPS and 3-axis magnetic compass for the location, altitude and orientation data. The camera sensor detects the green laser light by saturating the picture to the RGB (101, 255, 0) equivalent of 532 nm. Saturating for this colour allows the sensor channel to distinguish laser light from other bright non-laser light, such as sunlight reflection from ground objects. Using a raspberry pi computer with some independent python programme, the system can calculate the centre of the bright laser light to calculate the

approximate location. Ground testing of the system, at a relatively short distance (<100 m), gave an error of 15 meters. With some further development and improved accuracy, this low-cost system could provide key data for aircraft, air traffic control and police forces.

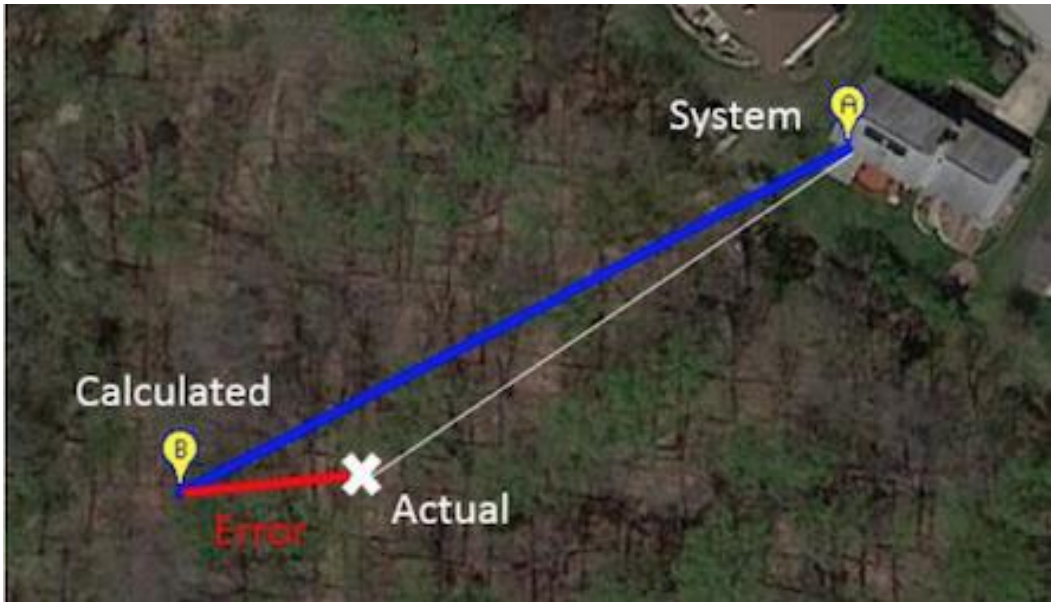


**Figure 2.49.** Satellite overview of the ground test location [89].

**BAE Systems Laser Protection Technology**

In late 2017, BAE Systems published an article claiming to have developed a low cost, lightweight, flexible system that can block dangerous laser light with applications for protecting pilots and other transport vehicles [90].

The research engineer, Daniel Black, and executive scientist, Dr Leslie Laycock, suggested that their novel solution was based on the way in which 3D glasses block light in the cinema by controlling the polarisation. After some research, they claimed to have been able to achieve a visible light transmission of over 70% whilst blocking three distinct laser wavelengths (445 nm, 532 nm and 650 nm). The active blocking layer to their design is a metamaterial formed from a holographic lithography method with an array of sufficiently small photodetectors that are invisible to "casual observers" [91]. The principles of the photodetectors are to act as a homing location device to aid police, other forces and air traffic control. In additional, the photodetectors can alert other aircraft in the area to be alert for laser attacks. It is unclear exactly what the holographic 'metamaterial' film consists of, just that it can be processed with a photosensitive polymeric film that has been exposed to one or more lasers. Another indistinct variable that was not mentioned was whether the filter was able to block at non-normal angles.

### MTI's Lambda Guard

Metamaterial Technologies Inc. (MTI) is a smart material and photonics company that was established in 2010. MTI are claiming to have achieved a wide-angle all dielectric metamaterial specifically designed for blocking laser light [92]. The metamaterial layer has a multilayer holographically recorded nanostructure patterned photopolymer film. The film is a photorefractive polymer (Bayfol HX photopolymer film) supplied from Covesto [93]. The nanostructured pattern consists of a triangular pattern with dimensions of 10 nm by 10 nm, comprising of over 2000 layers. Figure 2.50 Shows the MetaAir product and the performance.

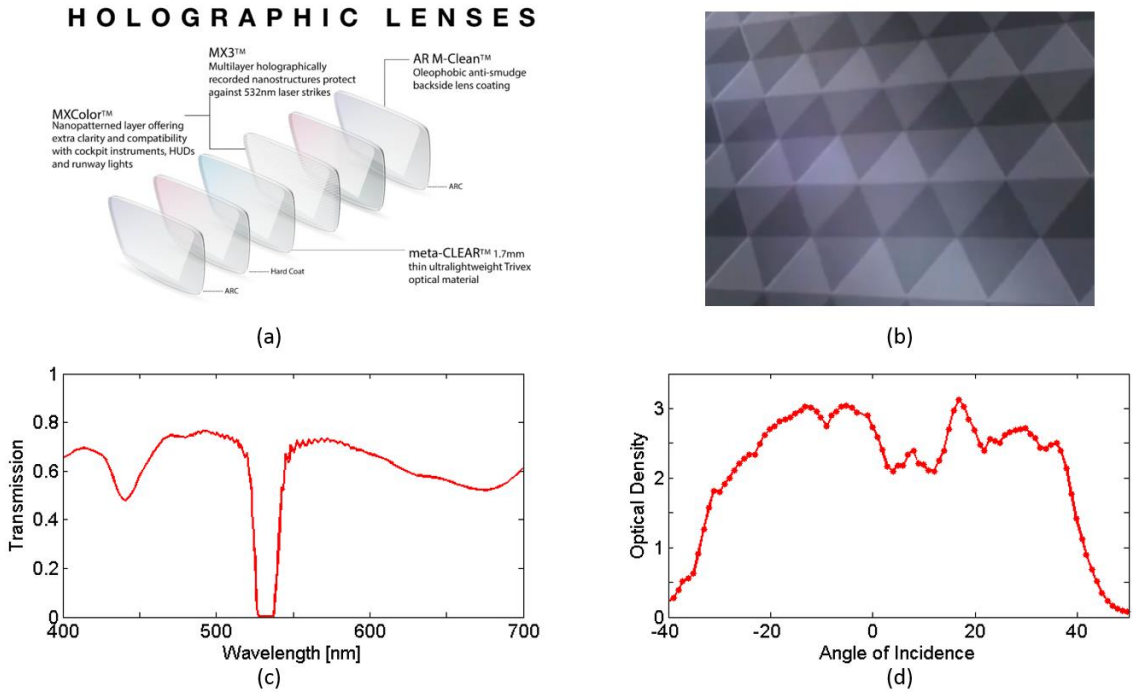


**Figure 2.50.** MTI's MetaAir laser protection device [92-93]. (a) MetaAir glass arrangement. (b) The holographic recorded nanopattern according to MTI. (c) Transmission response of the MetaAir glass arrangement. (d) The optical density performance against angle of incidence.

MTI are suggesting that their product operates at high angle of incidence. In reality the angular performance is around ±20° for OD2. This is comparable with current standard thin film technology.

The company has been developing this technology since 2010, has had a large sum of investment, in excess of $10mil+, and has won multiple awards for their product [94]. As of this date, the MetaAir product is yet to be released.

MTI's MetaAir product and BAE Systems technology propose metamaterials to be the key player for the next generation of laser protection devices and could provide significant improvement for the shortfalls of standard thin film technology.

## 2.3 **Metamaterials. Definition and Principles**

The definition of a metamaterial is still not completely clear. However, it is agreed that metamaterials are artificial man-made materials that do not exist in nature [95]. In electromagnetics, and optics in particular, there are many material properties that one would assume would be enabled within the laws of physics. Nevertheless, these properties are still yet to be found within nature. In order to monitor the physical world, one has to build the equipment to analyse it. However, if that material isn't available to build a specialised sensor, for example, then experiment presents some clear challenges. Thus, the introduction of metamaterials came into existence; not just for applications in electromagnetism, but also in acoustic, mechanical/structural, thermoelectric, etc [96]. Ordinary materials, i.e. materials that exist in nature, respond to an electromagnetic field in accordance to how the atoms and molecules polarise, with their average behaviour over the lattice providing the electromagnetic response. In contrast, metamaterials replace the atoms and molecules with larger elements that display a physical structure. These units are known as unit-cells or meta-atoms and remain much smaller than the wavelength of interest, typically on the order of ten times less. By existing at a much smaller size, compared to the wavelength, they begin to act like atoms and molecules, and by designing the shape, geometry, size, orientation and arrangement, it becomes possible to design the properties and responses of the metamaterials. The major advantage to metamaterials is the fact that they are not limited to the chemistry of the periodic table and allow for another dimension of design through the flexibility of structure.

### 2.3.6 **The Beginning of Metamaterials**

In 1967, Ukrainian physicist, Victor Veselago published a paper theoretically studying materials with simultaneous negative permittivity and permeability [97]. This paper was a thought-provoking idea for electromagnetic interactions with materials and debated hotly at the time. The paper mainly pointed to the idea of a negative refractive index, and the debate died out because nature provided zero examples of a material with a negative refractive index; thus, the idea lacked any practical applications. It wasn't until three decades later that metamaterial research truly began with Veselago's paper providing the foundational mathematical support. In 2000, a theoretical physicist, John Pendry, published his findings on the "Perfect lens" [98]. The work was an extension of Veselago's work and demonstrated that an unconventional slab of negative refractive index material has the ability to resolve beyond the diffraction limit which limit conventional lenses.

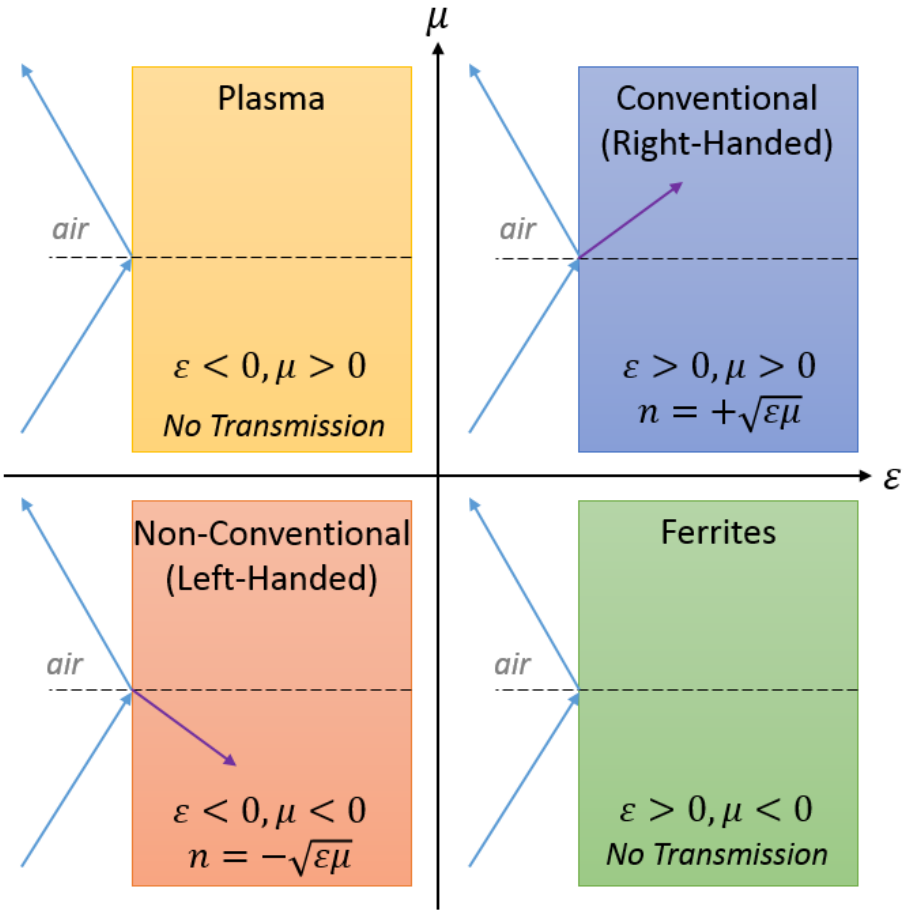


**Figure 2.51.** Classification of materials based on the permittivity and permeability.

In the early 2000's, Pendry developed a technique for invisibility cloaks with the inspiration from Einstein's theory of gravity [99]. Einstein regarded space almost as a material, which can stretch or compress, and if that space becomes distorted then objects moving through it no longer travel in a straight line, including light [98]. Arthur Stanley Eddington's experiment provided evidence of the bending of light around the sun during a solar eclipse [100] which delivered one of the foundation stones of Einstein's general theory of relativity. Pendry's solution was not to find something massive (galaxy or black hole) to bend light because he noticed that Einstein also showed that the effect produced by a bending or stretching of space is equivalent to a material with a precise refractive index distribution. Pendry was able to use the metric solutions provided by Einstein to design the refractive index distribution related to the bending and stretching of space.

The foundations laid by Veselago allowed Pendry to formulate some radical theories for new complex materials that are able to obtain their properties depending on their composite, shape and arrangement. This was the birth of the Superlens, transformation optics and the beginning of metamaterials.

### 2.3.7 **Rare Natural Metamaterials**

Metamaterials, as previously discussed, are man-made synthetic materials that extend beyond the periodic table by integrating the shape, orientation and periodicity into materials fundamental unit-cell design. The shape of the meta-atom, a single cell of the periodic material, must operate on the scale of approximately ten times smaller than the wavelength of interest to simulate a homogeneous material. Inherently, metamaterials are incredibly complex and although they are considered to be artificial materials; however a slight contradiction to the metamaterial definition, nature has found a way to mimic the complexity of unit-cell structures. This provides an additional inspiration for metamaterial research.

An example of a metamaterial found in nature are those which produce colour through structure rather than an absorbing pigment. An example of pigment can be found in the greenness of plants. Chlorophyll absorbs the red and blue wavelengths of light but does not absorb the green wavelengths. As such, the green wavelengths are reflected off the plants and into our eyes, making it appear that the plant is green. However, butterflies, or at least some species of butterfly (*morpho butterfly*), have a thin film of hardened protein on their wings called chitin [101]. Chitin is a long-chain polymer derived from glucose and can be found on the cell walls of fungi and the exoskeletons of insects. Though, on the butterfly wings, chitin is arranged into thousands of tiny scale layers and reflect a stunning blue colour.

Blue colour in nature is very infrequently found. Animals come in every colour, but blue seems to be the rarest. The magnification of a morpho butterfly shows that the wing is made from a repeated pattern of tiny ‘Christmas tree’ like structures. The arrangement of ‘branches’ on these tiny trees is what provides morpho wings with the vibrant blue colour. The trees are similar to nano-feathers. The Latin word for butterflies is Lepidoptera, translating to lepido – “scale” + pteron “wing, feather”.

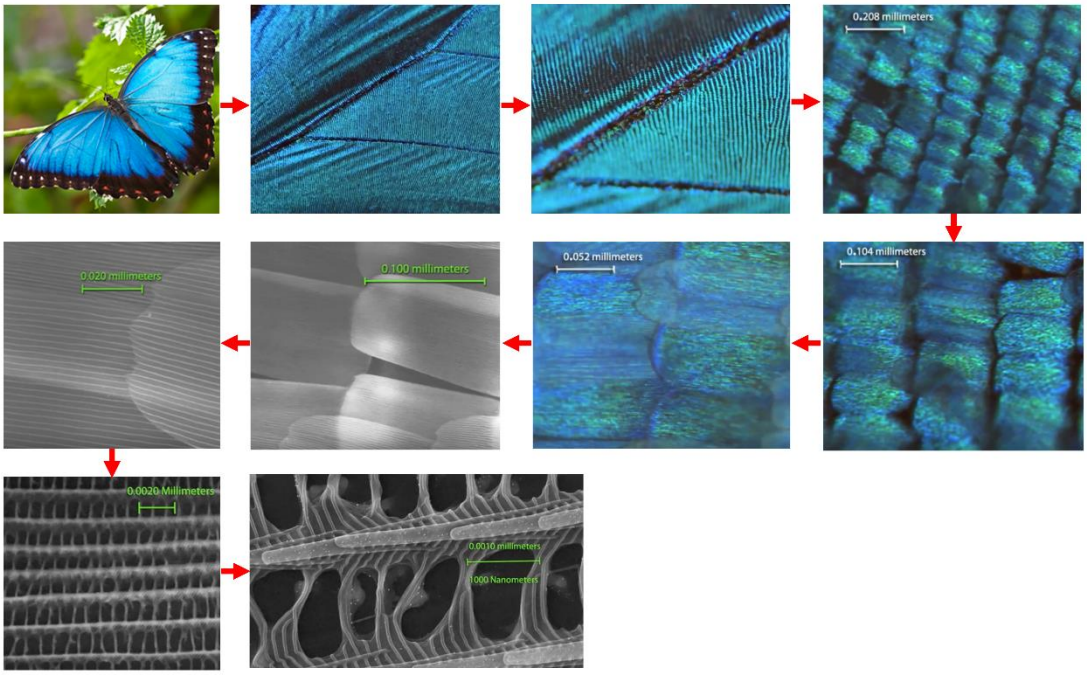


**Figure 2.52.** The morpho butterfly and the magnification of its wing. (*Adapted from* [102]).

When light travels through the nano-feathers, a portion of light bounces off the top surface structures whilst the remaining light transmits and reflects off the bottom surface. For most colours of light, this creates destructive interference due to the phase difference between the two reflective wavelengths. However, some non-blue visible light does make it through these structures and is absorbed by pigment. On the other hand, blue light creates constructive interference. This type of structure can be considered as single wavelength mirror, and with some adaptions (removal of pigment and transparent substrate), could produce a metamaterial bandstop filter.

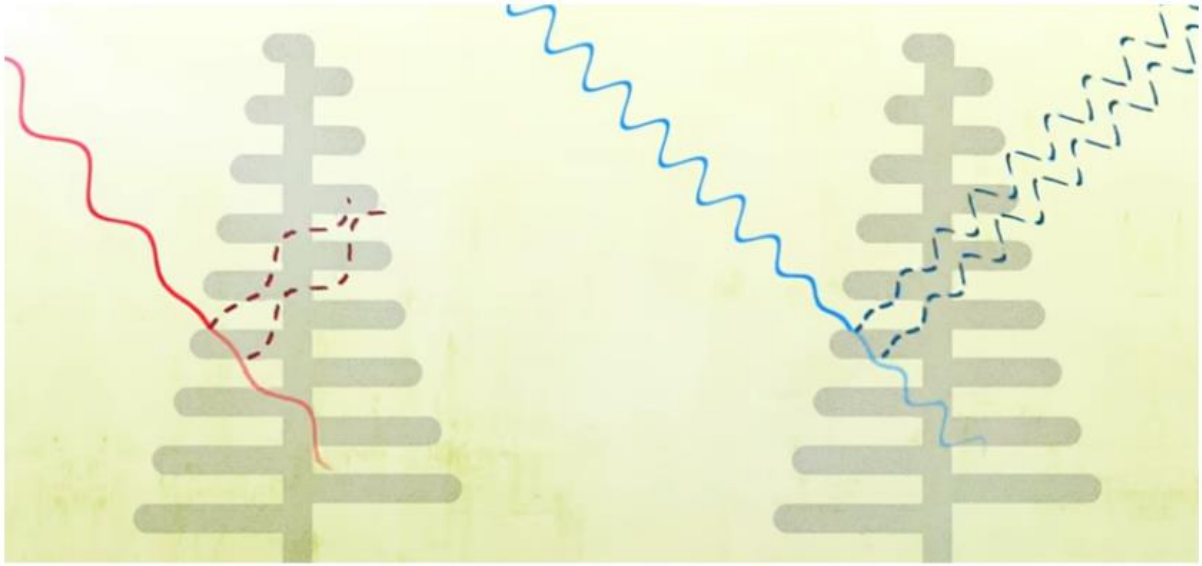

**Figure 2.53.** The morpho butterfly wing creating destructive and constructive interference [103].

### 2.3.8 Metamaterial Filtering

Often metamaterial filtering is achieved through frequency selective surfaces (FSS). A FSS is typically a flat planar surface composite material, designed to be transparent for some frequencies while remaining reflective, absorbing or redirecting for other frequencies. Predictably, when a periodic structure is placed/designed into a planar surface, frequency selectivity is achieved. Figure 2.54 presents a relatively famous slot array FSS which consists of geometric holes (Jerusalem cross) perforated through a metal sheet and has ability to produce a bandpass frequency response. FSS are not restricted to the bandpass Jerusalem cross, they come is all shapes and sizes, which is what dictates the filter type and frequency band.

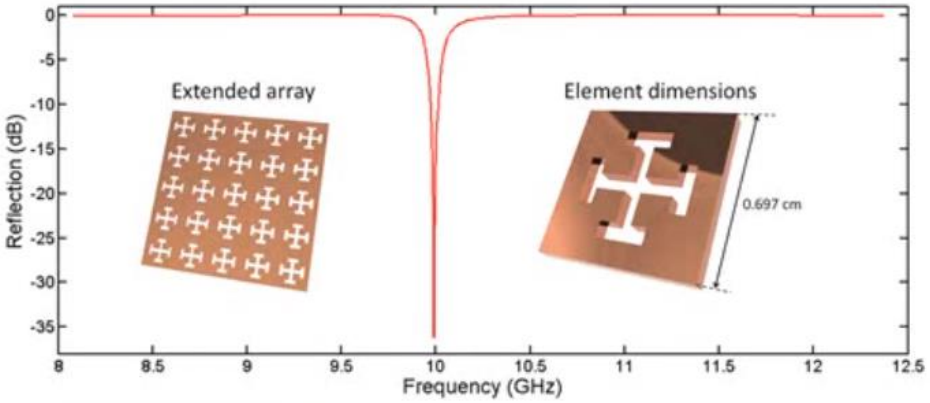


**Figure 2.54.** The Jerusalem cross frequency selective surface and its refraction response [104].

There are two main physical mechanisms to induce a frequency response, redirection and absorption. Absorption requires the incorporation of a lossy material. Both responses can be amplified by introducing resonant structures. The redirection principle, as shown in figure 2.55, can be broken down into further categories, 'longitudinal' resonance, 'transverse' resonance, and diffraction. Diffraction, in principle, is an efficient method providing the source location is known and constant. However, when the direction of light is unknown, diffraction offers little benefits.

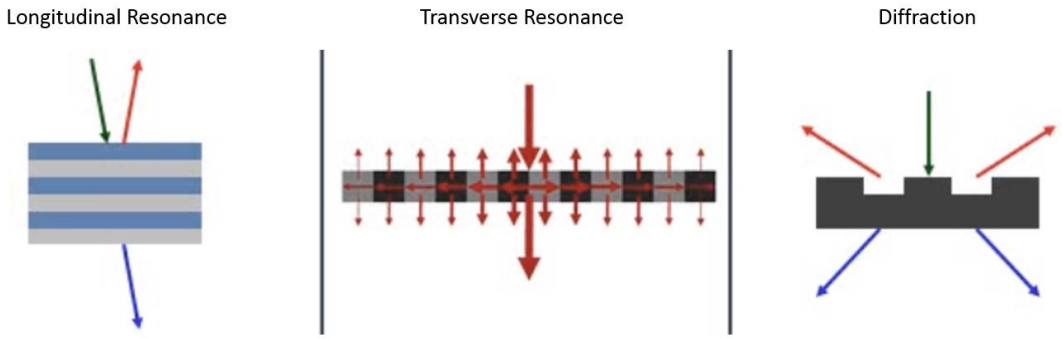


**Figure 2.55.** Sub-categories of the redirection mechanism [104].

Traditionally, an FSS consists of a single layer and requiring multiple FSS layers is considered a drawback, especially for modern day optics such as metalens [105]. Nonetheless, it can provide additional response improvements. Reference [106] demonstrated that by using cascaded periodic structures, a steeper and sharper response was obtained in comparison to a single layer. Yet, the addition of multilayers proved to be more sensitive to angle of incidence.

Figure 2.56 demonstrated a slot array where a repetition of periodic non-connecting structure provides a bandpass filter response. By forming a complimentary equivalent array, ideally speaking, the reflection response should present as the exact opposite allowing for a bandstop filter to be realised [107], as demonstrated in figure 2.56.

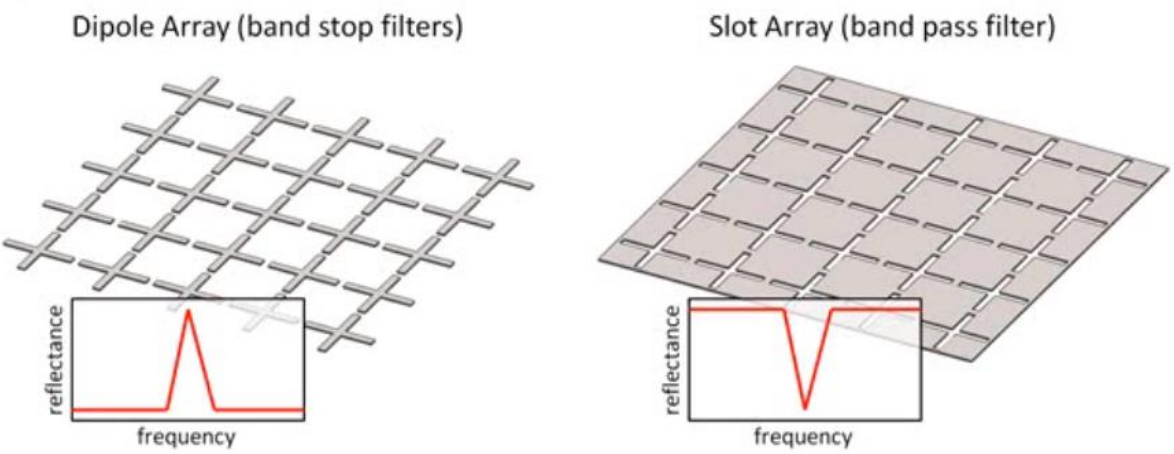


**Figure 2.56.** Sub-categories of the redirection mechanism [107].

Due to the fact that FSS are displaced on a single layer, the planar device is restricted to a two-dimensional symmetry which considers only five of the Bravais lattices, as shown in figure 2.57. There is a total of 14 Bravais lattice symmetries and are conceptually used to define the crystalline arrangement of atoms, ions and polymers [108]. Symmetry is an important aspect for metamaterials and as such, usually a high symmetry is desired. Often the hexagonal array is the symmetry of choice due to the high fill fraction (packing density) leading to a stronger frequency response. Furthermore, with the elements more closely packed, they become less sensitive to polarisation and angle of incidence.

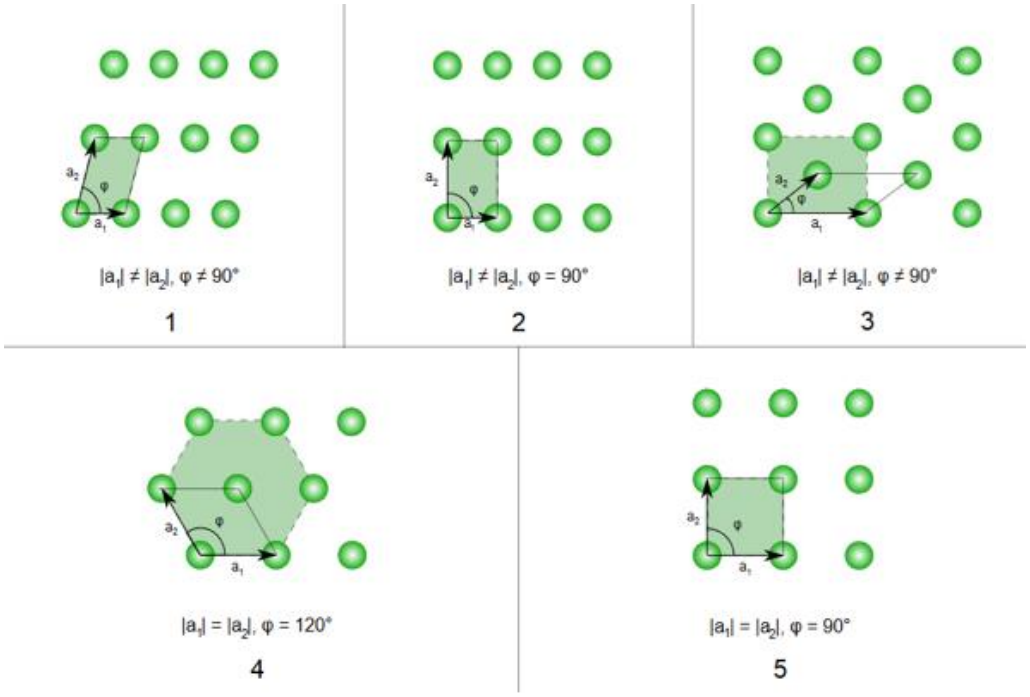


**Figure 2.57.** The available two-dimensional Bravais lattices [109].

Figure 2.58 presents a common solution for different elements depending on the filter properties desired.

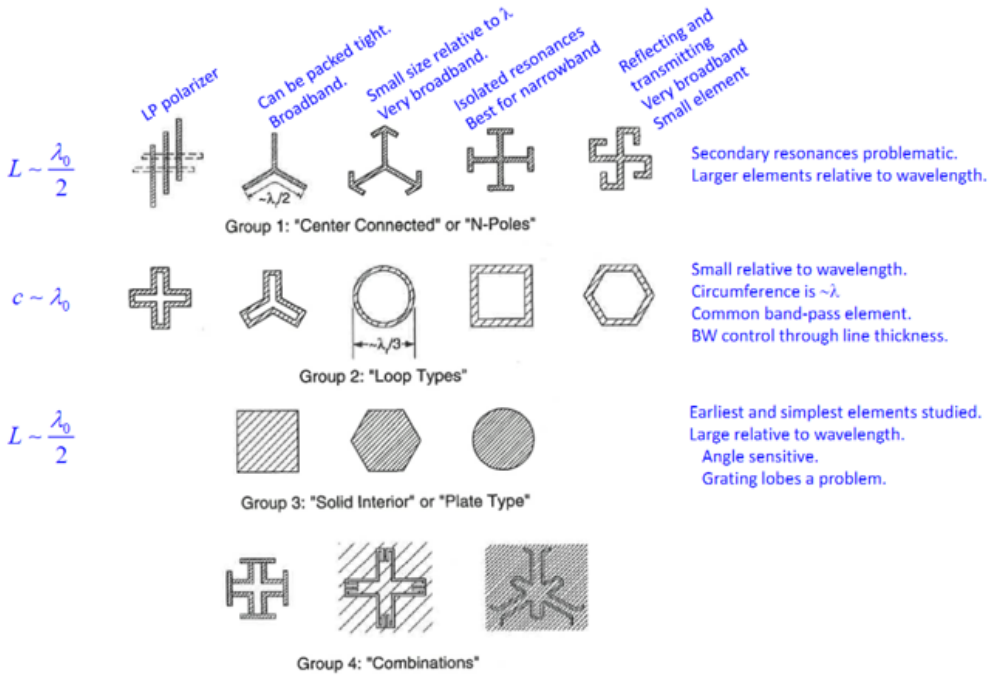


**Figure 2.58.** Common element types for frequency selective surfaces [104]. L is associated to the element length and c is related to the circumference.

Frequency selective surfaces provide excellent solutions for electromagnetic filtering; however, when approaching higher frequencies, particularly the infrared and optical frequencies, the

ability to fabricate such devices becomes elusive. Thus, FSS do not always present the best solutions for high frequency electromagnetic filtering.

Metamaterials are volumetric (three-dimensional) artificially crafted composite materials. They typically require multiple layer stacks for functionality, which can be challenging for nanofabrication and may also lead to extensive losses. Metasurfaces on the other hand are thin film two dimensional structures that were initially developed to overcome the complications of metamaterials. Frequency selective surfaces are a subsection of metasurfaces.

### 2.3.9 Angular Responses of Metamaterials

Considering the problem in hand, laser attacks can be positioned from varying angles of incidence. Thus, assessing the angular performance of metamaterials is critical. Yet, often when discoveries of metamaterials are published, they lack the information on angular performance. That being said, some groups do report the angular contribution [110-116]. Effects that dominate angular sensitivity and polarisation sensitivity at optical frequencies rely on the metamaterials ability to create a strong electric resonance at a particular wavelength which can create circulating currents to efficiently drive a magnetic response [117]. The strong electric and magnetic responses lead to an impedance mismatch, and angular stability remains as a result of the symmetry and equivalent inductance of the unit-cell [118]. Lossy materials are the key common material to achieve this effect, with reference [119] suggesting that in order to achieve insensitivity to the incident angle and polarisation, the metamaterial must contain an absorbing feature. Furthermore, wide-angle range operating metamaterials habitually lack the transmission elements needed to create an optical bandstop filter. This is a key aspect that needs to be addressed in order to create a shift-free wide-angle filter. Figure 2.59 presents an example of the optical responses of current wide-angle metamaterial devices.

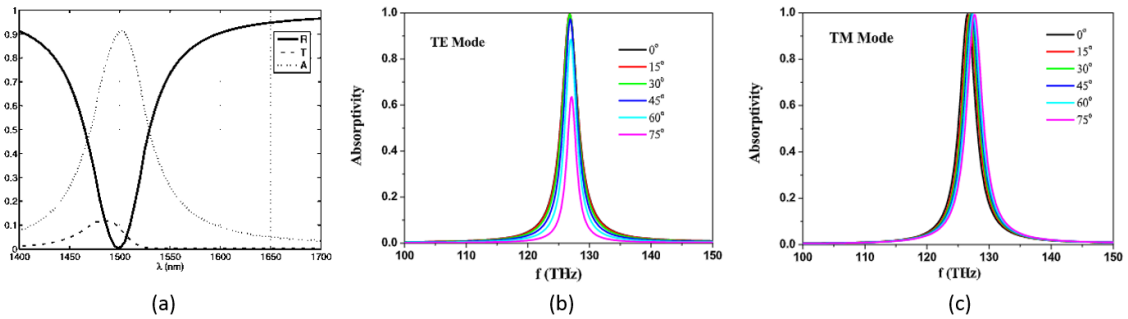


**Figure 2.59.** Common responses for wide-angle metamaterial devices. (a) Frequent example of the transmission, reflection and absorption for wide-angle devices [120]. (b) and (c) demonstrate wide-angle operation [117].

### 2.3.10 Direct and Inverse Design Methods

Designing metamaterials with a desired performance is not an easy task due to the complexity of the unit-cell structures and modelling their interactions with light. Often a brute force method is used where the designer mimics a structure from nature, or through educated guesswork, and tests its computational performance before further modifications and rerunning of the computational performance testing. Computational simulations are cheaper than fabrications but can present problems with accuracy and simulation time. This becomes a trial and error approach. Obviously, this is not a productive method and to combat this, research groups have been employing artificial intelligent (AI) systems to do the work (*examples and references can be found in the subsections below*). However, for an AI system to operate, it requires some starting point, whether that be training or an initial design. Yet, although the AI system produces some unique solutions, the designs can be difficult to construct in real life. The overall goal for scientists is to have a system where the engineer selects the desired output properties and the software produces the metamaterial design required with an understanding of modern fabrication techniques.

#### Genetic Algorithms

Genetic Algorithms (GA) take a set of search spaces and navigate for the optimum combination of solutions. The GA is not searching for the perfect solution, but examining a robust system rated against a criterion. The algorithm is a search and optimisation technique based on Darwin's principles of natural selection [121].

GAs have extensively been used for various problems in science and engineering, including metamaterials. Consequently, some interesting and unique designs have been produced. One such method by Pennsylvania State University established a set of equations that directly relate the design properties to the output performance [122]. They achieved this by tailoring the dispersion properties of the metamaterial so that the effective permittivity and permeability balanced the impedance to match the impedance of free space. This allowed the researchers to create a bandpass filter with a near ideal transmission. Using prior research, the group designed a conventional fishnet nanostructure composed of a three-layer metal-dielectric-metal stack and employed a GA technique coupled with an efficient full-wave electromagnetic solver to optimise and modify the fishnet design. The employment of the GA initiated deep-subwavelength inclusions into the design that had a marked effect on both the strength and the position of resonance.

### Neural Networks and Deep Learning

Neural networks and deep learning are not to dissimilar from one another [123,124]. The main difference is the number of networks within the "black box" section that is between the inputs and outputs. The inputs interconnect a group of nodes with the black box and the black box connects the output, with each node representing an artificial neuron. A neural network is more of a pattern recognition tool, with deep learning adding a statistical machine learning environment to that tool. Both neural networks and deep learning require training data in order to train the model for a specific task.

Like the genetic algorithm approach, research into the use of neural networks and deep learning has aided the metamaterial design process. A paper published in 2018 by Malkiel et al, demonstrated deep learning capability in designing and characterising plasmonic nanostructures [125]. The deep neural network was trained with thousands of synthetic experiments and was able to retrieve subwavelength plasmonic structure design from solely far-field measurements. This is a great example that could be realised for future inverse design method for optical metamaterial filters. There are also many other examples and research conducted into this algorithm and because they require a training data set, as the metamaterial community grows and more research output is generated, the algorithms will naturally have more examples to train from.

### Inverse Designs

A true inverse design system is highly difficult to implement due to the number of factors associated to the metamaterials (size, shape, orientation, periodicity, materials, target waveband, light-matter interactions, far- and near-field responses, etc). However, scientist at the Sandia National Laboratories, in mid-2019, claim to have developed the first inverse-design software for optical metamaterials. The software, called Mirage, claims to allow the user to start with the result that they want, and the software processes the steps to achieve that [126]. According to the research group leader, El-Kady, Mirage allows the operator to select the desired optical properties, how the metamaterial is required to interact with light, and the starting material. The Mirage software then generates the designs that matches the criteria from a library of over 100 templates [126]. Mirage does seem to be the earliest metamaterial software that allows the user to explore, simulate and validate metamaterial designs within predefined fabrication constraints. This is a required first steps to employing metamaterials in a real-world problem.

## 2.4 **References**

[1] "P9.0 – Electromagnetic Spectrum", IGCSE AID, 2019. [Online]. Available: https://igcseaid.wordpress.com/notes/coordinated-science-0654/p9-0-electromagnetic-spectrum/.
[2] D. Fleisch, A student's guide to Maxwell's equations. Cambridge University Press, 2008.
[3] H. White, "Pictorial Representations of the Electron Cloud for Hydrogen-Like Atoms", Physical Review, vol. 37, no. 11, pp. 1416-1424, 1931. Available: 10.1103/physrev.37.1416.
[4] H. Kragh, Niels Bohr and the quantum atom. Oxford: Oxford University Press, 2012.
[5] F. Monticone and A. Alù, "The quest for optical magnetism: from split-ring resonators to plasmonic nanoparticles and nanoclusters", J. Mater. Chem. C, vol. 2, no. 43, pp. 9059-9072, 2014. Available: 10.1039/c4tc01406e.
[6] J. Chen et al., "Optical Magnetic Field Enhancement by Strong Coupling in Metamaterials", Journal of Lightwave Technology, vol. 36, no. 13, pp. 2791-2795, 2018. Available: 10.1109/jlt.2018.2822777.
[7] A. Barreda, J. Saiz, F. González, F. Moreno and P. Albella, "Recent advances in high refractive index dielectric nanoantennas: Basics and applications", AIP Advances, vol. 9, no. 4, p. 040701, 2019. Available: 10.1063/1.5087402.
[8] M. Born and E. Wolf, Principles of optics. Electromagnetic theory of propagation, interference and diffraction of light. 4.ed. Oxford: Pergamon Press, 1970.
[9] P. Drude, "Zur Elektronentheorie der Metalle", Annalen der Physik, vol. 306, no. 3, pp. 566-613, 1900. Available: 10.1002/andp.19003060312.
[10] P. Huray, Maxwell's equations. Hoboken, NJ: Wiley, 2010.
[11] A. Sommerfeld, "Zur Elektronentheorie der Metalle auf Grund der Fermischen Statistik", Zeitschrift fur Physik, vol. 47, no. 1-2, pp. 1-32, 1928. Available: 10.1007/bf01391052.
[12] L. Novotny and B. Hecht, "Surface plasmons", Principles of Nano-Optics, pp. 369-413. Available: 10.1017/cbo9780511794193.014.
[13] R. Petrucci, F. Herring and J. Madura, General Chemistry. Toronto: Pearson Canada, 2011.
[14] B. Cooper, H. Ehrenreich and H. Philipp, "Optical Properties of Noble Metals. II.", Physical Review, vol. 138, no. 2, pp. A494-A507, 1965. Available: 10.1103/physrev.138.a494.
[15] P. Johnson and R. Christy, "Optical Constants of the Noble Metals", Physical Review B, vol. 6, no. 12, pp. 4370-4379, 1972. Available: 10.1103/physrevb.6.4370.
[16] L. Mendoza Herrera, D. Arboleda, D. Schinca and L. Scaffardi, "Determination of plasma frequency, damping constant, and size distribution from the complex dielectric function of noble metal nanoparticles", Journal of Applied Physics, vol. 116, no. 23, p. 233105, 2014. Available: 10.1063/1.4904349.
[17] Q. Flamant et al., "Direct retrieval method of the effective permittivity and permeability of bulk semi-infinite metamaterials by variable-angle spectroscopic ellipsometry", OSA Continuum, vol. 2, no. 5, p. 1762, 2019. Available: 10.1364/osac.2.001762.
[18] "Fresnel's Equations for Reflection and Transmission", https://www.brown.edu/research/labs/mittleman/sites/brown.edu.research.labs.mittleman/files/uploads/lecture13_0.pdf, 2019.

[19] R. Westfall, "The Mathematical Principles of Natural Philosophy. Isaac Newton , Andrew Motte", Isis, vol. 60, no. 4, pp. 576-576, 1969. Available: 10.1086/350565.
[20] Y. Chen and H. Ming, "Review of surface plasmon resonance and localized surface plasmon resonance sensor", Photonic Sensors, vol. 2, no. 1, pp. 37-49, 2012. Available: 10.1007/s13320-011-0051-2.
[21] S. Maier, Plasmonics. New York: Springer, 2010.
[22] J. Zhang, L. Zhang and W. Xu, "Surface plasmon polaritons: physics and applications", Journal of Physics D: Applied Physics, vol. 45, no. 11, p. 113001, 2012. Available: 10.1088/0022-3727/45/11/113001.
[23] G. Yao, Q. Liu and Z. Zhao, "Studied Localized Surface Plasmon Resonance Effects of Au Nanoparticles on TiO2 by FDTD Simulations", Catalysts, vol. 8, no. 6, p. 236, 2018. Available: 10.3390/catal8060236.
[24] D. Chahinez, T. Reji and R. Andreas, "Modeling of the surface plasmon resonance tunability of silver/gold core–shell nanostructures", RSC Advances, vol. 8, no. 35, pp. 19616-19626, 2018. Available: 10.1039/c8ra03261k.
[25] P. Rysselberghe, "Remarks concerning the Clausius-Mossotti Law", The Journal of Physical Chemistry, vol. 36, no. 4, pp. 1152-1155, 1932. Available: 10.1021/j150334a007.
[26] I. Mayergoyz, D. Fredkin and Z. Zhang, "Electrostatic (plasmon) resonances in nanoparticles", Physical Review B, vol. 72, no. 15, 2005. Available: 10.1103/physrevb.72.155412.
[27] D. Bohm and D. Pines, "A Collective Description of Electron Interactions. I. Magnetic Interactions", Physical Review, vol. 82, no. 5, pp. 625-634, 1951. Available: 10.1103/physrev.82.625.
[28] "Web of Science", webofknowledge.com, 2019. [Online]. Available: http://wcs.webofknowledge.com/RA/analyze.do?product=WOS&SID=D5ktc4IA4sABiQJ4JIt&field=PY_PublicationYear_PublicationYear_en&yearSort=true.
[29] A. González, C. Noguez, J. Beránek and A. Barnard, "Size, Shape, Stability, and Color of Plasmonic Silver Nanoparticles", The Journal of Physical Chemistry C, vol. 118, no. 17, pp. 9128-9136, 2014. Available: 10.1021/jp5018168.
[30] N. Khlebtsov and L. Dykman, "Optical properties and biomedical applications of plasmonic nanoparticles", Journal of Quantitative Spectroscopy and Radiative Transfer, vol. 111, no. 1, pp. 1-35, 2010. Available: 10.1016/j.jqsrt.2009.07.012.
[31] F. Enrichi, A. Quandt and G. Righini, "Plasmonic enhanced solar cells: Summary of possible strategies and recent results", Renewable and Sustainable Energy Reviews, vol. 82, pp. 2433-2439, 2018. Available: 10.1016/j.rser.2017.08.094.
[32] R. Aroca, "Plasmon enhanced spectroscopy", Physical Chemistry Chemical Physics, vol. 15, no. 15, p. 5355, 2013. Available: 10.1039/c3cp44103b.
[33] K. Lovchinov, O. Angelov and D. Dimova-Malinovska, "Optical properties of thin films with plasmonic effect for light scattering", Journal of Physics: Conference Series, vol. 398, p. 012017, 2012. Available: 10.1088/1742-6596/398/1/012017.
[34] G. Barbillon, "Plasmonics and its Applications", Materials, vol. 12, no. 9, p. 1502, 2019. Available: 10.3390/ma12091502.

[35] "Introduction to Nanoparticle Optical Properties", nanoComposix, 2019. [Online]. Available: https://nanocomposix.com/pages/introduction-to-nanoparticle-optical-properties.
[36] M. Faraday, "Experimental relations of gold (and other metals) to light.—The bakerian lecture", The London, Edinburgh, and Dublin Philosophical Magazine and Journal of Science, vol. 14, no. 95, 1857. Available: 10.1080/14786445708642410.
[37] G. Mie, "Beiträge zur Optik trüber Medien, speziell kolloidaler Metallösungen", Annalen der Physik, vol. 330, no. 3, pp. 377-445, 1908. Available: 10.1002/andp.19083300302.
[38] "Nanoeffects in Ancient Technology and Art and in Space", Fundamentals and Applications of Nano Silicon in Plasmonics and Fullerines, pp. 497-518, 2018. Available: 10.1016/b978-0-323-48057-4.00016-5.
[39] D. Bučar, S. Filip, M. Arhangelskis, G. Lloyd and W. Jones, "Advantages of mechanochemical cocrystallisation in the solid-state chemistry of pigments: colour-tuned fluorescein cocrystals", CrystEngComm, vol. 15, no. 32, p. 6289, 2013. Available: 10.1039/c3ce41013g.
[40] O. Hofmann et al., "Monolithically integrated dye-doped PDMS long-pass filters for disposable on-chip fluorescence detection", Lab on a Chip, vol. 6, no. 8, p. 981, 2006. Available: 10.1039/b603678c.
[41] A. Einstein, "Zur Quantentheorie der Strahlung (On the quantum theory of radiation)", Physikalische Zeitschrift, vol. 18, pp. 121-128, 1917.
[42] T. MAIMAN, "Stimulated Optical Radiation in Ruby", Nature, vol. 187, no. 4736, pp. 493-494, 1960. Available: 10.1038/187493a0.
[43] D. Titterton, Military laser technology and systems. Boston: Artech House, 2015.
[44] H. Jelínková, Lasers for medical applications. Philadelphia, PA: Woodhead Pub., 2013.
[45] T. ITOH, "Fundamentals of Laser Spectroscopy. II. Luminescence Spectroscopy.", The Review of Laser Engineering, vol. 28, no. 1, pp. 54-59, 2000. Available: 10.2184/lsj.28.54.
[46] F. Floux, "Nuclear fusion by laser radiation", Nuclear Fusion, vol. 11, no. 6, pp. 635-647, 1971. Available: 10.1088/0029-5515/11/6/006.
[47] R. Seisyan, "Nanolithography in microelectronics: A review", Technical Physics, vol. 56, no. 8, pp. 1061-1073, 2011. Available: 10.1134/s1063784211080214.
[48] D. Schmid and N. Stanton, "How are laser attacks encountered in commercial aviation? A hazard analysis based on systems theory", Safety Science, vol. 110, pp. 178-191, 2018. Available: 10.1016/j.ssci.2018.08.012.
[49] S. Kasap, Optoelectronics and photonics. Boston: Pearson, 2013.
[50] Pech-Canul. and Lekhwani., Semiconductors. [S.l.]: Springer International Publishing, 2019.
[51] A. Jalkh, K. Pflibsen, O. Pomerantzeff, C. Trempe and C. Schepens, "A New Solid-state, Frequency-Doubled Neodymium-YAG Photocoagulation System", Archives of Ophthalmology, vol. 106, no. 6, pp. 847-849, 1988. Available: 10.1001/archopht.1988.01060130917052.
[52] "Laser radiation: introduction and safety advice", GOV.UK, 2006. [Online]. Available: https://www.gov.uk/government/publications/laser-radiation-safety-advice.
[53] "Laser Classification", Warwick.ac.uk, 2019. [Online]. Available: https://warwick.ac.uk/services/healthsafetywellbeing/guidance/lasers/appendix1classification.

[54] "Aeromedical Safety Brochures", Faa.gov, 2019. [Online]. Available: https://www.faa.gov/pilots/safety/pilotsafetybrochures/.
[55] P. Murphy, "Laser/aircraft incident statistics", LaserPointerSafety.com, 2019. [Online]. Available: https://www.laserpointersafety.com/latest-stats/latest-stats.html.
[56] UK Civil Aviation Authority, "Laser Incidents reported to the UK CAA 2018", UK Civil Aviation Authority, 2019.
[57] UK Civil Aviation Authority, "Laser Incidents reported to the UK CAA 2016", Civil Aviation Authority, 2019.
[58] "Pilots call for greater safety in the skies at TUC | BALPA", Balpa.org, 2016. [Online]. Available: https://www.balpa.org/Media-Centre/Press-Releases/Pilots-call-for-greater-safety-in-the-skies-at-TUC.
[59] "Police laser attack hotspots revealed", BBC News, 2016. [Online]. Available: https://www.bbc.com/news/uk-england-leeds-37288329.
[60] Department for Business, Energy & Industrial Strategy, "CALL FOR EVIDENCE: LASER POINTERS A call for evidence on the market, and potential uses, for laser pointers", Department for Business, Energy & Industrial Strategy, 2017.
[61] I. Drury, "Yobs who shine lasers at planes could face up to five years in jail", Mail Online, 2017. [Online]. Available: https://www.dailymail.co.uk/news/article-5196773/Yobs-shine-lasers-planes-face-5-years-jail.html.
[62] J. Foley, "Laser Strikes on Aircraft (US Air Force Research Labs)", Bangor, United Kingdom, 2017.
[63] Federal Aviation Administration, "Reported Laser Incidents", Federal Aviation Administration, 2019.
[64] Federal Aviation Administration, "Reported Laser Incidents for 2016", Federal Aviation Administration, 2016.
[65] J. Forrester, A. Dick, P. McMenamin, F. Roberts and E. Pearlman, The eye. Edinburgh [etc.]: Elsevier, 2016.
[66] "The Eyes (Human Anatomy): Diagram, Function, Definition, and Eye Problems", WebMD, 2015. [Online]. Available: https://www.webmd.com/eye-health/picture-of-the-eyes.
[67] J. Barbur and A. Stockman, "Photopic, Mesopic and Scotopic Vision and Changes in Visual Performance", Encyclopedia of the Eye, pp. 323-331, 2010. Available: 10.1016/b978-0-12-374203-2.00233-5.
[68] "Vitreous Hemorrhage Treatment Miami FL | North Miami Beach | Coral Gables", Retina Macula Specialists of Miami, 2019. [Online]. Available: https://www.retinamaculamiami.com/common-retinal-diseases/vitreous-hemorrhage.
[69] B. Armitage, "Laser pointers not toys, experts warn, after teen burns retinas", ABC News, 2015. [Online]. Available: https://www.abc.net.au/news/2015-11-05/optometrist-warning-after-teen-burns-retinas-with-laser/6916564.
[70] J. Risma, T. Venckus and R. Verdick, "Thermal corneal burn", Webeye.ophth.uiowa.edu, 2013. [Online]. Available: http://webeye.ophth.uiowa.edu/eyeforum/atlas/pages/corneal-burn-thermal.htm.

[71] J. D'Orazio, S. Jarrett, A. Amaro-Ortiz and T. Scott, "UV Radiation and the Skin", International Journal of Molecular Sciences, vol. 14, no. 6, pp. 12222-12248, 2013. Available: 10.3390/ijms140612222.
[72] F. Mustafa and M. Jaafar, "Comparison of wavelength-dependent penetration depths of lasers in different types of skin in photodynamic therapy", Indian Journal of Physics, vol. 87, no. 3, pp. 203-209, 2012. Available: 10.1007/s12648-012-0213-0.
[73] C. Williamson and L. McLin, "Nominal ocular dazzle distance (NODD)", Applied Optics, vol. 54, no. 7, p. 1564, 2015. Available: 10.1364/ao.54.001564.
[74] C. Williamson and L. McLin, "Laser eye dazzle safety framework", International Laser Safety Conference, 2017. Available: 10.2351/1.5056871.
[75] C. Williamson and L. McLin, "Determination of a laser eye dazzle safety framework", Journal of Laser Applications, vol. 30, no. 3, p. 032010, 2018. Available: 10.2351/1.5029384.
[76] J. Coelho, J. Freitas and C. Williamson, "Optical eye simulator for laser dazzle events", Applied Optics, vol. 55, no. 9, p. 2240, 2016. Available: 10.1364/ao.55.002240.
[77] H. Macleod, Thin-film optical filters. Boca Raton, FL: CRC Press/Taylor & Francis, 2010.
[78] S. Wilson and M. Hutley, "The Optical Properties of 'Moth Eye' Antireflection Surfaces", Optica Acta: International Journal of Optics, vol. 29, no. 7, pp. 993-1009, 1982. Available: 10.1080/713820946.
[79] B. Bovard, "Rugate filter theory: an overview", Applied Optics, vol. 32, no. 28, p. 5427, 1993. Available: 10.1364/ao.32.005427.
[80] L. Dalton, P. Gunter, M. Jazbinsek, O. Kwon and P. Sullivan, "Photorefractive effect and materials", Organic Electro-Optics and Photonics, pp. 250-281. Available: 10.1017/cbo9781139043885.011.
[81] M. Niesten, N. Pulsford and L. Feiner, "Photorefractive effect at the interface between a photoconductor and an electro-optic crystal", Journal of the Optical Society of America B, vol. 15, no. 1, p. 73, 1998. Available: 10.1364/josab.15.000073.
[82] H. Owen, "Holographic notch filter", Computer and Optically Generated Holographic Optics; 4th in a Series, 1991. Available: 10.1117/12.50638.
[83] L. Yuan and P. Herman, "Laser Scanning Holographic Lithography for Flexible 3D Fabrication of Multi-Scale Integrated Nano-structures and Optical Biosensors", Scientific Reports, vol. 6, no. 1, 2016. Available: 10.1038/srep22294.
[84] Y. Su, "Nitride-Based LEDs and Superluminescent LEDs", *Comprehensive Semiconductor Science and Technology*, pp. 28-100, 2011. Available: 10.1016/b978-0-44-453153-7.00024-9.
[85] W. Wright, "A re-determination of the trichromatic coefficients of the spectral colours", *Transactions of the Optical Society*, vol. 30, no. 4, pp. 141-164, 1929. Available: 10.1088/1475-4878/30/4/301.
[86] L. Frey, L. Masarotto, M. Armand, M. Charles and O. Lartigue, "Multispectral interference filter arrays with compensation of angular dependence or extended spectral range", Optics Express, vol. 23, no. 9, p. 11799, 2015. Available: 10.1364/oe.23.011799.
[87] "Laser Misuse (Vehicles) Act 2018", Legislation.gov.uk, 2018. [Online]. Available: http://www.legislation.gov.uk/ukpga/2018/9/introduction/enacted.

[88] C. Williamson, "A laser event recorder smartphone APP", International Laser Safety Conference, 2013. Available: 10.2351/1.5056813.
[89] N. Hough, "Detection and location system for laser interference with aircraft." Available: https://www.laserpointersafety.com/resources/2016-12-Laser_Detection_System_Hough_Paper.pdf.
[90] "Our engineers develop novel technology to protect pilots from laser attacks", BAE Systems | Cyber Security & Intelligence, 2017. [Online]. Available: https://www.baesystems.com/en/cybersecurity/article/bae-systems-engineers-develop-novel-technology-to-protect-pilots-from-the-dangers-of-laser-attacks.
[91] BAE Systems plc, "FILTER", US20190093420, 2019.
[92] "The Product", Meta-air.com, 2019. [Online]. Available: https://www.meta-air.com/the-product.
[93] Metamaterial Technologies Inc., "Metamaterial optical filter and method for producing the same", GB2552551, 2018.
[94] "Press Releases", Metamaterial.com, 2019. [Online]. Available: http://www.metamaterial.com/news-and-events/press-releases/.
[95] Y. Liu and X. Zhang, "Metamaterials: a new frontier of science and technology", Chemical Society Reviews, vol. 40, no. 5, p. 2494, 2011. Available: 10.1039/c0cs00184h.
[96] F. Capolino, Metamaterials handbook. Boca Raton, FL: CRC Press/Taylor & Francis, 2009.
[97] V. Veselago, "THE ELECTRODYNAMICS OF SUBSTANCES WITH SIMULTANEOUSLY NEGATIVE VALUES OF $\epsilon$ AND μ", Soviet Physics Uspekhi, vol. 10, no. 4, pp. 509-514, 1968. Available: 10.1070/pu1968v010n04abeh003699.
[98] J. Pendry, "Negative Refraction Makes a Perfect Lens", Physical Review Letters, vol. 85, no. 18, pp. 3966-3969, 2000. Available: 10.1103/physrevlett.85.3966.
[99] J. Pendry, "Controlling Electromagnetic Fields", Science, vol. 312, no. 5781, pp. 1780-1782, 2006. Available: 10.1126/science.1125907.
[100] A. Einstein, Relativity. Mansfield, Conn.: Martino, 2010.
[101] M. Giraldo and D. Stavenga, "Brilliant iridescence of Morpho butterfly wing scales is due to both a thin film lower lamina and a multilayered upper lamina", Journal of Comparative Physiology A, vol. 202, no. 5, pp. 381-388, 2016. Available: 10.1007/s00359-016-1084-1.
[102] The Lawrence Hall of Science, "Zoom into a Blue Morpho Butterfly Wing", *Youtube.com*, 2011.
[103] It's Okay To Be Smart, "Why Is Blue So Rare In Nature?", *Youtube.com*, 2018.
[104] R. Rumpf, "21st Century Electromagnetics. Lecture 7a - FSS and Metasurfaces", Texas, United States, 2019.
[105] S. Shrestha, A. Overvig, M. Lu, A. Stein and N. Yu, "Broadband achromatic dielectric metalenses", Light: Science & Applications, vol. 7, no. 1, 2018. Available: 10.1038/s41377-018-0078-x.
[106] P. Samaddar, N. Begam, S. Sarkar, S. De, D. Sarkar and P. Sarakar, "Double layer hemispherical tripole slot loaded aperture type Frequency selective surface", 2016 International Conference on Microelectronics, Computing and Communications (MicroCom), 2016. Available: 10.1109/microcom.2016.7522423.

[107] Z. Tan and K. McDonald, "Babinet's principle for electromagnetic fields", Joseph Henry Laboratories, Princeton University, Princeton, NJ, 2012.
[108] G. Burns and A. Glazer, "Bravais Lattices", *Space Groups for Solid State Scientists*, pp. 45-64, 2013. Available: 10.1016/b978-0-12-394400-9.00003-4.
[109]"Bravais lattice | Just Physics", Justphysics.com, 2019. [Online]. Available: https://www.justphysics.com/bravais-lattice.html.
[110] C. Liu, Y. Huang, Z. Yao, L. Yu, Y. Jin and X. Xu, "Giant angular dependence of electromagnetic induced transparency in THz metamaterials", EPL (Europhysics Letters), vol. 121, no. 4, p. 44004, 2018. Available: 10.1209/0295-5075/121/44004.
[111] K. Chen, X. Luo, G. Ding, J. Zhao, Y. Feng and T. Jiang, "Broadband microwave metamaterial absorber with lumped resistor loading", EPJ Applied Metamaterials, vol. 6, p. 1, 2019. Available: 10.1051/epjam/2018011.
[112] K. Chen et al., "Microwave absorber based on permeability-near-zero metamaterial made of Swiss roll structures", Journal of Physics D: Applied Physics, vol. 48, no. 45, p. 455304, 2015. Available: 10.1088/0022-3727/48/45/455304.
[113] L. Gu et al., "Angular distribution of emission from hyperbolic metamaterials", Scientific Reports, vol. 4, no. 1, 2014. Available: 10.1038/srep07327.
[114] Y. Lee, S. Kim, H. Park and B. Lee, "Metamaterials and Metasurfaces for Sensor Applications", Sensors, vol. 17, no. 8, p. 1726, 2017. Available: 10.3390/s17081726.
[115] A. Ghobadi, H. Hajian, M. Gokbayrak, B. Butun and E. Ozbay, "Bismuth-based metamaterials: from narrowband reflective color filter to extremely broadband near perfect absorber", Nanophotonics, vol. 8, no. 5, pp. 823-832, 2019. Available: 10.1515/nanoph-2018-0217.
[116] D. Wu et al., "Wide-angle, polarization-insensitive and broadband absorber based on eight-fold symmetric SRRs metamaterial", Optics Communications, vol. 380, pp. 221-226, 2016. Available: 10.1016/j.optcom.2016.06.023.
[117] W. Zhu, X. Zhao, B. Gong, L. Liu and B. Su, "Optical metamaterial absorber based on leaf-shaped cells", Applied Physics A, vol. 102, no. 1, pp. 147-151, 2010. Available: 10.1007/s00339-010-6057-6.
[118] F. Bagci and B. Akaoglu, "Consequences of Unit Cell Design in Metamaterial Perfect Absorbers", Acta Physica Polonica A, vol. 129, no. 4, pp. 792-796, 2016. Available: 10.12693/aphyspola.129.792.
[119] H. Fernandez Alvarez, M. de Cos Gomez and F. Las-Hera, "A Six-Fold Symmetric Metamaterial Absorber", Materials, vol. 8, no. 4, pp. 1590-1603, 2015. Available: 10.3390/ma8041590.
[120] Y. Avitzour, Y. Urzhumov and G. Shvets, "Wide-angle infrared absorber based on a negative-index plasmonic metamaterial", Physical Review B, vol. 79, no. 4, 2009. Available: 10.1103/physrevb.79.045131.
[121] S. Forrest, "Genetic algorithms: principles of natural selection applied to computation", Science, vol. 261, no. 5123, pp. 872-878, 1993. Available: 10.1126/science.8346439.
[122] Z. Jiang, S. Yun, L. Lin, J. Bossard, D. Werner and T. Mayer, "Tailoring Dispersion for Broadband Low-loss Optical Metamaterials Using Deep-subwavelength Inclusions", Scientific Reports, vol. 3, no. 1, 2013. Available: 10.1038/srep01571.

[123] G. Parisi, R. Kemker, J. Part, C. Kanan and S. Wermter, "Continual lifelong learning with neural networks: A review", Neural Networks, vol. 113, pp. 54-71, 2019. Available: 10.1016/j.neunet.2019.01.012.
[124] A. Shrestha and A. Mahmood, "Review of Deep Learning Algorithms and Architectures", IEEE Access, vol. 7, pp. 53040-53065, 2019. Available: 10.1109/access.2019.2912200.
[125] I. Malkiel, A. Nagler, M. Mrejen, U. Arieli, L. Wolf and H. Suchowski, "Deep learning for design and retrieval of nano-photonic structures", arXiv:1702.07949, 2017.
[126] T. Rummler, "Mirage software automates design of optical metamaterials", Sandia National Laboratories:, 2019. [Online]. Available: https://www.sandia.gov/news/publications/labnews/articles/2019/04-12/mirage.html.

# CHAPTER III. DESIGN ON DEMAND: TAILORING OPTICAL RESPONSES OF METALLIC NANOPARTICLES

This chapter discusses the plasmonic behaviour of metallic nanoparticles and the ability to tune and tailor the scattering parameters. Having the ability to engineer the resonance of a material is a key principle for enabling the design of optical bandstop filters for different wavelengths; particularly when concerning an inverse design strategy. An investigation into isotropic plasmonic particles is explored through materials, size, configurations and surrounding indices. Furthermore, an expansion into alternative plasmonic materials and anisotropic particles is also discussed. The optical responses of these particles will be analysed theoretically through Mie theory and verified via computational full-wave simulations.

## 3.1 **Particle Plasmon Physics**

A plasmon is a quantum of plasma oscillations. It is defined as a quasi-particle that ascends from the quantisation of plasma oscillations. When coupled with photons, they create plasmon polaritons. With confined nanoparticles, the plasmons become localised and exhibit enhanced near-field properties at the resonant wavelength.

### 3.1.1 **Absorption vs. Scattering**

The physics of absorption is well understood for metals [1]. In conducting metals, including noble metals, the conduction and valance band intersect. This gives an effective zero band gap, which allow the electrons in the outer orbitals to form an electron sea. Due to the available energy states in a metal's partially filled valence band, the electrons that occupy this band are also able to absorb photons. Unlike interband transitions where the absorbed photon gives the electron energy to cross the band gap, due to the absence of a band gap in metals, the electron instead jumps into an unoccupied state within its own band. This is the intraband absorption. This property makes metals highly absorbing and reflective at optical frequencies.

The introduction of an oscillating external electric field can give rise to an oscillating dipole induction of a metallic nanoparticle. The oscillating dipoles can result in scattering. Like absorption, the scattering distribution is well understood from the theory of electrodynamics [2] and states that the frequency of scattered light is the same as the incident light, under dipole conditions.

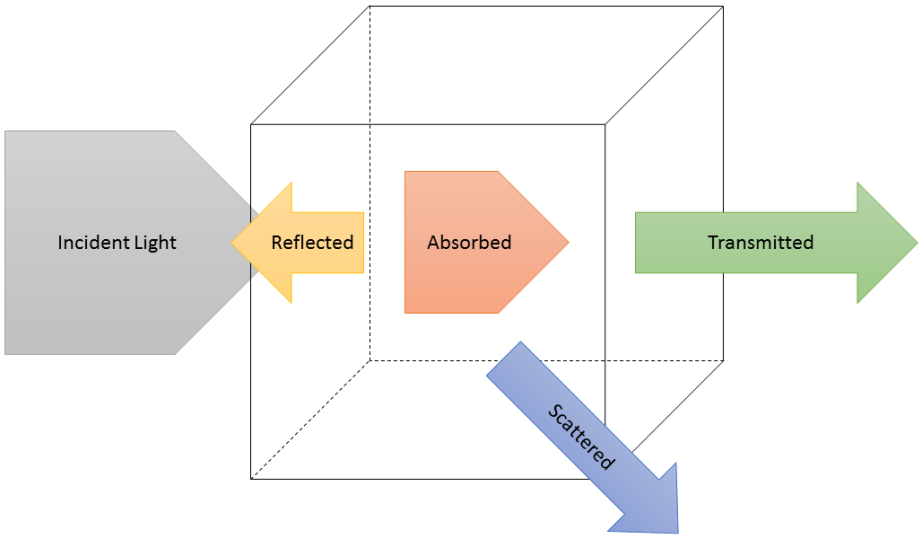


**Figure 3.1.** Schematic demonstrating the possible outcomes of incident light onto a nanoparticle.

The key property for photon absorption and photon scattering of a particle is characterised by the particle's polarisability (Eq. 2.1.31), which describes to what degree the incident field induces a dipole moment in a particle. Although the Clausius Mossotti equation (Eq. 2.1.31) described the polarisation of a single molecule in a bulk medium, it equally describes the polarisability for nanoparticles in an electrostatic limit of $\lambda \gg a$, where $a$ is the particle radius.

### 3.1.2 **Mie Theory**

Mie theory formulates the relation of light-matter interactions. The theory was established by Gustav Mie in 1908 and outlines a systematic solution for the light scattering by small spherical particles with the use of Maxwell's electromagnetic theory [3]. The solutions show that the electric and magnetic fields are present inside and outside a homogeneous spherical particle, this can be adapted to solve for more complex geometries. Mie theory describes the importance of four parameters, the incident light wavelength ($\lambda$), the refractive index ($\tilde{n} = n_r + ik_r$), the refractive index of the medium ($\tilde{n}_d = n_d + ik_d$) and the particle size ($a$).

Mie theory is formulated by expressing a plane wave in terms of spherical harmonics and calculating the fields that overlap the spherical harmonic modes supported by the particle. It is an exact analytical description of the electrodynamic response of a particle and described by the total absorption, scattering and extinction cross-section.

$$\sigma_{scatt} = \frac{2\pi}{|k|^2} \sum_{L=1}^{\infty} (2L+1)\left(|a_L|^2 + |b_L|^2\right) \tag{3.1.1}$$

$$\sigma_{ext} = \frac{2\pi}{|k|^2}\sum_{L=1}^{\infty}(2L+1)\,[Re(a_L + b_L)] \tag{3.1.2}$$

$$\sigma_{abs} = \sigma_{ext} - \sigma_{scatt} \tag{3.1.3}$$

Where $k$ is the wavevector and $L$ are integers representing the dipole, quadrupole, and higher multipoles of the cross-sections. $a_L$ and $b_L$ are parameters that are composed of Bessel functions $\varphi_L$ and $\chi_L$.

$$a_L = \frac{m\varphi_L(mx)\varphi_L'(x) - \varphi_L'(mx)\varphi_L(x)}{m\varphi_L(mx)\chi_L'(x) - \varphi_L'(mx)\chi_L(x)} \tag{3.1.4}$$

$$b_L = \frac{\varphi_L(mx)\varphi_L'(x) - m\varphi_L'(mx)\varphi_L(x)}{\varphi_L(mx)\chi_L'(x) - m\varphi_L'(mx)\chi_L(x)} \tag{3.1.5}$$

Where $m = \tilde{n}/n_d$, with $\tilde{n}$ is the complex refractive index of the metal nanoparticle, and $n_d$ is the refractive index of the non-absorbing surrounding medium. Moreover, $x = k_m a$, where $a$ is the radius of the particle and $k_m$ is the wavenumber in the medium.

If the nanoparticle is assumed to be much smaller than the incident wavelength $a \ll \lambda$, then the Bessel functions can be approximated by power series in accordance to Bohren and Huffman [4], where the terms are to order $x^3$, allowing (Eq. 3.1.4) and (Eq. 3.1.5) to simplify to the following, with the higher order terms of $a_L$ and $b_L$ equalling zero.

$$a_L \approx -\frac{i2x^3}{3}\frac{m^2-1}{m^2+2} \tag{3.1.6}$$

$$b_L \approx 0 \tag{3.1.7}$$

### 3.1.3 **Cross-Sections of Particles**

The cross-section analysis often is described as a function of area. The extinction cross-section can be described as the removal of a certain amount of light from a particle when under plane wave illumination. This extinction cross-section is paradoxical as it states that twice as much light is removed compared to the particles geometrical cross-sectional area [5]. There have been several explanations for this phenomenon including, destructive interference inside the particle shadow [6], diffraction and shadowing of light [7], the cancellation of incident wave inside the particle [8], and superposition of incident and scatter field [9].

The extinction cross-section in essence describes how much light is absent or removed due to the existence of the particle. This description can be further broken down to designate the contributions of absorption and scattering.

The scattering cross-section is the integral of the scattered Poynting vector ($\boldsymbol{S}_{scattered} = \boldsymbol{S}_{total} - \boldsymbol{S}_{incident}$) over a sphere that encloses the particle ($r \gg a$ where $r$ is the radius of the sphere and $a$ is radius of the particle). Thus, the scattering cross-section is not concerned with the direction of scattered light. The absorption cross-section is the integral of the total Poynting vector over the surface of the particle, the net total of light entering the particle.

The cross-sections of a given particle can mathematically be described by the following equations, which substitute (Eq. 3.1.6) into (Eq. 3.1.2) (Note, the refractive index has been replaced by the permittivity):

$$\sigma_{ext} = \frac{18\pi\varepsilon_m^{3/2}V}{\lambda} \frac{Im(\varepsilon_r)}{[Re(\varepsilon_r) + 2\varepsilon_m]^2 + Im(\varepsilon_r)^2} \tag{3.1.8}$$

$$\sigma_{scatt} = \frac{32\pi^4\varepsilon_m^2V^2}{\lambda^4} \frac{[Re(\varepsilon_r) - \varepsilon_m]^2 + Im(\varepsilon_r)^2}{[Re(\varepsilon_r) + \varepsilon_m]^2 + Im(\varepsilon_r)^2} \tag{3.1.9}$$

$$\sigma_{abs} = \sigma_{ext} - \sigma_{scatt} \tag{3.1.10}$$

Where $\sigma_{scatt}$, $\sigma_{abs}$ and $\sigma_{ext}$ are the scattering, absorption and extinction cross-section respectively, $k_0$ is the wave number and $\alpha$ is the particle's polarisability found in (Eq. 2.1.31).

$$Q_{ext} = \frac{\sigma_{scatt}}{\pi a^2} + \frac{\sigma_{abs}}{\pi a^2} \tag{3.1.11}$$

Additionally, and more commonly used, the cross-section efficiency ($Q_{ext}$, $Q_{scatt}$ and $Q_{abs}$) is a function of the area ($\pi a^2$), and is expressed in (Eq. 3.1.11).

## 3.2 **Tailoring a Particle's Optical Responses**

This section focuses on applying the above theory to analyse the absorption, scattering and extinction of metallic nanoparticles. The first aspect is studying single particles through Mie theory and verifying that behaviour through computational finite element methods. This provides quantitative comparisons for the techniques and supports later studies into anisotropic particles and multi-dimensional arrays.

### 3.2.1 **Single Particle**

To understand the collective behaviour of metamaterials, individual meta-atoms need to be studied to gauge the contribution of the periodicity.

#### 3.2.1.1 **Mie Theory Solution**

The following results have been established through DSIMie. DSIMie is a computational Mie theory software which simulates the electromagnetic field extinction of a single particle. The software presents an analytical method for accurately and rapidly simulating two dimensional models.

DSIMie was created by Dr. Z. Wang at the Data Storage Institute, Singapore, and is copyrighted and bares a US Patent no. 8,222,905.

**Effects of Surrounding Index**

The extinction spectrum from metallic spherical particles can be calculated using Drude's equations or experimental data. It is always best to use experimental data if available as it provides the highest accuracy. Considering the experimental data provided from Johnson & Christy for silver and gold particles with a 25 nm radius surrounded by air, the extinction, absorption and scattering spectra are shown in figure 3.2.

The plotted functions have a single resonance feature which is an attribute to the plasmonic resonance of the particle. The extinction, being the sum of the absorption and scattering, is principally subjugated by the absorption.

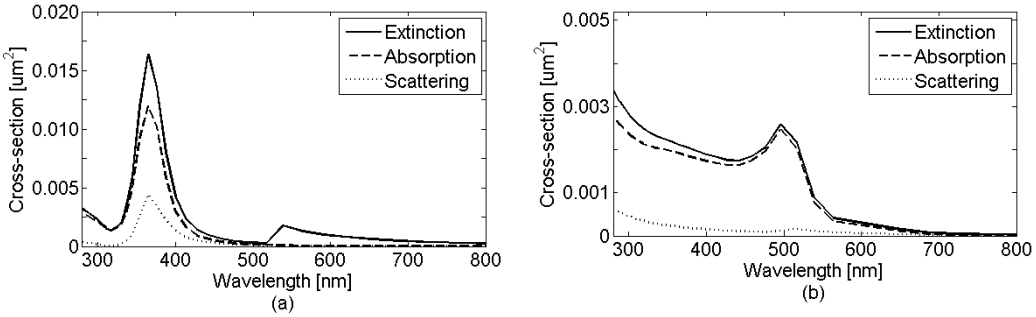


**Figure 3.2.** The cross-section extinction, scattering and absorption spectra of a 25 nm radius, (a) silver particle (b) gold particle, surrounded in air.

The presence of a surrounding dielectric medium has a substantial effect on the plasmonic resonance wavelength. As the dielectric medium's refractive index increases ($n_d$ and assuming $k_d = 0$), the plasmonic resonance wavelength also increases and the absorption and scattering contributions alter. Furthermore, as $n_d$ increases, the broadwidth of the resonance and the

efficiency increase. With respect to gold, the resonance point becomes more pronounced with the efficiency on the blue-side of the spectrum attenuated.

The plasmonic red-shift with increasing surrounding refractive indices is a consequence of charge accumulations. When an electromagnetic field is incident on a spherical particle, a dipole moment is induced and charges accumulate at the surface. If the particle is then place within a dielectric medium, the materials becomes polarised due to the internal fields. This results in an accumulation of bound charges at the surface interfacing with the dielectric, and the opposing charges accumulating in the dielectric (figure 3.4). The accumulated charges act as a retardant to the restoring force on the electrons in the particle due to the reduction of effective charge at the interface. The lessening of the restoring force depresses the resonant energy and the frequency of the system, resulting is a spectral red-shift of the plasmonic resonance [10].

This red-shift behaviour is the essential principle for tailoring optical responses for absorbing metamaterial filters.

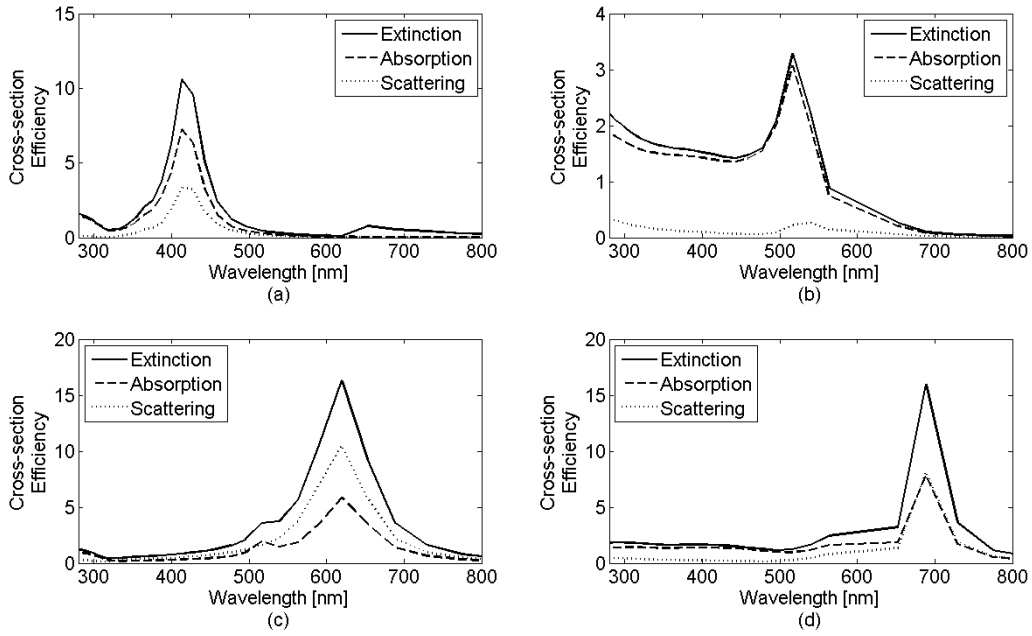


**Figure 3.3.** The efficiency of the cross section extinction, scattering and absorption spectra of a 20 nm radius, (a) and (c) silver particle, (b) and (d) gold particle, surrounded in $MgF_2$ [n=1.38] and $TiO_2$ [n=2.40], respectively.

The increase in the extinction cross-section and the presence of higher efficiency in scattered light is greater than that absorbed when $n_d$ increases is due to the amplified degree of phase delay across the sample.

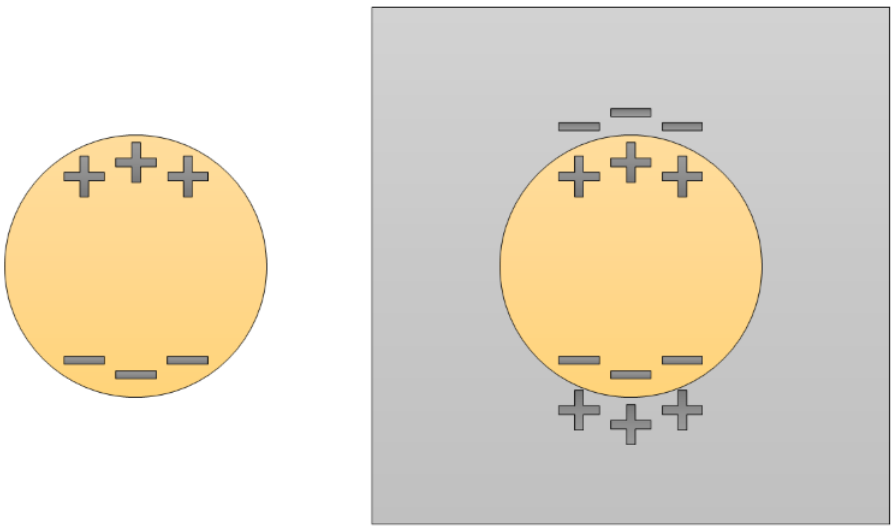

**Figure 3.4.** A plasmonic particle surrounded in (a) air and (b) a dielectric material. The bound chargers accumulate on the interface between the particle and neighbouring medium.

### Effects of Particle Size

For spherical nanoparticles smaller than the free mean path of the electron, typically around $a \leq 20nm$ [11], the size to wavelength ratio amounts to insufficient phase retardation across the particle itself; particularly within the visible region for metallic nanoparticles. This effectively enables a constant resonant wavelength with a scalable magnitude of the polarisability, by the volume of the particle.

Figure 3.5 shows that for silver nanoparticles with varying radii, the resonant wavelength remains approximately constant, predominantly with particles of a radii of $< 10nm$. This remains accurate when embedded within a dielectric as demonstrated with a surround medium of Magnesium Fluoride. The same is also true for gold, figure 3.6. However, gold displays a resonant feature at a longer wavelength.

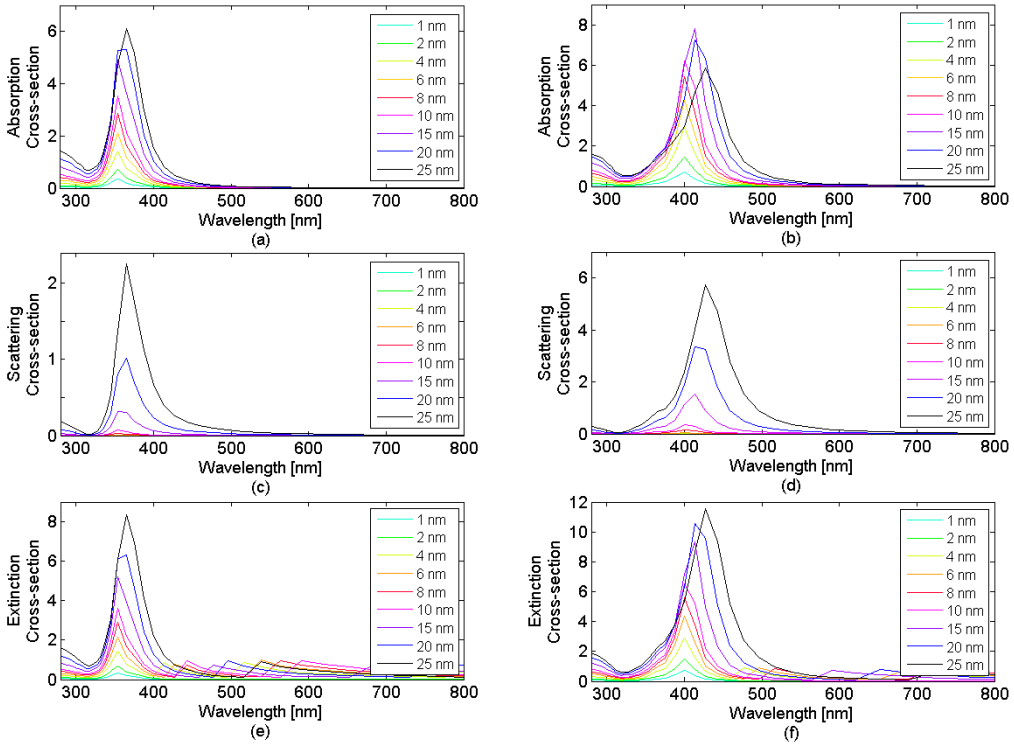


**Figure 3.5.** (a) and (b) Absorption, (c) and (d) scattering and (e) and (f) extinction cross-sections efficiency of Silver nanoparticles with varying radii surrounded in air [*Left*] and $MgF_2$ [*Right*].

As discussed, the noticeable difference between silver and gold is the shift in resonant wavelengths. However there is another obvious variance; gold exhibits a non-zero "flat" band at wavelengths shorter than the resonance. This additional absorption is related to the increased imaginary function of the permittivity varying with wavelength. However, this non-zero flat band begins to diminish with an increasing refractive index of the associated surrounding medium due to the retardation of the restoring force.

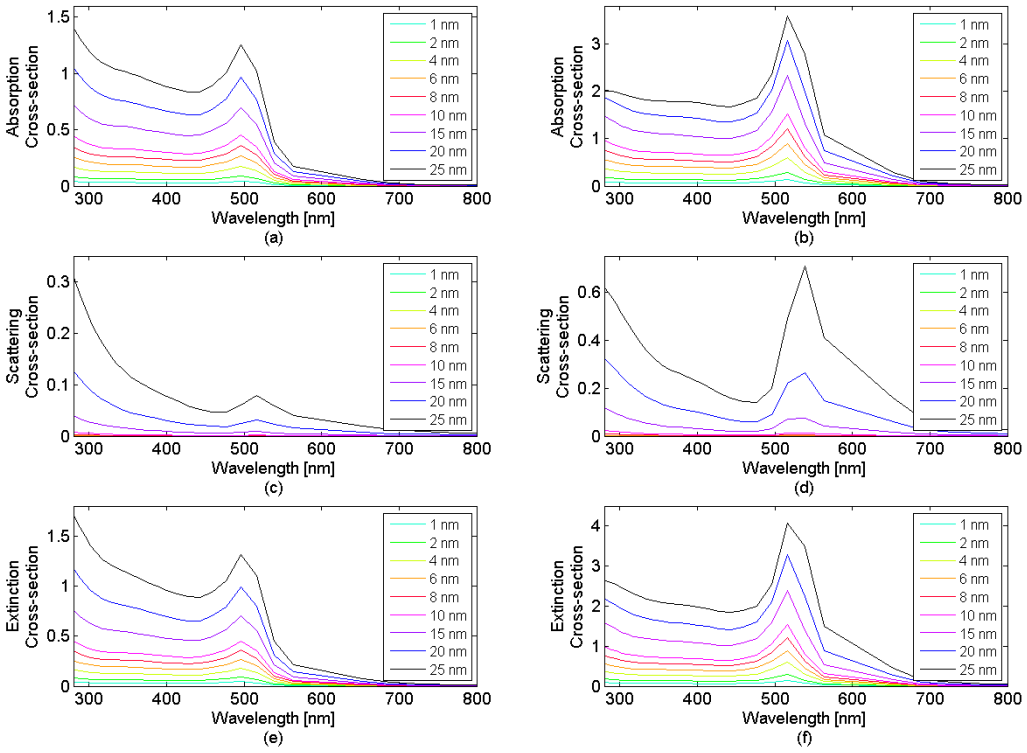


**Figure 3.6.** (a) and (b) Absorption, (c) and (d) scattering and (e) and (f) extinction cross-sections efficiency of Gold nanoparticles with varying radii surrounded in air [*Left*] and $MgF_2$ [*Right*].

With larger nanoparticles, the electrostatic limit, displayed in particles $a \leq 25nm$, is exceeded, as shown in figure 3.7. Therefore the absorption no longer dominates the extinction properties due to the increase in radiative dampening, which is proportional to the particle's volume. Physically, there is an uptake of photon scattering due to the abundance of electrons present, thus as the particle size exceeds the electrostatic limit, scattering becomes much more dominant than absorption, producing broadband effects.

Furthermore, for larger particles where the electrostatic limit is exceeded, the resonance no long remains at a constant wavelength and becomes red-shifted. This red-shift and broadened resonance is due to 'dynamic depolarisation' which is caused by a phase retardation across the particle due to sub-portion polarisation across the large particle [11].

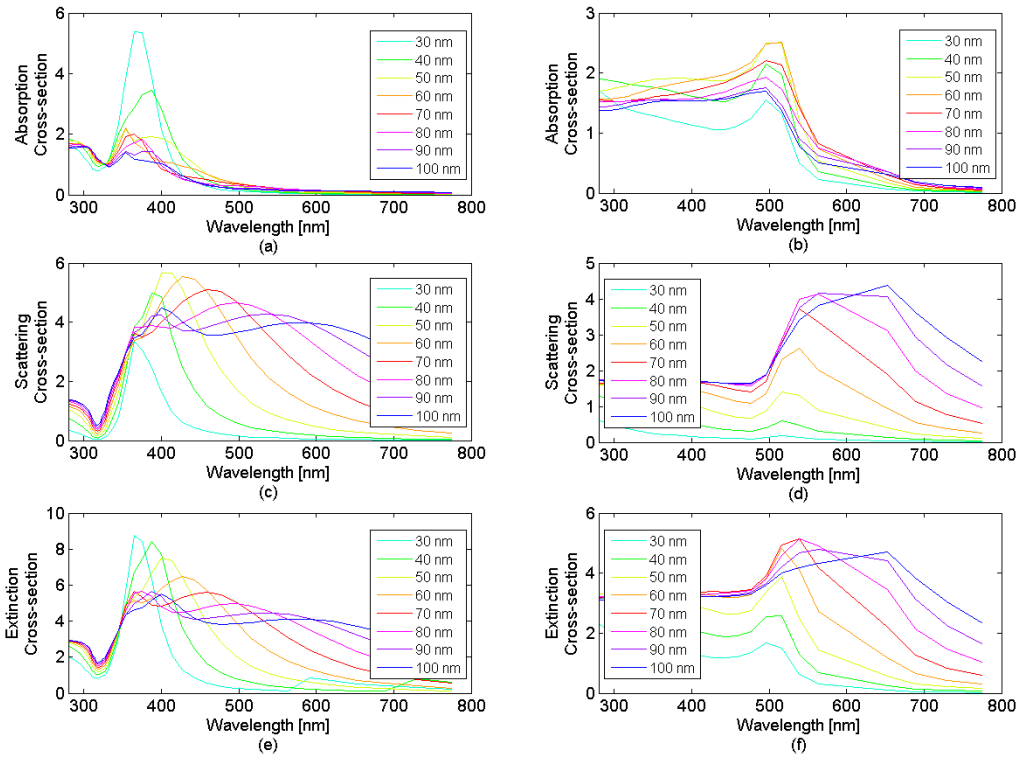


**Figure 3.7.** Dipolar contributions of large particles for the extinction, scattering and absorption efficiency spectra of varying radii, (a), (c) and (e) silver particle, and (b), (d) and (f) gold particle, surrounded in air.

### 3.2.1.2 **Computational Validation**

CST Studio Suite is a commercial electromagnetic solver. The software provides great flexibility for geometries, materials, and for far- and near- field modelling. This software has been extensively used throughout this thesis and for many other electromagnetic studies. Finite Element Method (FEM) is a well-established numerical method that utilises partial differential equations to solve the problem in hand [12]. FEM enables a tetrahedral element meshing that, with the number of elements and location, are specified to solve Maxwell's equations at the boundaries between the elements. The FEM solver has been used for verifying the single particle case to provide confidence for further analysis on ordered arrays of nanoparticles. Figure 3.8 shows the schematic modelling of a single particle with the boundary conditions defined as $2a$ for $\pm x$-, $\pm y$- and $\pm z$- *axis* and the location of the electric and magnetic field. For the study of arrayed nanoparticles, the boundary conditions have been set to "unit-cell" which provides a pseudo-infinite array of the design meta-atom. Once the model has been successfully meshed and solved, the transmission (T), reflection (R) and absorption (A) can be obtained from the S-parameters, which describes the transmission (t) and reflection (r) coefficients.

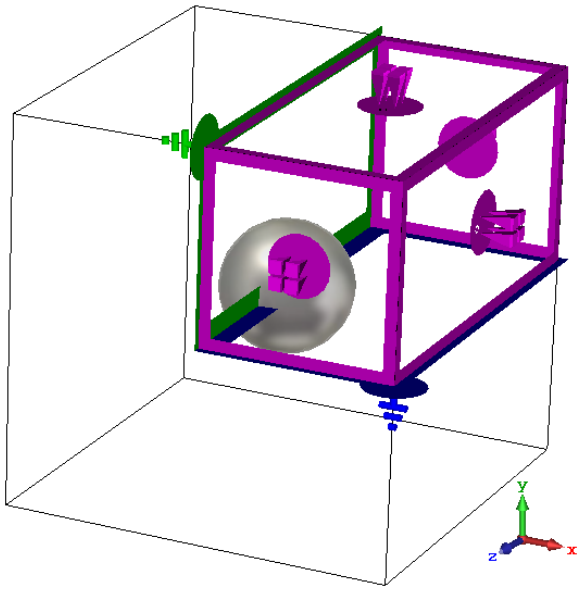


**Figure 3.8.** Schematic of the FEM validation simulation of the spherical particle showing the symmetric E-field (*y-axis*) and H-field planes (*x-axis*).

### Effects of Surrounding Index

The plotted data from the computational electromagnetic results accordingly match to Mie theory, table 3.1, with variation in air, magnesium fluoride to titanium dioxide. A single defined peak is present for silver and gold nanoparticles that undergoes a red-shift with the increasing refractive index of the surrounding dielectric.

Some slight differences between the two solutions could be a result of;

a. The number of data points taken. (i.e. FEM takes over a thousand data points for each simulation. The number data points from Mie theory is much less, hence the presence of a sharp peak [*figure 3.2 and 3.3*] compared to smooth peak [*figure 3.9*]).
b. Slight variations in optical parameters; although Johnson & Christy has been used for both cases, there might be a slight factor of variation.
c. Mie theory requires no meshing; however, the FEM solver utilises meshing for solving Maxwell's equations ($> \lambda/10$). High meshing will provide more accurate results as the mesh can conform to the spatially varying geometries.

**Table 3.1.** Comparison of the peak wavelength for the cross section extinction for Mie and FEM.

| **Material** | **Mie Theory ($\lambda_{peak}[Q_{ext}]$)** | **FEM ($\lambda_{peak}[Q_{ext}]$)** |
|---|---|---|
| Ag – Air | 364.7 nm | 365.3 nm |
| Ag – $MgF_2$ | 413.3 nm | 410.3 nm |
| Ag – $TiO_2$ | 619.9 nm | 615.4 nm |
| Au - Air | 495.9 nm | 501.4 nm |
| Au – $MgF_2$ | 516.6 nm | 522.4 nm |
| Au – $TiO_2$ | 688.8 nm | 690.5 nm |

Although some slight variance is present in the peak wavelength, the results highlighted in figure 3.9 show the ability to tune and tailor the plasmonic behaviours of metallic nanoparticles by varying the surrounding refractive index.

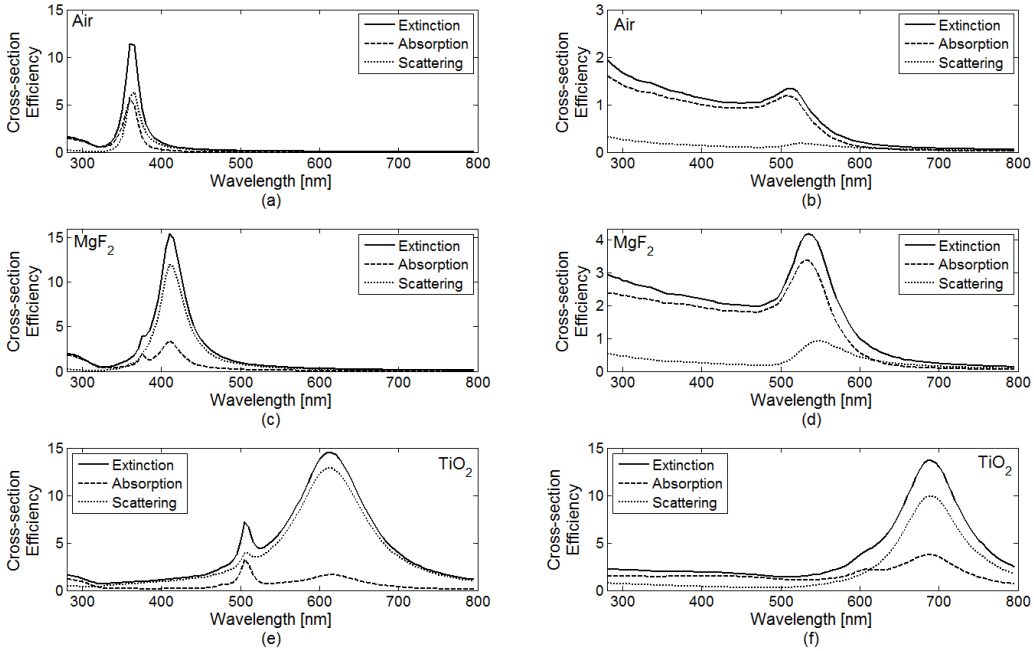


**Figure 3.9.** The cross section efficiency for extinction, scattering and absorption spectra of a 25 nm radius, (a), (c) and (e) silver particle, and (b), (d) and (f) gold particle, surrounded in air [n=1.00], $MgF_2$ [n=1.38] and $TiO_2$ [n=2.40], respectively.

### Effects of Particle Size

When the plasmonic particle becomes very small ($a < 10nm$), there is no significant presence of any phase retardation across the particle within the visible region due to the size to wavelength ratio. This enables the resonance wavelength to remain constant with respect to particle size with only the magnitude of the polarisability scaled by the volume of the particle.

Figure 3.10 demonstrates an example of the size-dependence of silver and gold nanoparticles surrounded by $MgF_2$. The example demonstrates that the resonant position remains approximately constant for particles with a radius of 1 nm to 10 nm, with an increasingly small red-shift change to the resonance as the radius exceeds 10 nm.

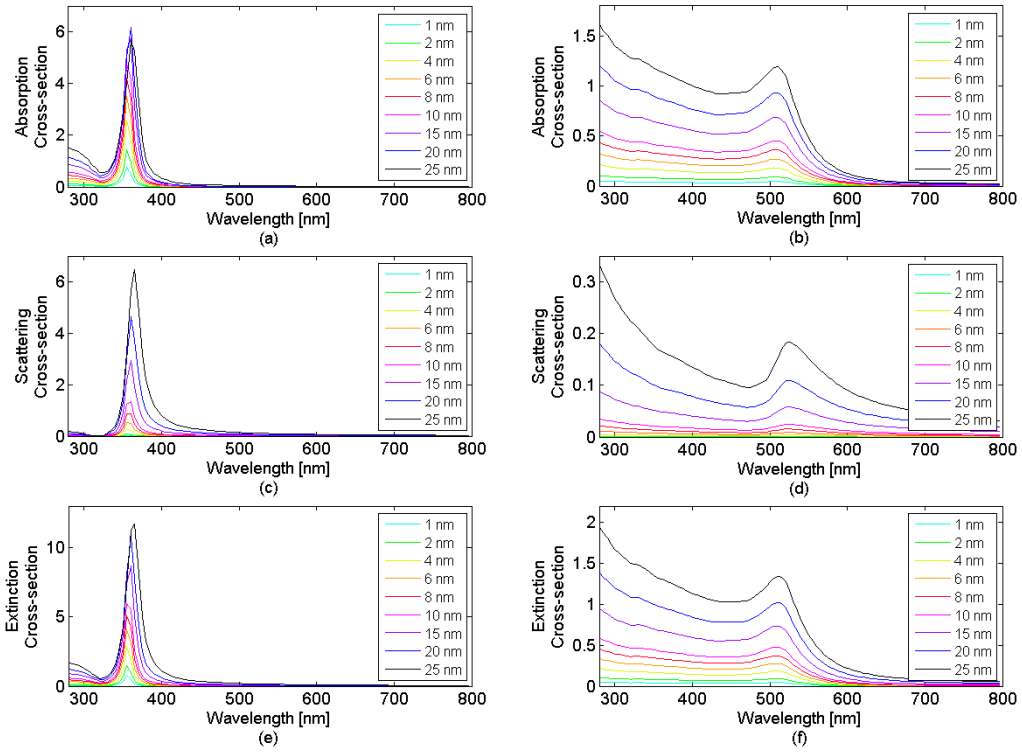


**Figure 3.10.** (a) and (b) Absorption, (c) and (d) scattering and (e) and (f) extinction cross-sections efficiency of nanoparticles with varying radii. Silver [*Left*] and Gold [*Right*].

The perceptible difference between the silver and gold nanoparticles' cross-section is the presence of a "flat band" at wavelengths shorter than the resonance for gold. This absorption band is allied with the amplified imaginary component of the permittivity. Furthermore, an obvious difference is the resonance position between gold and silver, where the gold is much more red-shifted in comparison. This computation validation matches that of Mie theory (figures 3.2 and 3.3).

### Alternative Plasmonics

Silver and gold have been at the forefront of plasmonics. However, the previous discussions have highlighted that silver and gold can be limiting. The resonant wavelength can be accurately predicted depending on the size and the surrounding medium. An alternative to tuning the plasmonic position without the need for a change in the surrounding refractive index could lie with alternative materials.

Figure 3.11 highlights the change in resonant wavelength with dependency on the proportion of silver to gold ratio. With the increase of gold percentage, the response red-shifts from ~390 nm to 500 nm. The silver and gold mix to create a metallic alloy, which can occur naturally

called Electrum. Gong and Leite reported on noble metal alloys for plasmonics in 2016 [13], emphasising tunable optical responses through binary mixtures of noble metals. This presents an alternative solution for the material selection for a given metamaterial. The alloy's refractive index was taken from Rioux et al, 2014 study [14], who also demonstrated a near linear shift of the plasmon peak positon.

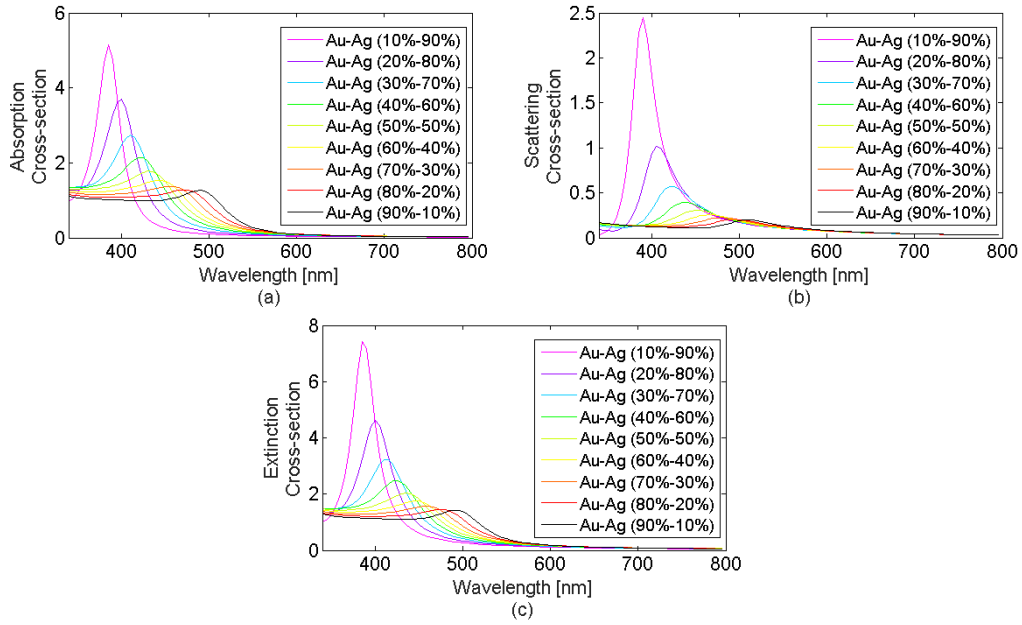


**Figure 3.11.** (a) Absorption, (b) Scattering and (c) extinction cross-section efficiency for Au-Ag (Gold-Silver) alloy metal nanoparticles of 25 nm diameter.

Similar to the noble metals, alkali metals exhibit a free electron in their outer shell, the s-orbital. The presence of the free electron enable the interactions between light and the materials structure. More specifically, the free electron is able to become polarised and display electric dipole properties. Plasmonic behaviour in alkali metals have been reported for some time [15-17]. However, the main concern is the stability of the metals. They are highly reactive at standard temperatures and pressure. Nevertheless, if this instability could be overcome by containing the alkali nanoparticles within a fixed dielectric, they could become an interesting candidate for a wider range of plasmonic tuning.

Figure 3.12 demonstrates the cross-section performance of the alkali metals. They exhibit a strong absorption and scattering at a range of different wavelengths across the visible region. The refractive index data was gained from the following sources [18-21]. Note that Francium has been excluded from the study due to its extreme radioactivity.

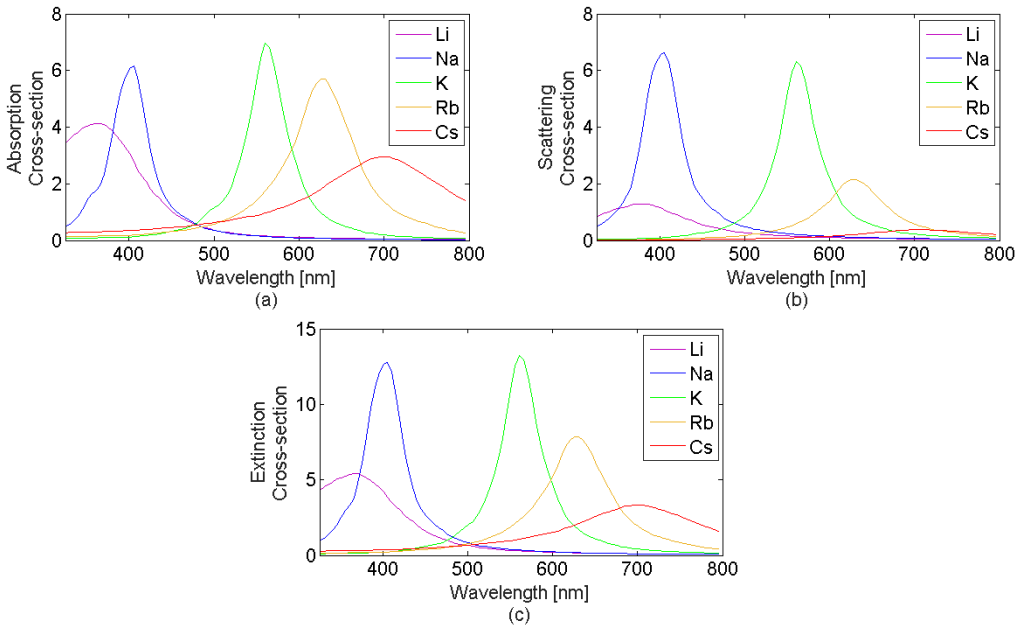


**Figure 3.12**. (a) Absorption, (b) Scattering and (c) extinction cross-section efficiency for Alkali metal nanoparticles of 25 nm diameter.

Heavily-doped semiconductor nanocrystal plasmonics have been gaining increasing attention [22]. An exciting aspect of this type of material is the tunable plasmonic band. Figure 3.13 shows the tunable aspect with dependence on the doping of the semiconductor. For this, a fixed dampening factor was applied. In reality this would be highly dependent on the semiconductor material. However, for demonstration, the change in doping strength highlights the effectiveness for absorption and scattering of a semiconductor nanoparticle.

$$\varepsilon_r = 1 - \frac{\left(\frac{nq^2}{\varepsilon_0 m}\right)}{\omega^2 + i\omega\gamma} \tag{3.2.1}$$

The Drude model (Eq.3.2.1) was introduced in the previous chapter. This equation has been used to define an estimated permittivity for the semiconductor properties found in figure 3.13. Where $n$ is the free-carrier density. The proficiency to regulate the free-carrier density of a material enables the new approach for plasmonic tuning, with the impending possibility to overcome some of the fundamental limitations that noble-metals demonstrate. Additionally, the ability to tailor the permittivity of the plasmonic medium signifies a new degree of freedom for engineering plasmonic metamaterials [23].

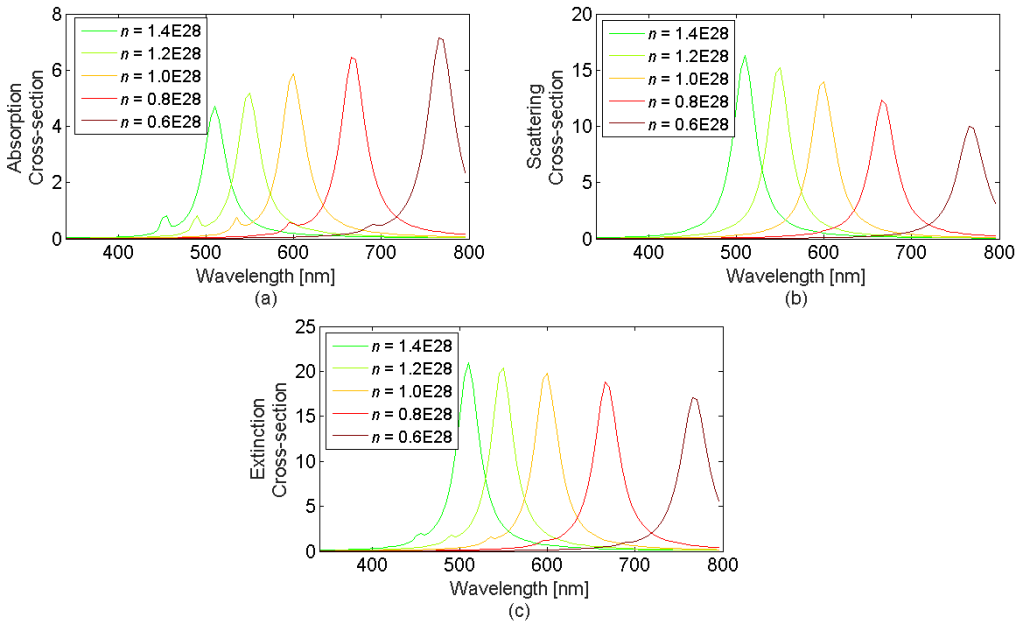


**Figure 3.13.** (a) Absorption, (b) Scattering and (c) extinction cross-section efficiency for varying doping in the carrier concentration ($n$) and a fixed $\Gamma = 0.05$ with particle sizes of 25 nm diameter.

### Anisotropic Particles

Anisotropic particles, i.e. particles that have physical properties that are direction dependent, have a rich history for metamaterials because they are able to provide unique electromagnetic properties [24]. They also provide another route to tunability because they are able to localise dipoles, produce multiple resonances and blue/red-shift the plasmonic peaks. This is achieved by limiting the free-mean path of the electron at certain orientations or positions within the particle itself. A truly isotropic particle would be a spherical particle due to its identical shape in all directions. In contrast, nearly all other shapes are anisotropic.

Figure 3.14 demonstrates a selection of anisotropic nanoparticles that display unique resonances. The particles have been designed to have the same cross-section area as that of a spherical particle with silver as the base metal. An obvious issue with anisotropic particles lies with multiple resonances. Providing a single notch filter would become a difficult problem with many shapes. However, like many bandstop metamaterial filters previously reported [25], the 'cross' shape provides a single resonant position. An issue with the silver spherical nanoparticle is its ability to go beyond the visible spectrum, the cross shaped particles could push into the near-infrared region with an increasing refractive index of the surrounding medium. With that being said, multi notch filters using traditional thin film stacks require a large number of layers. A route to creating ultra-thin multi notch filters could take advantage of the anisotropic nanoparticles.

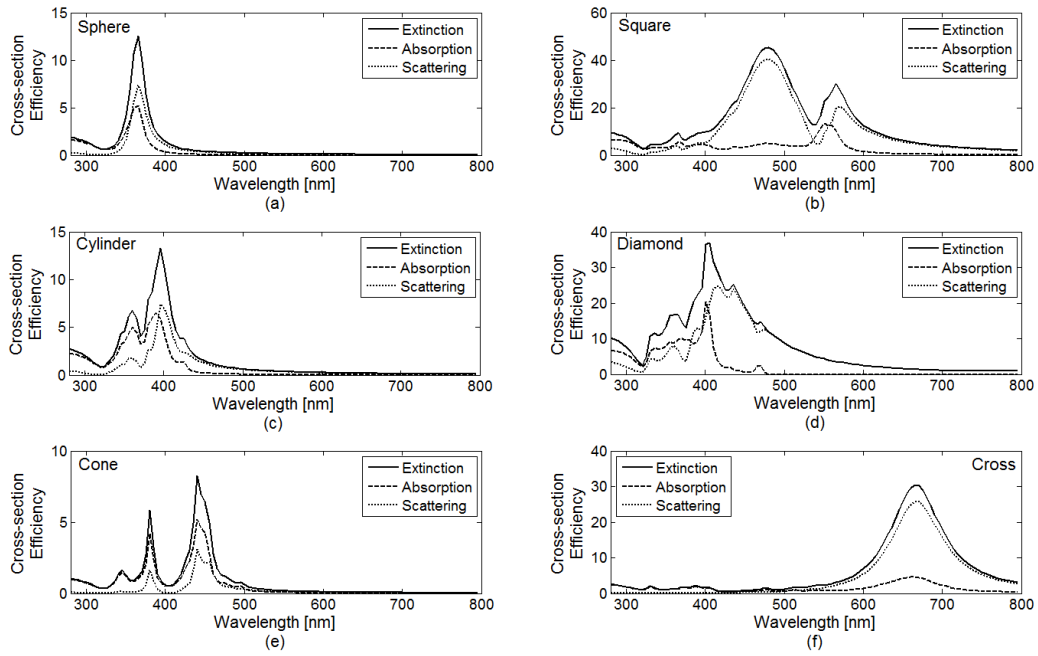


**Figure 3.14.** Absorption, Scattering and extinction cross-section efficiency for varying Silver particle shapes with a fixed cross-sectional area comparable to a spherical particle of 25 nm diameter. (a) Sphere, (b) Square, (c) Cylinder, (d) Diamond, (e) Cone, and (f) Cross.

### 3.2.2 **Two-Dimensional Particle Array**

Metamaterials deal with a repeated unit-cell to create the lattice configuration. Two-dimensional arrays are investigated as an extension to the single particle. The particles are placed in a square array so that the interactions between the adjacent particles experience indistinguishable illumination environments. The simulation will consider the particle array as a pseudo infinite array extending along the *x*- and *y*- *axis*. The squared infinite two-dimensional array of silver nanoparticles are illuminated at normal incidence with the TE polarisation along the *y*- *axis*. The square array with a set linear polarisation will enable the particle's electrons to experience a coherent dipole oscillation.

The idea of examining the two-dimensional array is to retrieve a similar response to the single particle (strong single peak resonance) as a collective repeating function. Thus; removing any unwanted interactions that may come about when particles approach a particular inter-particle distance that may provide unexpected optical responses.

### Inter-Particle Distance

The peak position of the silver nanoparticles within the two dimensional array remains fixed for the most part. When distances reach sub-10 nm, the particles interact much more strongly and increase the likeliness of the electron tunnelling resulting in unexpected optical responses [26]. As the distance increases and the particle-particle interactions weaken, the responses present a similar extinction cross-section strength when compared to the single particle case.

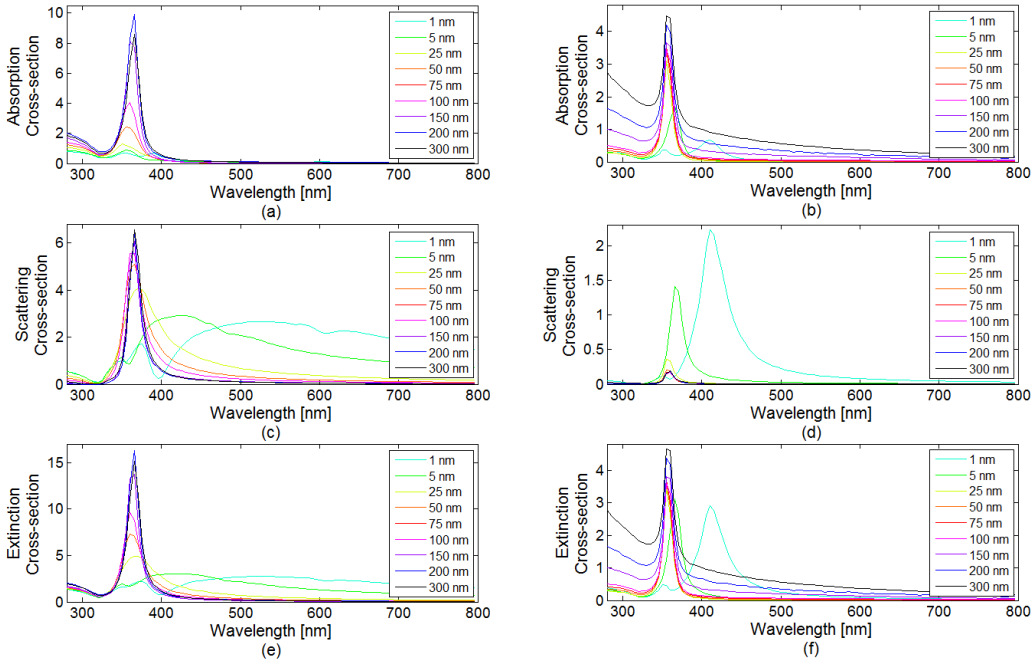


**Figure 3.15.** (a) and (b) Absorption, (c) and (d) scattering and (e) and (f) extinction cross-sections efficiency of Silver nanoparticles with varying inter-particle distance. Radius = 25 nm [*Left*] and Radius = 5 nm [*Right*].

### Varying Incident Angle

A fundamental aspect to this thesis is the study of angular performance. Figure 3.16 presents the optical density of the two-dimensional square array lattice. The results highlight the efficiency of resonance under illumination at various incidence angles. The resonant position does not experience any shifting behaviour. Furthermore, the electromagnetic interactions of the plasmonic nanoparticles display polarisation insensitivity, meaning that the resonant wavelength does not change with a variation in polarisation for a plasmonic two-dimensional array. With that being said, figure 3.16 does demonstrate some slight variation with polarisation dependency. The TE (*s*-) polarisation presents a stronger amplitude with a greater bandwidth than the TM (*p*-) polarisation, and is due to the orientation of the electric field vector.

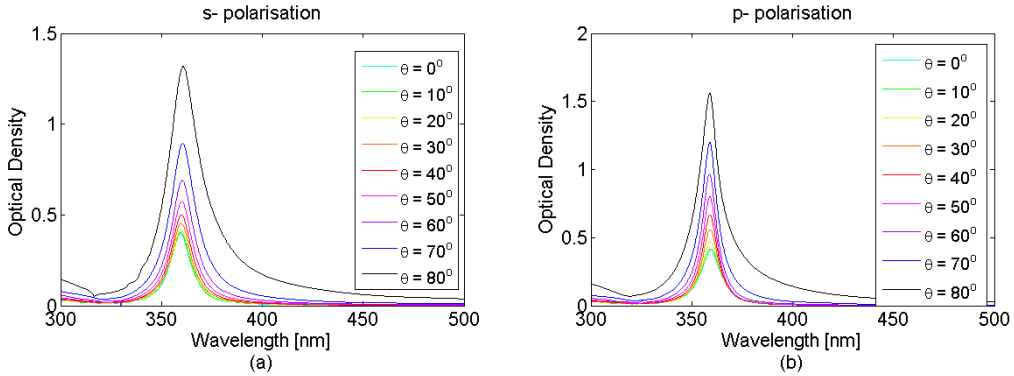


**Figure 3.16.** Optical density of a two-dimensional square array lattice of 25 nm Silver nanoparticles with an inter-particle distance of 100 nm for a range of incident angles for both s- and p- polarisation. The two-dimensional lattice consists of a pseudo infinite number of particles in the x- and y-axis.

### 3.2.3 **Three-Dimensional Particle Array**

The three-dimensional array of plasmonic nanoparticles is an extension to the two-dimensional study with the array extending with a pseudo infinite array ranging along the *x*- and *y- axis*. The *z-axis* hosts a series of three nanoparticles. Thus, the number of particles for the entire array assembly is $(\pm\infty_x, \pm\infty_y, 3_z)$. The particles are illuminated with the TE polarisation along the *y- axis*.

#### Inter-Particle Distance

The addition of layers along the *z-axis* is to further enhance the absorption and scattering efficiency rates. As the light of a certain wavelength enters the metallic nanoparticle array, the first set of particles begin to absorb and/or scatter that light. However, the efficiency of absorption and/or scattering is not 100%, so the remaining layers on the *z-axis* absorb/scatter the outstanding light that passes the preceding particle. Figure 3.17 shows a greater cross-sectional efficiency compared to the single and two-dimensional cases. The addition of two particles along the *z-axis* has more than doubled the cross-section efficiency for nanoparticles with a radius of 25 nm. Similar to the two-dimensional case, as the particles come closer together, a broadening effect begins to occur.

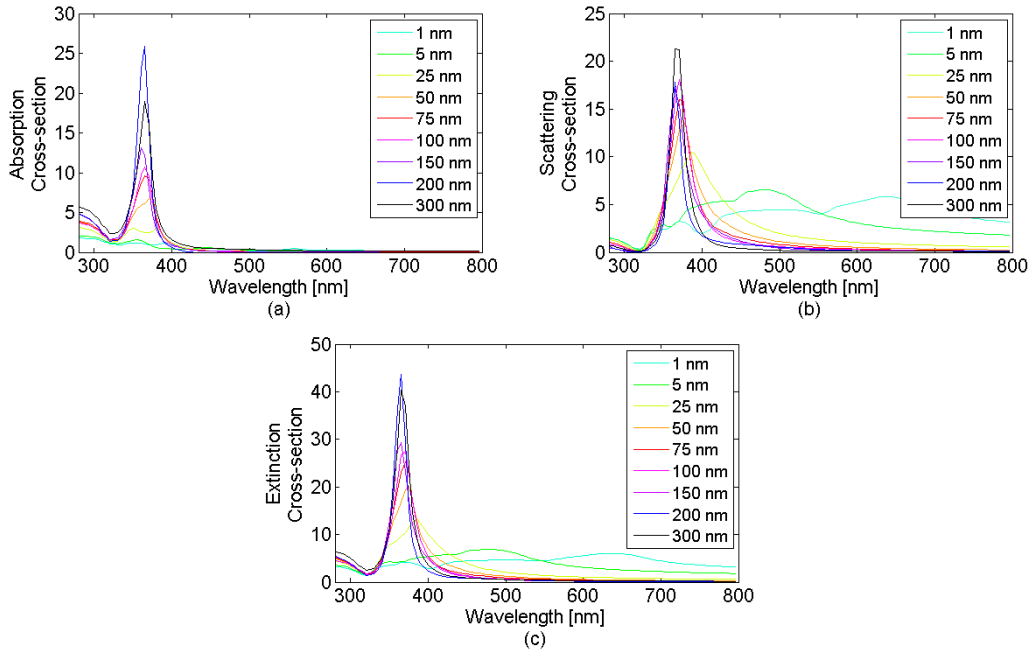


**Figure 3.17.** (a) Absorption, (b) scattering and (c) extinction cross-sections efficiency of Silver nanoparticles, radius = 25 nm, with varying inter-particle distance.

Figure 3.18 shows the contribution of improved extinction cross-section efficiency with the addition of multiple layers added along the *z-axis*.

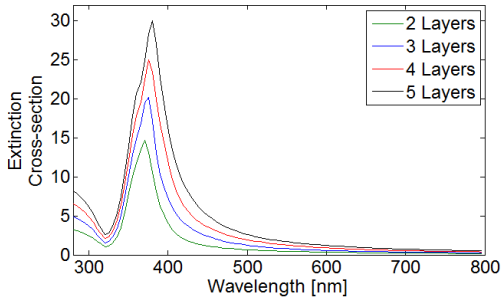


**Figure 3.18.** Extinction cross-sections efficiency of Silver nanoparticles, radius = 25 nm, with the addition of multiple layers.

### Varying Incident Angle

The results presented in three-dimensional array under angular illumination are similar to the two-dimensional study. The resonant peak does not shift with an increase angle of incidence and remains polarisation insensitive. The TE (*s*-) polarisation presents more broadly than the TM (*p*-) polarisation. The fundamental difference is the strength of absorption. The three-dimensional array offers a much stronger resonance. Thus, a deduction can be made that with an increased number of particles along the *z-axis*, a greater cross-sectional efficiency can be achieved, figure 3.19.

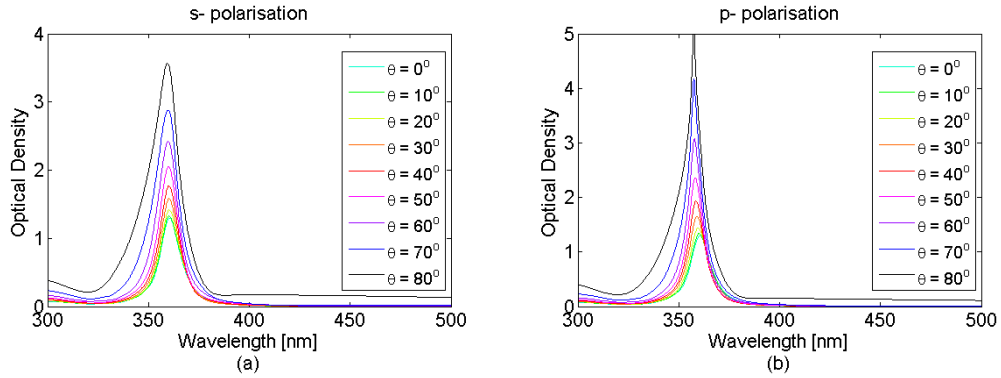


**Figure 3.19.** Optical density of a three-dimensional square array lattice of 25 nm Silver nanoparticles with an inter-particle distance of 100 nm for a range of incident angles for both s- and p- polarisation. The three-dimensional lattice consists of three particles along the *z-axis* with a pseudo infinite number of particles in the *x*- and *y-axis*.

### 3.2.4 **Random Particle Array**

To highlight the effectiveness of a periodic array, a study was completed on a random particle array. A computation script was generated within a full-wave electromagnetic simulator (CST studios). The script generated a 2D coordinate position for each particle. Each of the generated coordinates are pseudo-random and are forced to exist in a defined area. Additionally, a set inter-particle distance has been fixed to restrict any overlapping particles. The arrangement has been designed to resemble arrays of particles produced within a colloidal solution and present no periodicity effects. Unlike arrayed particles, the randomness prevents the reproduction of a single particle spectrum. Despite the randomness, neighbouring particles can still occupy in close proximity which can shift/broaden the spectral features. Furthermore, particles created in an array have the tendency to be uniform in size, where a random collection of nanoparticles can be a collection of sizes which tends to red-shift and broaden the spectrum as a collective response.

**Table 3.2.** Properties of random nanoparticle iterations where the surround medium is air and the nanoparticles are silver with a radius of 25 nm.

| Random Arrangement Iteration ($\boldsymbol{I_t}$) | Number of Particles ($\boldsymbol{n}$) | Total Volume of Particle ($\boldsymbol{nm^3}$) ($\boldsymbol{V_t = n \cdot \frac{4}{3}\pi r^3}$) | Volume of Surrounding Medium ($\boldsymbol{V_a}$) | Fill Fraction of Particles (%) |
|---|---|---|---|---|
| 1 | 11 | $7.1195x10^{-22}$ | $2.50x10^{-20}$ | 2.8478 |
| 2 | 8 | $5.2360x10^{-22}$ | $1.00x10^{-20}$ | 5.2360 |
| 3 | 18 | $1.1781x10^{-21}$ | $5.625x10^{-20}$ | 2.0944 |
| 4 | 20 | $1.3090x10^{-21}$ | $1.00x10^{-19}$ | 1.3090 |
| 5 | 4 | $2.6180x10^{-22}$ | $9x10^{-21}$ | 2.9089 |
| 6 | 8 | $5.2360x10^{-22}$ | $1.60x10^{-20}$ | 3.2725 |

As the particles are placed in a random array instead of a uniformed square array, the coherent behaviours are excluded. There is a slight blue-shifting behaviour as the particles are assembled in close proximity. As the particles begin to separate apart, the averaging effect begins to resemble a single particle solution. The density of the random array also induces a stronger extinction cross-section. The broadening effects presented in figure 3.20 demonstrate that periodicity is an important aspect for obtaining a strong narrow resonance.

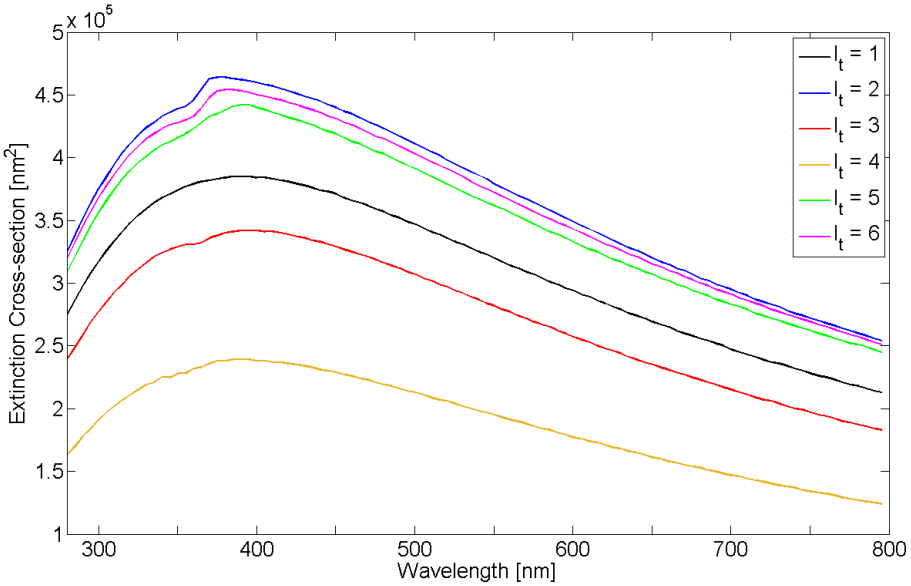


**Figure 3.20.** Extinction cross-sections of Silver nanoparticles, 25 nm radius, with varying random arrangement iterations.

### 3.2.5 **Tailoring Optical Notch Location**

Localised surface plasmon resonant (LSPR) is characterised by the resonant peaks. Previous research has discussed the linear dependence of LSPR peak wavelengths [27-29]. The linear dependency (Eq. 3.2.2) demonstrates that the plasmonic resonances are able to shift according to the surrounding refractive index.

$$\lambda_{max} = \lambda_p \sqrt{2n_m^2 + 1} \tag{3.2.2}$$

Where $\lambda_{max}$ is the resonant peak, $\lambda_p$ is the plasma wavelength (*associated with the plasma frequency found in Drude's formula*) and $n_m$ is the refractive index of the surrounding medium.

The resonant condition wavelength is approximately located at (Eq. 3.2.3), where $\varepsilon_{np}$ permittivity of the plasmonic nanoparticle, $\chi$ depolarisation/geometrical factor ($\chi = 2$ for spheres) and $\varepsilon_{host}$ is the permittivity of the non-absorbing host medium.

$$Re[\varepsilon_{np}] \approx -\chi\,[\varepsilon_{host}] \tag{3.2.3}$$

The research previously carried out is a valid approximate for a single particle case but does not take into account when particles are arranged into an array form. This traditional linear case can still provide an approximate solution to the resonant peak. Figure 3.21 presents a solution (Eq. 3.2.4) to the resonant peak when considering an array form. The Drude model slightly differs from the experimental data presented by Johnson and Christy. The Drude model and the Johnson and Christy data was ran through a MATLAB script to select the peak resonant position according to the Maxwell-Garnett theory, *discussed in Chapter IV*, and established a fitting equation (Eq. 3.2.4). A simulation model of a nanoparticle array (Johnson and Christy data) using CST was compiled to verify the results. The model assumes an inter-particle distance of $d \approx \lambda_{max}/16$, where $\lambda_{max}$ is according to the linear case.

$$\lambda_t = e^{\frac{c_1 + Re[n_{host}]}{c_2}} \tag{3.2.4}$$

Where $\lambda_t$ is the target wavelength, $n_{host}$ is the surrounding refractive index and $c_1$ and $c_2$ are plasmonic material coefficients.

**Table 3.2.** Plasmonic material coefficients.

| | $c_1$ | $c_2$ |
|---|---|---|
| Silver (Johnson & Christy) | 18.741 | 3.3654 |
| Silver (Drude) | 18.511 | 3.3191 |
| Gold (Johnson & Christy) | 30.068 | 5.0208 |
| Gold (Drude) | 25.755 | 4.3807 |

The selection of gold and silver materials are able to cover the entire range of the visible spectrum. The desired blocking wavelength for the optical metamaterial filter is located at the resonant wavelength.

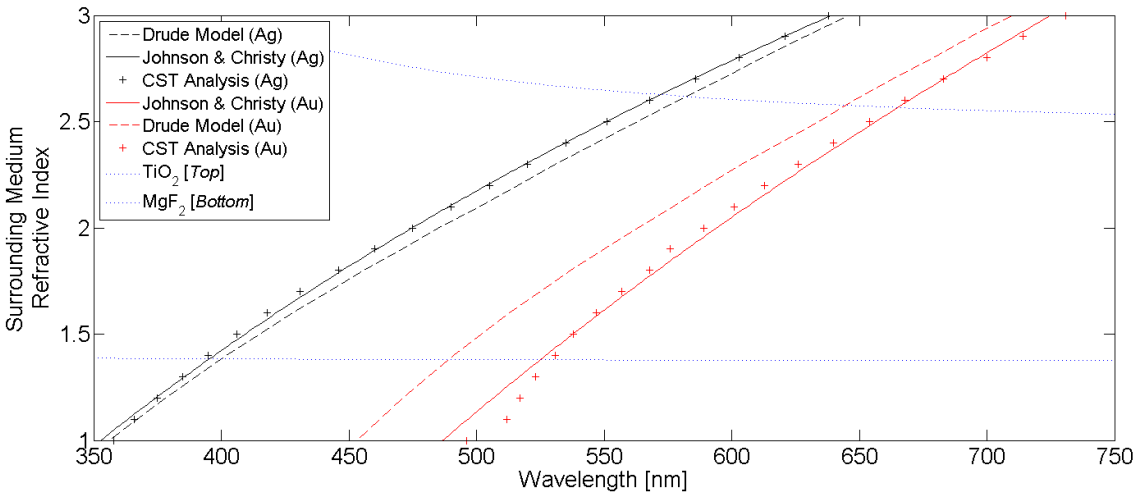


**Figure 3.21.** Resonant peak wavelength according to the surrounding medium refractive index.

According to (Eq. 3.2.4), table 3.3 provides material make-up for a given metamaterial meta-atom to target select visible laser wavelengths.

**Table 3.3.** A selection of visible laser wavelengths and the associated meta-atom combination where the plasmonic resonance matches the wavelength of the laser. [30]

| Operation Wavelength of Laser [nm] | Nanoparticle Material | Refractive Index of Surrounding Dielectric |
|---|---|---|
| 405 | Silver | 1.46 ($SiO_2$) |
| 450 | Silver | 1.82 ($Y_2O_3$) |
| 520 | Silver | 2.31 ($TiO_2$) |
| 532 | Silver | 2.38 (ZnS) |
| 637 | Gold | 2.35 (ZnS) |
| 650 | Gold | 2.45 (C –Diamond) |

## 3.3 **Summary**

This chapter examined the cross-sectional behaviour of nanoparticles to assess the performance as optical resonators. This is achieved through Mie theory followed by computation verification. The angular and polarisation behaviours of arrayed nanoparticles demonstrate the suitability for the rudimentary building block needed to establish a shift-free wide-angle filter. The plasmonic spherical nanoparticles do not present any resonance blue-shifting as the angle of incidence increases. This is due to the particles sharing a local field component and non-radiative interactions. The fields at the nanoparticle become highly localised and decay rapidly from the nanoparticle-dielectric interface into the dielectric background due to the provided inter-particle spacing distances. The addition of array layers in the *z-axis* enables greater extinction cross-section efficiency by retarding the light more and more at each nanoparticle array layer. An extension to the linear dependency of LSPR peak wavelengths has also been introduced as a method for selecting the target resonant wavelength depending on the surrounding refractive index of arrayed nanoparticles. The resonant wavelength directly corresponds to the blocking wavelength, and as such, provides a simplistic beginning for an inverse design method without the requirement of any computational algorithms.

## 3.4 **References**


[1] R. Wolfe, "On the Theory of Optical Absorption in Metals and Semiconductors", *Proceedings of the Physical Society. Section A*, vol. 67, no. 1, pp. 74-84, 1954. Available: 10.1088/0370-1298/67/1/312.

[2] G. Wurtz, J. Im, S. Gray and G. Wiederrecht, "Optical Scattering from Isolated Metal Nanoparticles and Arrays", *The Journal of Physical Chemistry B*, vol. 107, no. 51, pp. 14191-14198, 2003. Available: 10.1021/jp0357875.

[3] W. Hergert and T. Wriedt, *The Mie theory: Basics and applications*. Springer, 2015.

[4] C. Bohren and D. Huffman, *Absorption and scattering of light by small particles*. New York: Wiley, 2013.

[5] C. Bohren, "How can a particle absorb more than the light incident on it?", *American Journal of Physics*, vol. 51, no. 4, pp. 323-327, 1983. Available: 10.1119/1.13262.

[6] L. Brillouin, "The Scattering Cross Section of Spheres for Electromagnetic Waves", *Journal of Applied Physics*, vol. 20, no. 11, pp. 1110-1125, 1949. Available: 10.1063/1.1698280.

[7] H. Hulst, *Light scattering by small particles*. New York, NY: Dover, 2009.

[8] M. Berg, C. Sorensen and A. Chakrabarti, "A new explanation of the extinction paradox", *Journal of Quantitative Spectroscopy and Radiative Transfer*, vol. 112, no. 7, pp. 1170-1181, 2011. Available: 10.1016/j.jqsrt.2010.08.024.

[9] H. Lai, W. Wong and W. Wong, "Extinction paradox and actual power scattered in light beam scattering: a two-dimensional study", *Journal of the Optical Society of America A*, vol. 21, no. 12, p. 2324, 2004. Available: 10.1364/josaa.21.002324.

[10] J. Zhu, Y. Wang and L. Huang, "Simulation of the medium dielectric constant dependent optical properties for gold nanosphere", *Materials Chemistry and Physics*, vol. 93, no. 2-3, pp. 383-387, 2005. Available: 10.1016/j.matchemphys.2005.03.038.

[11] K. Mogensen and K. Kneipp, "Size-Dependent Shifts of Plasmon Resonance in Silver Nanoparticle Films Using Controlled Dissolution: Monitoring the Onset of Surface Screening Effects", *The Journal of Physical Chemistry C*, vol. 118, no. 48, pp. 28075-28083, 2014. Available: 10.1021/jp505632n.

[12] J. Jin, *Finite element method in electromagnetics*, 3rd ed. Wiley-IEEE Press, 2014.

[13] C. Gong and M. Leite, "Noble Metal Alloys for Plasmonics", *ACS Photonics*, vol. 3, no. 4, pp. 507-513, 2016. Available: 10.1021/acsphotonics.5b00586.

[14] D. Rioux, S. Vallières, S. Besner, P. Muñoz, E. Mazur and M. Meunier, "An Analytic Model for the Dielectric Function of Au, Ag, and their Alloys", *Advanced Optical Materials*, vol. 2, no. 2, pp. 176-182, 2013. Available: 10.1002/adom.201300457.

[15] H. Yu, Y. Peng, Y. Yang and Z. Li, "Plasmon-enhanced light–matter interactions and applications", *npj Computational Materials*, vol. 5, no. 1, 2019. Available: 10.1038/s41524-019-0184-1.

[16] G. Naik, V. Shalaev and A. Boltasseva, "Alternative Plasmonic Materials: Beyond Gold and Silver", *Advanced Materials*, vol. 25, no. 24, pp. 3264-3294, 2013. Available: 10.1002/adma.201205076.

[17] P. Alippi, P. La Rocca and G. Bachelet, "Alkali-metal plasmons, pseudopotentials, and optical sum rules", *Physical Review B*, vol. 55, no. 20, pp. 13835-13841, 1997. Available: 10.1103/physrevb.55.13835.
[18] A. Mathewson and H. Myers, "Absolute Values of the Optical Constants of Some Pure Metals", *Physica Scripta*, vol. 4, no. 6, pp. 291-292, 1971. Available: 10.1088/0031-8949/4/6/009.
[19] M. Rasigni and G. Rasigni, "Optical constants of lithium deposits as determined from the Kramers-Kronig analysis", *Journal of the Optical Society of America*, vol. 67, no. 1, p. 54, 1977. Available: 10.1364/josa.67.000054.
[20] N. Smith, "Optical Constants of Sodium and Potassium from 0.5 to 4.0 eV by Split-Beam Ellipsometry", *Physical Review*, vol. 183, no. 3, pp. 634-644, 1969. Available: 10.1103/physrev.183.634.
[21] S. Yamaguchi and T. Hanyu, "The Optical Properties of Rb", *Journal of the Physical Society of Japan*, vol. 35, no. 5, pp. 1371-1377, 1973. Available: 10.1143/jpsj.35.1371.
[22] F. Scotognella et al., "Plasmonics in heavily-doped semiconductor nanocrystals", *The European Physical Journal B*, vol. 86, no. 4, 2013. Available: 10.1140/epjb/e2013-40039-x.
[23] A. Agrawal, S. Cho, O. Zandi, S. Ghosh, R. Johns and D. Milliron, "Localized Surface Plasmon Resonance in Semiconductor Nanocrystals", *Chemical Reviews*, vol. 118, no. 6, pp. 3121-3207, 2018. Available: 10.1021/acs.chemrev.7b00613.
[24] N. Liu, H. Guo, L. Fu, S. Kaiser, H. Schweizer and H. Giessen, "Three-dimensional photonic metamaterials at optical frequencies", *Nature Materials*, vol. 7, no. 1, pp. 31-37, 2007. Available: 10.1038/nmat2072.
[25] M. Gil, J. Bonache and F. Martín, "Metamaterial filters: A review", *Metamaterials*, vol. 2, no. 4, pp. 186-197, 2008. Available: 10.1016/j.metmat.2008.07.006.
[26] J. Zuloaga, E. Prodan and P. Nordlander, "Quantum Description of the Plasmon Resonances of a Nanoparticle Dimer", *Nano Letters*, vol. 9, no. 2, pp. 887-891, 2009. Available: 10.1021/nl803811g.
[27] N. Cennamo et al., "Localized Surface Plasmon Resonance with Five-Branched Gold Nanostars in a Plastic Optical Fiber for Bio-Chemical Sensor Implementation", *Sensors*, vol. 13, no. 11, pp. 14676-14686, 2013. Available: 10.3390/s131114676.
[28] Y. Hong, Y. Huh, D. Yoon and J. Yang, "Nanobiosensors Based on Localized Surface Plasmon Resonance for Biomarker Detection", *Journal of Nanomaterials*, vol. 2012, pp. 1-13, 2012. Available: 10.1155/2012/759830.
[29] A. Agrawal, I. Kriegel and D. Milliron, "Shape-Dependent Field Enhancement and Plasmon Resonance of Oxide Nanocrystals", *The Journal of Physical Chemistry C*, vol. 119, no. 11, pp. 6227-6238, 2015. Available: 10.1021/acs.jpcc.5b01648.
[30] M. Polyanskiy, “RefractiveIndex.info – Refractive index database”, *Refractiveindex.info*, 2020. [Online]. Available: https://refractiveindex.info.

# CHAPTER IV. METAFILM DESIGN: TUNABLE OPTICAL NOTCH FILTERS BASED ON PLASMONIC NANOCOMPOSITES

This chapter outlines the effective medium approximation theory and how to utilise the theory to design individual metafilms and full optical notch filter systems that can exist with a single, duel or multiple notch in the transmission. The principles couple together plasmonic theory with traditional thin film optics to create a homogenous plasmonic compound optical metamaterial filter that can be tuned to a wavelength of interest. Comparative results from full-wave models will be discussed against metafilm models to test the validity of the system.

## 4.1 **Effective Medium Approximation**

When describing metamaterials for industry practice, it is important to obtain results with sufficient accuracy within an acceptable time. An issue with designing metamaterials relates to the inefficiency of obtaining desirable results. Traditionally, researchers may use a brute force method [1,2] or algorithms (evolutionary [3], neural networks [4], etc [5]) to establish the required outcome. This is a slow technique that makes an inverse design strategy difficult to accomplish. This raises an important fundamental question, "*how to describe complex metamaterial structures through macroscopic parameters?*"

A common method to describe these macroscopic parameters is via a homogeneous effective medium [6,7]. Existing homogenisation processes often take advantage of the Maxwell Garnett [8] and, extended, Bruggeman's approximations [9]. The Maxwell Garnett model, and its extension, are first-order approximations, yielding simple and effective solutions for linear and far field problems (i.e. for this study, establishing an effective thin film; metafilms).

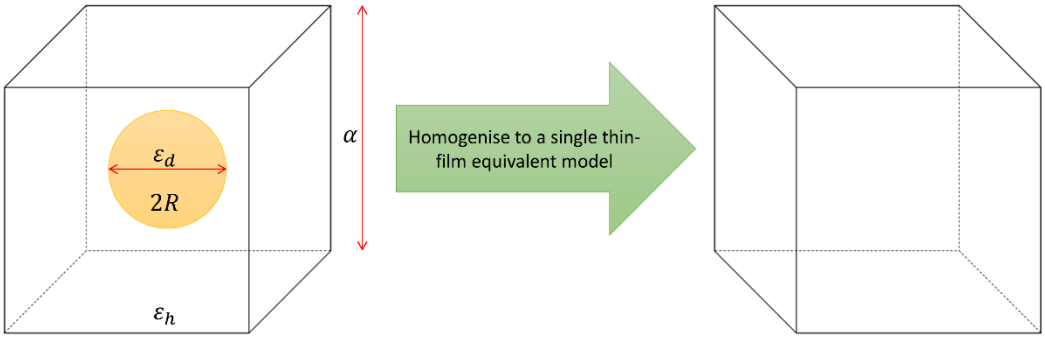


**Figure 4.1.** Process of converting meta-atom to single thin film equivalent.

Homogenisation is the process of describing a single uniformed layer from a more complicated meta-atom structure. Figure 4.1 shows a simplistic block diagram of creating a homogenised system.

Homogenisation of a metamaterial affects the dispersive properties. The inclusion of Drude-type particles (Metallic) embedded in a dielectric matrix exhibits a resonating response. Assuming a well-defined ordered lattice, the metallic particles become isolated, prohibiting a continuum conducting medium that results in an asymptotically real value outside the resonant band.

The effective thin film permittivity allows the computation for a heterogeneous structure as a function of the structural and material parameters of the components that make up the meta-atom (Figure 4.2). Metamaterials provide a lattice that consists of a repeating function of the meta-atoms that are much smaller than the wavelengths of interest. An effective thin film equivalent description is valid when the size of the heterogeneities is adequately smaller than the excitation wavelength, which is why an effective description can be developed [8].

Figure 4.2 discusses the geometric and optical parameters for a meta-atom, and can simply be described from four distinct features;

1. The permittivity of the nano-resonator ($\varepsilon_d$).
2. The permittivity of the host medium ($\varepsilon_h$).
3. The fill fraction ($p$), a property designated from the nano-resonators radius ($R$) and the length/width/height ($\alpha$) of the surrounding medium.
4. Shape of the nano-resonator ($\chi$ [$depolarisation\ factor$]).

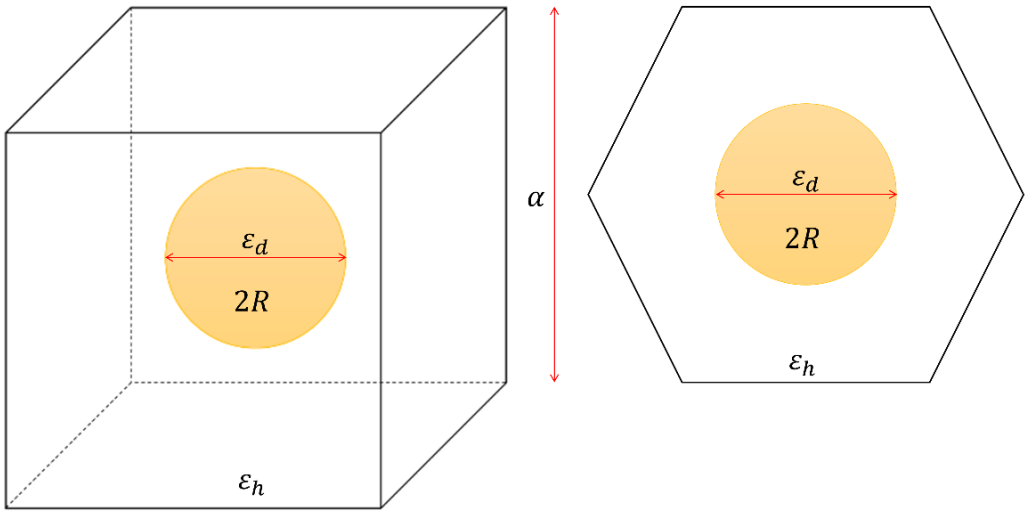


**Figure 4.2.** Geometries of the metamaterials pseudo-lattice. (a) Meta-atom of an electromagnetic metamaterial formed by (a) cubic array and (b) hexagonal array, of spherical dielectric inclusions embedded in a host medium.

### 4.1.1 **Maxwell-Garnett Theory**

The Maxwell-Garnett (MG) approximation has been commonly used to describe composite materials and their macroscopic properties for a uniformed composite with two or more mixed elements [10]. The MG method is a slight extension to the Clausis-Mossotti formula [11]. The method provides an approximation for liquids, gases and solids.

#### Clausius-Mossotti Formula

Clausius Mossotti relation is near identical to that of the Lorentz-Lorenz equation [12], and differs in the relation to the dielectric constant, rather than the refractive index, of a material. This equation became the foundations for deriving an effective medium model.

$$\frac{4\pi}{3}\sum_{i} N_i\alpha_i = \frac{\varepsilon - 1}{\varepsilon + 2} \tag{4.1.1}$$

Where $\varepsilon$ is the permittivity, $N$ is the number of molecules per unit volume and $\alpha$ is the polarisability.

For a spherical inclusion with the permittivity $\varepsilon_i$ and radius $a$, the polarisability can be defined as:

$$\alpha = \left(\frac{\varepsilon_i - 1}{\varepsilon_i + 2}\right) a^3 \tag{4.1.2}$$

Combining (Eq.4.1.2) with (Eq.4.1.1) provides a solution for obtaining an effective permittivity $\varepsilon_{eff}$ for spherical inclusions within a constant medium. With $p$ defining the volume fraction of the spherical inclusions where the two extreme values are $p = 0$ and $p = 1$.

$$\left(\frac{\varepsilon_{eff} - 1}{\varepsilon_{eff} + 2}\right) = p\left(\frac{\varepsilon_i - 1}{\varepsilon_i + 2}\right) \tag{4.1.3}$$

#### Maxwell-Garnett Approximation

The Maxwell-Garnett Theory (MGT) describes the bulk effective permittivity of a composite mixture in terms of the inclusion materials and the host materials.

$$\frac{\varepsilon_{eff} - \varepsilon_h}{\varepsilon_{eff} + \chi\varepsilon_h} = p\frac{\varepsilon_m - \varepsilon_h}{\varepsilon_m + \chi\varepsilon_h} \tag{4.1.4}$$

The formula can be rewritten to express the effective permittivity $\varepsilon_{eff}$ in an explicit manner.

$$\varepsilon_{eff} = \varepsilon_h \left( \frac{1 + \chi p \left( \frac{\varepsilon_m - \varepsilon_h}{\varepsilon_m + \chi \varepsilon_h} \right)}{1 - p \left( \frac{\varepsilon_m - \varepsilon_h}{\varepsilon_m + \chi \varepsilon_h} \right)} \right) \tag{4.1.5}$$

Where $\varepsilon_{eff}$, $\varepsilon_h$ and $\varepsilon_m$ defines the permittivity of the effective, host and inclusion material respectively, and $\chi$ defines the inclusion material depolarisation factor.

Generally, MGT is predictable and accurate at low volume fractions, substantially less than 1. This is where Bruggeman made a significant improvement to the MGT by establishing a method for treating two constituent materials in a symmetric fashion and improving the accuracy for higher volume fractions [13].

### 4.1.2 **Effective Drude-Lorentz Formulation**

More commonly, MGT is used for describing effective parameters in metamaterials [14]. However, this can display some limitations, particularly when considering dispersive materials. Dispersive material can traditionally be described with several constants that can be formulated into either a Drude equation or a Drude Lorentz equation, depending whether the material is metallic, semiconductor or dielectric.

The effective Drude Lorentz formula enables the input of constants, which describe traditional Drude style materials, and formulates new effective constants to describe a dispersive metamaterial.

$$\varepsilon_{eff}(\omega) = \varepsilon_{\infty,eff} + \frac{\omega_{p,eff}^2}{\omega_{0,eff}^2 - \omega^2 + i\omega\Gamma} \tag{4.1.6}$$

Where the effective constant offset (high frequency) permittivity $\varepsilon_{\infty,eff}$, plasma frequency $\omega_{p,eff}$ and the resonance frequency $\omega_{0,eff}$, formulas are described below.

$$\varepsilon_{\infty,eff} = \varepsilon_h + 3p\,\varepsilon_h \left( \frac{\varepsilon_\infty - \varepsilon_h}{\varepsilon_\infty + \chi\,\varepsilon_h - p\,(\varepsilon_\infty - \varepsilon_h)} \right) \tag{4.1.7}$$

$$\omega_{p,eff} = \sqrt{p} \left( \frac{3\,\varepsilon_h}{(1-p)\,\varepsilon_\infty + (\chi + p)\,\varepsilon_h} \right) \omega_p \tag{4.1.8}$$

$$\omega_{0,eff} = \left( \sqrt{\frac{1-p}{(1-p)\,\varepsilon_\infty + (\chi + p)\,\varepsilon_h}} \right) \omega_p \tag{4.1.9}$$

With $\omega$ indicating angular frequency, $\varepsilon_h$ denoting the permittivity of the host medium, $p$ describing the fill fraction and $\chi$ describing the polarisability of the particle which is determined by the particle shape. The remaining parameters ($\varepsilon_\infty$, $\omega_p$ and $\Gamma$) are defined from the Drude type particle.

### 4.1.3 **Refractive Index Relation**

The conversion from permittivity to refractive index can be calculated from (Eq.4.1.10), with $n$ equalling the effective refractive index and $k$ equalling the effective extinction coefficient.

$$n = \sqrt{\frac{|\varepsilon_{eff}| + Re(\varepsilon_{eff})}{2}} \qquad k = \sqrt{\frac{|\varepsilon_{eff}| - Re(\varepsilon_{eff})}{2}} \tag{4.1.10}$$

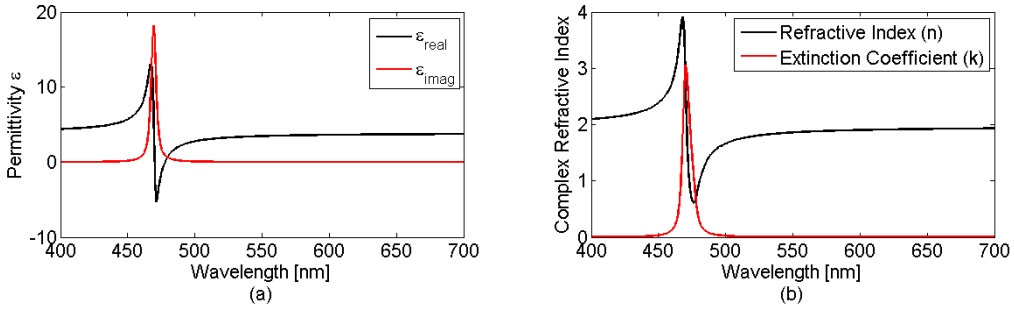


**Figure 4.3.** The (a) effective permittivity and (b) effective refractive index, of a thin film equivalent for spherical silver inclusion embedded within a dielectric host medium ($n = 2$) and a of fill fraction ($p = 0.0122$).

### 4.1.4 **Non-Spherical Particles**

The morphology of a particle can influence the plasmonic behaviour, either by shifting the response or creating multiple resonance positions that can be electromagnetically polarisation sensitive. As previously mentioned, $\chi$ describes the depolarisation factor of the particle which is fundamentally determined by the particles shape. The factor for $L_i$ (in the $a_i$ axis direction) is;

$$\chi = \frac{1 - L_i}{L_i} \tag{4.1.11}$$

$$L_i = \frac{a_i a_j a_k}{2} \int_0^\infty \frac{ds}{(s + a_i^2)\sqrt{(s + a_i^2)(s + a_j^2)(s + a_k^2)}} \tag{4.1.12}$$

The other depolarisation factors ($L_j$ *and* $L_k$), are results of the interchange of $a_j$ *and* $a_k$ in the above integral.

The three depolarisation factors must satisfy;

$$L_i + L_j + L_k = 1 \tag{4.1.13}$$

For spherical particles, $\chi = 2$, due to the isotropic behaviour of the three semi-axis $a_i, a_j \; and \; a_k$.

**Table 4.1.** Depolarisation factors for varying particle shape.

| Particle Shape [*Aspect Ratio*] | $L_i$ | $L_j$ | $L_k$ |
|---|---|---|---|
| Spherical | $1/3$ | $1/3$ | $1/3$ |
| Ellipsoid (Prolate) [*1,1,2*] | $1/4$ | $1/4$ | $1/2$ |
| Ellipsoid (Oblate) [*2,2,1*] | $1/(3+(1/-2))$ | $1/(3+(1/-2))$ | $1/5$ |
| Disc | 0 | 0 | 1 |
| Needle | $1/2$ | $1/2$ | 0 |

Figure 4.4 Indicates that the depolarisation factor, associated with particle shape, can have considerable influence on the resonant wavelength, resonant strength and the bandwidth.

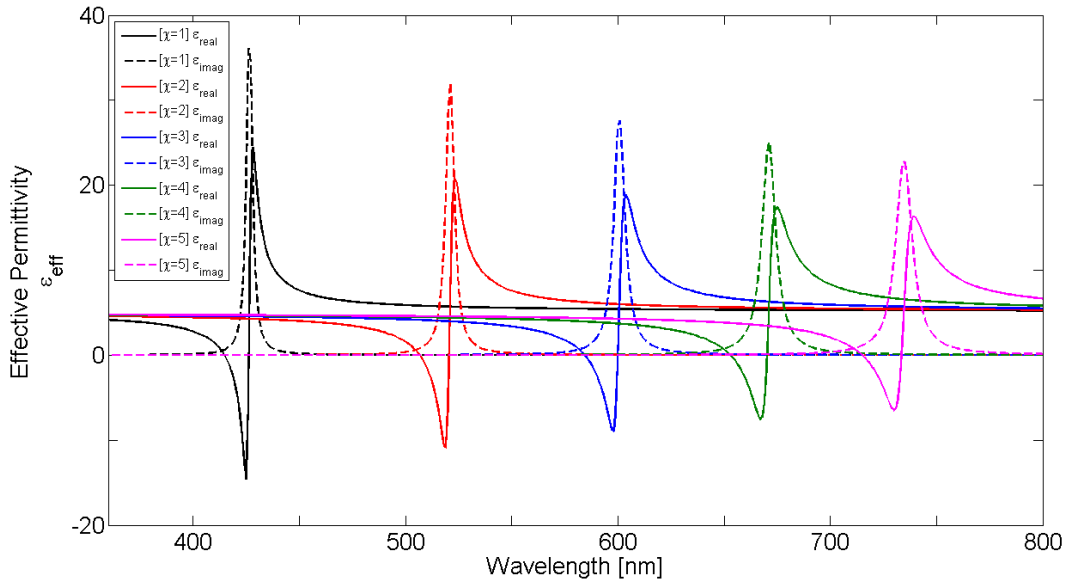


**Figure 4.4.** Effective permittivity of varying depolarisation factor for Silver in a surrounding medium with a refractive index of 2.20.

## 4.2 **Tuning Plasmonic Compound Metafilms**

Dispersive and resonant effects are principal properties in plasmonic metamaterial applications. A key principle is the ability to tailor this dispersive response. When a plasmonic particle is surrounded by a dielectric medium, the plasmonic resonance redshifts [15]. The strength of the shift depends on the refractive index of the surrounding material. Furthermore, another influencing feature relates to the fill fraction which is governed by the dimension of the meta-

atom. However, the increase in fill fraction percentage results in high permittivity solutions. The subwavelength particles with high positive dielectric permittivity support strong resonances with a large displacement current [16]. This can give rise to a strong magnetic field induced by contra-directional displacement currents [2]. Moreover, the average effective index can change considerably. Therefore it is preferable, where possible, to tailor the resonant wavelength by varying the surrounding refractive index, then utilise the fill fraction for really fine tuning.

As discussed in the previous chapter, the increasing refractive index of the surrounding medium influences the plasmonic resonances by increasing the bound charge accumulation at the surface interface. This results in a dampening of the restoring force leading to a depression of the resonant energy, ultimately causing a spectral red shift.

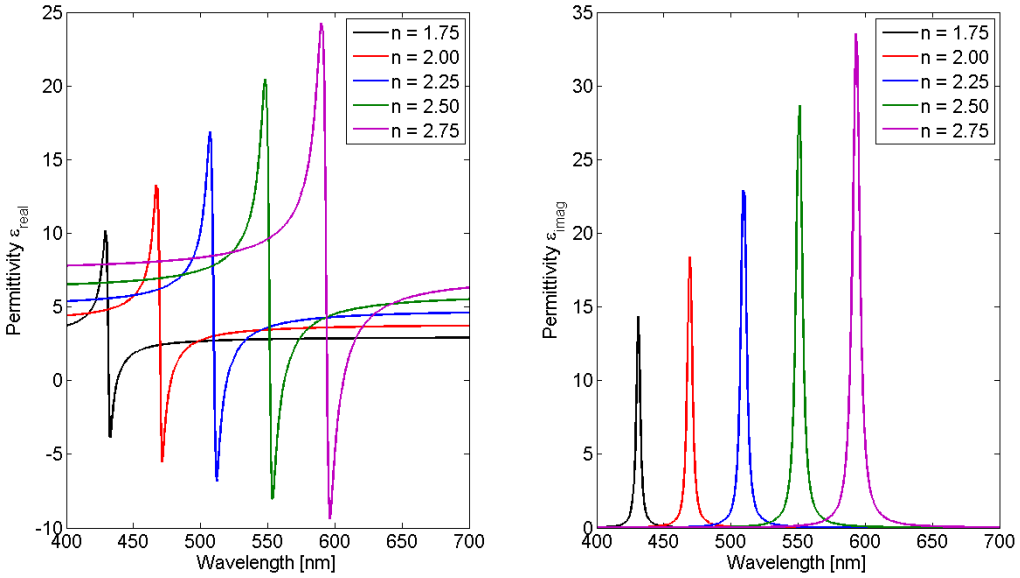


**Figure 4.5.** The influence of the surrounding materials refractive index of the meta-atom's permittivity with varying values a fixed fill fraction of ($p = 0.0125$) and Silver plasmonic particle.

The figures found in table 4.2, highlights that the average effective index (AEI) is near that of the surrounding refractive index. Providing the AEI is near the surround refractive index value, a clear and common notch can be established without the presence of a strong magnetic field influence, which could induce polarisation dependent resonances outside the plasmonic response.

**Table 4.2.** Effects of varying refractive index on resonant wavelength.

| Surrounding Refractive Index ($\boldsymbol{n}$) | Average Effective Index ($\boldsymbol{n_{eff}}$) | Resonant Wavelength ($\boldsymbol{\lambda_{Res}}$) [nm] |
|---|---|---|
| 1.75 | 1.6843 | 431 |
| 2.00 | 1.9366 | 469 |
| 2.25 | 2.1924 | 509 |
| 2.50 | 2.4569 | 551 |
| 2.75 | 2.7359 | 593 |

Figure 4.6 shows the increasingly high permittivity by altering the fill fraction. In turn, this drastically affects the effective dispersive refractive index, creating broadband regions of near zero refractive index with broadband regions of high extinction coefficients.

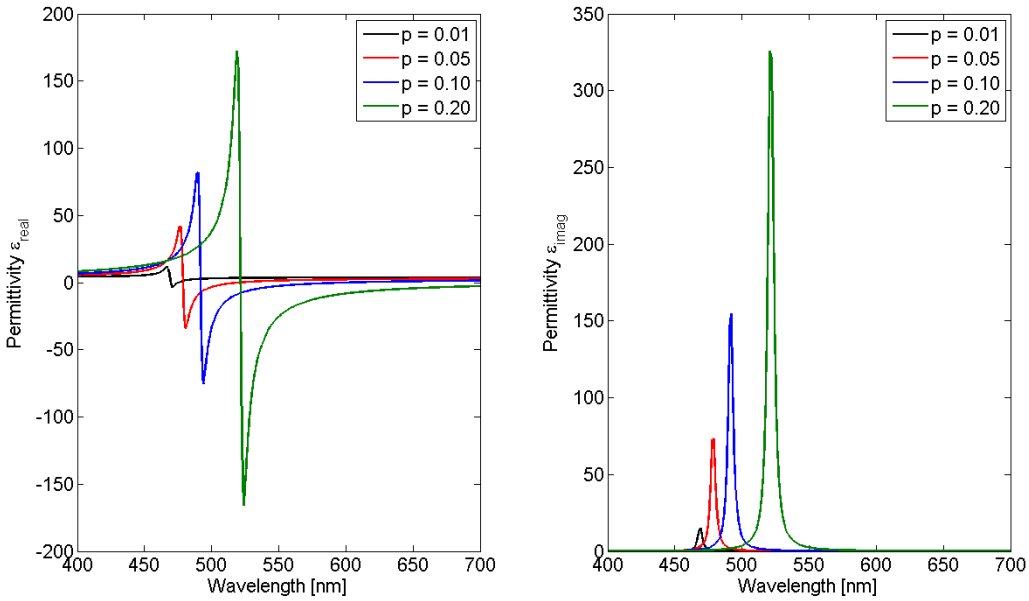


**Figure 4.6.** The influence of the fill factor ($p$) on the permittivity with varying values and a fixed surrounding medium refractive index ($n = 2.00$) and Silver plasmonic particle.

The figures displayed in table 4.3, clearly show that the AEI can become unstable and shift to an undesirable index when subject to change in fill factors.

**Table 4.3.** Effects of varying fill fractions of the resonant wavelengths.

| Fill Factor ($\boldsymbol{p}$) | Average Effective Index ($\boldsymbol{n_{eff}}$) | Resonant Wavelength ($\boldsymbol{\lambda_{Res}}$) [nm] |
|---|---|---|
| 0.01 | 1.9491 | 469 |
| 0.05 | 1.7626 | 479 |
| 0.10 | 1.5968 | 492 |
| 0.20 | 2.1447 | 521 |

## 4.3 **Equivalent Circuit Approximation**

An equivalent circuit approximation is a useful approach for quickly establishing the estimated behaviour of a metafilm that uses well defined methods of electronic resonant circuits [17,18]. The equivalent circuit is sought to simplify the calculations and broadly streamline the metamaterial unit-cell evaluation process but does not take into consideration the substrate and alternative layers.

An equivalent bandstop circuit consists of an RLC (Resistor, Inductor, and Capacitor) network to define the meta-atom. Establishing the components can be inversely obtained through defining the nanoparticle. The inductance can be defined through Gauss's law for electric fields. At first, this seems an odd situation to start with, due to inductance resulting from the magnetic behaviour. However, due to the negative permittivity of the material, the assumption can be made that a negative capacitance will be achieved [19,20]. This can linearly be represented by inductance due the sign change of $Z_c = -i/\omega C$, where $-i$ indicates that the voltage lags current, to $Z_c = -i/-\omega C \equiv Z_L = i\omega L$, where $+i$ specifies that the voltage leads the current.

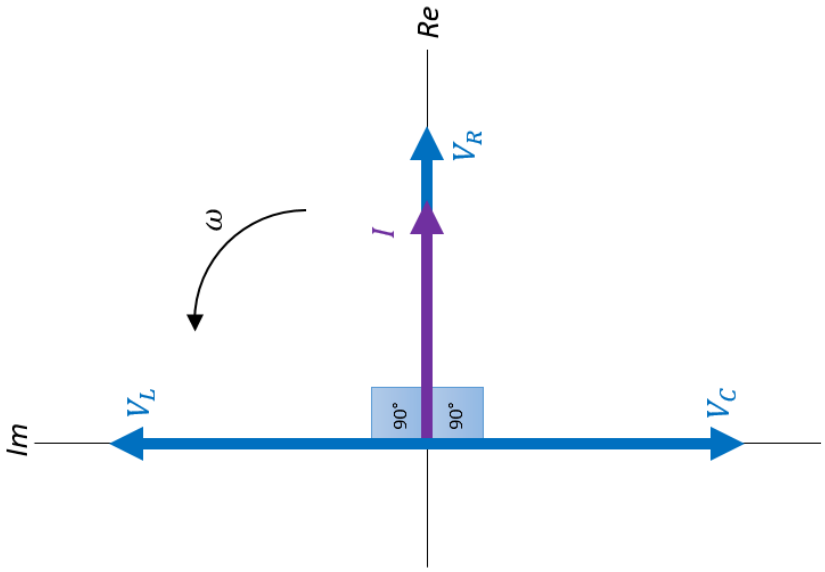


**Figure 4.7.** Voltage vectors for RLC components.

Reviewing Gauss's Law for electric fields;

$$\oint E\, dA = \frac{q_{enc}}{\varepsilon_0} \tag{4.3.1}$$

At the Gaussian surface the electric field is constant.

$$E = \frac{Q}{4\pi r^2 \varepsilon_0} \tag{4.3.2}$$

The established electric potential can be defined by V.

$$V = -\frac{Q}{4\pi\varepsilon_0}\int \frac{1}{r^2}\, dr \tag{4.3.3}$$

The charge of the spherical nanoparticle is now distinct, and with rearranging for the capacitance the charges will be cancelled out.

$$Q = CV \equiv (4\pi r\varepsilon_0\varepsilon_r)V \tag{4.3.4}$$

Due to the negative permittivity ($\varepsilon_r$) of the metallic nanoparticles at optical frequencies, the capacitance becomes negative and nicely represents the inductance of the particle.

$$-C = L, \quad \varepsilon_r < 0 \tag{4.3.5}$$

Now that the inductance is defined, the resistance and capacitance can be inversely calculated.

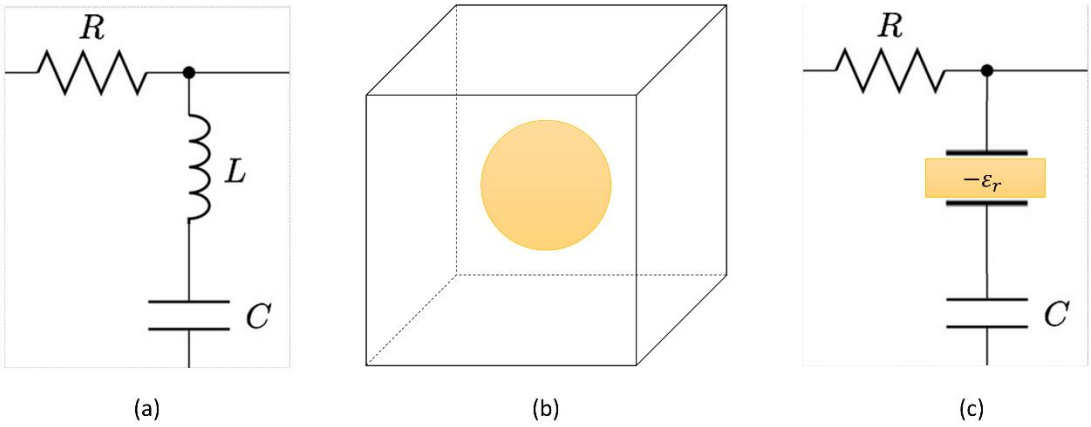


**Figure 4.8.** Meta-atom equivalent circuit of RLC network. (a) Passive RLC bandstop filter. (b) meta-atom consisting of metallic nanoparticle surrounding in dielectric. (c) Equivalent RLC network where a capacitor with a negative dielectric function acts as the inductor and can resonate with another capacitor, with a positive dielectric function.

The resonant angular frequency can be determined from the Maxwell-Garnett theory by selecting the wavelength associated with the peak effective permittivity.

$$\omega_0 = 2\pi\left(\frac{c}{\lambda\left(\varepsilon_{eff,peak}\right)}\right) \tag{4.3.6}$$

Rearranging $\omega_0 = 1/\sqrt{LC}$ will give rise to the capacitance value.

$$C = \frac{1}{\omega_0^2\, L} \tag{4.3.7}$$

The resistance can be established from $\lambda_{BW}$ and inductance, where the bandwidth is approximately the bandwidth when $Im[\varepsilon_{eff}] \approx 1$.

$$R = 2\pi L\left(\frac{c}{\lambda_{BW}}\right) \tag{4.3.8}$$

The transmission of the equivalent circuit model matches the description of the generated output magnitude (Eq.4.3.9) and can also provide a description of the phase (Eq.4.3.10).

$$H(i\omega) = \left| \frac{\left(\frac{1}{LC}\right) - \omega^2}{\sqrt{\left(\left(\frac{1}{LC}\right) - \omega^2\right)^2 + \left(\frac{\omega R}{L}\right)^2}} \right| \tag{4.3.9}$$

$$Phase\ \theta(i\omega) = -\tan^{-1}\left(\frac{\left(\frac{\omega R}{L}\right)}{\left(\frac{1}{LC}\right) - \omega^2}\right)\left(\frac{180}{\pi}\right) \tag{4.3.10}$$

An example of the transmission and phase can be found in figure 4.9. An equivalent model has been established from a metafilm containing silver nanoparticles of 20 nm diameter, surrounded in a dielectric medium with a fixed refractive index of 2.11. The silver nanoparticles permittivity has been defined through the Drude equation, with discussed parameters found in *Chapter II.*

**Table 4.4.** The values for the example equivalent circuit approximation.

| | Value |
|---|---|
| Resistance | 0.7384 Ω |
| Inductance | 1.4102e-15 H |
| Capacitance ($\boldsymbol{\lambda_{max}}$) | 5.3760e-17 F |
| Q Factor | 6.9 |

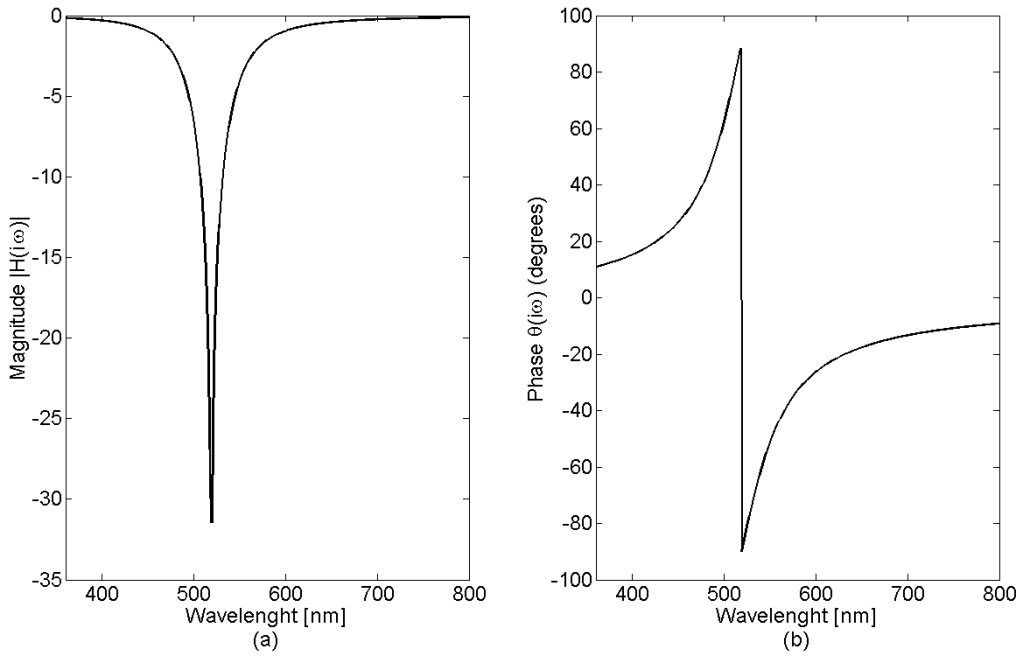


**Figure 4.9.** RLC network equivalent circuit for meta-atom with Silver nanoparticle with radius of 20 nm surrounded a medium (n = 2.11) with particle fill fraction of 12.86%. (a) Magnitude plot in dBs. (b) Phase plot in degrees.

The set of well-defined equations provides a simplistic idea for the behaviour of the associated metafilm by establishing an equivalent model approximation. This provides the user with a quick and flexible method for the dynamic study of key parameters within the metafilm before the design of an entire multi-layered filter.

## 4.4 **Thin Film Analysis**

Describing and analysing thin films at a single interface can easily be obtained through Fresnel's equation [21]. However, when considering multiple interfaces, a more robust method is required. Fundamentally, this can be computed by application of a matrix method [22]. This methodology is evaluated because it is a very common approach in the design and analysis of thin film coatings.

### 4.4.1 **Transfer Matrix Method**

The transfer matrix method (TMM) is a system often used within optics, particularly to analyse electromagnetic waves through a stratified medium. The method goes beyond Fresnel's equations and describes the partial transmission, reflection and absorption resulting from multiple interfaces [23]. The TMM uses Maxwell's equations in a one dimensional form and takes advantage of the continuity conditions across two boundaries. Simplistically, if the field

is known at the start of a layer, then the field can be derived for the end of layer through a matrix operation.

The transfer matrix method provides the model for many industry standard optic thin film software tools, including Essential Macleod [24]; which has been used throughout this chapter to compare the effective medium model against the full wave model. Furthermore, the development of an in-house metamaterial software, "Optical Meta-Analysis", utilises a TMM model to solve for thin film and metafilm devices. *The in-house software was developed by the author to combine the theories presented in this thesis (Appendix A).* The following sub-section highlights the methodology behind the transfer matrix method.

The opening assumption accepts a linear, homogeneous isotropic material.

$$\frac{\partial E_z}{\partial y} - \frac{\partial E_y}{\partial z} = k_0 \mu_r H_x, \quad \frac{\partial E_x}{\partial z} - \frac{\partial E_Z}{\partial x} = k_0 \mu_r H_y, \quad \frac{\partial E_y}{\partial x} - \frac{\partial E_x}{\partial y} = k_0 \mu_r H_z \quad \text{(4.4.1a,b,c)}$$

$$\frac{\partial H_z}{\partial y} - \frac{\partial H_y}{\partial z} = k_0 \varepsilon_r E_x, \quad \frac{\partial H_x}{\partial z} - \frac{\partial H_z}{\partial x} = k_0 \varepsilon_r E_y, \quad \frac{\partial H_y}{\partial x} - \frac{\partial H_x}{\partial y} = k_0 \varepsilon_r E_z \quad \text{(4.4.1d,e,f)}$$

A wave propagating in a homogenous layer can be represented by a plane wave with the following mathematical form, expressing the three different vector components, with $k$ being the wavevector and $r$ being the position of the wave.

$$E(r) = E_0 e^{-ik \cdot r} = E_0 e^{-ik_x x} e^{-ik_y y} e^{-ik_z z} \quad (4.4.2)$$

$$H(r) = H_0 e^{-ik \cdot r} = H_0 e^{-ik_x x} e^{-ik_y y} e^{-ik_z z} \quad (4.4.3)$$

To achieve a one-dimensional form, the derivatives need to be applied to (Eq.4.4.2) and (Eq.4.4.3) for the *x*- and *y*- directions.

$$\begin{aligned} \frac{\partial}{\partial x} E(r) &= \frac{\partial}{\partial x} \left( E_0 e^{-ik_x x} e^{-ik_y y} e^{-ik_z z} \right) \\ &= ik_x E_0 e^{-ik_x x} e^{-ik_y y} e^{-ik_z z} = ik_x E(r) \\ &\rightarrow \frac{\partial}{\partial x} = ik_x \end{aligned} \quad (4.4.4)$$

Note the same is true in the *y*- direction, thus $\partial/\partial y = ik_y$, however, it does not hold true for the *z*- direction, $\partial/\partial z \neq ik_z$, because the structure is not homogenous in the z-direction due to the interfaces of the thin film.

Utilising the derivatives of $\partial/\partial x = ik_x$ and $\partial/\partial y = ik_y$ for Maxwell's equations provides the following mathematical form which enables the removal of the *x* and *y* parameters, allowing

the $z$ parameter to be the only independent variable. This permits the derivatives to become ordinary, excluding any partial derivatives from the equations. Maxwell's equations now describe a one-dimensional system where the assumption of infinite extension to the *x*- and *y*-directions has been made. Additionally, the equations have been normalised by the free space wavenumber (i.e. $z' = k_0 z$, $\tilde{k}_x = k_x/k_0$, $\tilde{k}_y = k_y/k_0$ and $\tilde{k}_z = k_z/k_0$).

$$i\tilde{k}_y E_z - \frac{dE_y}{dz'} = \mu_r H_x \qquad i\tilde{k}_y H_z - \frac{dH_y}{dz'} = \varepsilon_r E_x \qquad (4.4.5a,d)$$

$$\frac{dE_x}{dz'} - i\tilde{k}_x E_z = \mu_r H_y \qquad \frac{dH_x}{dz'} - i\tilde{k}_x H_z = \varepsilon_r E_{y,} \qquad (4.4.5b,e)$$

$$i\tilde{k}_x E_z - i\tilde{k}_y E_z = \mu_r H_z \qquad i\tilde{k}_x H_z - i\tilde{k}_y H_z = \varepsilon_r E_z \qquad (4.4.5c,f)$$

Solving for the longitudinal field components $E_z$ and $H_z$, (Eq. 4.4.5c) and (Eq. 4.4.5f) can be replaced by the following:

$$H_z = \frac{i}{\mu_r}\left(\tilde{k}_x E_z - \tilde{k}_y E_z\right) \qquad (4.4.6)$$

$$E_z = \frac{i}{\varepsilon_r}\left(\tilde{k}_x H_z - \tilde{k}_y H_z\right) \qquad (4.4.7)$$

With the longitudinal field components established, they can be substituted back into (Eq.4.4.5a,b,d,e) to eliminate the $E_z$ and $H_z$ components to give the following forms.

$$\tilde{k}_y^2 H_x - \tilde{k}_x \tilde{k}_y H_y - \varepsilon_r \frac{dE_y}{dz'} = \varepsilon_r \mu_r H_x \qquad (4.4.8a)$$

$$\varepsilon_r \frac{dE_x}{dz'} + \tilde{k}_x^2 H_y - \tilde{k}_x \tilde{k}_y H_x = \varepsilon_r \mu_r H_y \qquad (4.4.8b)$$

$$\tilde{k}_y^2 E_x - \tilde{k}_x \tilde{k}_y E_y - \mu_r \frac{dH_y}{dz'} = \varepsilon_r \mu_r E_x \qquad (4.4.8c)$$

$$\mu_r \frac{dH_x}{dz'} + \tilde{k}_x^2 E_y - \tilde{k}_x \tilde{k}_y E_x = \varepsilon_r \mu_r E_y \qquad (4.4.8d)$$

Simply rearranging the above equations to give the derivatives equal to additional terms provides the basic matrix form for the TMM method.

$$\frac{d}{dz'}\begin{bmatrix}E_x\\E_y\\H_x\\H_y\end{bmatrix}=\begin{bmatrix}0 & 0 & \frac{\tilde{k}_x\tilde{k}_y}{\varepsilon_r} & \mu_r-\frac{\tilde{k}_x^2}{\varepsilon_r}\\ 0 & 0 & \frac{\tilde{k}_y^2}{\varepsilon_r}-\mu_r & \frac{\tilde{k}_x\tilde{k}_y}{\varepsilon_r}\\ \frac{\tilde{k}_x\tilde{k}_y}{\mu_r} & \varepsilon_r-\frac{\tilde{k}_x^2}{\mu_r} & 0 & 0\\ \frac{\tilde{k}_y^2}{\mu_r}-\varepsilon_r & \frac{\tilde{k}_x\tilde{k}_y}{\mu_r} & 0 & 0\end{bmatrix}\begin{bmatrix}E_x\\E_y\\H_x\\H_y\end{bmatrix} \tag{4.4.9}$$

The matrix can be rewritten as a matrix differential equation in the form of:

$$\frac{d\psi}{dz'}-\Omega\psi=0 \tag{4.4.10}$$

Due to the fact that the matrix equation is a set of four coupled differential equations, the solution of the four fields as a function of *z* is an exponential.

$$\psi(z')=e^{\Omega z'}\psi \tag{4.4.11}$$

The matrix exponential can be evaluated through the eigenvalues and eigenvectors of the matrix $\Omega$. This can be achieved by utilising the eigendecomposition of the matrix.

$$e^{\Omega z'}=We^{\gamma z'}W^{-1} \tag{4.4.12}$$

Where $W$ is the eigenvector matrix and $\gamma$ is the eigenvalue matrix.

Thus, the final solution for the matrix differential equation is as follows.

$$\frac{d\psi}{dz'}-\Omega\psi=0\ \rightarrow\ \psi(z')=We^{\gamma z'}c \tag{4.4.13}$$

With $c=W^{-1}\psi$ in order to give a product of a single column vector. The solution is broken down so that $\psi$ is the overall field solutions, $W$ describes the modes that exist in the materials, $e^{\gamma z'}$ describes the propagation of the modes and $c$ contains the amplitude of the modes.

The problem of inherent instability arises with this method due to the method which treats all waves as if they are forward propagating. Thus, decaying fields associated with backwards waves become exponentially increasing fields, leading to the unstable solutions. The resolution for this is to distinguish between the forward and backwards waves and treat them individually. The simple way of distinguishing this is by observing the positives and negatives within the eigenvalue matrix. Rearranging and grouping the eigenvector and eigenvalue matrices will allow for the separation of the forward and backwards propagation.

$$W' = \begin{bmatrix} W_E^+ & W_E^- \\ W_H^+ & W_H^- \end{bmatrix} \tag{4.4.14}$$

$$e^{\gamma z'} = \begin{bmatrix} e^{\gamma^+ z'} & 0 \\ 0 & e^{\gamma^- z'} \end{bmatrix} \tag{4.4.15}$$

Thus, the new solution can be formulated.

$$\psi(z') = \begin{bmatrix} W_E^+ & W_E^- \\ W_H^+ & W_H^- \end{bmatrix} \begin{bmatrix} e^{\gamma^+ z'} & 0 \\ 0 & e^{\gamma^- z'} \end{bmatrix} \begin{bmatrix} c^+ \\ c^- \end{bmatrix} \tag{4.4.16}$$

Now that the propagating waves have been defined for a given layer with *z* thickness, the transmission, reflection and absorption can be derived. However, deriving the outputs becomes problematic with its current form and only makes sense to use when considering anisotropic materials. Therefore separating (Eq.4.4.9) matrix into two, *2x2* matrices so that the electric and magnetic components are separate results in the established PQ form [25,26].

$$\frac{d}{dz'} \begin{bmatrix} E_x \\ E_y \end{bmatrix} = P \begin{bmatrix} H_x \\ H_y \end{bmatrix} \tag{4.4.17}$$

$$\frac{d}{dz'} \begin{bmatrix} H_x \\ H_y \end{bmatrix} = Q \begin{bmatrix} E_x \\ E_y \end{bmatrix} \tag{4.4.18}$$

Where;

$$P = \frac{1}{\varepsilon_r} \begin{bmatrix} \tilde{k}_x \tilde{k}_y & \varepsilon_r \mu_r - \tilde{k}_x^2 \\ \tilde{k}_y^2 - \varepsilon_r \mu_r & -\tilde{k}_x \tilde{k}_y \end{bmatrix} \tag{4.4.19}$$

and

$$Q = \frac{1}{\mu_r} \begin{bmatrix} \tilde{k}_x \tilde{k}_y & \varepsilon_r \mu_r - \tilde{k}_x^2 \\ \tilde{k}_y^2 - \varepsilon_r \mu_r & -\tilde{k}_x \tilde{k}_y \end{bmatrix} \tag{4.4.20}$$

By taking the derivative of (Eq.4.4.17) and substituting into (Eq.4.4.18), the definition of the wave equation can be concluded in terms of the electric field.

$$\frac{d^2}{dz'^2} \begin{bmatrix} E_x \\ E_y \end{bmatrix} = \Omega^2 \begin{bmatrix} E_x \\ E_y \end{bmatrix} \tag{4.4.21}$$

Presenting a dispersion relation with normalised wave vectors ($\varepsilon_r\mu_r = \tilde{k}_x^2 + \tilde{k}_y^2 + \tilde{k}_z^2$):

$$\begin{aligned}\Omega^2 &= PQ \\ &= \frac{1}{\varepsilon_r\mu_r}\begin{bmatrix} \tilde{k}_x\tilde{k}_y & \varepsilon_r\mu_r - \tilde{k}_x^2 \\ \tilde{k}_y^2 - \varepsilon_r\mu_r & -\tilde{k}_x\tilde{k}_y \end{bmatrix}\begin{bmatrix} \tilde{k}_x\tilde{k}_y & \varepsilon_r\mu_r - \tilde{k}_x^2 \\ \tilde{k}_y^2 - \varepsilon_r\mu_r & -\tilde{k}_x\tilde{k}_y \end{bmatrix} \\ &= \begin{bmatrix} -\tilde{k}_z^2 & 0 \\ 0 & -\tilde{k}_z^2 \end{bmatrix} = -\tilde{k}_z^2 I\end{aligned} \tag{4.4.22}$$

With $I$ equalling the identity matrix. Due to the linear, homogeneous, isotropic material assumed, $\Omega^2$ produces a diagonal matrix, which indicates that the eigenvector matrix will always be equal to the identity matrix. With $\gamma^2 = \Omega^2$ :

$$\gamma = \begin{bmatrix} i\tilde{k}_z & 0 \\ 0 & i\tilde{k}_z \end{bmatrix} = i\tilde{k}_z I \rightarrow e^{\gamma z'} = \begin{bmatrix} e^{i\tilde{k}_z z'} & 0 \\ 0 & e^{i\tilde{k}_z z'} \end{bmatrix} \tag{4.4.23}$$

The second-order differential equation requires no 'mode sorting', as previously discussed because the general solution (Eq.4.4.25) describes modes that only travel in one direction, therefore the solution is written twice to explicitly cater for the forward and backwards waves.

$$E(z) = E^+ e^{-ik_z} + E^- e^{ik_z} \tag{4.4.24}$$

The general solution to include the magnetic field can also be derived with the propagation distance of $L$ and $\eta$ equalling the optical admittance.

$$\begin{aligned}E(z+L) = \frac{1}{2}[E(z) + \eta H(z)]e^{-ik_z L} \\ + \frac{1}{2}[E(z) - \eta H(z)]e^{ik_z L}\end{aligned} \tag{4.4.25}$$

To summarise the contribution of the general solution into a common T-matrix, the generalisation of the complex exponentials to gives tangential components of the fields + and – at the extremes of the multilayers to define the interference matrix for both polarisations in the following form.

$$\begin{bmatrix} E(z+L) \\ H(z+L) \end{bmatrix} = \begin{bmatrix} \cos k_z L & \dfrac{i\sin k_z L}{\eta} \\ i\eta \sin k_z L & \cos k_z L \end{bmatrix}\begin{bmatrix} E(z) \\ H(z) \end{bmatrix} \equiv M_j \begin{bmatrix} E(z) \\ H(z) \end{bmatrix} \tag{4.4.26}$$

Through normalising the electric and magnetic fields, (Eq.4.4.26) can be rewritten into the following form, where B and C are the electric and magnetic fields at the front interface, respectively.

$$\begin{bmatrix} B \\ C \end{bmatrix} = \left\{ \prod_{j=1}^{N} \begin{bmatrix} \cos k_z L & \frac{i \sin k_z L}{\eta_j} \\ i\eta_j \sin k_z L & \cos k_z L \end{bmatrix} \right\} \begin{bmatrix} 1 \\ \eta_m \end{bmatrix} \tag{4.4.27}$$

For a device with $N$ layers, each layer of $j$ has a transfer matrix $M_j$, where $j$ increases in thickness towards higher $z$ thickness values.

$$M_{Total} = M_1 \cdot M_2 \cdot \cdots \cdot M_N \tag{4.4.28}$$

### 4.4.2 **Thin Film Transmission, Reflection and Absorption**

Sufficient information can be concluded from (Eq.4.4.27) to allow for the transmission, reflection and absorption of a given thin film assembly to be calculated.

To establish a given thin film's optical performance, consideration is given to the input and output intensities. The net intensity describes the intensity at the exit side of the thin film assembly, which is taken at the $K^{th}$ interface. With the intensity normal to the interface, the output intensity is given by:

$$I_K = \frac{1}{2} Re(\eta_s)(E_K H_K^*) \tag{4.4.29}$$

Providing the characteristic matrix of the assembly:

$$\begin{bmatrix} B \\ C \end{bmatrix} \tag{4.4.30}$$

Thus, the net intensity at the entrance of the thin film assembly is;

$$I_i = \frac{Re(BC^*)(E_K H_K^*)}{2(1-R)} \tag{4.4.31}$$

The transmission ($T$) can be defined by the net intensity leaving and entering the assembly.

$$T = \frac{I_K}{I_i} = \frac{Re(\eta_s)(1-R)}{Re(BC^*)} \tag{4.4.32}$$

The absorption ($A$) is a related to the transmission and the reflection ($R$).

$$A = 1 - R - T = (1-R)\left(1 - \frac{Re(\eta_s)}{Re(BC^*)}\right) \tag{4.4.33}$$

In the absence of any absorption, $1 = T + R$.

Manipulation of (Eq.4.4.32) and (Eq.4.4.33) provides a more manageable form.

$$R = \left(\frac{\eta_0 B - C}{\eta_0 B + C}\right)\left(\frac{\eta_0 B - C}{\eta_0 B + C}\right)^* \tag{4.4.34}$$

Substituting (Eq.4.4.34) back into (Eq4.4.32).

$$T = \frac{4\eta_0 Re(\eta_s)}{(\eta_0 B + C)(\eta_0 B + C)^*} \tag{4.4.35}$$

Followed by substituting (Eq.4.4.34) and (Eq4.4.35) into (Eq.4.4.36).

$$A = \frac{4\eta_0 Re(BC^* - \eta_s)}{(\eta_0 B + C)(\eta_0 B + C)^*} \tag{4.4.36}$$

The final forms for the transmission $T$, reflection $R$ and absorption $A$ are the most useful expressions for a given thin film assembly.

## 4.5 **Effective Optical Thin Film Equivalent Model**

The distinct behaviour of the metafilm allows for the reduction of layers compared to a traditional Rugate filter. The metafilm structure can be designed around the principles of a stepped index anti-reflection coating, where one or more dielectric layers that make up the AR coating, depending on the configuration complexity, can be replaced by a metafilm. The ability to actively describe a metafilm in terms of an equivalent model enables an easy design route using techniques that have already been established by thin film optical design engineers.

Utilising the methodology for anti-reflection coatings to design an entire metamaterial construction is a sensible choice as it enables an overall high transmission output, allowing the blocking component to only take place at the plasmonic resonant wavelengths.

This subsection analyses the effectiveness of using an effective medium to design the metamaterial layer as a homogenous dispersive complex refractive index layer and compares that effectiveness against a “full” metamaterial model. The advantage of this limits the use of a full-wave simulator to design complete models and takes advantage of traditional thin film industry standard software that utilise TMM, so that this technique can be easily integrated into industry for the design of a metamaterial bandstop filter.

The following examples show the behavioural difference between;

1. Full metamaterial model – Full wave simulator, CST Studios. [Figure 4.11, 4.13, 4.14. a,d,g].
2. Metafilm model (*Maxwell-Garnett Theory (MGT)*) – Full wave simulator, CST Studios. [Figure 4.11, 4.13, 4.14. b,e,h].
3. Metafilm model (*Effective Drude-Lorentz Model*) – Thin Film Center, Essential Macleod. [Figure 4.11, 4.13, 4.14. c,f,i].

### 4.5.1 **Single Layer Metafilm Coatings**

The simplest coating design is a single layer. With the incident medium of air and a coating film with a refractive index lower than the index of the substrate, the reflection coefficient at each interface will be negative, allowing the wave to experience a 180° ($\pi\ radians$) phase change. This results in a good degree of destructive interference between the waves of both the interfaces (thin film layer and glass substrate). The reduction of reflections naturally increases the transmission when $n_{substrate} > n_{coating}$ which, as previously stated, requires a phase difference of $\pi$ or odd multiples of $\pi$, $m\pi$.

The design of a single layered metafilm can be established providing that the surrounding medium has a low refractive index. The presence of high index will introduce unwelcomed reflections due to the out of phase reflected waves from each interface.

$$R = \left(\frac{n_0 - (n_1^2/n_{sub})}{n_0 + (n_1^2/n_{sub})}\right)^2 \tag{4.5.1}$$

Where $R$ is the reflection amplitude, $n_0$ is the refractive index of air, $n_1$ is the average refractive index of the metafilm and $n_{sub}$ is the refractive index of the substrate.

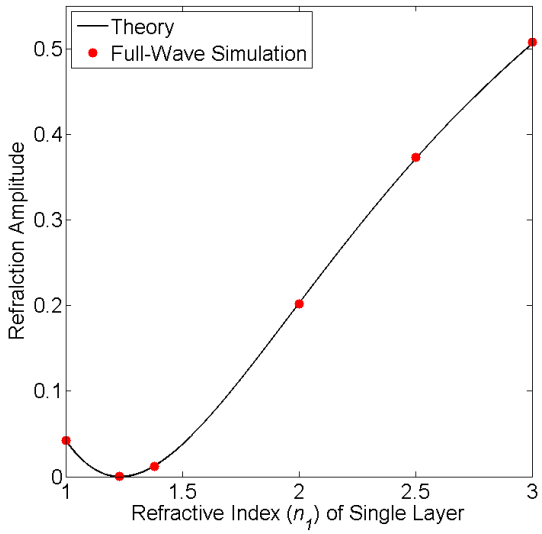


**Figure 4.10.** Reflection produced from varying index of single layer on glass substrate, $n_{sub} = 1.52$.

The conditions for a perfect single layer, i.e zero reflections, is given when the surrounding medium for the metafilm is $n_1 = (n_0 n_{sub})^{1/2}$. For a glass substrate with a refractive index of 1.52, the perfect single layer index is required to be 1.23. However, this presents a slight issue, the lowest useful film of low index obtained is magnesium fluoride with a refractive index ~1.38 [27]. Whilst not perfect, is does provide a practical solution, with a ~1.3% reflectance given at each surface.

The thickness of the metafilm layer is governed by (Eq. 4.5.2).

$$\left(\frac{2\pi n_1}{\lambda_0}\right) 2d = m\pi \qquad \text{or} \qquad d = m\left(\frac{\lambda_0}{4n_1}\right) \tag{4.5.2}$$

Where $d$ is the thickness of the metafilm, $\lambda_0$ is the reference wavelength, usually a fraction of the resonant wavelength of the metafilm, $n_1$ is the average refractive index of the metafilm and $m$ represents an odd integer to reduce the reflected light by allowing a phase difference. Additionally, by increasing $m$, the metafilm will assume that there is an increase in the number of meta-atoms along the *k*-vector of light due to the increase in volume available.

**Example 1.** Single layer, single notch Metafilm. *Nanoparticle radius of 5 nm with a metafilm volume fill fraction of 0.0168.*

| Air | $MM_{405}$ | Glass |
|---|---|---|
| 1.00 | $1.38_{Ag}$ | 1.52 |

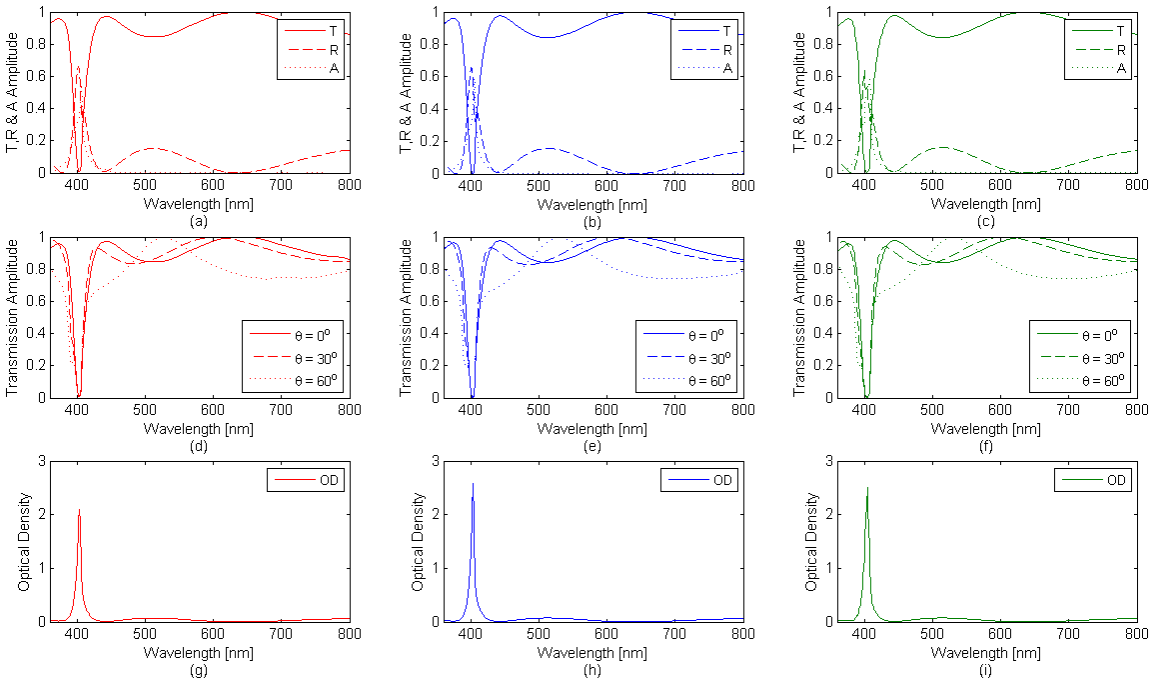


**Figure 4.11.** Single layer metamfilm comparison analysis against full model. (a,b,c) represent the transmission, reflection and absorption amplitude; (d,e,f) represents the transmission at varying angle of incidences; and (g,h,i) represent the optical density; for full metamaterial model (a,d,g), MGT metafilm (b,e,h) and Drude-Lorentz metafilm (c,f,i).

### 4.5.2 **Double Layer Coatings**

Like the single layer design, double and multi layers are able to be designed from the principles of anti-reflection coatings. A single layer metafilm suffers from a lack of high index metafilm options, which is important for establishing a resonance at a higher wavelength; thus, blocking out that resonant wavelength. A high index single metafilm would result in unwelcomed reflections. A method to combat this is to introduce another layer that acts as an anti-reflection coating and matching layer to air.

The design aspect for double layer is governed by the metafilm layer. The blocking wavelength is equal to the resonant wavelength of the metafilm, which in turn can be tailored according to the meta-atom design and surrounding medium. Therefore, the second layer ($n_2$) is chosen depending on the desired blocking wavelength, and the substrate ($n_{sub}$) can be predefined. Hence the first layer can be described by (Eq.4.5.3).

$$n_1 = n_2 \sqrt{\frac{n_0}{n_{sub}}} \tag{4.5.3}$$

Once all refractive indices have been obtained, an analytical solution can be produced to yield the thickness of each layer.

The Schuster diagram [28] for coatings on a glass substrate with index of 1.52 provides the realistic possible solutions that are bound by the lowest possible index, 1.38, and the upper limit index, 2.45.

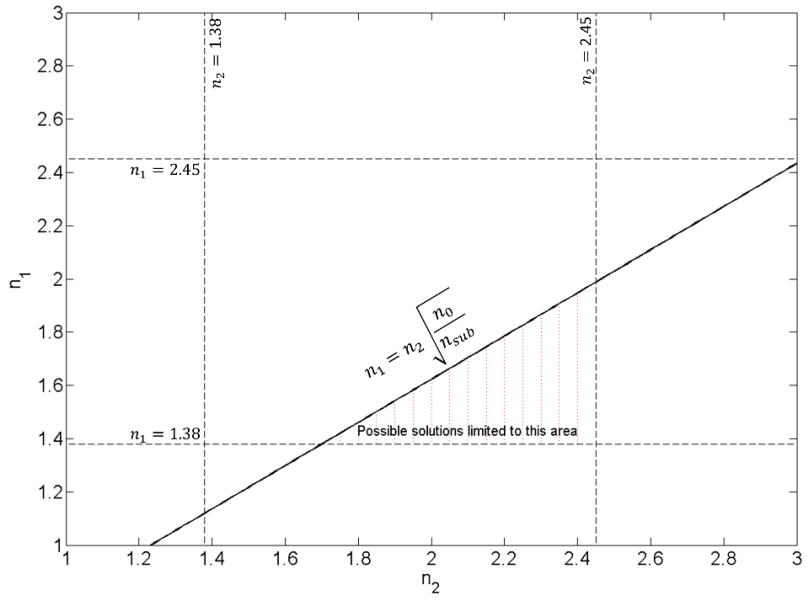


**Figure 4.12.** Schuster diagram for a two-layer coating on glass substrate ($n_{sub} = 1.52$), and incident medium of air.

The presence of a high-index metafilm positioned next to the low-index substrate, make it appear that the substrate has a high index [29]; thus, the subsequent first layers becomes more effective as an antireflection (AR) coating. The thicknesses of the two-layer coating design are formulated from (Eq.4.5.10a and Eq.4.5.10b). These equations can be established using the matrix method and analysis by Catalan [30].

The characteristic matrix for the two-layer coating design to establish coating thickness and assembly can be found in (Eq.4.5.4). For optical frequencies, characteristic admittance, $y_x$, can be replaced with the refractive index.

$$\begin{bmatrix} B \\ C \end{bmatrix} = \begin{bmatrix} \cos\delta_1 & \dfrac{i\sin\delta_1}{n_1} \\ i\,n_1\,\sin\delta_1 & \cos\delta_1 \end{bmatrix} \begin{bmatrix} \cos\delta_2 & \dfrac{i\sin\delta_2}{n_2} \\ i\,n_2\,\sin\delta_2 & \cos\delta_2 \end{bmatrix} \begin{bmatrix} 1 \\ n_{sub} \end{bmatrix} \tag{4.5.4}$$

$$= \begin{bmatrix} \cos\delta_1 \left[\cos\delta_2 + i\left(\dfrac{n_{sub}}{n_2}\right)\sin\delta_2\right] + \dfrac{i\,\sin\delta_1\,(n_{sub}\cos\delta_2 + i\,n_2\sin\delta_2)}{n_1} \\ i\,n_1\sin\delta_1\left[\cos\delta_2 + i\left(\dfrac{n_{sub}}{n_2}\right)\sin\delta_2\right] + \cos\delta_1(n_{sub}\cos\delta_1 + i\,n_2\sin\delta_2) \end{bmatrix}$$

Zero reflection will be obtained if the surface admittance, $Y = C/B$, is equal to admittance of the incident medium, typically air, thus $Y_0 = \sqrt{\varepsilon_0/\mu_0}$.

$$\begin{aligned} i\,n_1\sin\delta_1\left[\cos\delta_2 + i\left(\frac{n_{sub}}{n_2}\right)\sin\delta_2\right] + \cos\delta_1(n_{sub}\cos\delta_1 + i\,n_2\sin\delta_2) \\ = n_0\left(\cos\delta_1\left[\cos\delta_2 + i\left(\frac{n_{sub}}{n_2}\right)\sin\delta_2\right]\ldots \right. \\ \left. + \frac{i\sin\delta_1\,(n_{sub}\cos\delta_2 + i\,n_2\sin\delta_2)}{n_1}\right) \end{aligned} \tag{4.5.5}$$

The real and imaginary components of these expressions must be solved discretely.

$$\begin{aligned} -\left(\frac{n_1 n_{sub}}{n_2}\right)\sin\delta_1\sin\delta_2 + n_{sub}\cos\delta_1\cos\delta_2 \\ = n_0\cos\delta_1\cos\delta_2 - \left(\frac{n_0 n_2}{n_1}\right)\sin\delta_1\sin\delta_2 \end{aligned} \tag{4.5.6}$$

and

$$\begin{aligned} n_1\sin\delta_1\cos\delta_2 + n_2\cos\delta_2\sin\delta_2 \\ = \left(\frac{n_0 n_{sub}}{n_2}\right)\cos\delta_1\sin\delta_2 + \left(\frac{n_0 n_{sub}}{n_1}\right)\sin\delta_1\cos\delta_2 \end{aligned} \tag{4.5.7}$$

Thus, using the appropriate trigonometric identities, $tan(x) = sin(x)/cos(x)$.

$$\tan\delta_1 \tan\delta_2 = \frac{(n_{sub} - n_0)}{\left[\left(\frac{n_1 n_{sub}}{n_2}\right) - \left(\frac{n_0 n_2}{n_1}\right)\right]} = \frac{n_1 n_2 (n_{sub} - n_0)}{(n_1^2 n_{sub} - n_0 n_2^2)} \tag{4.5.8}$$

and

$$\frac{\tan\delta_2}{\tan\delta_1} = \frac{n_2(n_0 n_{sub} - n_1^2)}{n_1(n_2^2 - n_0 n_{sub})} \tag{4.5.9}$$

Therefore, two solutions can be obtained in order to establish the coating thicknesses.

$$\tan^2\delta_1 = \frac{(n_{sub} - n_0)(n_2^2 - n_0 n_{sub})n_1^2}{(n_1^2 n_{sub} - n_0 n_2^2)(n_0 n_{sub} - n_1^2)} \tag{4.5.10a}$$

$$\tan^2\delta_2 = \frac{(n_{sub} - n_0)(n_0 n_{sub} - n_1^2)n_2^2}{(n_1^2 n_{sub} - n_0 n_2^2)(n_2^2 - n_0 n_{sub})} \tag{4.5.10b}$$

Where $\delta$ is a positive real number that satisfies the quarter wavelength relationship and $n$ is the refractive index of the subscripted layer. Two solutions for each $\delta$ value will be produced that must be correctly paired, with the $\delta_1$ component being a relation to the AR coating and the $\delta_2$ component being a relation to the metafilm coating. The selected solution should be selected to minimise the number of odd multiples of quarter wavelengths and to sufficiently host the required number of nanoparticle structured lattice layers. The requirement for a minimum number of odd multiples is for simplicity and practicality.

**Example 2.** Double layer, single notch Metafilm. *Nanoparticle radius of 5 nm with a metafilm volume fill fraction of 0.0177.*

| Air | AR | $MM_{520}$ | Glass |
|---|---|---|---|
| 1.00 | 1.38 | $2.20_{Ag}$ | 1.52 |

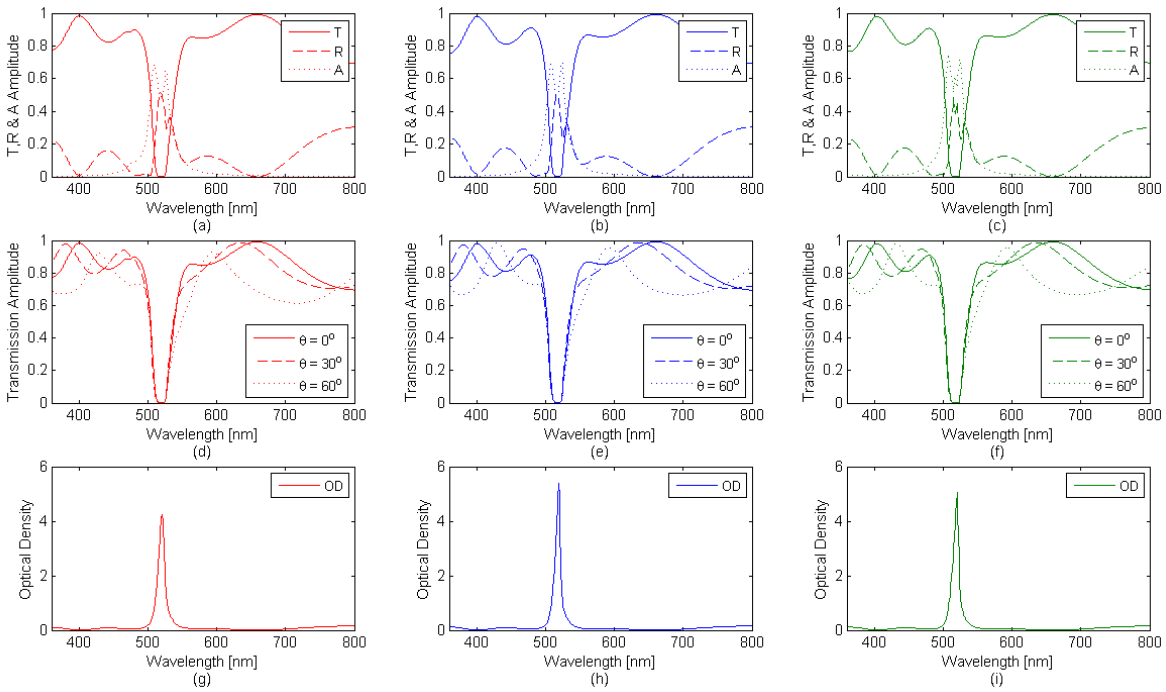


**Figure 4.13.** Double layer metamfilm comparison analysis against full model. (a,b,c) represent the transmission, reflection and absorption amplitude; (d,e,f) represents the transmission at varying angle of incidences; and (g,h,i) represent the optical density; for full metamaterial model (a,d,g), MGT metafilm (b,e,h) and Drude-Lorentz metafilm (c,f,i).

### 4.5.3 **Multilayer Coatings**

There is little functional reason to select a multi-layer coating over a double layer coating for an improved performance with regards to high transmission with a single resonant feature. The fundamental reasoning for the selection of a multi-layer coating is to enable the selection of multiple resonant features. This could employ multiple notch positions and/or enabling near colour neutral filters. The overall transmission and IVPT may fall as a consequence of this though. However, the ability to produce multiple notches within a single filter that can achieve a wide-angle performance requires a fraction of the number of layers compared to conventional multi-notch Rugate filter, which are of hundreds, sometimes thousands, of layers thick.

The design of a multi-layer coating takes advantage of quarter-wave (QW) and half-wave (HW) optical thicknesses, with alternating low-to-high refractive index layers [29]. The addition of a half-wave optical coating next to the substrate allows for an increase in bandwidth of the coating, which is particularly useful when assessing a multi-notch filter approach.

**Example 3.** Multi-layer, triple notch Metafilm. *Nanoparticle radius of 5 nm with a metafilm volume fill fraction of 0.0268.*

| Air | AR | $MM_{512}$ | $MM_{405}$ | $MM_{622}$ | HW | Glass |
|---|---|---|---|---|---|---|
| 1.00 | 1.38 | $2.13_{Ag}$ | $1.38_{Ag}$ | $2.30_{Au}$ | 1.38 | 1.52 |

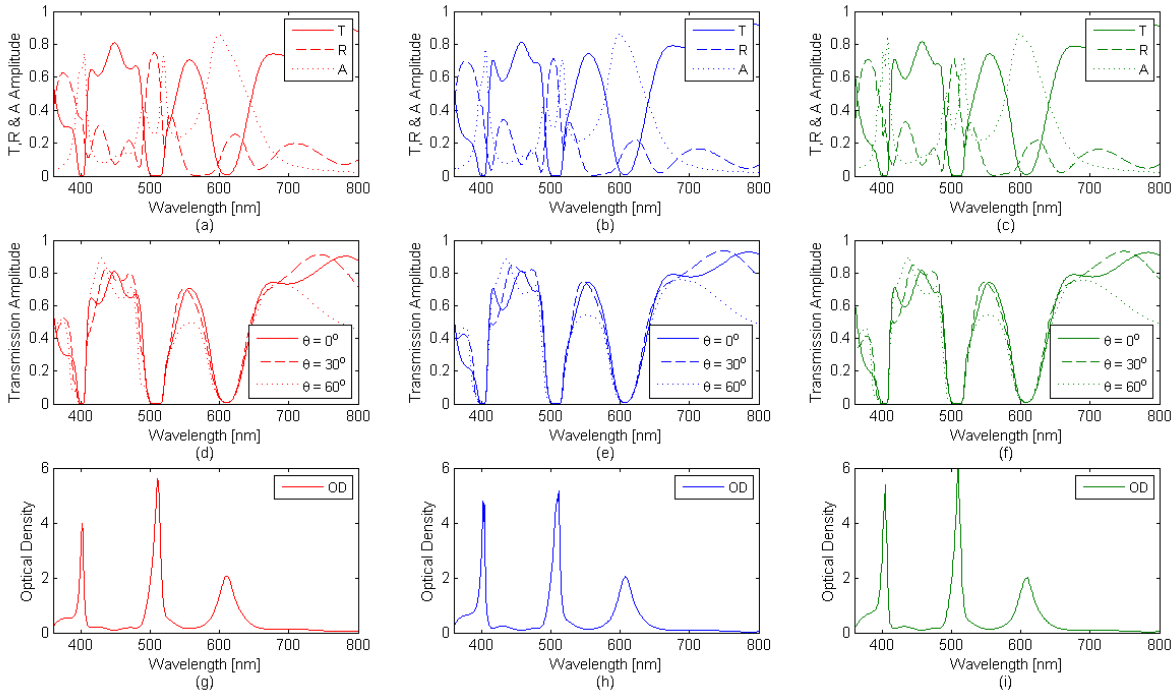


**Figure 4.14.** Multi-layer metamfilm comparison analysis against full model. (a,b,c) represent the transmission, reflection and absorption amplitude; (d,e,f) represents the transmission at varying angle of incidences; and (g,h,i) represent the optical density; for full metamaterial model (a,d,g), MGT metafilm (b,e,h) and Drude-Lorentz metafilm (c,f,i).

## 4.6 **Summary**

This chapter has focused on the design process of establishing a tunable fixed-line metamaterial thin film, namely metafilm. The design method takes advantage of an effective medium model and introduces the effective Drude Lorentz method. The effective Drude Lorentz model permits a metafilm to be described by three independent constants. The metafilm approach enables the creation of designs in quick succession and analysis of the films through either an equivalent circuit model, or a more detailed study using the transfer matrix method (TMM). Details of designing single and multiple layer filters have also been discussed. Furthermore, a comparative study has been investigated, comparing a full metamaterial model, with the well know Maxwell-Garnett approximated metafilm and the newly introduced effective Drude-Lorentz approximated film. The effective Drude Lorentz film was simulated in an industry standard thin film software tool that uses TMM, where the full metamaterial model and the MG approximated film were simulated in a full-wave electromagnetic simulation tool. The major contribution to

using the industry standard software enabled all polarisation states, angles and performance curves to be simulated almost instantaneously, which is extremely valuable for industry practice when designing metamaterials.

## 4.7 **References**


[1] P. Chaturvedi, "Optical Metamaterials: Design, Characterization and Applications", PhD, University of Illinois at Urbana-Champaign, 2009.

[2] W. Cai and V. Shalaev, *Optical metamaterials*. New York, N.Y.: Springer, 2010.

[3] P. Chen, C. Chen, H. Wang, J. Tsai and W. Ni, "Synthesis design of artificial magnetic metamaterials using a genetic algorithm", *Optics Express*, vol. 16, no. 17, p. 12806, 2008. Available: 10.1364/oe.16.012806.

[4] W. Ma, F. Cheng and Y. Liu, "Deep-Learning-Enabled On-Demand Design of Chiral Metamaterials", *ACS Nano*, vol. 12, no. 6, pp. 6326-6334, 2018. Available: 10.1021/acsnano.8b03569.

[5] W. Zhang, K. Cheng, C. Wu, Y. Wang, H. Li and X. Zhang, "Implementing Quantum Search Algorithm with Metamaterials", *Advanced Materials*, vol. 30, no. 1, p. 1703986, 2017. Available: 10.1002/adma.201703986.

[6] B. Slovick, Z. Yu and S. Krishnamurthy, "Generalized effective-medium theory for metamaterials", *Physical Review B*, vol. 89, no. 15, 2014. Available: 10.1103/physrevb.89.155118.

[7] X. Zhang and Y. Wu, "Effective medium theory for anisotropic metamaterials", *Scientific Reports*, vol. 5, no. 1, 2015. Available: 10.1038/srep07892.

[8] V. Markel, "Introduction to the Maxwell Garnett approximation: tutorial", *Journal of the Optical Society of America A*, vol. 33, no. 7, p. 1244, 2016. Available: 10.1364/josaa.33.001244.

[9] O. Zhuromskyy, "Applicability of Effective Medium Approximations to Modelling of Mesocrystal Optical Properties", *Crystals*, vol. 7, no. 1, p. 1, 2016. Available: 10.3390/cryst7010001.

[10] R. Ruppin, "Evaluation of extended Maxwell-Garnett theories", *Optics Communications*, vol. 182, no. 4-6, pp. 273-279, 2000. Available: 10.1016/s0030-4018(00)00825-7.

[11] J. Hannay, "The Clausius-Mossotti equation: an alternative derivation", *European Journal of Physics*, vol. 4, no. 3, pp. 141-143, 1983. Available: 10.1088/0143-0807/4/3/003.

[12] K. Oughstun and N. Cartwright, "On the Lorentz-Lorenz formula and the Lorentz model of dielectric dispersion", *Optics Express*, vol. 11, no. 13, p. 1541, 2003. Available: 10.1364/oe.11.001541.

[13] Skorobogatiy. and Maksim., *Nanostructured and Subwavelength Waveguides*. John Wiley & Sons, 2012.

[14] I. Tsukerman, "Classical and non-classical effective medium theories: New perspectives", *Physics Letters A*, vol. 381, no. 19, pp. 1635-1640, 2017. Available: 10.1016/j.physleta.2017.02.028.

[15] M. Mahmoud, M. Chamanzar, A. Adibi and M. El-Sayed, "Effect of the Dielectric Constant of the Surrounding Medium and the Substrate on the Surface Plasmon Resonance Spectrum and Sensitivity Factors of Highly Symmetric Systems: Silver Nanocubes", *Journal of the American Chemical Society*, vol. 134, no. 14, pp. 6434-6442, 2012. Available: 10.1021/ja300901e.

[16] G. Papadakis, D. Fleischman, A. Davoyan, P. Yeh and H. Atwater, "Optical magnetism in planar metamaterial heterostructures", *Nature Communications*, vol. 9, no. 1, 2018. Available: 10.1038/s41467-017-02589-8.
[17] F. Bilotti, A. Toscano, L. Vegni, K. Aydin, K. Alici and E. Ozbay, "Equivalent-Circuit Models for the Design of Metamaterials Based on Artificial Magnetic Inclusions", *IEEE Transactions on Microwave Theory and Techniques*, vol. 55, no. 12, pp. 2865-2873, 2007. Available: 10.1109/tmtt.2007.909611.
[18] H. Chen, L. Ran, J. Huangfu, T. Grzegorczyk and J. Kong, "Equivalent circuit model for left-handed metamaterials", *Journal of Applied Physics*, vol. 100, no. 2, p. 024915, 2006. Available: 10.1063/1.2219986.
[19] E. Avignon-Meseldzija, T. Lepetit, P. Ferreira and F. Boust, "Negative inductance circuits for metamaterial bandwidth enhancement", *EPJ Applied Metamaterials*, vol. 4, p. 11, 2017. Available: 10.1051/epjam/2017009.
[20] A. Ghadiri and K. Moez, "Wideband Active Inductor and Negative Capacitance for Broadband RF and Microwave Applications", *IEEE Transactions on Components, Packaging and Manufacturing Technology*, vol. 4, no. 11, pp. 1808-1814, 2014. Available: 10.1109/tcpmt.2014.2349523.
[21] H. Weber, "The Fresnel equations for lossy dielectrics and conservation of energy", *Journal of Modern Optics*, vol. 61, no. 15, pp. 1219-1224, 2014. Available: 10.1080/09500340.2014.928375.
[22] S. Byrnes, "Multilayer optical calculations", *arXiv.org*, 2016. [Online]. Available: https://arxiv.org/abs/1603.02720v3.
[23] M. Troparevsky, A. Sabau, A. Lupini and Z. Zhang, "Transfer-matrix formalism for the calculation of optical response in multilayer systems: from coherent to incoherent interference", *Optics Express*, vol. 18, no. 24, p. 24715, 2010. Available: 10.1364/oe.18.024715.
[24] Thin Film Center Inc, *Thinfilmcenter.com*, 2019. [Online]. Available: https://www.thinfilmcenter.com/essential.
[25] Y. Kiyotoshi, *Electromagnetic Theory*. Boca Raton: C R C Press LLC, 2005.
[26] R. Rumpf, "Advanced Computation: Computational Electromagnetics. Lecture 2: Transfer Matrix Method", University of Texas at El Paso, 2019.
[27] X. Zhang et al., "Ordered 3D Thin-Shell Nanolattice Materials with Near-Unity Refractive Indices", *Advanced Functional Materials*, vol. 25, no. 42, pp. 6644-6649, 2015. Available: 10.1002/adfm.201502854.
[28] B. PRIYADARSHINI and A. SHARMA, "Design of multi-layer anti-reflection coating for terrestrial solar panel glass", *Bulletin of Materials Science*, vol. 39, no. 3, pp. 683-689, 2016. Available: 10.1007/s12034-016-1195-x.
[29] H. Macleod, *Thin-Film Optical Filters*, 5th ed. CRC Press, 2017.
[30] L. Catalán, "Some Computed Optical Properties of Antireflection Coatings", *Journal of the Optical Society of America*, vol. 52, no. 4, p. 437, 1962. Available: 10.1364/josa.52.000437.

# CHAPTER V. COMBINING THIN FILM INTERFERENCE STACKS WITH METAFILM COATINGS FOR VISIBLE LASER PROTECTION APPLICATIONS

The chapter introduces an enhanced traditional optical thin film interference filter through the assistance of a plasmonic compound metafilm that was introduced in the previous chapter. The additional optical metamaterial layer enables an optical density boost and improved angular sensitivity compared to the standard traditional thin film filters. This chapter discusses the design principles of optical notch/bandstop filters utilising quarter-wave stacks, followed by the combination filter (*thin film filter + metafilm filter*). The combination filter designs presented are centred on visible laser light wavelengths.

## 5.1 **Thin Film Interference Coatings**

Thin film interference coatings make up several types of filters including antireflection and edge filters. Edge filters are primary characterised by abrupt changes between the region of transmission and reflection. Edge filters can be subdivided into longwave (*high*) pass, shortwave (*low*) pass, bandstop and bandpass filters. Primarily, this thesis concentrates on the bandstop filters, often called notch filters but sometimes termed minus filters [1].

The basic design principles for achieving an optical bandstop filter centres around interchanging dielectric structures of quarter-wave stacks. Quarter-wave stacks, also called Bragg mirrors, consist of alternating sequences of two or more different optical materials, typically dielectric media [2]. The name "quarter-wave" originates from the fact that each given layer within the stack has an optical layer thickness corresponding to a quarter wavelength [3]. This wavelength is often referred to as the reference wavelength where the peak reflection is found. For example, a notch filter with a reference wavelength $\lambda_0$, would provide a standard solution found in figure 5.1. The filter's bandwidth is dependent on the difference between the refractive indices of the alternative dielectric materials that make up the stack.

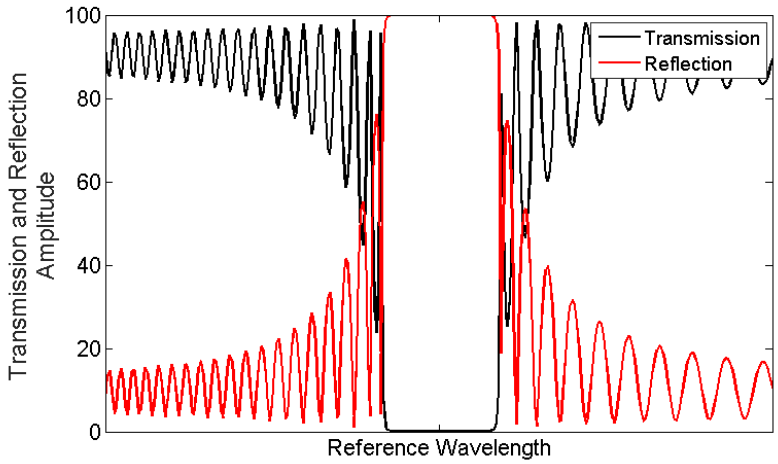


**Figure 5.1.** Example of the transmission and reflection amplitude for a quarter-wave stack consisting of 100 layers with varying refracting index of 1.7 and 2.4.

An intrinsic problem arises with quarter-wave stacks which introduce ripples in the transmitted regions. As the curves in figure 5.1 shows, the ripples can be rather severe. The performance of the filter can be improved with the reduction of ripples [1]. The lessening of the ripples is not always an easy task due to the complexity of the mathematics. In 1952, L. Ivan Epstein published a paper titled "the design of optical filters" [4]. This paper laid the foundations to not only predict the issue of the ripples, but also how to mitigate them. The paper published by Epstein became one the most important publications for optical filters.

Epstein articulated that according to Herpin's theorem [5-7], a symmetrical combination of thin films is equivalent to a single film. A symmetrical combination is defined by each half of the stack being a mirrored copy and often referred to as a symmetrical period. This provides two possible configurations for a symmetric bandstop filter.

$$[LH]^s \text{ and } [HL]^s \tag{5.1.1}$$

Where $L$ denotes the low index material, $H$ represents the high index material and $s$ is the number of pairs which makes up the stack configuration.

A slight improvement to this design, whilst maintaining symmetry, can be made so that the equivalent phase thickness of a symmetrical arrangement is equal, or close to the value, of the total phase thickness. This is achieved by simply adding a pair of eighth-wave layers to the stack at each end.

$$\left[\frac{L}{2}H\frac{L}{2}\right]^s \text{ and } \left[\frac{H}{2}L\frac{H}{2}\right]^s \tag{5.1.2}$$

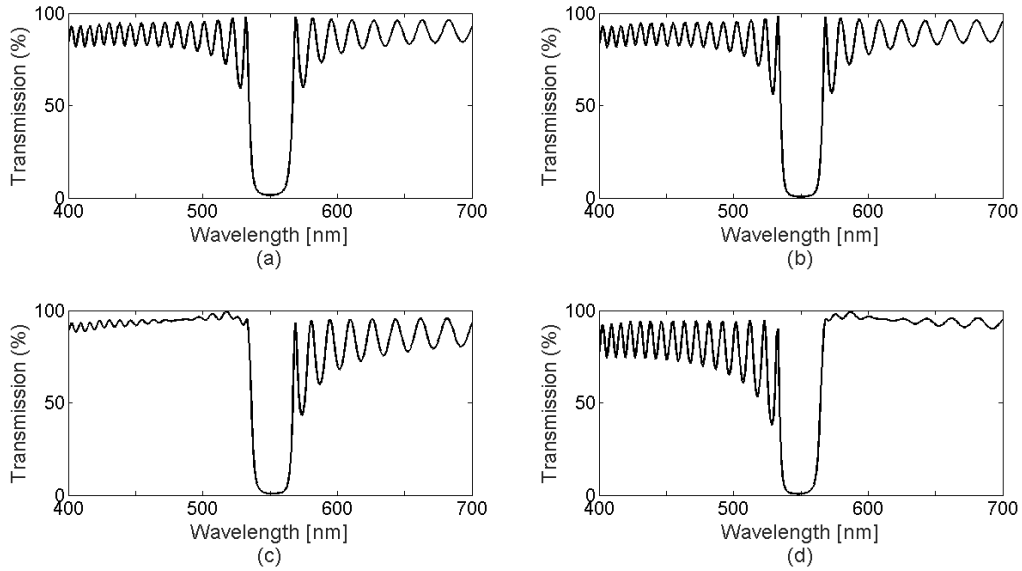


**Figure 5.2.** The transmission of symmetrical periodic stacks with $L = 1.8$ and $H = 1.9$. (a) $Air|[LH]^{40}|Glass$. (b) $Air|[HL]^{40}|Glass$. (c) $Air|\left[\frac{L}{2}H\frac{L}{2}\right]^{40}|Glass$. (d) $Air|\left[\frac{H}{2}L\frac{H}{2}\right]^{40}|Glass$.

Epstein noted that the presence of the ripples was a consequence of a mismatch between the thin film stack and the medium which surrounds it. Thus, a deduction can be made that improving the matching would result in the lessening of the ripples. This could essentially be achieved via antireflection (AR) coatings either side of the stack, one coating to match with air and another to match the substrate. However, the introduction of the antireflection coating is likely to match one side of the zone and unlikely to match the other, resulting in matching layers for bandstop filters becoming very complex.

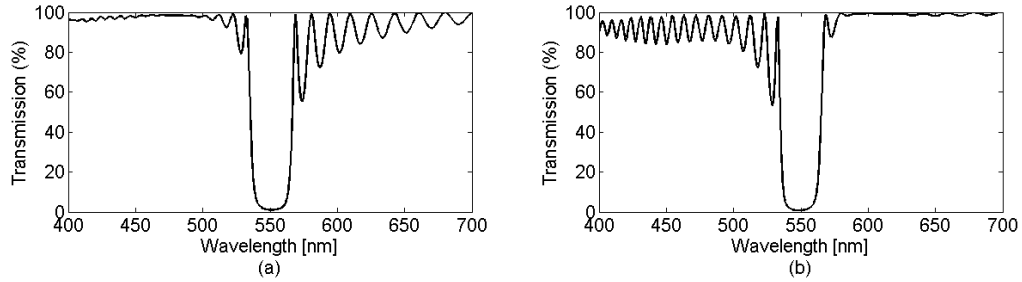


**Figure 5.3.** Matched layers on one side of the zone due to the presence of a wideband antireflection coating. (a) $Air|AR|\left[\frac{L}{2}H\frac{L}{2}\right]^{40}|AR|Glass$. (b) $Air|AR|\left[\frac{H}{2}L\frac{H}{2}\right]^{40}|AR|Glass$.

A method for overcoming the mismatch is to employ a technique of thickness modulation [8]. Thickness modulation is inspired by Rugate filters, discussed in *Chapter II*, which modulate the optical thicknesses instead of the indices of the layers. The key principle for modulation is apodization which involves modulating the layer thickness with a function that is gradually changing: Gaussian, sinusoidal, etc.

Figure 5.4 provides an example for thickness modulated designs. There are many solutions to this depending on the envelope function used. The envelope used in the figure 5.4a uses an amplitude modulation method with the following function.

$$T(L) = T_{avg}[1 + k\sin(2\pi f_1 L_z)\cos(2\pi f L_z)] \quad (5.1.3)$$

Where $T(L)$ is the new modulated thickness for a given layer, $T_{avg}$ is the average quarter-wave thickness of the layers, $k$ is the modulation amplitude, $f_1 = 1/(2\,L_{total})$ is the amplitude modulation frequency, $f$ is the thickness modulation frequency and $L_z$ is the layer number.

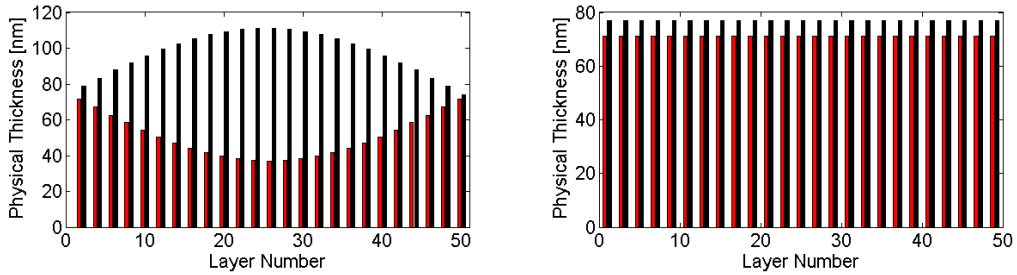


**Figure 5.4.** (a) Thickness modulated design and (b) unmodulated thickness for indices of $L = 1.79$ and $H = 1.93$, at $\lambda_0 = 550nm$. The red bars represent the high index material and the black bars represent the low index material.

Ripples and improving overall transmission are issues that can be fixed with the use of matching -layers and modulation [1]. The intrinsic problems that thin films present is the blue-shifting behaviours due to the incident beam varying with angle [9]. A method to try and combat this issue of angular intolerance is to broaden the bandstop response. This allows the blocking response to still cover a fixed wavelength (figure 5.5). Furthermore, to improve the optical density (OD) of a system, that is to say to improve the degree to which the filter blocks the transmitted light, more layers are needed (figure 5.6). However, the addition of more layers obviously makes the stack thicker, resulting in delamination issues particularly on high mechanically stressed surfaces.

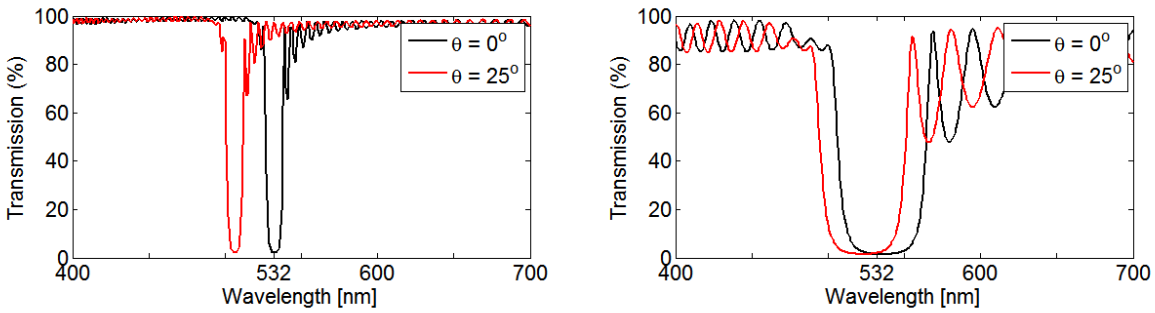


**Figure 5.5.** Blue shifting properties of thin film filters at 532 nm laser wavelength. (a) 80 layers with the indices of L = 1.38 and H = 1.42. (b) 26 layers with the indices of L = 1.78 and H = 2.38.

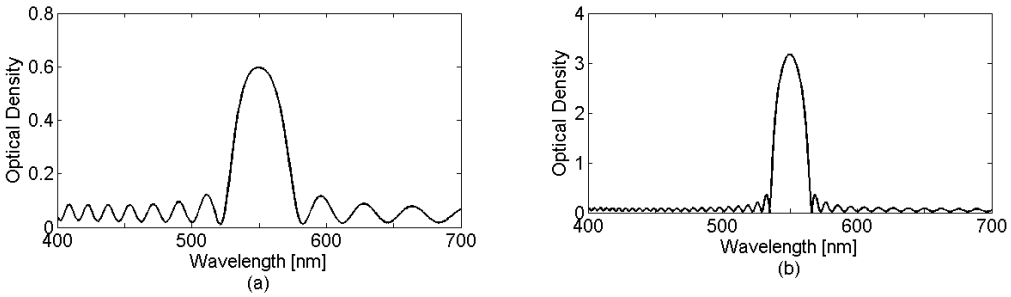


**Figure 5.6.** The optical density of (a) thin film stack consisting of a total of 20 layers and (b) thin film stack consisting of a total of 60 layers, with indices of L = 1.78 and H = 2.38.

A method for aiding angular sensitivity and boosting optical density without the need for tens or hundreds of additional layers could be found with the addition of a single metafilm layer.

## 5.2 **Metafilm Coatings**

As previously discussed, metamaterials are man-made materials that are purposely designed to have key behaviours [10]. They are a complex material made from a periodic arrangement of meta-atoms. The precise shape, geometry, size, orientation and arrangement of the meta-atoms governs the electromagnetic interactions. Metafilm coatings consists of metallic spherical nanoparticles arranged into a two- or three- dimensional hexagonal lattice. The level of dimension depends on the required transmission attenuation. The resonating behaviour of the optical metamaterial provides a sudden change in the refractive index, resulting in an increased extinction coefficient, which enables for fixed line resonance engineering. The metamaterial layer can be treated as a single homogenous material, namely metafilm.

The detailed discussion of metafilms was introduced in the previous chapter, *Chapter IV*. That highlighted the significance of utilising an effective model, namely the "effective Drude Lorentz model", to establish the optical properties for an optical metamaterial coating and implemented optical design principles for bandstop filters.

The designs for the metafilm coatings within this chapter mainly is to enhance the performance of the well-established thin film interference filters. This will be achieved by considering the attenuation and bandwidth of the metafilm, which can be controlled by the dampening frequency (figure 5.7) and the spacing between the plasmonic nanoparticles.

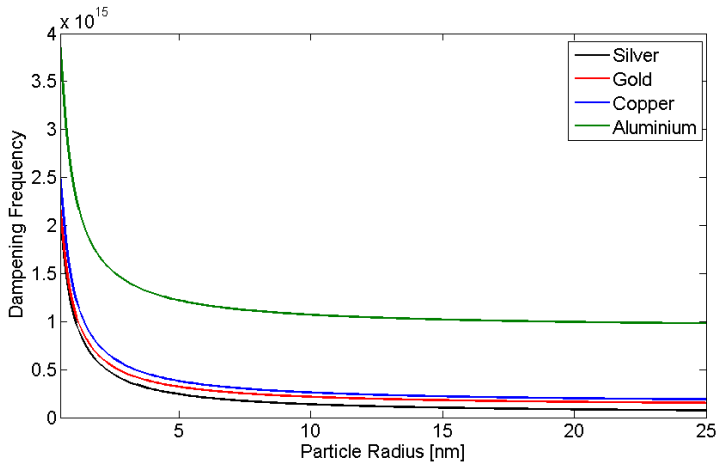


**Figure 5.7.** Dampening frequency changing as a function of particle size.

Utilising the effective Drude Lorentz model, different scenarios can be established in order to achieve the desired requirements for the metafilm. The two main properties of control (*reference wavelength* and *bandwidth*) can be tuned according to the surrounding refractive index, *discussed in chapter III and IV*, and the dampening frequency. As the dampening frequency increases, the permittivity's resonant feature becomes broader, figure 5.8. Additionally, by increasing the dampening frequency, the system also undergoes a reduction in attenuation.

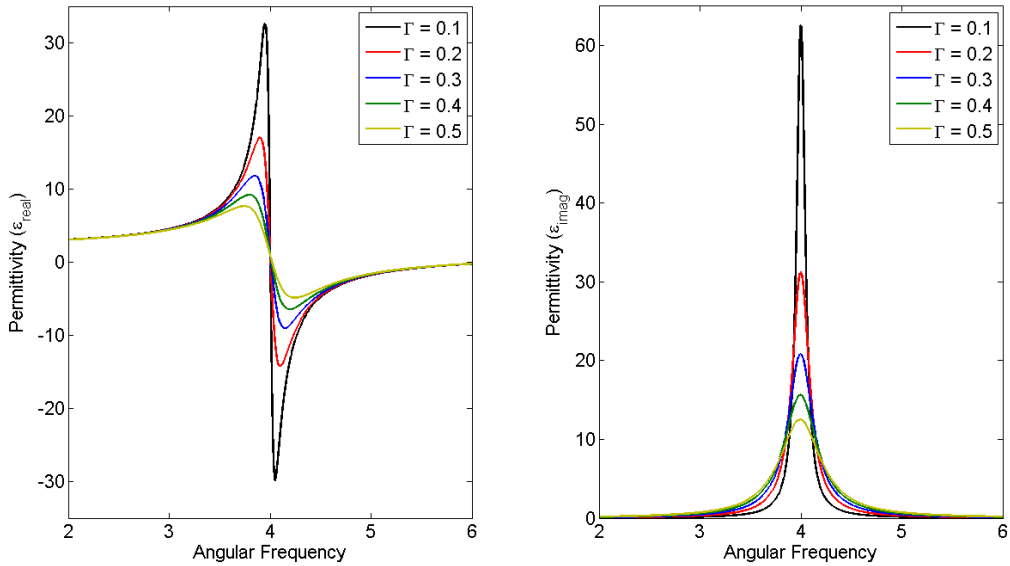


**Figure 5.8.** An example of the effective of dampening frequency on the Drude-Lorentz permittivity.

The design difference of tailoring a response for a narrowband and broadband combination filter will also depend on the metafilm's complex refractive index. Figure 5.9 provides the complex refractive indices used for case 1 and case 2 for the provided combination filter examples. Additionally, adjustments have been made for figure 5.10 for case 3, which provides

an example of a triple notch combination filter. The metamaterial optical properties have been established from the developed inverse design software tool (*Appendix A*).

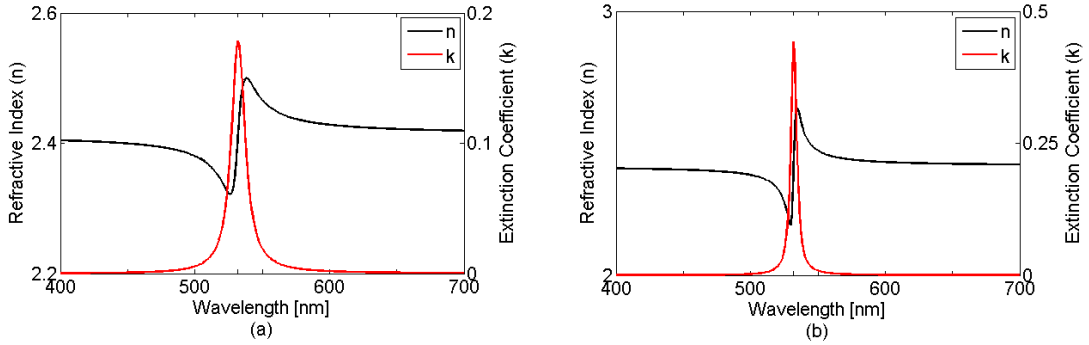


**Figure 5.9.** Refractive index for metafilm (ZnS-AgNPs) with dampening frequency of (a) $\Gamma = 0.08e15\ s^{-1}$ and (b) $\Gamma = 0.032e15\ s^{-1}$.

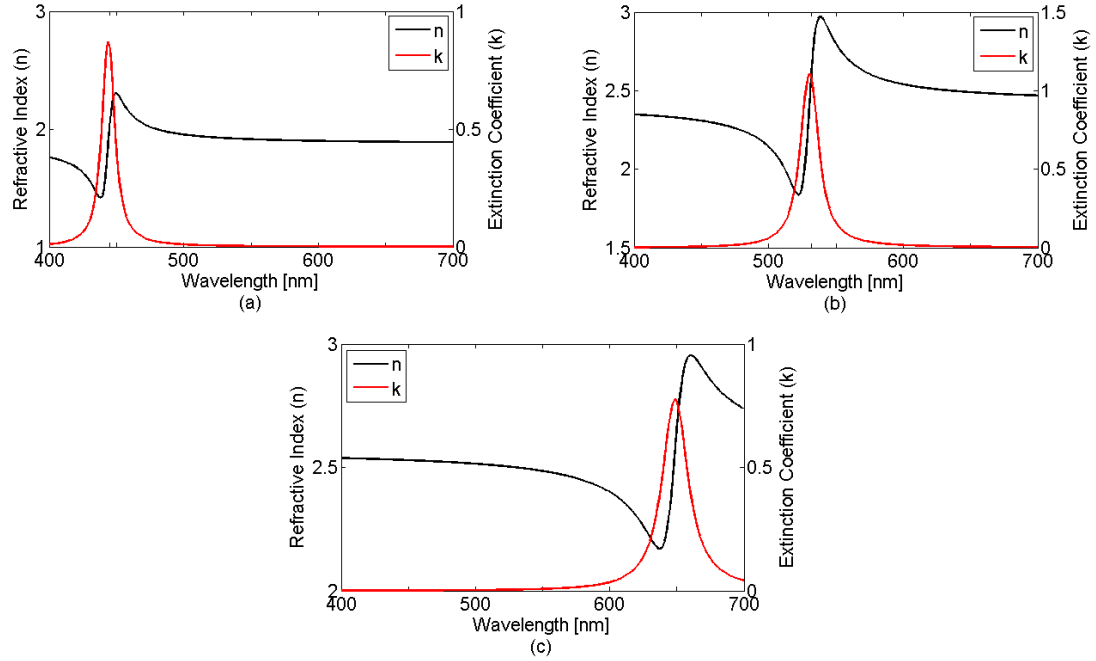


**Figure 5.10.** Refractive index for the three metafilms found in the triple notch combination filter with notch influencing locations at (a) 445 nm, (b) 532 nm and (c) 650 nm.

## 5.3 **Combination Filters**

The combination filter consists of adding a single or multiple metafilms to the standard thin film stack to improve the optical performance of thin films. The addition of this metafilm allows for improved angular sensitivity through the metafilm influencing the stability of the blue-shifting behaviour by keeping the optical density peak central to the reference wavelength until the OD has decreased to match the performance of the thin films' contribution. Furthermore, the metafilm boosts the OD performance of the thin film and provides some protection across

all angles of incidence. Finally, the metafilm also allows for a reduction of stack thickness, for example, a thin film stack may require almost two times additional stack thickness to achieve twice the amount of optical density for a given system, with the presence of the metafilm, that additional stack is no longer required.

For simplicity, unmodulated thin film bandstop filter design will be assessed. The resulting solutions will display ripples within the optical performance due to the lack of modulation. A following modulation example has also been presented to demonstrate a method for diminishing the ripples present.

Figure 5.11 shows the schematic layout for the standard thin film interference filter and the metamaterial enhanced filter, for a single notch solution. The layers conform to the equations (Eq.5.1.1) and (Eq.5.1.2). The notation $N$ ascribes the number of layers between the thin film stacks. The basic construction of low-high interchanging refractive indices has been illustrated with the addition of a matching layer and metafilm layer.

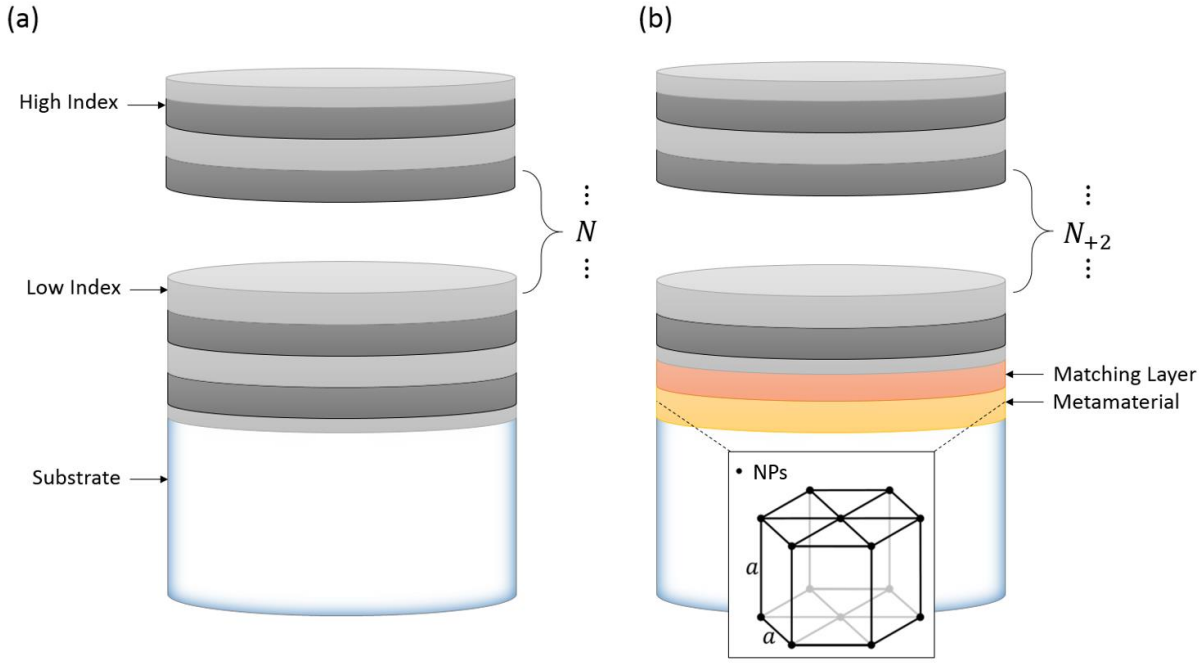


**Figure 5.11.** (a) Standard thin film interference filter design. (b) Metamaterial enhanced thin film interference filter design. Insert shows the hexagonal lattice arrangement of the metallic nanoparticles within the surrounding medium with an equal separation distance.

A non-modulated single notch combination filter can be described by (Eq.5.3.1) and a multi notch combination filter can be described by (Eq.5.3.2). The multi notch describes a triple notch filter. $L$ and $H$ describe the low and high index materials for the thin film stack with $s$ representing the number of pairs, $A$ denotes a matching layer, $M$ defines the metafilm and the

subscribes $a, b, c$ highlight the different metamaterials layers to obtain reference wavelengths at $\lambda a, \lambda b \; and \; \lambda c$.

$$[LH]^s[AM] \tag{5.3.1}$$

$$[[LH]^s[AM]_a]_{\lambda a}[[LH]^s[AM]_b]_{\lambda b}[[LH]^s[AM]_c]_{\lambda c} \tag{5.3.2}$$

The notations ascribed in Table 5.1, highlight the material properties for the designs with reference wavelengths for a single notch at 532 nm and triple notch at 445 nm, 532 nm and 650 nm.

**Table 5.1.** Notation and materials for combination stacks [11].

| Notation | Material | Complex Indices |
|---|---|---|
| **Case 1: Single notch at 532 nm** | | |
| Low (L) | Yttrium Oxide ($Y_2O_3$) | $1.79179 + i0$ |
| High (H) | Hafnium Dioxide ($HfO_2$) | $1.93351 + i0$ |
| Additional Matching Layer (A) | Magnesium Fluoride ($MgF_2$) | $1.38483 + i0$ |
| Metamaterial (M) | Metamaterial (ZnS-AgNPs) | $2.51886 + i1.07581$ |
| **Case 2: Single ultra-thin notch at 532 nm** | | |
| Low (L) | Sodium Hexafluoroaluminate ($Na_3AlF_6$) | $1.35 + i0$ |
| High (H) | Magnesium Fluoride ($MgF_2$) | $1.38483 + i0$ |
| Additional Matching Layer (A) | Magnesium Fluoride ($MgF_2$) | $1.38483 + i0$ |
| Metamaterial (M) | Metamaterial (ZnS-AgNPs) | $2.39112 + i0.44192$ |
| **Case 3: Triple notch at reference wavelengths ($a = 445\ nm, b = 532\ nm, c = 650\ nm$)** | | |
| Low (L) | Yttrium Oxide ($Y_2O_3$) | $1.78811 + i0$ |
| High (H) | Hafnium Dioxide ($HfO_2$) | $1.9291 + i0$ |
| Additional Matching Layer ($A_a$) | Magnesium Fluoride ($MgF_2$) | $1.38772 + i0$ |
| Metamaterial ($M_a$) | Metamaterial ($ZrO_2$-AgNPs) | $2.01966 + i0.8427$ |
| Additional Matching Layer ($A_b$) | Magnesium Fluoride ($MgF_2$) | $1.38483 + i0$ |
| Metamaterial ($M_b$) | Metamaterial (ZnS-AgNPs) | $2.51886 + i1.07581$ |
| Additional Matching Layer ($A_c$) | Magnesium Fluoride ($MgF_2$) | $1.38260 + i0$ |
| Metamaterial ($M_c$) | Metamaterial ($BaTiO_3$-AuNPs) | $2.65212 + i0.7650$ |

**Case 1: Single notch filter at 532nm wavelength**

The standard thin filter design (Eq.5.3.3) for case 1 consists of 61 layers of $Y_2O_3$ and $HfO_2$ on a glass substrate with a refractive index of ~1.52. The overall physical thickness of this filter is 4137.71 nm.

$$L\left[\frac{L}{2}H\frac{L}{2}\right]^{30} \tag{5.3.3}$$

The metamaterial layer consists of silver spherical nanoparticles, ~28 nm in size, surrounded in Zinc Sulphide. The Zinc Sulphide allows the resonance to red shift to ~532 nm. The addition of the metamaterial layer to create the combination filter (Eq.5.3.4) provides an overall physical thickness of the metamaterial enhanced thin film filter of 4370.46 nm, with the thin film stack equalling quarter-wave thickness, the $MgF_2$ layer equating to 99.75 nm thickness and the metamaterial consisting of the remaining 133 nm thickness.

$$L\left[\frac{L}{2}H\frac{L}{2}\right]^{30}[AM] \tag{5.3.4}$$

Figure 5.12 shows the transmission response for case 1 and compares the standard thin film interference filter compared with that of the metamaterial assisted thin film interference filter, both at zero degree of incident light. The ripples found in the transmission response are a consequence of a mismatch between the quarter-wave stack and the sounding media and can be cancelled out with the correct matching layers. It is evident that the metamaterial assisted filter improves the attenuation of the standard filter by accumulating the transmission loss of the metafilm with the transmission loss of the standard thin film contribution. Furthermore, the bandwidth of the standard thin film filter is 31 nm and the metamaterial enhanced filter has a bandwidth of 32 nm.

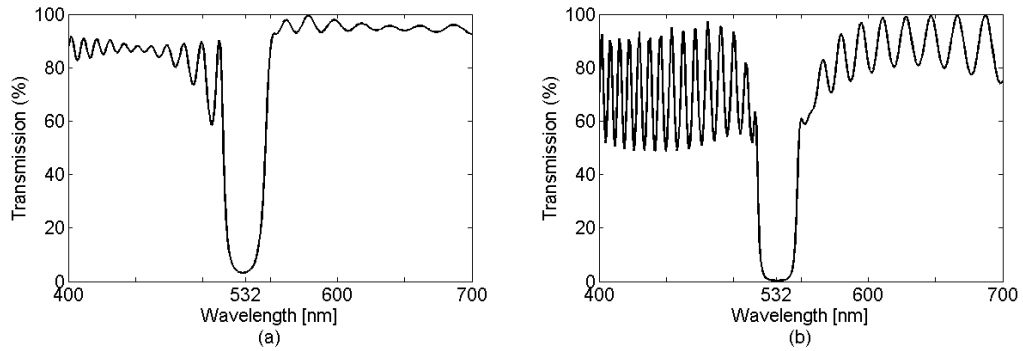


**Figure 5.12.** The transmission responses at normal incident for (a) standard thin film filter and (b) metamaterial enhanced filter.

The true performance measurements of a laser protection filter often lie with the optical density which described the degree at which the filter retards the transmitted light. Figure 5.13 shows the comparison of the standard filter and the metamaterial assisted filter.

$$OD = -log_{10}\left(\frac{T}{100}\right) \tag{5.3.5}$$

Where *OD* is the optical density and *T* is the transmission percentage.

The results in figure 5.13 show that the contribution of the metamaterial boosts the optical density performance and aids angular sensitivity. The OD has been enhanced by an additional 1.3OD, from 1.5OD to 2.8OD, at zero angle of incidence (AOI). The OD of the standard thin film filter demonstrates the clear blue-shifting effect of thin films. The metamaterial influence stabilises the blue shifting, keeping the OD peak central to 532 nm until the OD has decreased to match the performance of the thin film's contribution, in the provided example ~25° AOI. The standard filter design experiences a 12 nm blue shift in peak OD for 20° AOI, where the metamaterial enhanced filter design exhibits zero shift in peak OD for 20° AOI. The optical density has been described by the mean density from p- and s- polarisation. In order to achieve that same optical density at zero degrees AOI for a thin film filter, the stack would have to be 110 layers with an overall physical thickness of 7556.22 nm, almost 3.2 µm thicker than the metamaterial enhanced filter.

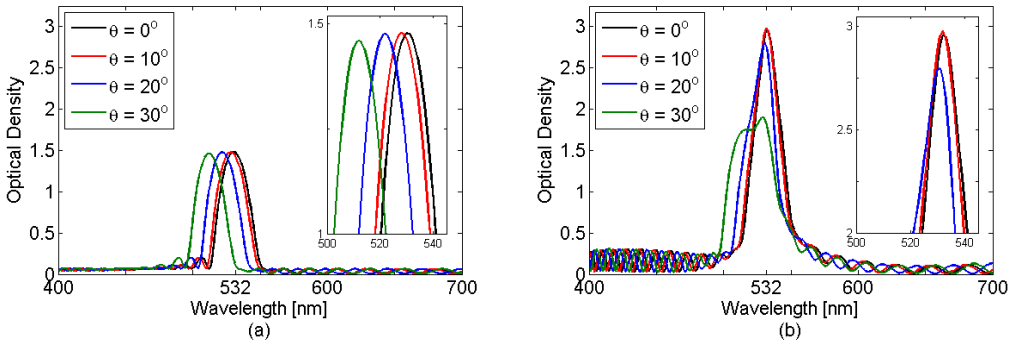


**Figure 5.13.** The optical density of (a) the standard thin film filter and (b) the metamaterial enhanced filter for varying angles of incidence. Inserts for (a) and (b) showcase the peak shifts with AOI.

Figure 5.14 demonstrates the optical density performance over varying angle of incidence for the single 532 nm wavelength. The results further demonstrate the OD boosting performance of the metamaterial enhanced thin film filter. The standard filter's mean OD diminishes when the transmission response has blue shifted beyond the zero-degree AOI notch central wavelength, 532 nm. The metamaterial enhanced filter retains some protection (~1.7OD) for higher angle of incidence, further demonstrating the enhanced ability for the addition metamaterial coating combined with traditional thin film interference coatings.

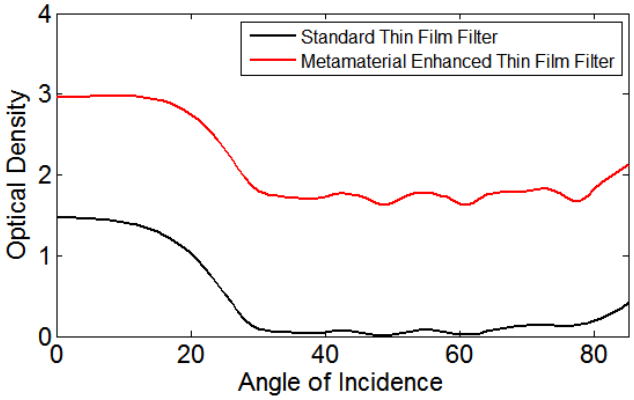


**Figure 5.14.** The optical density vs angle of incidence at a fixed wavelength of 532 nm.

**Case 2: Single ultra-thin notch filter at 532 nm wavelength**

The standard thin film filter design (Eq.5.3.6) for case 2 consists of 121 layers of $Na_3AlF_6$ and $MgF_2$ on a glass substrate with a refractive index of ~1.52. The overall physical thickness of this filter is 11772.06 nm.

$$L\left[\frac{L}{2}H\frac{L}{2}\right]^{60} \tag{5.3.6}$$

The metamaterial layer consists of silver spherical nanoparticles, ~40 nm in size, surrounded in ZnS. Similar to the previous case, the Zinc Sulphide allows the resonance to red shift to ~532 nm. The addition of the metamaterial layer to create the combination filter (Eq.5.3.7) provides an overall physical thickness of the metamaterial enhanced thin film filter of 12004.81 nm, with the thin film stack equalling quarter-wave thickness, the $MgF_2$ layer equating to 99.75 nm thickness and the metamaterial consisting of the remaining 133 nm thickness.

$$L\left[\frac{L}{2}H\frac{L}{2}\right]^{60}[AM] \tag{5.3.7}$$

Figure 5.15 shows the transmission response for case 2 and compares the standard thin film interference filter with that of the metamaterial assisted thin film interference filter, both at normal incidence. The ripples are less present than case 1 due to the choice of the refractive indices of the given materials. Again, the addition of the metafilm layer further enhances the attenuation of the transmission at the resonant wavelength, providing a bandwidth of 14 nm, an increase in bandwidth of 2 nm compared to the standard thin film filter.

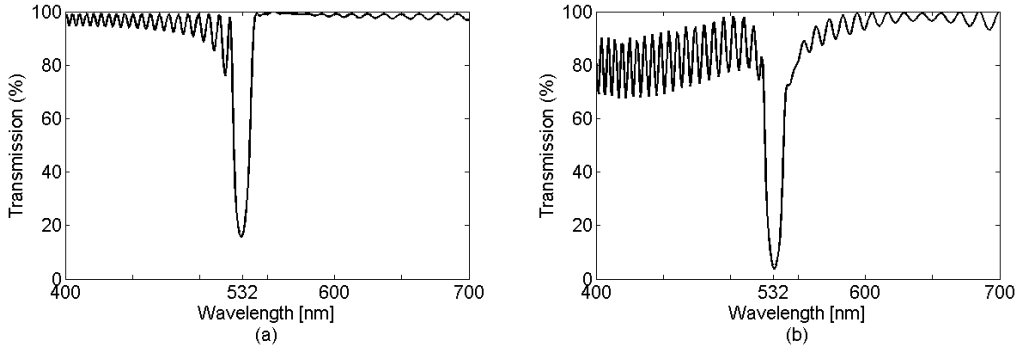


**Figure 5.15.** The transmission responses at normal incident for (a) standard thin film filter and (b) metamaterial enhanced filter.

The OD has been enhanced by an additional 0.6OD, from 0.8OD to 1.4OD, at zero angle of incidence (AOI). The OD of the standard thin film filter demonstrates the clear blue-shifting effect of thin films as expected. The metamaterial influence stabilises the blue shifting, keeping the OD peak central to 532 nm until the OD has decreased to match the performance of the thin film's contribution, in the provided example ~12° AOI. The conventional filter design experiences a 6 nm blue shift in peak OD for 10° AOI, where the metamaterial enhanced filter design has experienced zero shift in peak OD for 10° AOI. In order to achieve that same optical density at zero degrees AOI for a thin film filter, the stack would have to be 180 layers with an overall physical thickness of 17608.83 nm, over 5.8 µm thicker than the metamaterial enhanced filter.

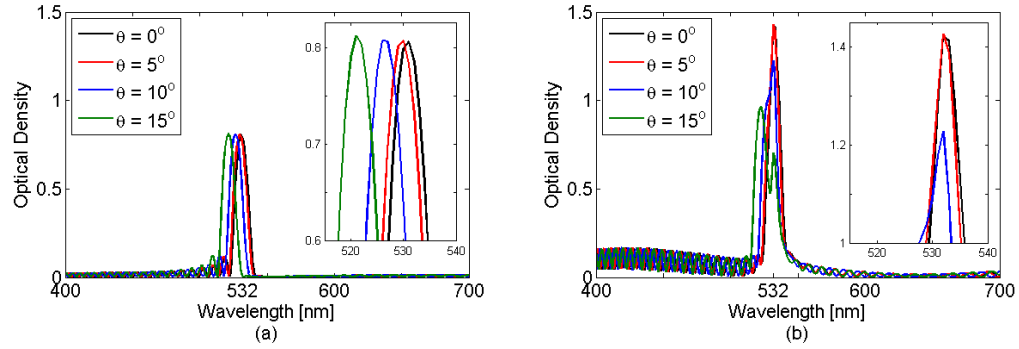


**Figure 5.16.** The optical density of (a) the standard thin film filter and (b) the metamaterial enhanced filter for varying angles of incidence. Inserts for (a) and (b) showcase the peak shifts with AOI.

Figure 5.17 demonstrates the optical density performance over varying angle of incidence for the single 532 nm wavelength. Like that of the case 1, the results further demonstrate the OD boosting performance of the metamaterial enhanced thin film filter. The standard filter's mean OD diminishes when the transmission response has blue shifted beyond the zero-degree AOI notch central wavelength, 532 nm. The metamaterial enhanced filter retains some protection (~0.8OD) for higher angle of incidence.

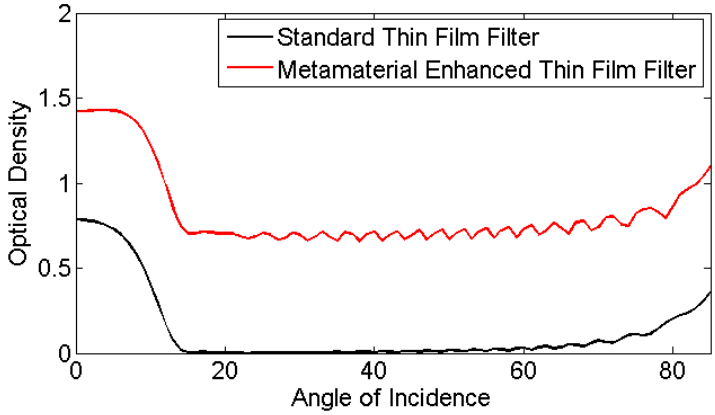


**Figure 5.17.** The optical density vs angle of incidence at a fixed wavelength of 532 nm.

### Case 3: Multi notch filter at 445 nm, 532 nm and 650 nm wavelengths

The standard thin filter design (Eq.5.3.8) for case 3 consists of 183 layers of $Y_2O_3$ and $HfO_2$ on a glass substrate with a refractive index of ~1.52. The overall physical thickness of this filter is 13356.61 nm. Differing from case 1 and case 2, the third case is centred on the summation of three different quarter-wave stacks to create a notch at 445 nm, 532 nm and 650 nm.

$$\left(L\left[\frac{L}{2}H\frac{L}{2}\right]^{30}\right)_{445}\left(L\left[\frac{L}{2}H\frac{L}{2}\right]^{30}\right)_{532}\left(L\left[\frac{L}{2}H\frac{L}{2}\right]^{30}\right)_{650} \tag{5.3.8}$$

The metamaterial layer consists of silver and gold spherical nanoparticles, ~40 nm in size. The silver is used for resonant wavelengths at 445 nm and 532 nm, while gold is used for the 650 nm resonance. The addition of the metamaterial layer to create the combination filter (Eq. 5.3.9) provides an overall physical thickness of the metamaterial enhanced thin film filter of 14049.35 nm, with the thin film stack equalling quarter-wave thicknesses for the three wavelengths of interest.

$$\left(L\left[\frac{L}{2}H\frac{L}{2}\right]^{30}[AM]\right)_{445}\left(L\left[\frac{L}{2}H\frac{L}{2}\right]^{30}[AM]\right)_{532}\left(L\left[\frac{L}{2}H\frac{L}{2}\right]^{30}[AM]\right)_{650} \tag{5.3.9}$$

Figure 5.18 shows the transmission response for case 3 and compares the standard thin film interference filter compared with that of the metamaterial assisted thin film interference filter, both at normal incidence. The addition of the metamaterial layers does further attenuate the transmission at the three selected wavelengths, however, the extent of the mismatch between the layers further induces multi-frequency ripples and supplementary attenuation to the overall transmission spectrum.

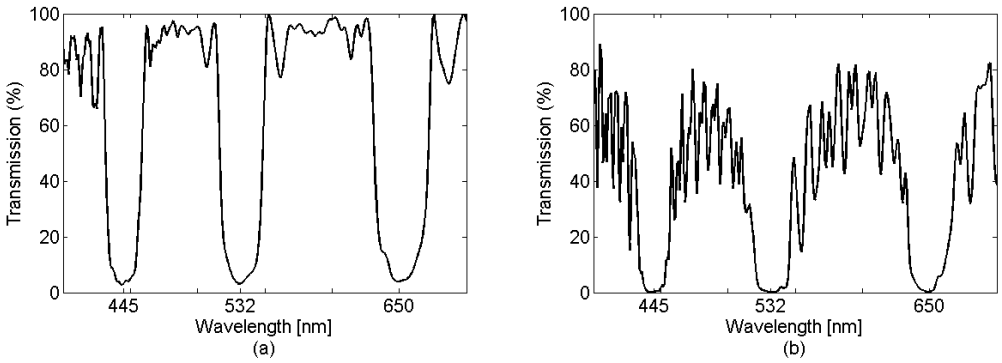


**Figure 5.18.** The transmission responses at normal incident for (a) standard thin film filter and (b) metamaterial enhanced filter.

The OD for the three resonant wavelengths has been enhanced by $1.5OD_{445}$, $1.5OD_{532}$ and $1.1OD_{650}$, at zero angle of incidence (AOI). As shown in the figure, and as expected, the standard thin film filter exhibits a clear blue-shift. Like the two previous cases, the addition of the metamaterial has stabilised the blue-shifting effect, allowing the peak OD to remain central to the resonant wavelength, until around ~22° AOI.

The standard thin film filter design experiences a 7 nm, 9 nm and 11 nm blue shift in the peak OD at 20° AOI for 445 nm, 532 nm and 650 nm respectively. The metamaterial enhanced filter design experienced a zero shift in peak OD for 20° AOI. In order to achieve the same optical density at zero degrees AOI for a thin film filter, the stack would have to consist of 303 layers with an overall thickness of 22109.61 nm, over 8µm thicker than the metamaterial enhanced filter.

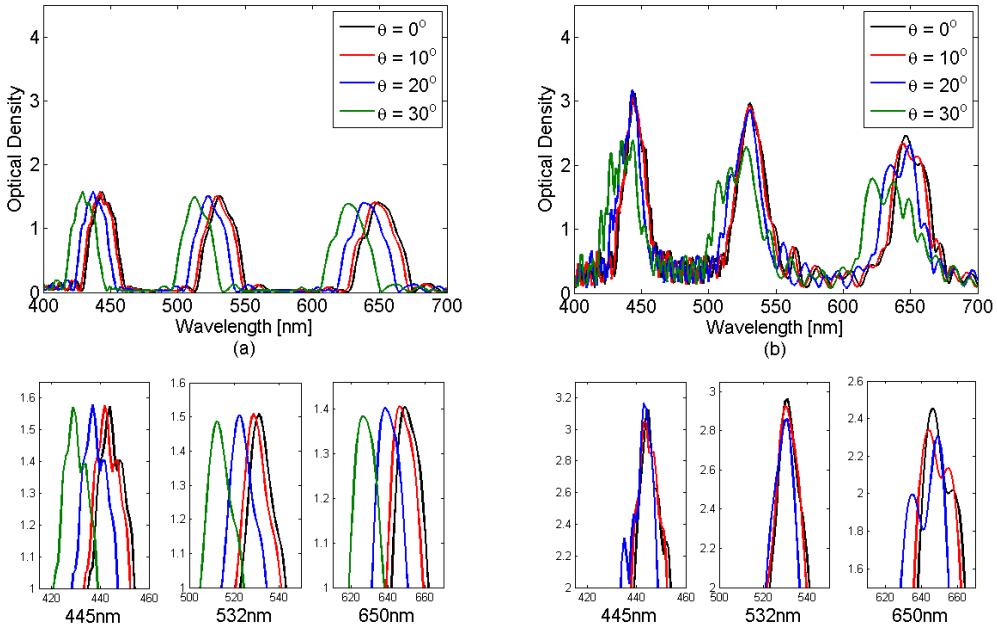


**Figure 5.19.** The optical density of (a) the standard thin film filter and (b) the metamaterial enhanced filter for varying angles of incidence. Inserts for (a) and (b) showcase the peak shifts with AOI.

Figure 5.20 shows the optical density performance over varying angle of incidence for the three selected laser wavelengths. Compared to the previous cases, the performance of the metamaterial displays some irregularities due to a combination of constructive and destructive interference owing to the mismatches within the complete stack assembly. However, the metamaterial enhanced filter still presents with an OD performance boost at all AOI, with protection enabled at higher angles of incidence.

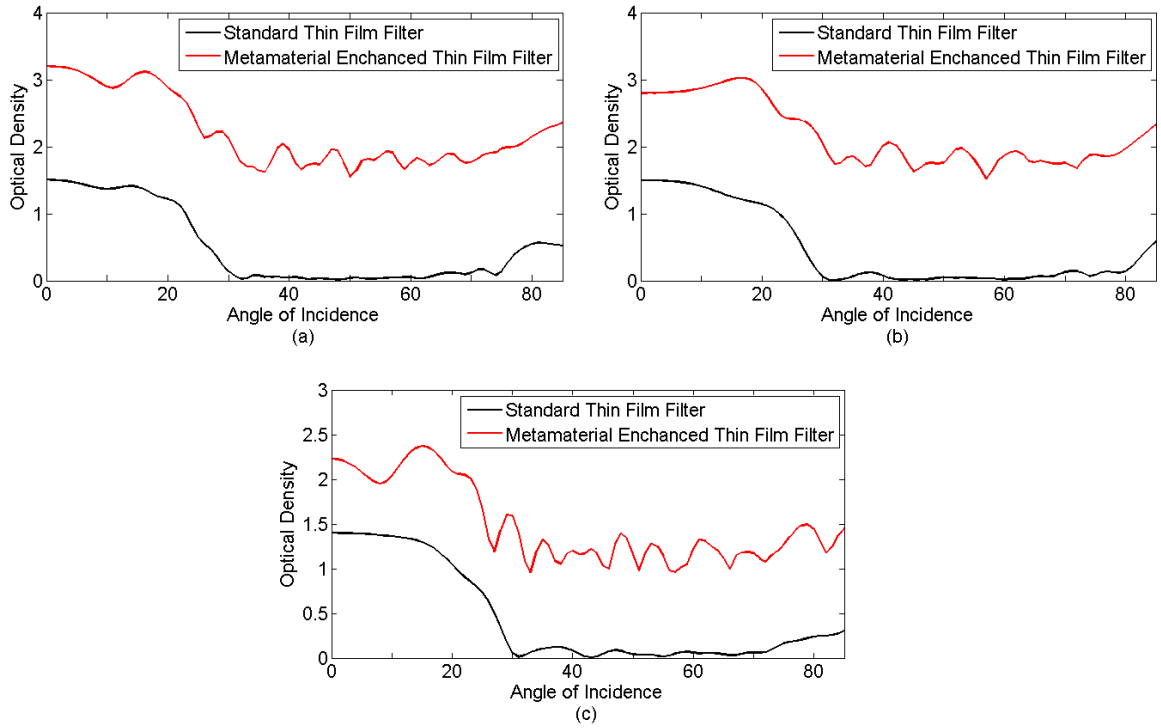


**Figure 5.20.** The optical density vs angle of incidence at a fixed wavelength for (a) 445 nm, (b) 532 nm and (c) 650 nm.

### Shifting Behaviour

Figure 5.21 highlights the transmission spectrum of the three cases at AOI of 0° and 50°. It is evident that the thin film contribution to the filter still experience blue-shifting behaviours at large angles. Nonetheless, the metamaterials contribution permits a fixed notch for the stack at the zero-degree AOI resonant wavelength. This does not present a huge problem for the single notch combination filter. However, the triple notch filter experiences several problems. As the AOI increases and the thin film contribution begins to blue-shift, the loss in the transmission greatly increases. Table 5.2 reveals the extent of the problem for the average transmission. Case 1 and case 2 experience very little transmission loss, around 0.4-0.7%. Case 3 though experiences ~37% loss in transmission at 50°. This is because the metamaterial remains at the fixed wavelength, while the thin film blue shifts between the adjacent optical notches.

**Table 5.2.** The average transmission of the three cases of metamaterial enhanced

| | **Average Transmission $\theta = 0^o$** | **Average Transmission $\theta = 50^o$** |
|---|---|---|
| **Case 1** | 70.0877% | 69.7768% |
| **Case 2** | 85.3307% | 84.7558% |
| **Case 3** | 39.5996% | 24.8419% |

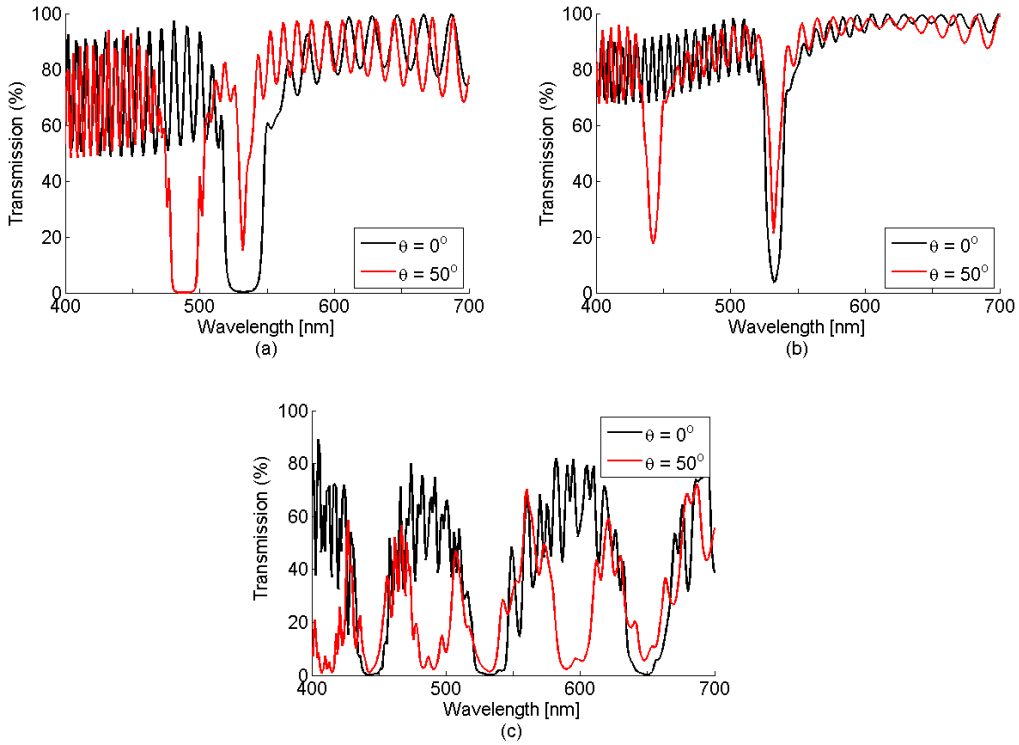


**Figure 5.21.** The transmission for each case showing the shifting behaviour.

## 5.4 **Combination Filter with Modulated Thin Film Thickness**

The presence of ripples in the optical performance can be exaggerated with the introduction of the metamaterial coating due to some mismatching between the layers. A method to minimise the ripples and to improve the optical performance is to introduce thickness modulation to the standard thin film stack.

The standard thin film filter design (Eq. 5.4.1) consists of 61 layers of $SiO_2$ and $Ta_2O_5$ on a glass substrate. The physical thickness of the unmodulated filter of 4684.79 nm, with the modulated physical thickness at 5557.05 nm.

$$[LH]^{30}L \tag{5.4.1}$$

Identically to the previous design, the metamaterial layer consists of silver nanoparticles surrounding in Zinc Sulphide and added to the thin film stack at the glass interface to establish the combination filter (Eq. 5.4.2). The dispersive refractive index for the metafilm can be found in figure 5.9a. The overall physical thickness of the metamaterial enhanced thin film is 5384.89

nm for the unmodulated filter and 6257.15 nm for the modulated filter. For both the modulated and unmodulated cases, the matching layer is 492.46 nm thick and the metamaterial layer is 270.64 nm thick.

$$[LH]^{30}L\ [AM] \tag{5.4.2}$$

Table 5.3 describes the element structure for the combination filter in this study.

**Table 5.3.** Notation and materials for combination stacks.

| Notation | Material | Complex Indices |
|---|---|---|
| Low (L) | Silicon Dioxide ($SiO_2$) | $1.45933 + i0$ |
| High (H) | Tantalum Pentoxide ($Ta_2O_5$) | $2.13955 + i0$ |
| Additional Matching Layer (A) | Magnesium Fluoride ($MgF_2$) | $1.38483 + i0$ |
| Metamaterial (M) | Metamaterial (ZnS-AgNPs) | $2.51886 + i1.07581$ |

The unmodulated thickness relies on the quarter-wave stack of interchanging dielectric materials, figure 5.22a. The modulated thickness, figure 5.22b, is presented in an envelope function that tappers and modulates the film thicknesses throughout the thin film stack [8].

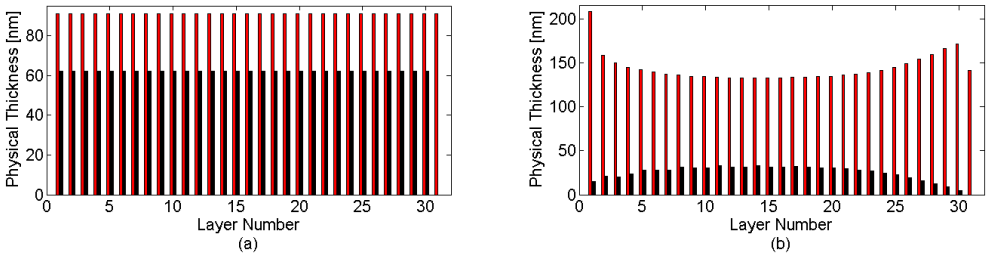


**Figure 5.22.** (a) Unmodulated thickness design and (b) modulated thickness for indices of $L = 1.46$ and $H = 2.14$, at $\lambda_0 = 532nm$. The red bars represent the low index material and the black bars represent the high index material.

The transmission spectrum for the modulated case is shown in figure 5.23 and is directly compared to an unmodulated filter. The unmodulated filters demonstrate mismatched layers in the form of ripples. The modulated filter substantially improves this mismatch and reduce the ripples significantly. The small ripples found in the standard thin film modulated thickness filter are amplified by the introduction of the metamaterial layer but are considerably less in comparison to the unmodulated case. Furthermore, the bandwidth of the modulated filters (95 nm) is smaller than the unmodulated filters (144 nm) due to the absence of extreme ripples.

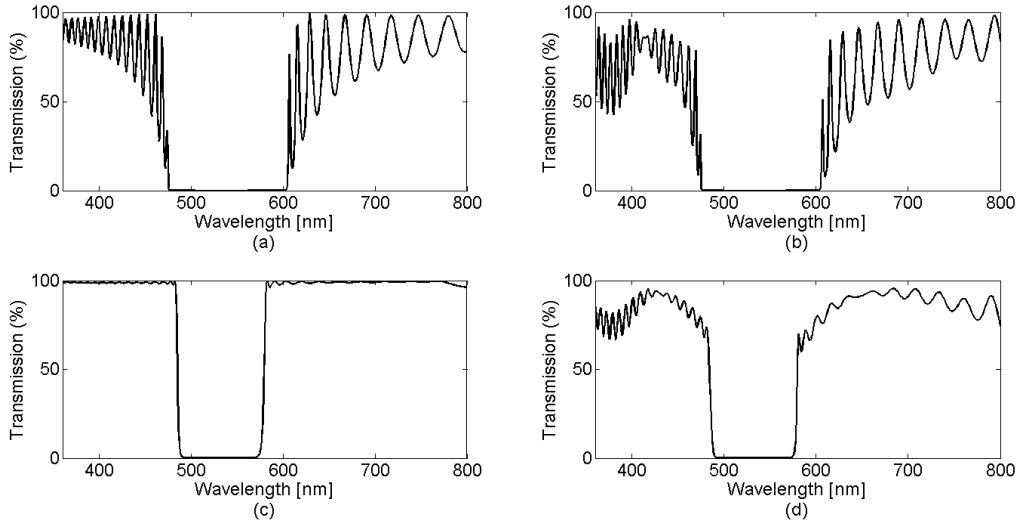


**Figure 5.23.** The transmission responses at normal incident for (a) standard thin film filter with unmodulated thickness, (b) metamaterial enhanced filter with unmodulated thickness, (c) standard thin film filter with modulated thickness and (d) metamaterial enhanced filter with modulated thickness.

Table 5.4 highlights the efficiency to the average transmission when comparing the unmodulated and modulated filters between the wavelength 360 nm and 800 nm.

**Table 5.4.** The average transmission comparing the unmodulated filters against the modulated filters.

| | **Average Transmission $\theta = 0^o$** |
|---|---|
| Standard Thin Film Filter (Unmodulated) | 53.8% |
| Metamaterial Enhanced Filter (Unmodulated) | 49.1% |
| Standard Thin Film Filter (Modulated) | 77.7% |
| Metamaterial Enhanced Filter (Modulated) | 66.9% |

The optical density for this study differs from the previous one because the thin films OD impact is considerably greater. The blue-shift behaviour is clearly visible for both the unmodulated and modulated standard thin film stacks. The contribution of the metamaterial can improve the angular sensitivity of the thin film by allowing the peak OD to remain central to the chosen 532 nm wavelength, until the thin films angular behaviour is the dominating factor of the filter. The optical density for each filter case is presented in figure 5.24.

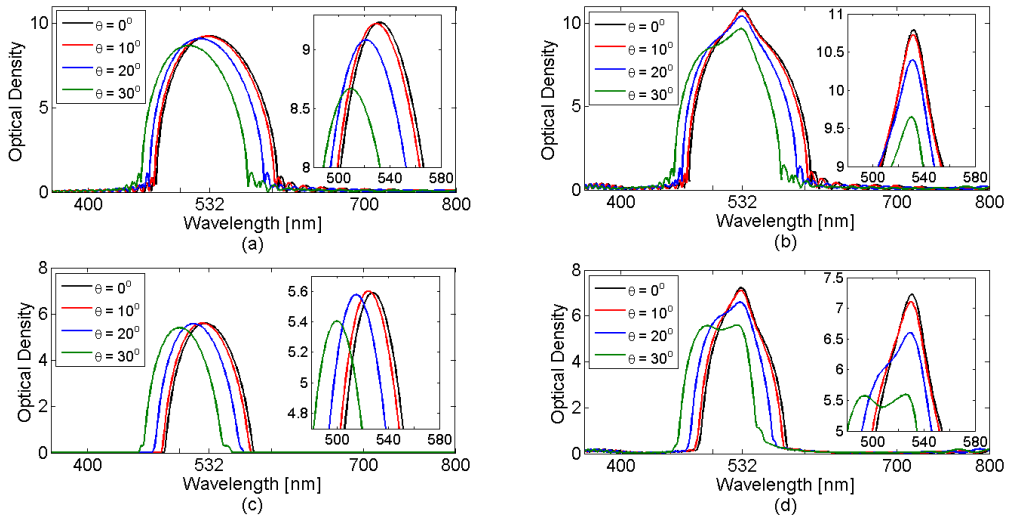


**Figure 5.24.** The optical density of for (a) standard thin film filter with unmodulated thickness, (b) metamaterial enhanced filter with unmodulated thickness, (c) standard thin film filter with modulated thickness and (d) metamaterial enhanced filter with modulated thickness, for varying angles of incidence. Inserts showcase the peak shifts with AOI.

The optical density performance over a range of incidence angles at 532 nm wavelength is presented in figure 5.25. The metamaterial provides improved optical density across all AOI, particularly supplying a baseline OD beyond the thin film's contribution.

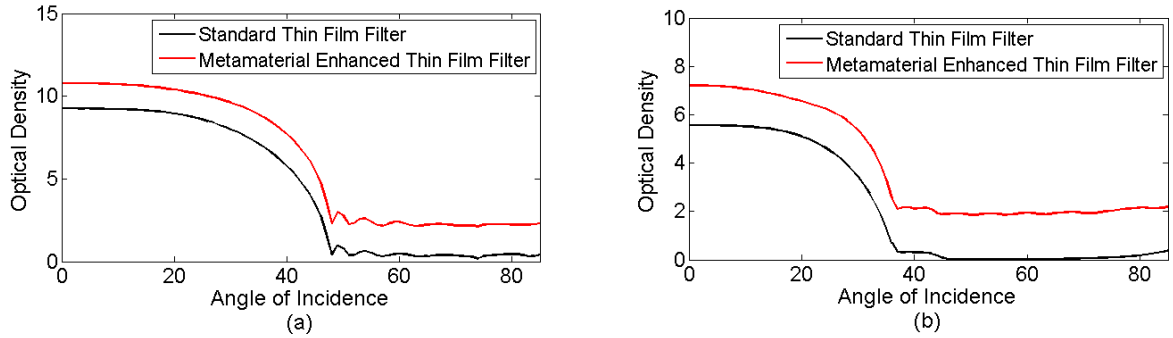


**Figure 5.25.** The optical density vs angle of incidence at a fixed wavelength of 532 nm for (a) unmodulated thickness and (b) modulated thickness.

## 5.5 **Summary**

The work presented in this chapter provides a new solution for partial shift-free behaviour for optical notch filters. The combination filter design provides a novel solution and has not previously been reported. The shifting behaviour of the combination filter does not conform to the standard performance of a traditional thin film filter. Instead, the combination filter, consisting of a dielectric thin film stack and a metafilm, stabilises the optical density (OD) peak until the thin film blue-shift has overcome the bandwidth of the metafilm's contribution. Stabilisation occurs due to the extinction coefficient of the metafilm acting as an envelope to the thin film response. Additionally, the introduction of the metamaterial boosts the OD performance, and due to the relation of OD and transmission, also attenuates the transmission further. This supplementary attenuation also results in a thinner overall stack when compared to an exclusively thin film stack with similar performance, which aids for delamination issues and the environmental performance. The addition of a physical thickness modulation improves the optical performance of both the standard and metamaterial enhanced filters by reducing the ripples. To summarise, the research presented in this chapter provides an incremental development to improve and overcome the inherent problems associated with the well-established principles of thin film interference filters. This provides a promising avenue for advanced thin film filters, as well as an introduction of metamaterials to the optical industry.

## 5.6 **References**

[1] H. Angus Macleod, “Chapter 7. Edge Filters and Notch Filters”, in *Thin-Film Optical Filters*, 5th ed., CRC Press, pp. 243-249, 2017

[2] M. Matin, T. Benson, L. Chen and P. Smith, "Analysis of distributed Bragg reflectors using thin-film optics", *Microwave and Optical Technology Letters*, vol. 21, no. 1, pp. 11-15, 1999. Available: 10.1002/(sici)1098-2760(19990405)21:1<11::aid-mop4>3.0.co;2-o.

[3] Macleod, Angus, “Fundamentals of optical coatings”, *SVC News Bulletin*. p. 29-42, 2005

[4] L. Epstein, "The Design of Optical Filters", *Journal of the Optical Society of America*, vol. 42, no. 11, p. 806, 1952. Available: 10.1364/josa.42.000806.

[5] A. Herpin, "Optique electromagnetique-calcul du pouvoir reflecteur dun systeme stratifie quelconque (electromagnetic optics-calculation of the reflector power of any laminate system)", *Comptes Rendus Hebdomadaires Des Séances De L'Académie Des Sciences*, vol. 225, no. 182, 1947.

[6] P. Young, "Extension of Herpin’s Theorem", *Journal of the Optical Society of America*, vol. 60, no. 10, p. 1422, 1970. Available: 10.1364/josa.60.001422.

[7] K. Chopra, "Thin Films in Optics", in *Thin Film Device Applications*, 1st ed., Springer, 2019, pp. 55-88.

[8] B. Perilloux, *Thin-film design: Modulated Thickness and Other Stpband Design Methods*. Bellingham, Wash. (1000 20th St. Bellingham WA 98225-6705 USA): SPIE, 2002.

[9] U. Mescheder, I. Khazi, A. Kovacs and A. Ivanov, "Tunable optical filters with wide wavelength range based on porous multilayers", *Nanoscale Research Letters*, vol. 9, no. 1, 2014. Available: 10.1186/1556-276x-9-427[10] S. Zhu and X. Zhang, "Metamaterials: artificial materials beyond nature", *National Science Review*, vol. 5, no. 2, pp. 131-131, 2018. Available: 10.1093/nsr/nwy026.

[11] M. Polyanskiy, “RefractiveIndex.info – Refractive index database”, *Refractiveindex.info*, 2020. [Online]. Available: https://refractiveindex.info.

# CHAPTER VI. OPTICAL THREE-DIMENSIONAL NOTCH FILTER FOR VISIBLE LASER PROTECTION

This chapter discusses the tailoring optical resonances and puts forward a theoretical and computational study of an optical band stop filter to block out chosen laser wavelengths. The active laser protection component consists of a crystallographic plane cluster of spherical metallic nanoparticles formed in a multi-hexagonal layered array, combined in a contiguous dielectric medium with selected refractive indices to fine tune the resonance to the desired operational wavelength. A discussion of the results and advancements are put forward as a leading argument for the next generation of visible laser protection devices. The unique behavioural response of the proposed designs is of great interest, not only to the civil and military aviation industry, but displays the ability to be utilised in a wide area of scientific research and manufacturing, where visible lasers are operated.

## 6.1 **Filter Design Parameters**

The desired optical bandstop laser protection filter will be measured by its angular performance of key parameters including transmission spectrum $T(\lambda)$, optical density (OD), integrated visual photonic transmission (IVPT) and colouration, under different polarisation states.

### 6.1.1 **Transmission and Optical Density**

An ideal transmission response is that which has near 100% transmission for all wavelengths with the exception of the wavelength of interest, which must be attenuated to zero or near-zero. Figure 6.1 illustrates an ideal transmission response for optical filtering of a 532 nm wavelength green laser whilst passing through all other wavelengths. The insert to figure 6.1 demonstrates an artistic impression of the metamaterial laser protection eyewear and its ability to block the wavelength at non-incident angles. The bandwidth of the filter is desired to cover a minimal range of wavelengths, however, takes into account that lasers may operate at different wavelengths depending on the operational temperature (not perfectly monochromatic).

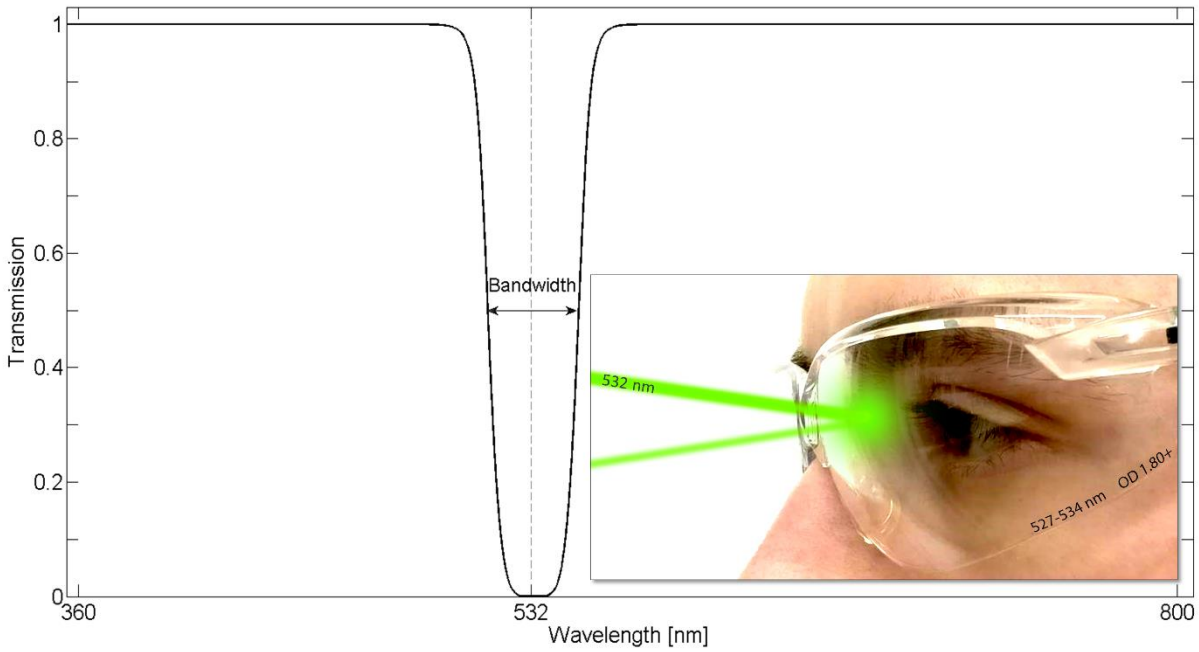


**Figure 6.1.** The conceptual aim examples. The figure indicates the ideal transmission response with the insert showing an artist impression of the optical metamaterial notch filter on personnel goggles, deflecting a 532 nm laser beam (527 nm – 534 nm) with a bandwidth smaller than 50 nm.

The blocking performance of the filter can be measured from the optical density (OD), previously defined in (Eq. 5.3.5).

### 6.1.2 **Design Methodology**

The designs and responses found in this chapter have been computationally verified by a full-wave analysis approach using CST Microwave Studio software which is a widely used tool for three-dimensional electromagnetic simulations for high frequency components. The optical properties for the discussed refractive indices and extinction coefficients have been obtained from literature [1-4]. The light propagation direction, *k*, with normal incidence is perpendicular to the design facets. The electric field, *E*, is directional to the *y-axis* and the magnetic field, *H*, is directional to the *x-axis*, and initiated for the required transverse modes. Where circular and elliptical polarisation is active, the electric field vector can be found on the *x-axis* with a reference wavelength equal to the desired laser wavelength. The elliptical polarisation at the reference wavelength exhibits a phase difference of -90° with an axial ratio of 0.5, the ratio between the amplitudes of the two field vectors. The wave propagation angle, *theta*, has been adjusted accordingly to compute *k* at various angle of incidence. The incidence source is located beyond the Rayleigh range (Eq.6.1.1) to activate the far field properties of the device [5]. The far field region is employed to characterise a stable and divergence constant to the plane wave incidence source.

$$Z_0 \geq \frac{\pi W_0^2}{\lambda} \tag{6.1.1}$$

$Z_0$ is the Rayleigh range and $W_0$ is the waist radius of the embedded fundamental Gaussian beam of the computational laser wavelength.

## 6.2 **532 nm Laser Protection Design**

As discussed in *Chapter II*, the obvious laser protection eyewear to design a 532 nm green laser. Another green wavelength exists at 520 nm; however, these are much less common. Additionally, a 532 nm laser protection design makes sense from the human eyes perspective as the eye is most sensitive at 555 nm (green colour wavelength), photopic vision, and 507 nm (cyan colour wavelength), scotopic vision.

### 6.2.3 **Proposed Design**

The filter design is built on the merging of plasmonics with traditional anti-reflection (AR) coating theory. Both theory components contribute to the design's performance, with the plasmonics inducing the notch attenuation and the AR coating being responsible for containing the plasmonic nanoparticles in a range of different refractive mediums in order to tailor the plasmonic response and to enable high transmission outside of the wavelength of interest.

Figure 6.2 shows the proposed anti-laser notch filter design. The design consists of three layers: antireflection coating (AR- top), active blocking layer (AB, middle) and substrate (bottom). The active layer is a three-dimensional artificial media made of silver nanoparticles (AgNPs) organised in a primitive hexagonal Bravais lattice planar array form and embedded in a surrounding dielectric. As discussed in previous chapters, AgNPs have been selected as a main active element because of its flexibility in its resonance engineering and the hexagonal arrangement was chosen to increase the fill fraction and boost the device's angular performance.

The AgNPs size is fixed at 9 nm in diameter. This follows the design requirements of a narrow blocking bandwidth of less than 50 nm. However, at 9 nm in diameter, the AgNPs permittivity deviates from its bulk and requires adjustment. Finally, the AR layer is deposited on top of the active blocking layer to ensure that incoherent light outside of the blocking band (e.g. daylight) are able to pass through the device at a high transmission rate. This is important to ensure that the device has a clear visibility while blocking out the 532 nm laser beam.

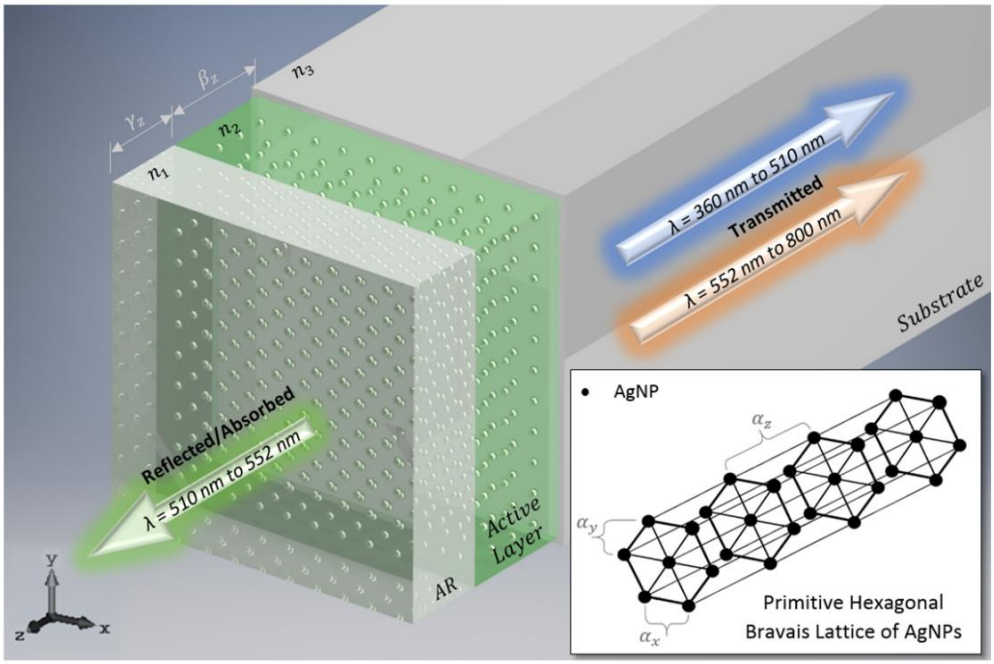


**Figure 6.2.** The configuration of the 532 nm anti-laser device based on a three dimensional hexagonal planar array of AgNPs as the active component with $\alpha_x = \alpha_y = \alpha_z = \lambda_{laser}/16$; $\beta_z = 4\alpha_z$ and $\gamma_z = 3\alpha_z$. Insert shows the hexagonal lattice arrangement of the AgNPs within the 'active layer'.

### 6.2.4 **Design Theory and Process**

The basic design theory is based on plasmonics, namely localised surface plasmon resonances of silver nanoparticles (AgNPs). A coupled design approach involving both analytical theory and numerical simulations was used. The analytical theory centred around Mie theory and thin film interference theory, as a base to find approximate design parameters and subsequently the use of a full-wave numerical simulation software CST Microwave Studio to tune and verify the design to meet the design targets.

#### **Host Medium for AgNPs**

The active layer consists of a 3D primitive hexagonal Bravais lattice of 9 nm diameter AgNP. The composite's effective refractive index can be determined from the Maxwell-Garnett formula (Eq. 6.2.1), which defines the bulk effective permittivity of the metal-dielectric composite [6], and relationship between refractive index and permittivity (Eq. 6.2.2).

$$\frac{\varepsilon_{eff} - \varepsilon_h}{\varepsilon_{eff} + 2\varepsilon_h} = f\frac{\varepsilon_m - \varepsilon_h}{\varepsilon_m + 2\varepsilon_h} \tag{6.2.1}$$

$$\tilde{n}^2 = (n + i\,k)^2 \equiv \varepsilon_{eff} = \varepsilon_r + i\,\varepsilon_i \tag{6.2.2}$$

$\varepsilon_{eff}$ represents the effective permittivity with its respective complex notation, $\varepsilon_m$ and $\varepsilon_h$ signifies the permittivity for silver and the dielectric host respectively, and $n$ and $k$ denote the

refractive index and extinction coefficient. An additional term has been added to the classical Drude dampening frequency, $\gamma_{particle} = \gamma + \left(v_F/(\alpha\, r_p)\right)$ to compensate for the particle becoming smaller than the free mean path of the electron (for silver the bulk mean free path at room temperature is about 53 nm [7]); $\gamma$ and $\gamma_{particle}$ represents the dampening frequency of the bulk metal and new dampening frequency according to the particle size ($r_p$), with relation to the Fermi velocity ($v_F$) and $\alpha$, where due to the spherical nature of the particles $\alpha = 4/3$. Accordingly, the particle size has been taken into consideration for this design.

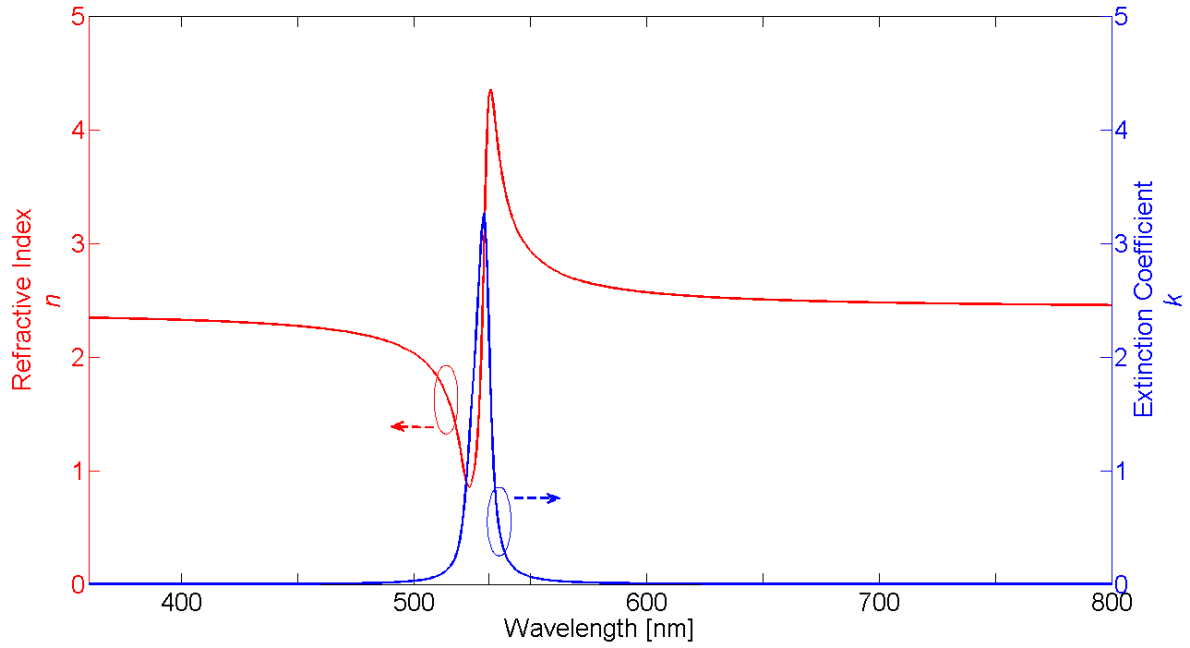


**Figure 6.3.** The effective refractive index and extinction coefficient for the active layer.

The following equation (Eq. 6.2.3) can be used to find the notch location according to the plasmonic material and surrounding medium. Once the surrounding medium's refractive index has be decided, the effective refractive index of the active layer can be determined.

$$\lambda_t = e^{\frac{c_1 + Re[n_{host}]}{c_2}} - \sigma \tag{6.2.3}$$

Where $\lambda_t$ is the desired wavelength and is equal to the wavelength associated with the peak value of the extinction coefficient ($k$) of the active layer. $\lambda_t = 532nm$ when $Re[n_{host}] = 2.382$. The $c$ values are the coefficients of Silver ($c_1 = 18.741$ and $c_2 = 3.3654$), $n_{host}$ is the refractive index of the surrounding dielectric medium and $\sigma$ is a particle size correction function ($\sigma = 1.24$). This formula applies to all other wavelengths. For example, if the desired wavelength was to block out a 450 nm blue laser, the surrounding dielectric medium would need a refractive index of $n_{host} = 1.82$ instead.

**Particle Spacing**

The blocking bandwidth ($\Delta\lambda$) is affected by both the AgNP particle size and its 3D hexagonal lattice array density. The Q-factor, defined as $Q = \lambda_t/\Delta\lambda$, was used to calculate the blocking wavelength bandwidth. The Q-factor was optimised for high blocking performance while remaining with a minimal bandwidth, resulting in an optimum design of $\alpha_x = \alpha_y = \alpha_z = \lambda_{laser}/16$; $\beta_z = 4\alpha_z$ and $\gamma_z = 3\alpha_z$, as shown in figure 6.3.

**Anti-Reflection Coating and Layer Thickness**

The 532 nm laser protection device has an active layer that is sandwiched between a glass substrate (n=1.52) and an AR coating layer of Magnesium fluoride ($MgF_2$, n=1.38). The introduction of $MgF_2$ is to reduce the reflected light intensity and improve the overall transmittance of the device by allowing the natural incoherent light (sunlight) to experience a phase difference of $\pi$, resulting in constructive interference of the waves. The thin film anti-reflection coating is chosen to match the relationship of the reflection coefficient between air, the active layer and the glass substrate, so that:

$$n_{AR} \approx \frac{1}{\sqrt{n_{air}/n_{sub}}} \tag{6.2.4}$$

The presence of the high-index ZnS (surrounding medium for the active layer) positioned next to the low-index substrate, makes it appear that the substrate has a high index, thus, the subsequent layer of $MgF_2$ becomes more effective as an AR coating [8]. The thickness of the two-layer coating design has been formulated from conventional double-layer coating principles and is expressed in (Eq.6.2.5).

$$tan^2\delta_1 = \frac{(n_{sub} - n_{air})(n_{ZnS}^2 - n_{air}n_{sub})n_{MgF_2}^2}{(n_{MgF_2}^2 n_{sub} - n_{air}n_{ZnS}^2)(n_{air}n_{sub} - n_{MgF_2}^2)} \tag{6.2.5a}$$

$$tan^2\delta_2 = \frac{(n_{sub} - n_{air})(n_{air}n_{sub} - n_{MgF_2}^2)n_{ZnS}^2}{(n_{MgF_2}^2 n_{sub} - n_{air}n_{ZnS}^2)(n_{ZnS}^2 - n_{air}n_{sub})} \tag{6.2.5b}$$

Where $\delta$ is a positive real number that satisfies the quarter wavelength relationship and $n$ is the refractive index of the subscripted materials. Two solutions for each $\delta$ value will be produced that must be correctly paired, with the $\delta_1$ component being a relation to the AR coating and the $\delta_2$ component being a relation to the active layer. However, for this study, the solutions found in Eq.10a have been selected to minimise the number of odd multiples of quarter wavelengths and to sufficiently host the required number of AgNP structured lattice layers. Each $\delta$ solution

is multiplied by a reference wavelength, $\lambda_{Ref} = 275nm$, to solve for the layer thickness, such that the active layer is approximately equal to $\lambda_{laser}/4$.

$$\delta_1/2\pi = 0.1749 \qquad \delta_2/2\pi = 0.4803 \qquad (6.2.6a)$$

and

$$\delta_1/2\pi = 0.3251 \qquad \delta_2/2\pi = 0.0197 \qquad (6.2.6b)$$

### 6.2.5 **Filter Performance**

Figure 6.4 shows the key result of the designed filter for linear, elliptical and circular polarisation; the transmission response at various incidence angles of 0° (solid line), 50° (dashed line) and 70° (dotted line). Note that the transmission responses are near identical for all given polarisation, with a variation of ~0.5%. The dielectric host material, ZnS, tunes AgNP resonance peak from 354 nm (*same lattice configuration but with air as host medium*) to ~531 nm. The resulting bandwidth is 41.8 nm at the full width at half maximum, qualifying the performance of the filter to introduce a band rejection at the 532 nm lasing wavelength, whilst providing high transmission outside of the rejected band. As the incidence angle increases, it is clear to see that zero-shift occurs at the rejection band. The blocking at the rejection band continues to 85° of incidence. The natural light transmission outside of the 532 nm wavelength would remain at maximum at the angle of the users mid-to-near peripheral vision ($\theta$ = 30° - 60°), whilst the ocular focus would remain at the macular region of the peripheral vision ($\theta$ = 0° - 18°) [9]. From the wavelengths, outside of the notch bandwidth, of 360 nm to 510 nm and 552 nm to 800 nm, the average transmission across the filter is 81.09% and 89.06%, respectively; with an overall spectral response of 77.87% from 360 nm to 800 nm.

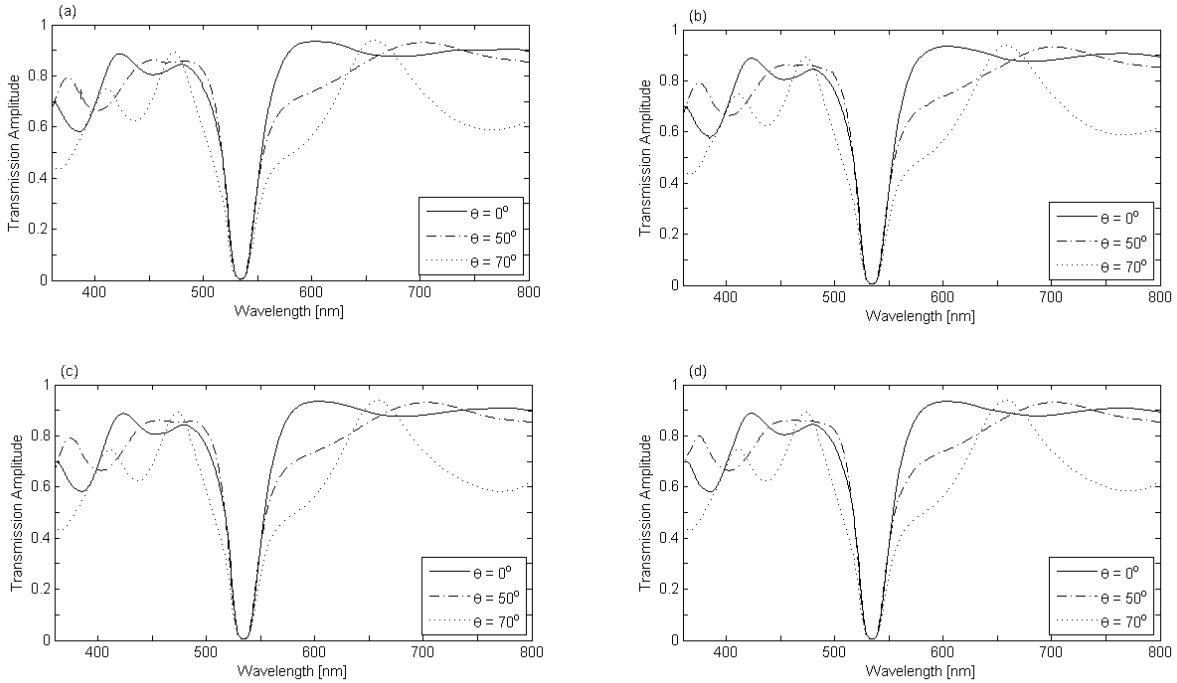


**Figure 6.4.** Transmission of the three-dimensional optical metamaterial filter versus wavelength for incident angle at $\theta$ = 0°, $\theta$ = 50° and $\theta$ = 70°. The solid, dashed and dotted lines denote the cases of the incident angle. (a) Linear pol. (b) Elliptical pol. (c) Left circular pol. and (d) Right circular pol.

The IVPT response of the discussed filter is 61%. The transmission colouration response is at the coordinates ($x = 0.36$ and $y = 0.27$) and the reflection colouration response is at the coordinates ($x = 0.26$ and $y = 0.35$) of the standard CIE 1931 colour map. As seen in figure 6.5, the calculated transmission and reflection colouration are close to neutral but experience a slight magenta and turquoise hue, respectively.

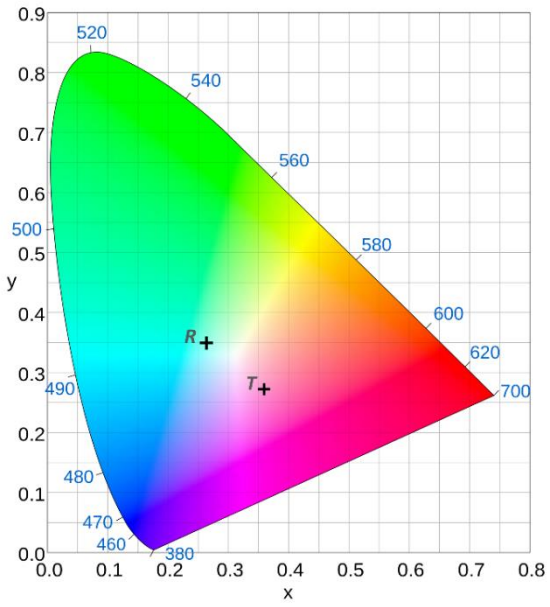


**Figure 6.5.** The CIE 1931 colour map for the transmission (T) and reflection (R) for the three-dimensional 532 nm optical metamaterial filter.

Figure 6.6 shows the calculated optical density (OD) of the filter for angles between 0° and 85° for linear, elliptical and circular polarisation. The OD remains above 1.88 across the whole range of angles. This indicates that the described filter is able to perfectly block a common low power (<76mW) Class 3B 532 nm DPSS laser of continuous-wave operation at all angles of incidence without blue shift occurring. Blocking of <100mW is achievable between the angles of 0° and 20°. However, despite having zero shift of the notch at the point of resonance, the out of resonance wavelengths begin to attenuate and results in broader bandwidths. This attenuation is greatly augmented beyond the incidence angle of 70° and lies within the far peripheral vision region of the human eye. Due to this attenuation, the device design can be labelled as having a critical angle of 70°.

Another factor to consider is the polarisation sensitivity of the optical filter, figure 6.6 illustrates that the results are independent of the incidence angle in two polarisation modes p and s. The slight fluctuation between p and s polarisation for angles between 45° to 70° is a consequence of the Brewster angle of the AR coating, ~54° [10], and is not caused by the active blocking layer of the three-dimensional AgNP planar array. The variation beyond 70° is due to a minor change (~±1 nm) in resonance between s and p polarisation.

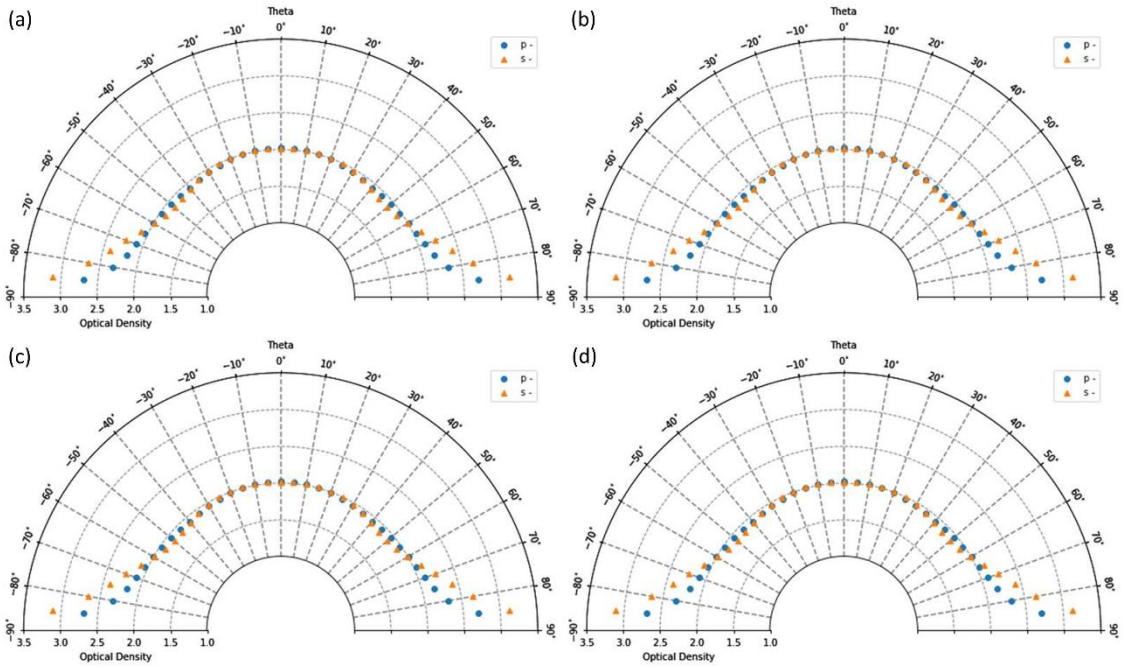


**Figure 6.6.** OD of the designed filter at the laser wavelength of 532 nm. The circle and triangle data points denote the transverse mode of the electromagnetic radiation. Theta represents the angle of incidence. The peripheral vision regions have been noted in accordance to theta. (a) Linear pol. (b) Elliptical pol. (c) Left circular pol. and (d) Right circular pol.

### 6.2.6 **Light-Matter Interaction Mechanism**

The wide-angle shift-free features of the design result from its three-dimensional topological arrangement (primitive hexagonal Bravais lattice) [11] and the excitation of similar resonance modes under different incident angle beams at 532 nm. Figure 6.7 shows the power flows of Poynting vector calculated for the 9 nm diameter AgNP when it is irradiated by a 532 nm laser at 0 and 45 degrees for both TE (a, b) and TM (c, d) polarisation incident beams. Under TE wave illumination, the AR layer has a matched phase with the air layer so that angles were preserved at this Air-AR interface. However, the power flows are undergoing a 45-degree rotation to 0-degree when it reaches the AR-AB interface, as shown in (figure 6.7b). As a result, regardless of the angle differences, the power flows passing through the AB layer in (figure 6.7a) and (figure 6.7b) are almost the same, leading to the near-identical field absorption and flow patterns under 0 and 45-degree incidences in the AB layer. This figure holds true for other angles up to about 85 degree and the laser energy was most completely absorbed by four layers of AgNPs in AB media for TE polarisation. Under TM wave illumination, however, the situation is slightly different. As shown in (figure 6.7d), the beam rotates by around 45-degree clockwise to 0-degree at the air-AR interface, but rotates anti-clockwise back to 45-degree at the AR-AB interface, which leads to differences in light absorption between normal (figure 6.7c) and non-normal incidence beams (figure 6.7d), but does not affect the resonance wavelength.

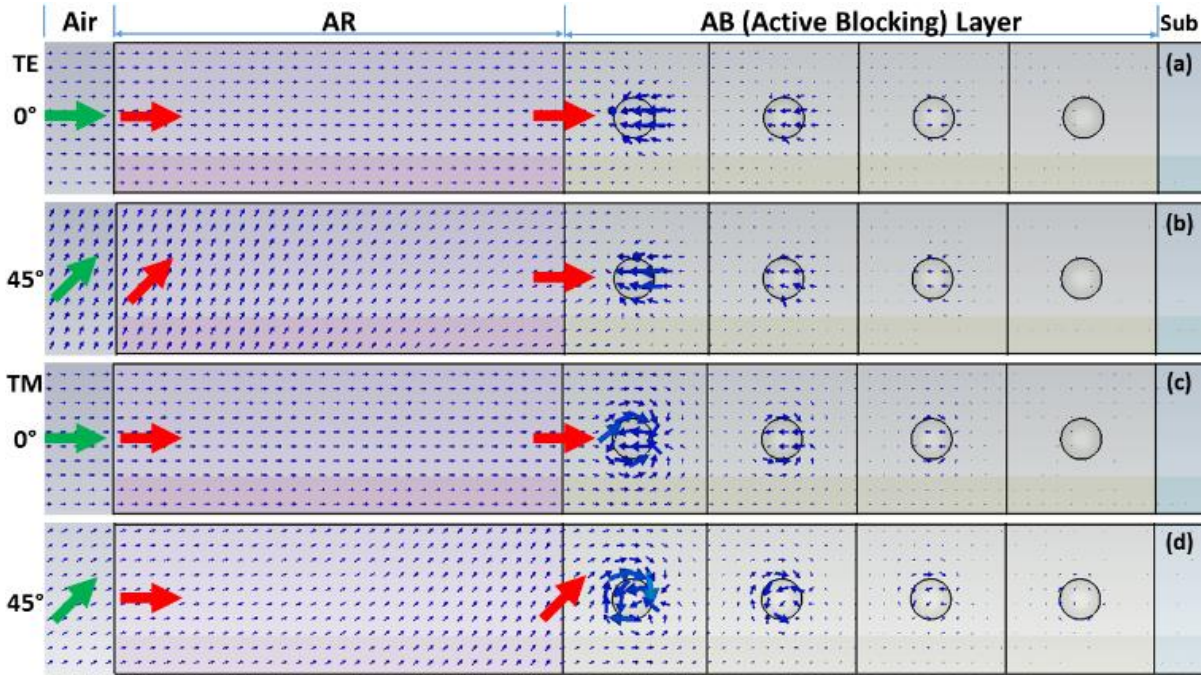


**Figure 6.7.** Power flow plots for TE and TM incident beams with linear polarisation at 532 nm wavelength with varying angles of incidence of 0 and 45 degrees. (a) TE with AOI = 0°, (b) TE with AOI = 45°, (c) TM with AOI = 0°, and (d) TM with AOI = 45°.

### 6.2.7 **Thermal Distribution Mechanism**

Visible light absorption converts the short wavelength light into long wavelength heat [12]. As such, due to the absorption properties of the silver nanoparticles, thermal radiation will inevitably be produced. Consequently, it is important to study the thermal effects of the active blocking layer.

Due to the nanoscale features of the active blocking layer, coupled with the fact that a laser spot size would be distributed over a relatively large area (millimetre range in comparison to nanometre range), an effective thermal property solution can be concluded. Thermal conductivity ($k$), film density ($\rho$) and heat capacity ($C_p$) should be considered.

**Table 6.1.** Thermal properties for the materials found in the active blocking layer.

| **Material** | $\boldsymbol{k(W.m^{-1}.K^{-1})}$ | $\boldsymbol{\rho(kg/m^3)}$ | $\boldsymbol{C_p(kJ.K^{-1}.kg^{-1})}$ |
|---|---|---|---|
| Zinc Sulphide | 27.2 | 4,100 | 0.515 |
| Silver | 429 | 10,500 | 0.23 |
| Effective film (ZnS-AgNPs) | 28.1920 | 4192.5 | 0.5109 |

The effective thermal conductivity can be described by (Eq. 6.2.7). Where $k_h$ is the ZnS host medium and $k_m$ is the silver nanoparticles, with $f$ denoting the fill fraction.

$$k_{eff} = k_h \left( \frac{1 + 2f\left(\frac{k_m - k_h}{k_m + 2k_h}\right)}{1 - f\left(\frac{k_m - k_h}{k_m + 2k_h}\right)} \right) \tag{6.2.7}$$

The effective density is given by (Eq. 6.2.8).

$$\rho_{eff} = (\rho_h f_h) + (\rho_m f_m) \tag{6.2.8}$$

Finally, the effective heat capacity can be determined by (Eq. 6.2.9), where $M$ represents the mass.

$$C_{p,eff} = \left(\frac{M_h}{M_{total}}\right) C_{p,h} + \left(\frac{M_m}{M_{total}}\right) C_{m,h} \tag{6.2.9}$$

Considering a standard CW DPSS laser diode at 532 nm wavelength with a beam divergence of $\theta = 12mrad$ and a power output of 10mW, at a distance of 100 m from the source, with a spot size of 12mm; the power density would be $88.4\,W/m^2$. *The following thermal equations have been sourced from* [13] *and applied to this scenario.*

The temperature distribution within the active blocking layer, $T_{AB} = 300 + T(x, y, z, t)$, can be found from the heat equation (Eq. 6.2.10).

$$C_{p,eff}\,\rho_{eff}\,\frac{dT}{dt} = \nabla\cdot\left[k_{eff}\,\nabla T\right] + \alpha A_0 I(x,y,t)e^{-\alpha z}, \tag{6.2.10}$$

$$T|_{z=\infty} = T|_{x,y=\pm\infty} = T|_{t=0} = 0$$

Where the surface intensity is generally understood as:

$$I(x,y,t) = I_{xy}(x,y)\,I_0(t) \tag{6.2.11}$$

For a continuous wave laser $I_0$ is constant. The time duration for the laser being active can be considered as a flat top beam with a pulse duration lasting for the illumination period. Thus, the spatial profile of the beam can be written such that $r^2 = x^2 + y^2 = 0$.

$$I_{xy}(x,y) = S_0 e^{-\left(x^2+y^2\right)/r^2} = S_0 e^0 = 1 \tag{6.2.12}$$

For a linear heat equation, the solution can be expressed via Green's function. $A_0$ is the materials absorptivity and $\alpha$ is the absorption coefficient.

$$T(r,z,t) = \frac{A_0\alpha}{C_{p,eff}\,\rho_{eff}}\int_0^t dt_1\, I_0(t-t_1)\,F(z,t) \tag{6.2.13}$$

The function *F* is given by (Eq. 6.2.14) where the thermal diffusivity is $\chi = k_{eff}/\left(C_{p,eff}\,\rho_{eff}\right)$ and erfc is the error function.

$$\begin{aligned} F(z,t) = \frac{1}{2}e^{\alpha^2\chi t}\Bigg\{ & e^{\alpha z}erfc\left[\alpha\sqrt{\chi t} + \frac{z}{2\sqrt{\chi t}}\right] \\ & + e^{-\alpha z}erfc\left[\alpha\sqrt{\chi t} - \frac{z}{2\sqrt{\chi t}}\right]\Bigg\} \end{aligned} \tag{6.2.14}$$

Figure 6.8 shows the temperature increase in kelvin for the active blocking layer when treated as a single composite material. The laser light exposure time is 10 seconds for the 532 nm 10mW CW DPSS laser diode at a distance of one meter.

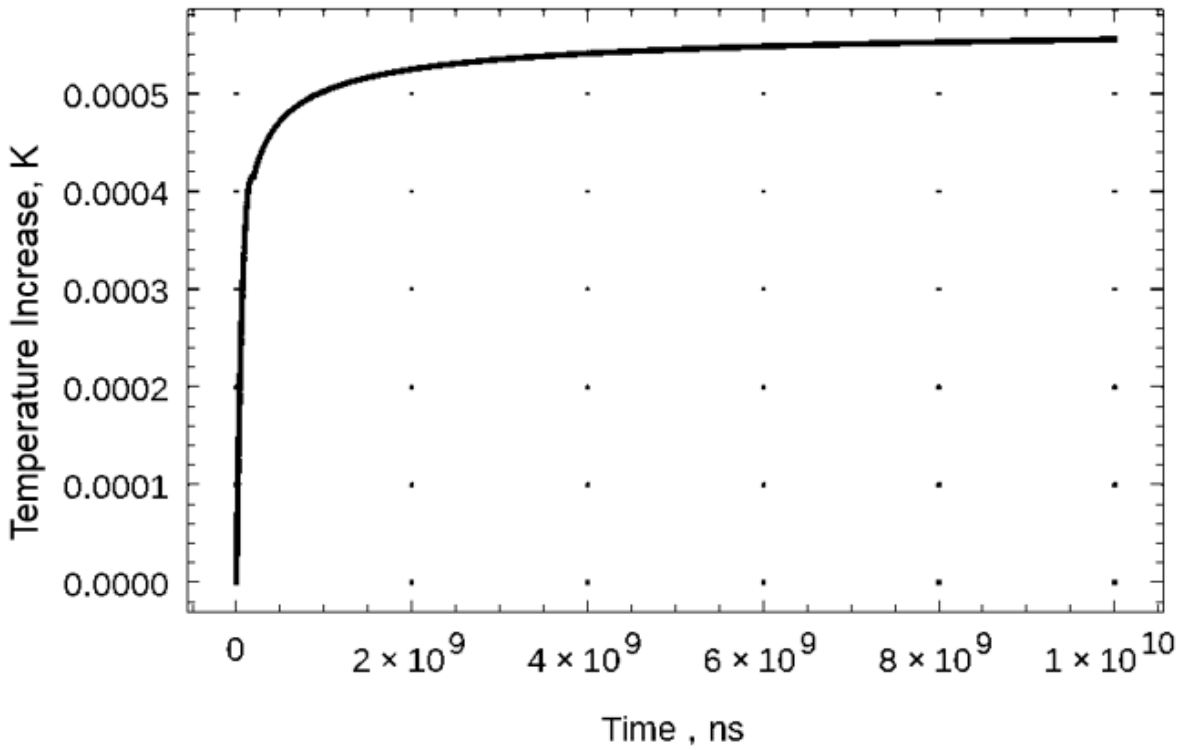


**Figure 6.8.** Temperature increase at the centre point of a homogenous active blocking layer when exposed to a standard 10mW CW laser diode with a distance of one meter.

Obviously, reality may differ due to the 'hot spot' localised heating [14]. However, this small study suggests that the temperature increase of the active blocking layer could cope with the demands of laser light when incident at a distance. The laser spot size increases as the source distance increases; thus, the power of the laser is distributed over a larger area, further aiding damage limitation of localised nanoscale heating.

### 6.3 **405 nm, 532 nm and 650 nm Laser Protection Design**

Like the common 532 nm laser wavelength, deep blue and deep red are also wavelengths of interest due to their ease of accessibility, with blue and red wavelength lasers making up 4% of the laser attacks on aircraft [15,16]. As such, a complete filter would preferably block every laser wavelength without hindering the users' visuals performance (transmission, colour, defined features, etc.). Obviously, this is near impossible but a multi notch filter approach can assist as a multi-functional filter.

As previously discussed, an ideal transmission response for a near 100% transmission across the visible spectrum except for the wavelengths of interest. A multi notch filter provides more complexity for both standard thin film interference filters and the metamaterial filters proposed in this chapter. Figure 6.9 exemplifies an ideal transmission for a multi notch filter that exhibits

three notch locations. The insert provides an illustration of the triple notch metamaterial laser protection eyewear and its aptitude for blocking large angles. Bandwidths for multi notch filters has to be carefully considered and the design may have to sacrifice transmission attenuation in order to keep a sufficient integrated visual photonic response.

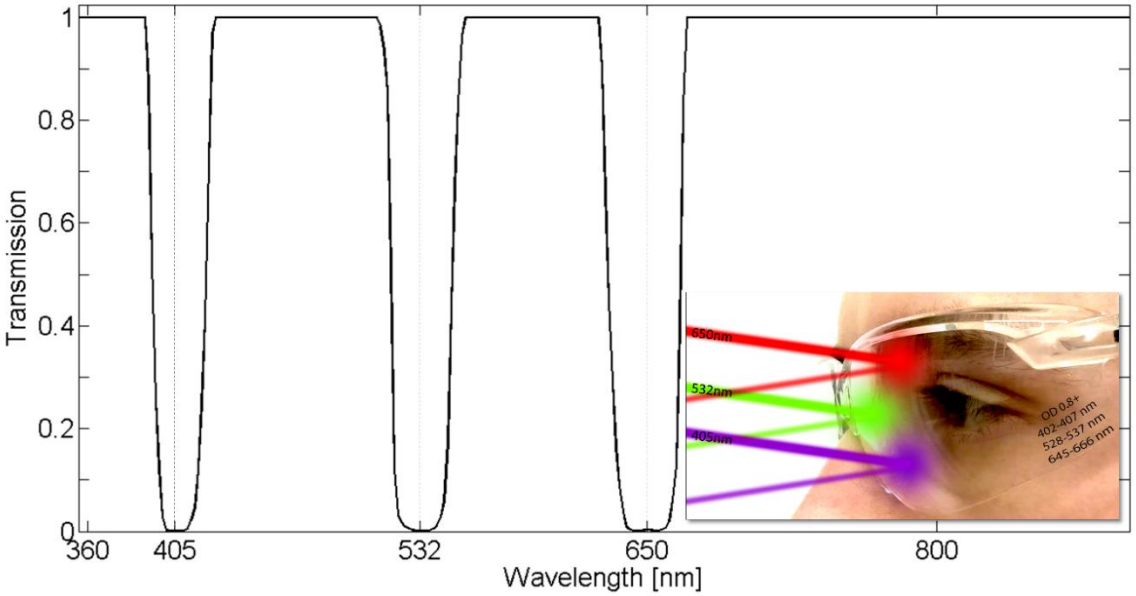


**Figure 6.9.** The conceptual aim example for multi notch device. The figure indicates the ideal transmission response with the insert showing an artist impression of the optical metamaterial notch filter on personnel goggles, deflecting 405 nm, 532 nm and 650 nm laser beam.

### 6.3.8 **Proposed Design**

Comparable to the 532 nm metamaterial filter, the multi notch amalgamates plasmonic nanoparticles with traditional anti-reflection coating theory. However, unlike the 532 nm filter, which employs a simple two-layer coating design, the multi notch occupies several layers that mitigate constructive interference and resonate at the desired wavelength.

The proposed triple notch metamaterial filter assembly can be found in figure 6.10. The design comprises of nine layers that are designed for maximum broadband transmission with three dedicated notches. The metamaterial layers are predetermined according to the chosen blocking wavelength with the remaining four layers acting as matching layers. The layers are designed around quarter wavelengths to allow for destructive interference, with a half-wave layer to achieve a broadening effect for the transmission [8]. The active layers are an odd multiple of the quarter-wave to allow for a sufficient number of nanoparticles within the assembly. The assembly consists of multi-arrayed silver and gold nanoparticles (10 nm in diameter) organised in a primitive hexagonal Bravais lattice planar array form and embedded within a surrounding dielectric that enables a shift in the plasmonic response.

$$d = m\left(\frac{\lambda_0}{4n}\right) \tag{6.3.1}$$

Where $d$ is the layer thickness, $m$ is an odd-multiple, $\lambda_0 = 550nm$ is the reference wavelength and $n$ is the refractive index of the layer.

Figure 6.10 also demonstrates the point at which the particular lasing wavelengths stop due to the metamaterial layers. The 532 nm wavelength is affected by the third layer, the 405 nm wavelength by the fifth layer and the 650 nm by the seventh layer. The location of layer assembly is key to achieve the highest possible transmission outside the metamaterial's resonant positions.

| Air | $MgF_2$ | $Y_2O_3$ | $MM_{532}$ | $Y_2O_3$ | $MM_{405}$ | $HfO_2$ | $MM_{650}$ | $HfO_2$ | $SiO_2$ | Glass |
|---|---|---|---|---|---|---|---|---|---|---|
| 1.00 | 1.38 | 1.79 | $2.38_{Ag}$ | 1.79 | $1.47_{Ag}$ | 1.92 | $2.45_{Au}$ | 1.92 | 1.47 | 1.52 |
| | $0.25\lambda_0$ | $0.25\lambda_0$ | $0.75\lambda_0$ | $0.25\lambda_0$ | $0.75\lambda_0$ | $0.25\lambda_0$ | $1.75\lambda_0$ | $0.25\lambda_0$ | $0.5\lambda_0$ | |

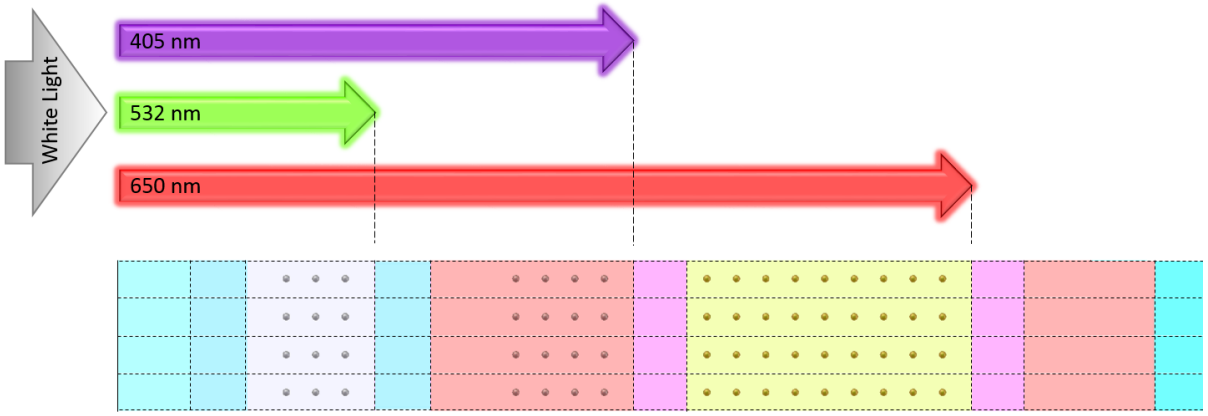


**Figure 6.10.** The configuration of the multi notch metamaterial anti-laser device based on a three-dimensional hexagonal planar array of plasmonic nanoparticles.

The active layers contain silver nanoparticles for the 405 nm and 532 nm blocking layers, and gold nanoparticles for the 650 nm blocking layer. All nanoparticles have a 10 nm fixed diameter. The composite's effective refractive index has been determined by the Maxwell-Garnett formula (Eq. 6.2.1) and converted from permittivity to the complex refractive index (Eq. 6.2.2).

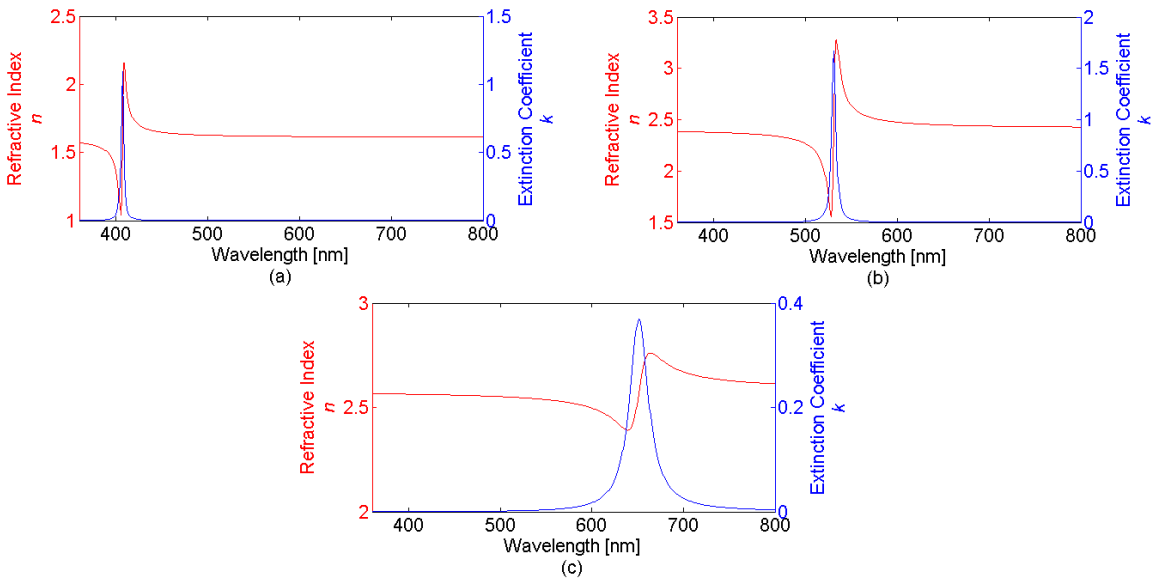


**Figure 6.11.** The effective refractive index and extinction coefficient for the active layers with associated wavelength of (a) 405 nm, (b) 532 nm and (c) 650 nm.

### 6.3.9 **Filter Performance**

Figure 6.12 displays the transmission response for the designed filter under linear polarisation for angler of incidents varying from 0° (solid line), 30° (dashed line) and 60° (dotted line). The red dashed line represents the filter assembly without the plasmonic nanoparticle. It is clear to see the effects the plasmonic resonance has on the design assembly by creating optical notches at specific wavelengths. The filter reveals a bandwidth of 14.1 nm, 25.4 nm and 58.3 nm respectively around the 405 nm, 532 nm and 650 nm central wavelengths. The filter's resonant wavelength is 406 nm, 531 nm and 651 nm.

With increasing incidence angles, it is evident that there is a zero-shift behaviour at the rejection bands. This blocking continues to angle of incidence >85°; however at these extreme angles, the visual transmission is seriously diminished. The overall spectral responses are 64.23% from 360 nm to 700 nm.

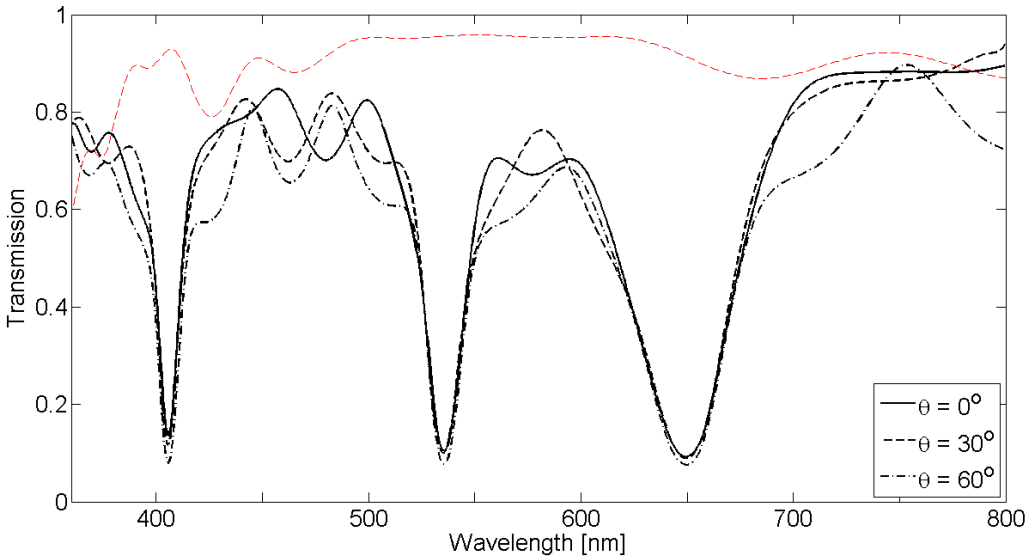


**Figure 6.12.** Transmission of the multi notch anti-laser device versus wavelength for incident angle at $\theta$ = 0°, $\theta$ = 30° and $\theta$ = 60° for linear polarisation. The red dashed line represents the filter design without the metamaterial component at $\theta$ = 0°.

The IVPT response of the triple notch metamaterial filter is 58.4%. The transmission colouration response is at the coordinates ($x = 0.31$ and $y = 0.31$) and the reflection colouration response is at the coordinates ($x = 0.27$ and $y = 0.27$) for a standard CIE 1931 colour map. As seen on the CIE 1931 colour map (figure 6.13), the calculated transmission colouration is colour neutral and the reflection colouration is near neutral but displays a very slight purple hue.

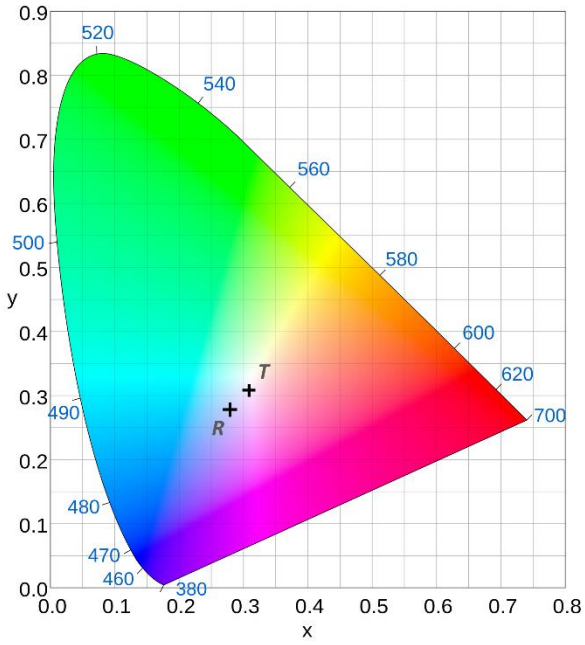


**Figure 6.13.** The CIE 1931 colour map for the transmission (T) and reflection (R) for the triple notch optical metamaterial design.

Figure 6.14 displays the calculated optical density (OD) of the filer at the three blocking wavelengths for all angles between 0 and 85 degrees for linear polarisation. The OD remains above 0.8 across the whole range of angles. This shows that the filter is able to block a common low power Class 3R laser for each wavelength (<7 mW for 405 nm, <9 mW for 532 nm, and <10 mW for 650 nm) of continuous-wave operation at all angles of incidence without blue shift occurring. Furthermore, each blocking wavelength demonstrates that the p and s polarisation modes remain closely related.

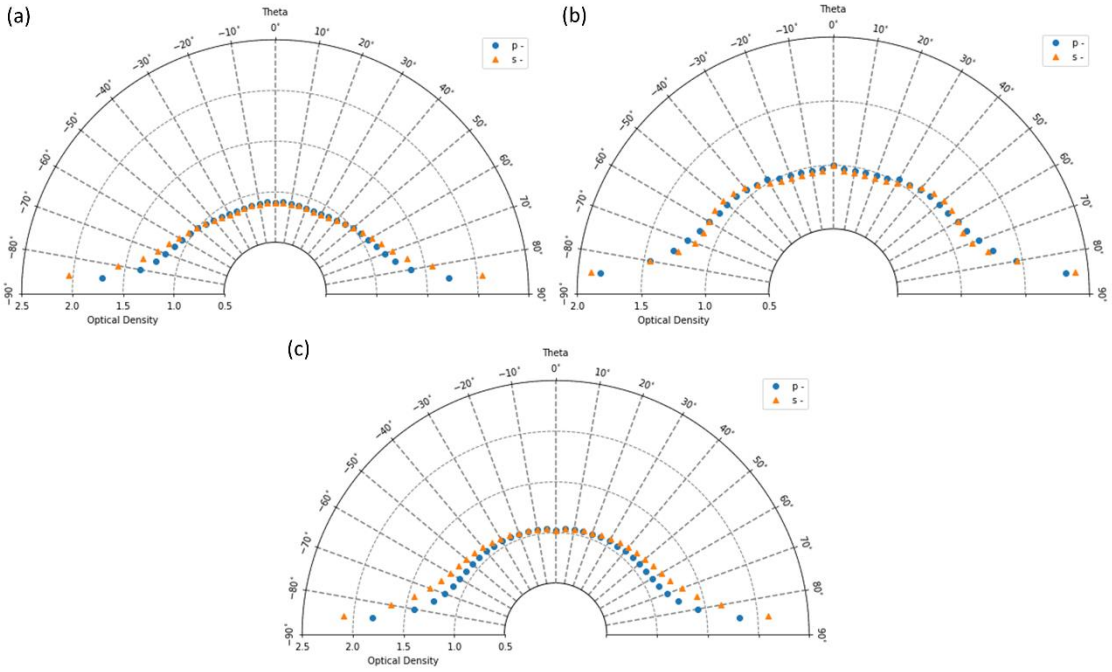


**Figure 6.14.** OD of the designed filter at the laser wavelength of (a) 405 nm, (b) 532 nm and (c) 650 nm. The circle and triangle data points denote the transverse mode of the electromagnetic radiation. Theta represents the angle of incident.

## 6.4 **Device Fabrication**

Manufacturing sub 10 nm structures on a complex three-dimensional plane presents several major challenges [17], especially when dealing with large area fabrication. Overcoming the diffraction limit that is experienced with conventional photolithography methods is now made possible with the introduction of block co-polymers (BCP), which have gained significant attention as a nanoscale self-assembling material [18]. The unique ability of BCPs stems from the tendency to assemble discrete ordered morphologies at equilibrium over a large area [19]. Utilising the ability of the BCP to achieve spot feature dimensions of sub 10 nm [20-22] with a continuously uniform natural period separation could be a progressive move in the fabrication of the described laser protection design. The fabrication process can be enabled with material

systems that include PS-b-PMMA, which can exhibit a high-order natural spacing length of 10 nm to 200 nm depending on the annealing process [23]. Two-dimensional periodic and symmetric metasurfaces have previously been demonstrated and reported by Ju Young Kim et al. in 2016, where it was successfully demonstrated that a large area assembly of structured plasmonic materials using block copolymer self-assembly method was possible [24]. Moving towards a three-dimensional array can be achieved with multi-layer thin film BCP's [25,26] and would empower the next generation of complex optical metamaterials for various applications. Another possible approach is to use the latest dielectric superlens technology with extremely high spatial resolution (15 nm) coupled with a femtosecond laser for direct parallel writing of the proposed device in transparent media [27,28]. The succeeding chapter, *Chapter VII*, presents a novel fabrication process by exploring block copolymers.

## 6.5 **Summary**

The study presented in this chapter discusses an application of optical metamaterials in the form of a laser protection device. The full metamaterial filter design, for both single and multi-notch, provides a novel solution and has not previously been reported. The designs amalgamate the anti-reflection design process with plasmonic nanoparticles to form a three-dimensional metamaterial. The study was conducted using a full-wave electromagnetic solver to view the interaction mechanisms. The designs put forward a single notch filter to protect against a 532 nm laser wavelength, and a triple notch filter to protect against 405 nm, 532 nm and 650 nm. Although, the filter design process could be used to protect against other wavelengths with some design adjustments. The main improvement over traditional thin film filters is the ability to block laser light at all angles and all polarisation states, without experiencing any blue shift behaviour. Higher optical density can be achieved at the expense of a wider bandwidth to block pulsed and higher power CW lasers. This is shown with a comparison to the single notch and triple notch filters. The filters offer a reasonable visual transmission for the user and remain near colour neutral. The addition of the 405 nm and 650 nm notches allow for a complete colour neutral filter by balancing the colouration distribution. The work explores the advancement of the next generation of laser protection devices and offers a promising avenue for future high-performance laser protection systems that could be used in a wide variety of industries.

## 6.6 **References**


[1] P. Johnson and R. Christy, "Optical Constants of the Noble Metals", *Physical Review B*, vol. 6, no. 12, pp. 4370-4379, 1972. Available: 10.1103/physrevb.6.4370.

[2] S. Ozaki and S. Adachi, "Optical Constants of Cubic ZnS", *Japanese Journal of Applied Physics*, vol. 32, no. 1, 11, pp. 5008-5013, 1993. Available: 10.1143/jjap.32.5008.

[3] L. Rodríguez-de Marcos, J. Larruquert, J. Méndez and J. Aznárez, "Self-consistent optical constants of MgF_2, LaF_3, and CeF_3 films", *Optical Materials Express*, vol. 7, no. 3, p. 989, 2017. Available: 10.1364/ome.7.000989.

[4] J. Wray and J. Neu, "Refractive Index of Several Glasses as a Function of Wavelength and Temperature*", *Journal of the Optical Society of America*, vol. 59, no. 6, p. 774, 1969. Available: 10.1364/josa.59.000774.

[5] C. Nelson and J. Crist, "Predicting laser beam characteristics", *Laser Technik Journal*, vol. 9, no. 1, pp. 36-39, 2012. Available: 10.1002/latj.201290006.

[6] S. Kumar, "Effective medium treatment of multicomponent metal-dielectric systems", *Solid State Communications*, vol. 69, no. 1, pp. 107-111, 1989. Available: 10.1016/0038-1098(89)90037-9.

[7] D. Gall, "Electron mean free path in elemental metals", *Journal of Applied Physics*, vol. 119, no. 8, p. 085101, 2016. Available: 10.1063/1.4942216.

[8] H. Angus Macleod, "Chapter 4: Antireflection Coatings", in *Thin Film Optical Filters*, 4th ed., H. Angus Macleod, Ed. CRC Press, 2010, pp. 105-184.

[9] L. Loschky, A. Nuthmann, F. Fortenbaugh and D. Levi, "Scene perception from central to peripheral vision", *Journal of Vision*, vol. 17, no. 1, p. 6, 2017. Available: 10.1167/17.1.6.

[10] H. Mahlein, "Generalized Brewster-angle conditions for quarter-wave multilayers at non-normal incidence*", *Journal of the Optical Society of America*, vol. 64, no. 5, p. 647, 1974. Available: 10.1364/josa.64.000647.

[11] A. Maradudin, *Structured Surfaces as Optical Metamaterials*. Cambridge: Cambridge University Press, 2011, pp. 58-93.

[12] J. Kim, S. Lee, S. Kang and T. Kim, "Materials and design of nanostructured broadband light absorbers for advanced light-to-heat conversion", *Nanoscale*, vol. 10, no. 46, pp. 21555-21574, 2018. Available: 10.1039/c8nr06024j.

[13] L. Yue, "Laser Cleaning of Slotted Components", PhD, University of Manchester, 2012.

[14] L. Khosravi Khorashad, L. Besteiro, Z. Wang, J. Valentine and A. Govorov, "Localization of Excess Temperature Using Plasmonic Hot Spots in Metal Nanostructures: Combining Nano-Optical Antennas with the Fano Effect", *The Journal of Physical Chemistry C*, vol. 120, no. 24, pp. 13215-13226, 2016. Available: 10.1021/acs.jpcc.6b03644.

[15] UK Civil Aviation Authority, "Laser Incidents reported to the UK CAA 2016", Civil Aviation Authority, 2016.

[16] Federal Aviation Administration, "Reported Laser Incidents for 2016", Federal Aviation Administration, 2016.

[17] X. Zhang, C. Sun and N. Fang, "Manufacturing at Nanoscale: Top-Down, Bottom-up and System Engineering", *Journal of Nanoparticle Research*, vol. 6, no. 1, pp. 125-130, 2004. Available: 10.1023/b:nano.0000023232.03654.40.

[18] M. Park, C. Harrison, P. Chaikin, R. Register and D. Adamson, "Block Copolymer Lithography: Periodic Arrays of 1011 Holes in 1 Square Centimeter", *Science*, vol. 276, no. 5317, pp. 1401-1404, 1997. Available: 10.1126/science.276.5317.1401.
[19] F. Bates and G. Fredrickson, "Block Copolymer Thermodynamics: Theory and Experiment", *Annual Review of Physical Chemistry*, vol. 41, no. 1, pp. 525-557, 1990. Available: 10.1146/annurev.pc.41.100190.002521.
[20] M. Kim and G. Yi, "Nanostructured Colloidal Particles by Confined Self-Assembly of Block Copolymers in Evaporative Droplets", *Frontiers in Materials*, vol. 2, 2015. Available: 10.3389/fmats.2015.00045.
[21] A. Horechyy et al., "A Step-Wise Approach for Dual Nanoparticle Patterning via Block Copolymer Self-Assembly", *Advanced Functional Materials*, vol. 23, no. 4, pp. 483-490, 2012. Available: 10.1002/adfm.201201452.
[22] J. Chai, F. Huo, Z. Zheng, L. Giam, W. Shim and C. Mirkin, "Scanning probe block copolymer lithography", *Proceedings of the National Academy of Sciences*, vol. 107, no. 47, pp. 20202-20206, 2010. Available: 10.1073/pnas.1014892107.
[23] F. Ferrarese Lupi et al., "High Aspect Ratio PS-b-PMMA Block Copolymer Masks for Lithographic Applications", *ACS Applied Materials & Interfaces*, vol. 6, no. 23, pp. 21389-21396, 2014. Available: 10.1021/am506391n.
[24] J. Kim et al., "Highly tunable refractive index visible-light metasurface from block copolymer self-assembly", *Nature Communications*, vol. 7, no. 1, 2016. Available: 10.1038/ncomms12911.
[25] A. Tavakkoli K. G., S. Nicaise, K. Gadelrab, A. Alexander-Katz, C. Ross and K. Berggren, "Multilayer block copolymer meshes by orthogonal self-assembly", *Nature Communications*, vol. 7, no. 1, 2016. Available: 10.1038/ncomms10518.
[26] B. Kuila, P. Formanek and M. Stamm, "Multilayer polymer thin films for fabrication of ordered multifunctional polymer nanocomposites", *Nanoscale*, vol. 5, no. 22, p. 10849, 2013. Available: 10.1039/c3nr03607c.
[27] W. Fan, B. Yan, Z. Wang and L. Wu, "Three-dimensional all-dielectric metamaterial solid immersion lens for subwavelength imaging at visible frequencies", *Science Advances*, vol. 2, no. 8, p. e1600901, 2016. Available: 10.1126/sciadv.1600901.
[28] Z. Wang et al., "Laser micro/nano fabrication in glass with tunable-focus particle lens array", *Optics Express*, vol. 16, no. 24, p. 19706, 2008. Available: 10.1364/oe.16.019706.

# CHAPTER VII. EXPERIMENTAL DEMONSTRATION OF DESIGNED SHIFT-FREE OPTICAL NOTCH FILTERS

The chapter deliberates on the limitation of optical lithography as a method for large area nano array features and presents a promising solution in the form of self-assembled layers. The self-assembly is provided from the block copolymer interactions and produces defined nanofeatures through microphase separation. The structured block copolymer layer has the ability to selectively impregnate the features with metallic nanoparticles giving rise to ordered plasmonic topographies. This chapter examines the microphase separation through a simulation study and experimentally verifies the solution. The experimental work affords a proof of concept for a shift-free wide-angle metamaterial narrowband filter for blue light.

## 7.1 **Optical and Alternative Lithography Methods**

Optical lithography, or photolithography, is a process widely used through the microfabrication process. It is a technique to pattern thin films, using light to transfer a geometric pattern to the thin film/substrate. This is achieved through the use of a photomask, which displays the geometry pattern, and a photosensitive film. A sequence of chemical and physical treatments is used to etch the exposed pattern and deposit new material in the desired location. This method is used for the fabrication of complex CMOS circuits which may cycle through the optical lithographic process up to 50 times [1].

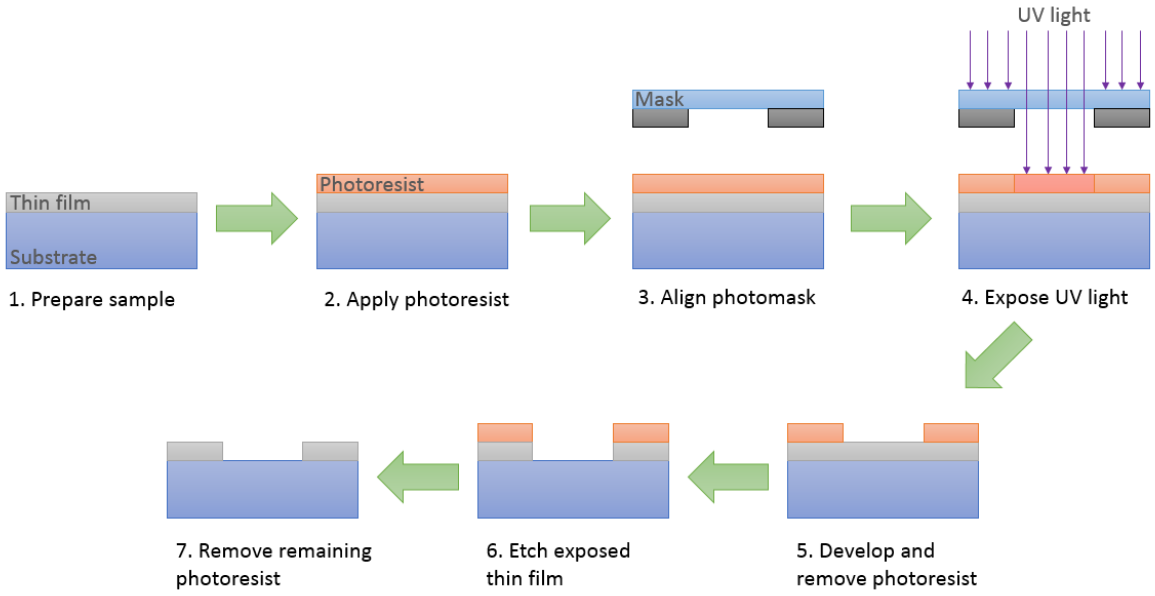


**Figure 7.1.** Simple illustration of the optical lithography process with positive resist.

### 7.1.1 **Diffraction Limit**

Metamaterials can be, and are often, much simpler than CMOS designs. Optical lithography has been used to develop many metamaterial [2]. The repeatable feature displayed over a large area is a key principle for metamaterials. However, optical lithography has limitations that prevent achieving optical metamaterials who's feature sizes are $a \ll \lambda/10$. This limitation is known as the diffraction limit.

In 1873, physicist Ernst Abbe identified that light waves cannot be detained to a minimum resolvable distance in order to image anything less than one half of the input wavelength [3]. This led to the formula of the optical diffraction limit, which describes the resolution limit of far field objects, within microscopes and telescopes.

$$d = \frac{\lambda}{2\,N.A} \tag{7.1.1}$$

Where $d$ is the minimum resolvable feature size, $\lambda$ is the inpuit wavelength of light and $N.A$ is the numerical aperture of the optical system.

(Eq.7.1.2) sets the resolution limit for optical lithography, where the coefficient $k_1$ is a process-related factor with a typical value of 0.4.

$$d = k_1 \frac{\lambda}{N.A} \tag{7.1.2}$$

The capability to project a clear geometric pattern of sufficiently small features onto a thin film or substrate is dependent on the wavelength of light. The present state of the art optical lithographic methods utilises deep ultraviolet light from an excimer laser with wavelength of 248 nm and 193 nm and are able to achieve feature sizes of 50 nm [4]. However, this equipment quickly becomes costly, as does the price of fabricating something so small.

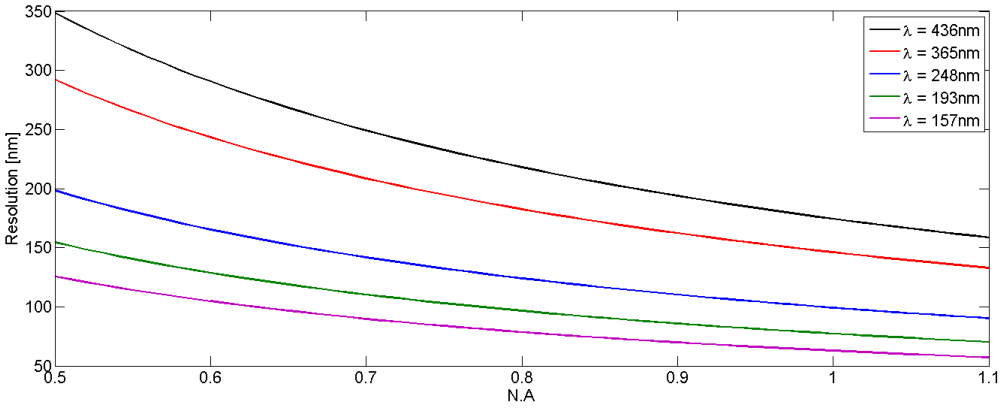


**Figure 7.2.** Optical lithography resolution limit.

Allowing for a very simple cost model for metamaterial manufacturing as a function of the optical lithographic feature size, the cost of making this is proportional to the area of substrate processed divided by the final yield of the metamaterial [5].

$$Yield = 1 - e^{-\frac{(w-w_0)^2}{2\sigma^2}} \tag{7.1.3}$$

$$Production\ Cost = \frac{w^2}{Yield} \tag{7.1.4}$$

Where $w$ is the feature size in nm, $w_0$ is the ultimate resolution and $\sigma$ is the sensitivity of yield to feature size.

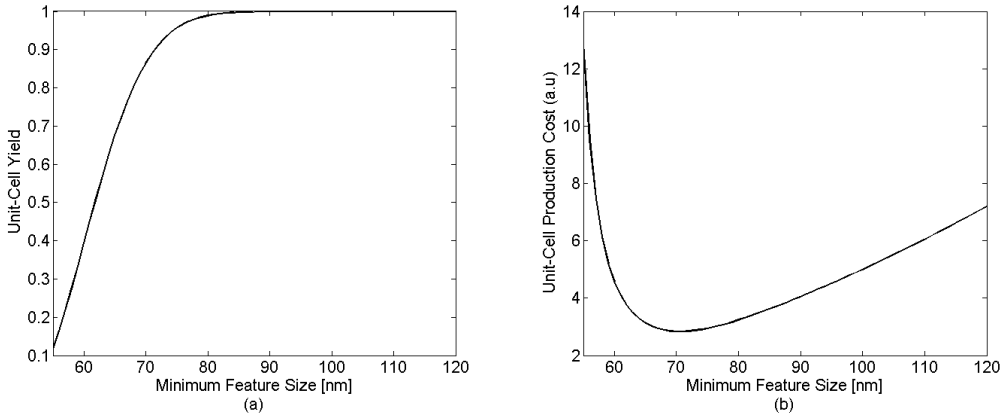


**Figure 7.3.** Simplistic yield and cost model for an Optical metamaterial with $w_0 = 50\ nm$ and $\sigma = 10\ nm$.

It is evident from a simple cost analysis, *adapted from semiconductor industry cost analysis* [5], that optical lithography for optical metamaterials is not a viable route for mass manufacturing due to both the resolution available, the product yield and production cost.

### 7.1.2 **Alternative Lithography Techniques**

Alternatively to optical lithography, other fabrications methods have been employed throughout the development of metamaterials and nanoscale features.

#### **Electron Beam Lithography**

Electron beam, or E-beam lithography is a method that advances the resolution limit of optical lithography and can achieve sub-10 nm resolution. E-beam is a form of maskless lithography but can only provide low-volume production with a main target of research and development [6]. The difficulty with E-beam is achieving a large area but it does allow for the flexibility of complex unit-cell designs.

E-beam lithography works by focusing a beam of electrons by an electromagnetic force. Unlike the optical lithography where the resist is photo sensitive, the resist for e-beam has to be sensitive to electrons.

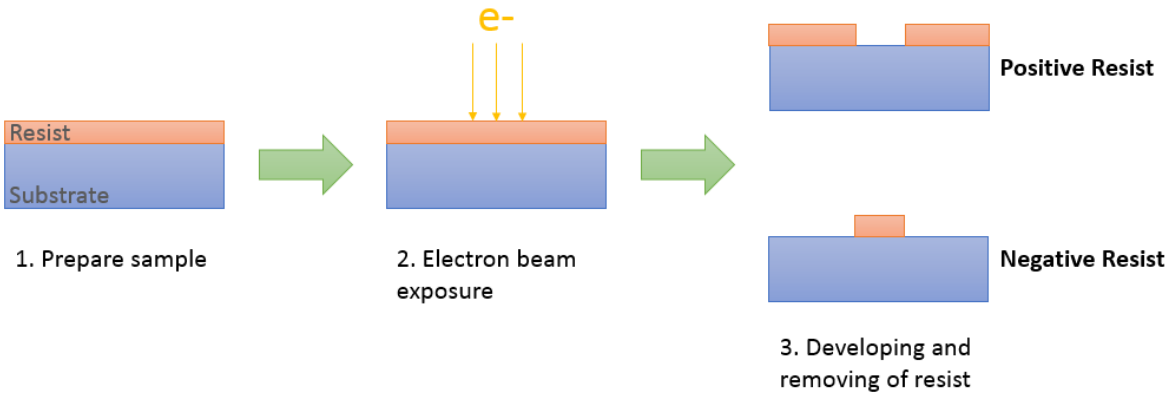


**Figure 7.4.** Simple illustration of the electron lithography process.

The minimum exposure time ($T$) for a given area ($A$) depends on the dose ($D$) and the beam current ($I$).

$$T = \frac{DA}{I} \tag{7.1.5}$$

For example, to expose a two-dimensional area of 10cm by 10cm, with a dose of $10^{-3}$ coulombs/cm$^2$ and a beam current of $10^{-9}$ amperes, the minimum write time would be 1157 days, assuming continuous writing without any stoppages. Like optical lithography, clearly this is not a viable route for optical metamaterials.

## Colloidal Lithography

Colloidal or microsphere lithography is a method for attaining ordered nanostructures over a large area [7]. The process can be used as a mask, template or super-resolution optical lithographic assist. The method involves a distributed uniform layer of microspheres, tightly compact, displaced on a substrate or resist layer.

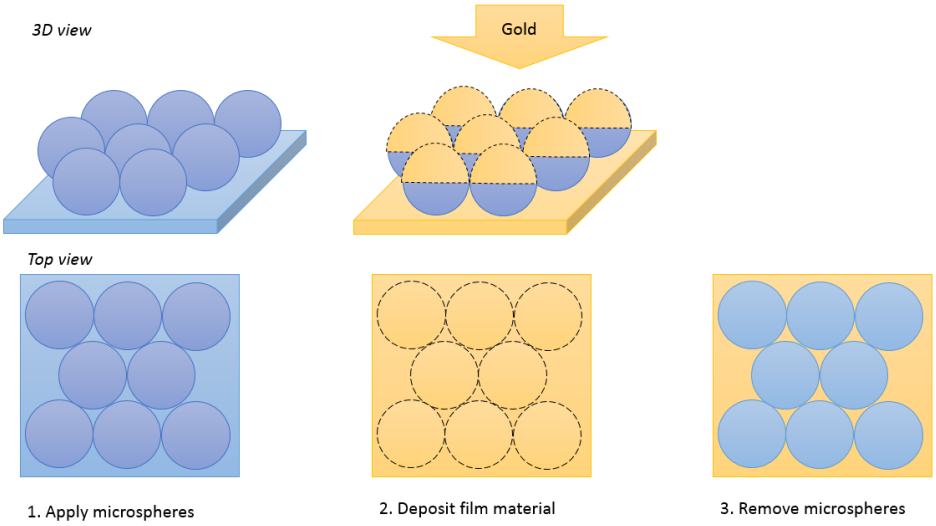


**Figure 7.5.** Simple illustration of the colloidal lithography process.

Figure 7.5 shows a simplistic example for the process of using microspheres as a mask for creating a large area nano patterned array. Applying multiple layers of microspheres can result in some complex features after deposition.

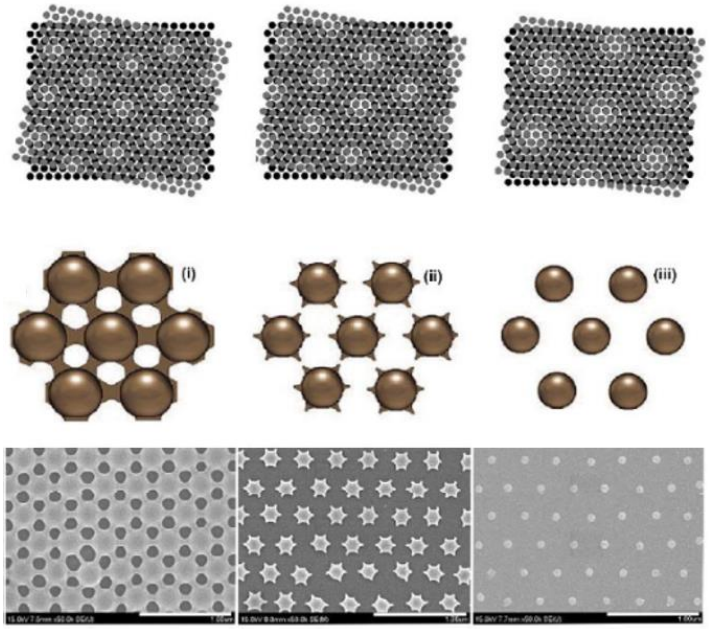


**Figure 7.6.** Example of applying multiple layers of microsphere arrays for increased complexity of nano features. *Adapted from* [8].

The colloidal lithography process often involves all-dielectric microspherical particles. When illuminated the all-dielectric microspheres converge in such a manner than the light becomes strongly confined into a jet, namely 'photonic nanojet' (PNJ) [9]. This PNJ has the ability to overcome the diffraction limit and has achieved resolvable features of down to 45 nm under white light [10]. The PNJ can also be used to expose a photoresist to create nanoparticle arrays or remove a thin film [11].

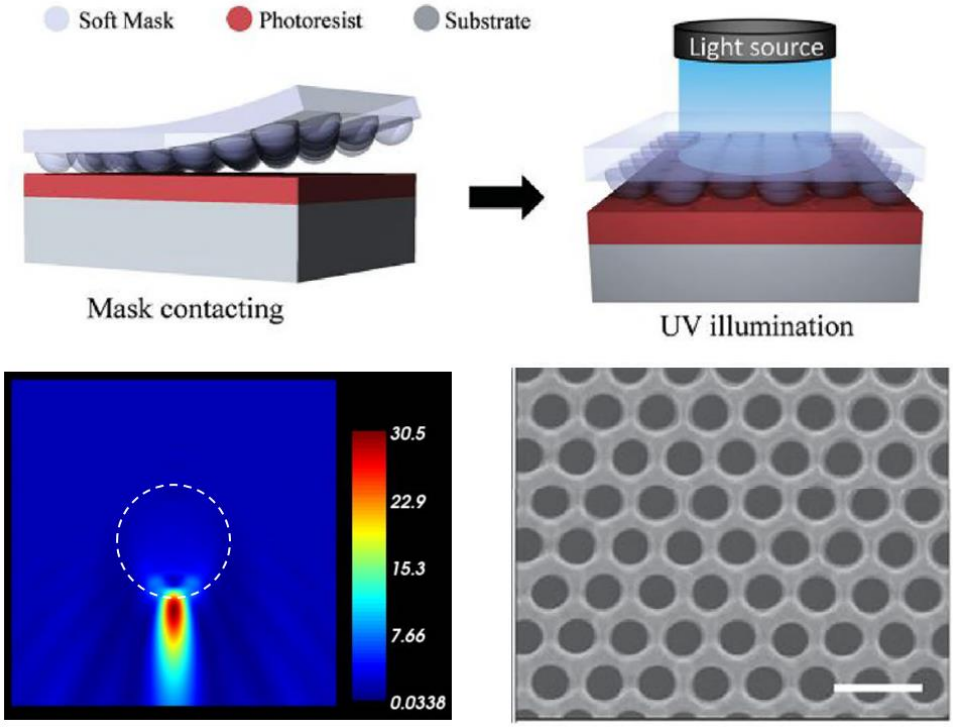


**Figure 7.7.** Example of microsphere arrays for sub-diffraction exposure. *Adapted from* [8].

### Ultrathin Anodic Aluminium Oxide Templates

Ultrathin anodic aluminium oxide (AAO) templates have been broadly used for the fabrication of large area ordered arrays of surface nanostructures. Due to this, they have been employed as a method of fabricating metamaterials [12-14], and other device such as ferroelectric nanocapacitors [15], nanowires [16], flexible nanocone films [17] and more [18]. AAO is a self-organised honeycomb structure of aluminium oxide, that forms high density uniformed pores. The size of the pore holes can range from 5 nm to several hundred nanometers, with interspacing distances varying from few tens of nanometers to a few hundred nanometers [19].

Anodising is an electrochemical process that oxidises the aluminium plate in an electrolyte acid to balance the growth process of the pores and the AAO film thickness. The AAO material ($Al_2O_3$) becomes transparent to visible and near-infrared light. AAO can both be directly grown

on a substrate with an aluminium coating or from an aluminium block and transferred onto a substrate.

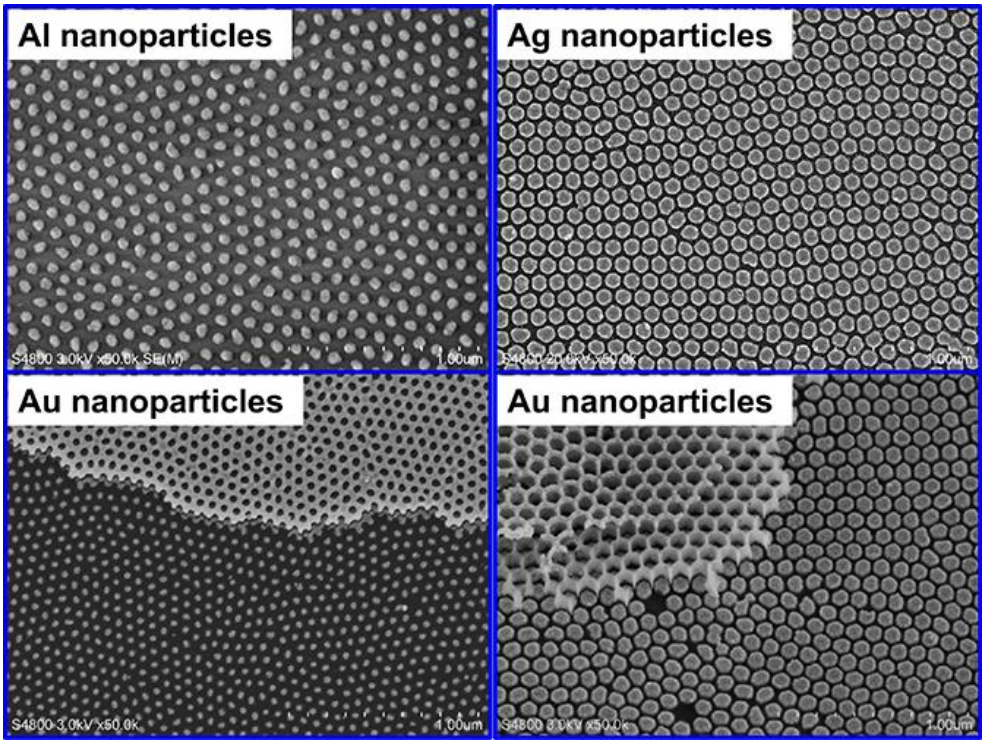


**Figure 7.8.** Ultrathin AAO templates used to fabricate metal nanoparticles via E-beam evaporation [20].

The AAO template bound to a substrate acts as a template for physical vapour deposition (E-beam evaporation). The template can be removed by Kapton tape, 5% phosphate acid at 30°C, or 5%wt NaOH at room temperature. However, AAO is a one-time-use template and can be difficult to bond with the substrate.

### Holographic Lithography

Holographic, or interference lithography is a technique for patterning features in an array without the use of complex systems. This technique can also be maskless. The basic principles of this technique, as the name suggests, takes advantage of the interference of waves. The interference pattern generated from two or more coherent waves can project into a photoresist and record the given interference pattern [21].

Figure 7.9 shows the basic illustration of the holographic lithography steps. The incoming beams, *found in step 3*, can exist at different angles and different polarisations, depending on the type of grating pattern desired. The beams are interfered within the photoresist to give an aerial image, the three-dimensional interference pattern that creates light and dark spots. This aerial interference image induces a chemical change in the resist and results in a latent image

[22]. The aerial image is an electromagnetic interaction and the latent image is a chemical interaction. Ideally, the aerial image and the latent image should match with some slight diffusion appearing in the latent image compared to the sharp aerial image. The exposed photoresist can then be placed within a developer solution to dissolve away the unexposed areas, leaving behind a three-dimensional array pattern.

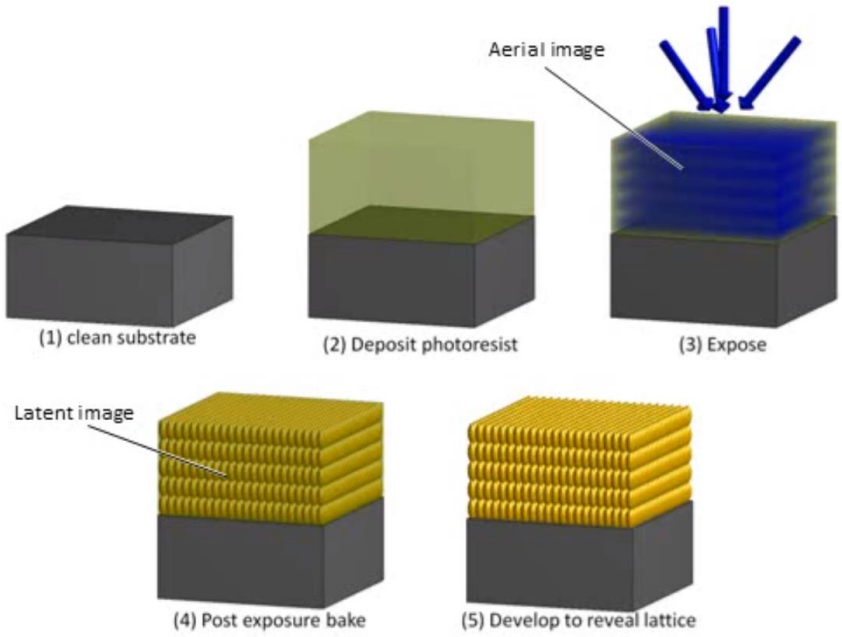


**Figure 7.9.** Simple illustration of the holographic lithography method [23].

Holographic lithography commonly consists of four beams to generate the interference pattern as it allows for the exposure of any of the 14 Bravais lattices depending on the polarisation and angle of incidence for each beam [24]. Through beam synthesis, it is possible to determine the four beam combinations are required to achieve a desired Bravais lattice [25].

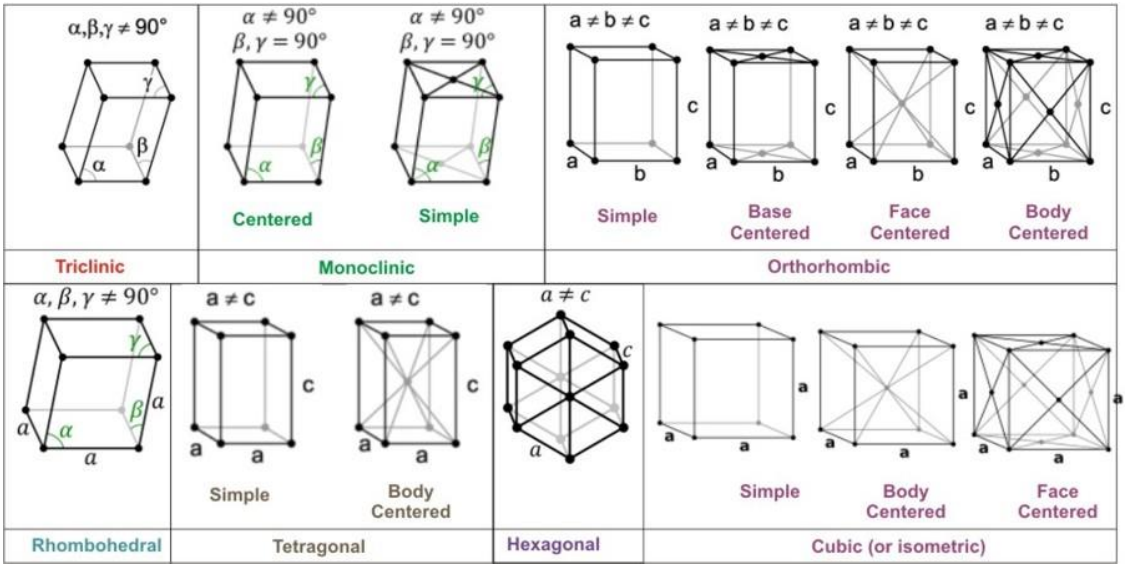


**Figure 7.10.** The fourteen Bravais lattices [26].

One of the main problems associated with holographic lithography is vibrations. When interfering the beams under the presence of vibrations, the aerial image becomes distorted and blurred. Thus, as a replacement for the four beams, a single coherent diffracted beam could be used together with a phase mark placed directly in contact with the photoresist. When exposed by a single beam, the beam would diffract into a select number of beams depending on the phase mask used [27]. This would form the aerial image within the photoresist and would follow the same sequence as described in figure 7.9. The main advantage of this technique is the fact that the phase mask is in direct contact with the photoresist allowing the aerial image to vibrate with the resist. Figure 7.11 shows an example of how multiple beams can be generated through a diffraction grating and the associated pattern when using an extreme ultraviolet light source.

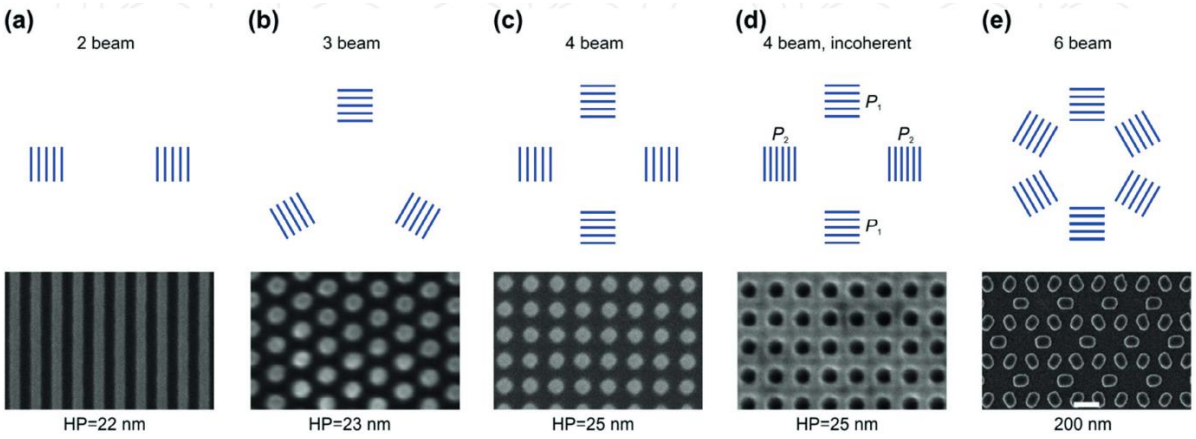


**Figure 7.11.** Schematic of different configuration for generating multiple diffracted beams through a phase mask and the corresponding SEM images of the exposed photoresist [27].

Each of the above methods mentioned have advantages and disadvantages linked with them, including how easy the method is to employ or the cost of setup, etc. However, a growing technique that is being closely explored is the use of self-assembled devices that can create simple or complex two- and three-dimensional nano patterns. Block copolymers are part of the self-assembly group and provide a unique, cheap, and easily employable method for large area nano fabrication.

The experimental component of this research sets out to explore block copolymers capability for fabricating large area nano features. Comparing to the fabrication procedures previously discussed, this method is flexible, cheap and time efficient. The majority of fabrication processes highlighted were not available to draw a direct comparison due to the lack of nanofabrication facilities at Bangor University. This puts block copolymers in a unique position to be able to fabricate nano features without traditional nanofabrication equipment.

## 7.2 **Introduction to Block Copolymers**

Self-assembly of block copolymers (BCPs) is a remarkable technology with the potential to offer low cost substitutes to alternative lithography techniques.

Block copolymers are a distinctive class of polymers that have the ability to self-assemble into ordered microdomains. The domain sizes can vary from 3 nm to 50 nm over a large area. The domain features develop into a repeating pattern displayed over a large area. This makes block copolymer an appealing technology for nanofabrication and metamaterials. The long-range large area lateral order provides an ideal template for patterning without complex lithography methods.

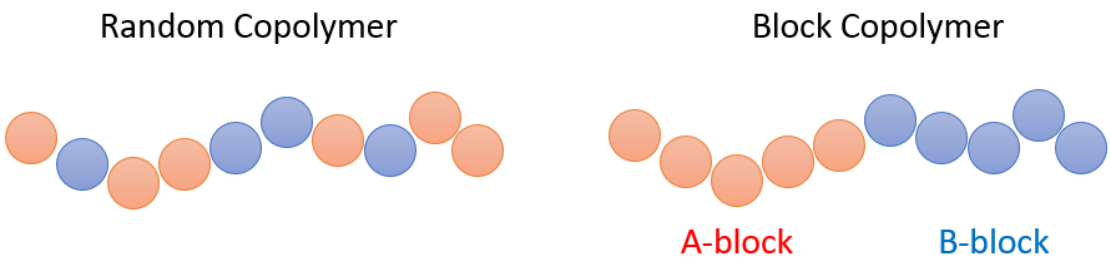


**Figure 9.12.** Diblock copolymer BCP phase diagram.

BCPs contain two or more chemically dissimilar polymers that are covalently linked. Diblock copolymers are the simplest form, with triblock copolymers becoming considerably more complex. Adverse segmental interactions, together with the intrinsic entropy loss results in a separation of the individual polymer blocks into domains. Entropy loss arises due to the nature of the long-chain BCP. The size of the domains is dependent on the molecular weight of the block copolymer chain, with the shape of the domains depending on the fill fraction of A and B polymers. The domain shape for diblock can differ between spheres, cylinders, gyroids and lamellar [28]. Like oil and water, if the segments are immiscible with one another, the material will phase-separate. However, unlike oil and water, the block chains are physically connected to one another which leads to the distinct nanoscopic features.

BCP self-assembled theory is well developed and can effectively forecast the phase diagram of the morphology of the BCPs at equilibrium [29]. Figure 7.13 demonstrates the morphology of the BCPs according to the Flory-Huggins segmental interaction parameter $\chi$ (measure of the incompatibility between the two polymers), the degree of polymerisation $N$, and the volume fill fraction $f$. When polymer A is small in comparison to polymer B, the BCP forms a spherical morphology. As the polymer A content increases, the morphology transitions from spheres to cylinders to gyroids and finally to lamellae. The Flory-Huggins parameter measures the penalty

of mixing of similar polymer types and the degree of polymerisation is related to the molecular weight. The $\chi^N$ factor, or segregation strength, must exceed a certain threshold for self-assembly to occur. As shown in figure 7.13, if the $\chi^N$ factor is below the threshold, the BCP will form a disordered morphology.

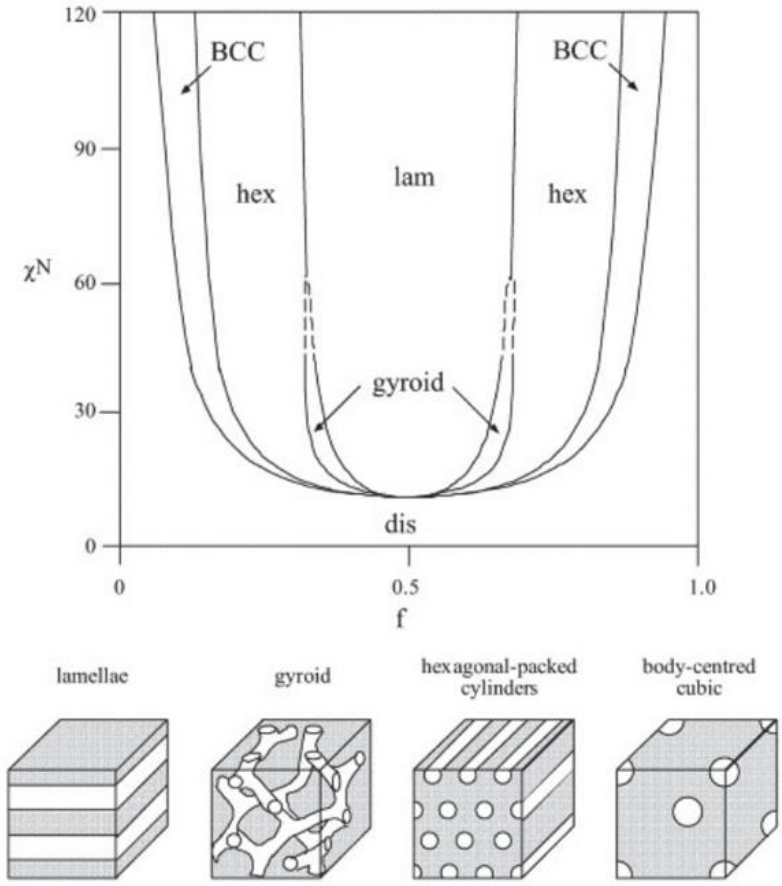


**Figure 7.13.** Theoretical diblock copolymer BCP phase diagram [30].

The BCP chain kinetics are strongly associated with the $\chi^N$ factor. With large values of $\chi^N$, the self-assembly time will be sufficiently large. The BCPs phase separation behaviour is strongly associated with temperature [29].

### 7.2.1 **Block Copolymer Thin Films**

The phase behaviour of block copolymer thin films provides more complications compared to bulk BCPs, owing to the interfacial surface energy of the substrate and the potential confinement effects, which can be imposed at the substrate-polymer interface and the polymer-air interface.

The orientation of BCP microdomains are of vital importance for thin film BCP geometry [31,32]. For template lithographic patterning of the BCP, the orientation must have perpendicular microdomains, particularly for the cylindrical and lamellae domains. However,

a perpendicular orientation is not always sympathetic by nature due to different surface energies of the two polymers between the polymer-air and polymer-substrate. Thus, the BCP thin film morphology is subject to the strength of interfacial interactions at the defined interfaces [33]. Low surface energy or preferential interactions between one of the blocks and the surface or air will consequently produce segregation of that particular block to either the surface or substrate interface of the thin film. To obtain the perpendicular orientation, the substrate surface energy is required to be neutral (balanced interfacial interactions). This enables a non-preferential segregation of the air-polymer-substrate components. There are several methods for neutralising the surface energy and balancing the interactions of the blocks; brush layers [34], confinements [35], external fields [36] and solvent vapour gradient [37].

## 7.3 **Theoretical Evaluation of Block Copolymers**

The simulations of block copolymer interactions have been made accessible with the introduction of PolySwift++ engine that enables a flexible simulation tool for studying complex polymer materials by combining the self-consistent field theory with high-performance computing. The Polyswift++ engine is a C++ object-oriented code language [38].

### 7.3.1 **Self-Consistent Field Theory**

Self-consistent field theory (SCFT) is a prevailing technique for reviewing complex morphologies of multi-component block copolymers and blend mixtures. SCFT qualifies a "systematic coarse-graining of length scales at the molecular level" [39] to competently label meso- and nano- scale features of phase separated block copolymers.

SCFT affords a solution where the Hamiltonian of a complex system can be transformed into a field theory description. The field theory transformation permits discrete density operators to define the Hamiltonian of the block copolymer system as density fields. This transformation further enables the complicated chain-to-chain interaction to be reformulated in terms of a single chain interacting with a chemical potential field $\widehat{\omega}$. The individual polymer density fields can be self-possessed from constrained chain partition functions $q(\vec{r}, s)$, which can be considered as the solution to a modified diffusion equation [40].

$$\frac{\partial q(\vec{r}, s)}{\partial s} = R_{g0}^2 \nabla^2 q(\vec{r}, s) - \widehat{\omega}(\vec{r}) q(\vec{r}, s) \tag{7.3.1}$$

Where $\vec{r}$ is the spatial position, $s$ is the distance along the polymer chain, and $R_{g0}^2$ is the unperturbed radius of gyration with $q(\vec{r}, s) = 1$.

### 7.3.2 **Block Copolymer Modelling**

The Hamiltonian for a dense melt of monodisperse diblock copolymer system is given in (Eq. 7.3.2), according to [40].

$$\widehat{H} = \frac{1}{4R_{g0}^2}\sum_{a=1}^{n}\int_0^1 ds\left(\frac{d\vec{r}_a(s)}{ds}\right)^2 + \rho_0^{-1}\int d\vec{r}\,\chi\,\widehat{\rho}_A(\vec{r})\;\widehat{\rho}_B(\vec{r}) \tag{7.3.2}$$

Where the initial term denotes the free energy of a Gaussian thread model [41]. The second term signifies the Flory-type interaction energy between the distinct polymer chains (*A* and *B*).

The individual polymer density operators for the *A* and *B* species can be described by (Eq. 7.3.3) and (Eq. 7.3.4).

$$\widehat{\rho}_A(\vec{r}) = N\sum_{a=1}^{n}\int_0^f ds\;\delta\big(\vec{r}-\vec{r}_a(s)\big) \tag{7.3.3}$$

$$\widehat{\rho}_B(\vec{r}) = N\sum_{a=1}^{n}\int_f^1 ds\;\delta\big(\vec{r}-\vec{r}_a(s)\big) \tag{7.3.4}$$

Where $0 < f > 1$ describes the fill fraction of the polymers.

The self-consistent field theory yields a partition function (*statistical properties of a system in thermodynamic equilibrium*) that enables the transformation of the described Hamiltonian [40], where *D* is the normalised segmental density.

$$Z = \int\prod_{a=1}^{n}\vec{D}\,\vec{r}_a e^{\{-\rho_0^{-1}\int d\vec{r}\,\chi\,\widehat{\rho}_A(\vec{r})\,\widehat{\rho}_B(\vec{r})\}}\,\delta[\rho_0-\widehat{\rho}_A-\widehat{\rho}_B] \tag{7.3.5}$$

With

$$\vec{D}\vec{r}_a = D\vec{r}_a e^{\left\{-\frac{1}{4R_{g0}^2}\int_0^1 ds\left(\frac{d\vec{r}_a(s)}{ds}\right)^2\right\}} \tag{7.3.6}$$

The targeted self-assembled array is a hexagonal lattice, similar to the designs found in *Chapter VI*. This can provide a template for the selective nanoparticle impregnation, enabling a periodic hexagonal lattice of metallic nanoparticles. The target lattice arrangement for the diblock copolymer is cylindrical features, where the polymer has a fill fraction of $f_A \approx 0.7$ and $\chi^N = 21$.

As seen in figure 7.14, the phase morphology self-assembles over time. The rate of disorder-to-order change is dependent on the blocks, substrate, annealing temperature and environment.

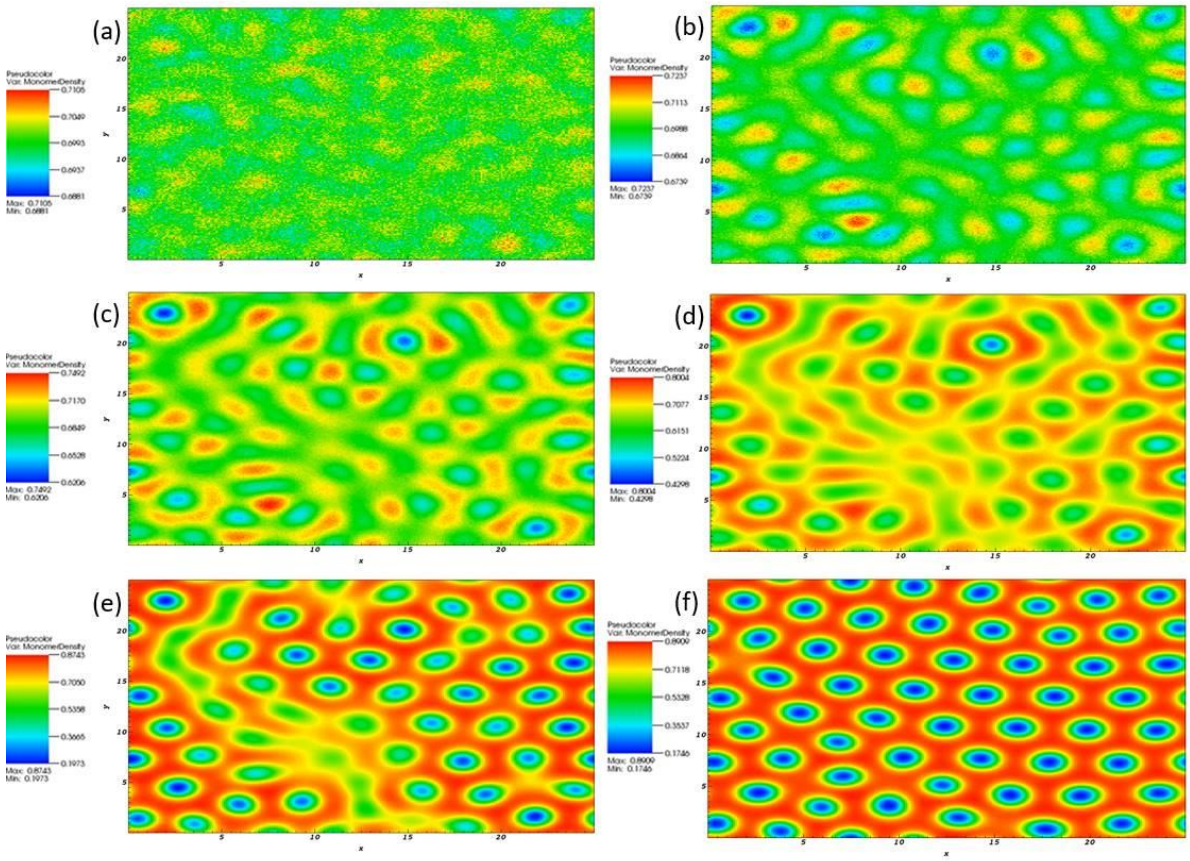


**Figure 7.14.** Time progression microphase change, disorder-order transition, with the diblock copolymer.

Figure 7.14f provides a large area view of the targeted self-assembled features. It is notable that according to the conditions set out under the "perfect" experimental settings, some defects within the template may also exist. Once the thin BCP layer contains the metallic nanoparticle components, the far field response will be averaged accordingly. As such, due to the non-perfect nano array, the resultant response may be broader and dampened compared with a perfectly positioned periodic array. Though, in reality, the lattice configuration is probable to contain some lattice defects.

The BCP thin film can be used to capture nanoparticles through ion exchanges [42] or chemical interactions, or they can be used as a template where one of the polymers has been selectively removed [43].

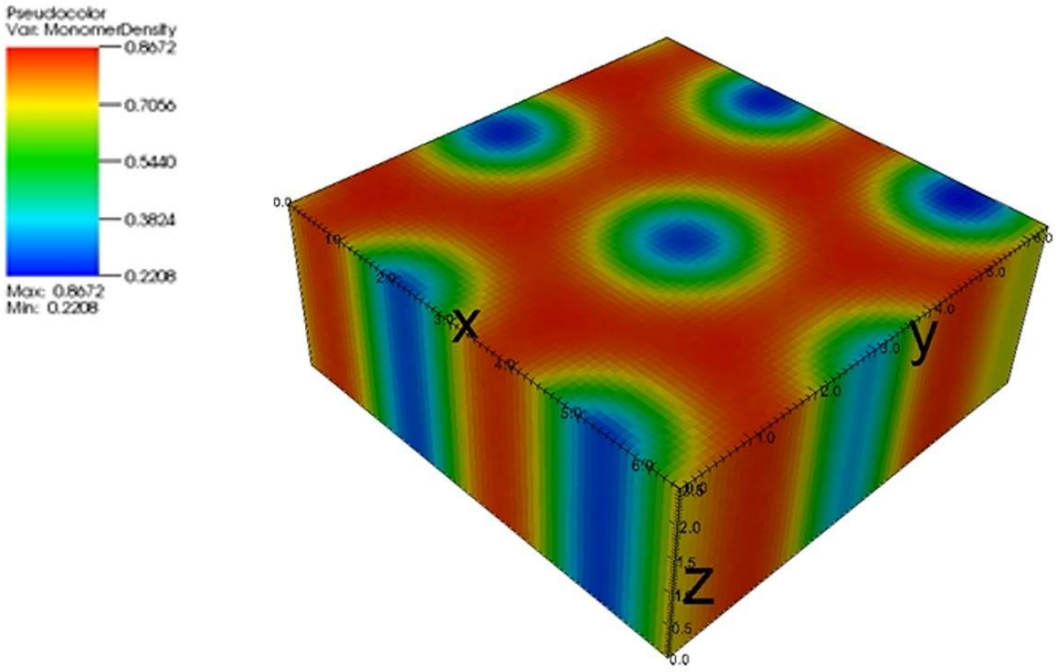


**Figure 7.15.** Three-dimensional BCP thin film formation of 'hex' location.

## 7.4 **Experimental Developments of Block Copolymer Based Optical Filters**

The experimental aspects of this work are to provide a proof-of-concept study for the optical metamaterial filters discussed throughout this thesis. The block copolymers allow for a large area nano arrayed pattern to form as a thin film on a transparent substrate. This BCP thin film is then able to capture the plasmonic nanoparticles, either directly or through ion exchanges, to order the nanoparticles over the entire area of the BCP film. This will demonstrate the capability to study the optical performance, including the shift-free behaviours. The processes, methodology and results are discussed below.

### 7.4.1 **Solvent Vapour Annealing**

BCPs in the thin film form display unique geometry that are demanded for a variety of applications, particularly in the field of microelectronics where uniformed repeated nanofeatures are required. Spin coating is the main method for coating a BCP thin film onto a substrate to enable high uniformity across a large area. This does however present a problem. The rate of the solvent evaporation occurs quickly and traps the BCP chain into states of nonequilibrium, disorganised and poorly ordered. A method to combat the undesired states is to introduce mobility to the polymer chain to further facilitate microphase separation and annihilation of defects [44]. This can be achieved with solvent vapour annealing (SVA).

SVA provides a solution to anneal BCP films that are sensitive to thermal degradation and is an effective method to remove defects. By providing a solvent vapour, the method enables mediation between the polymer-air surface energy and acts as a neutral layer. This permits the perpendicular orientation of the microdomains without the need for a neutral brush layer on the substrate [44]. Furthermore, through the selection of solvent, an asymmetric swelling can occur that alters the relative volume ratio between the BCP blocks, forcing a change to the morphology of the BCP film.

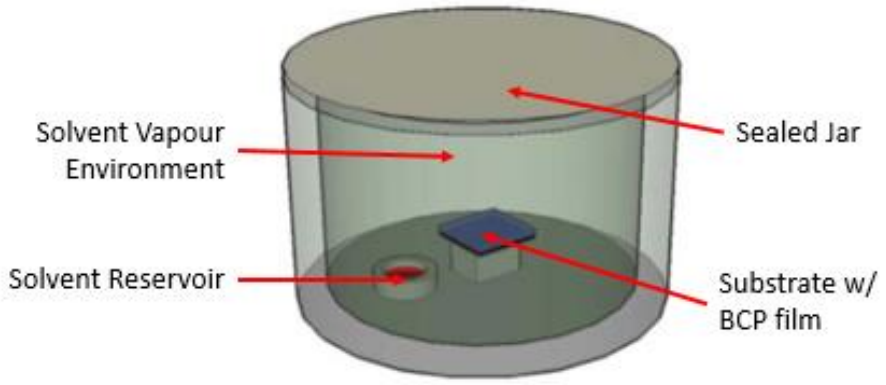


**Figure 7.16.** Diagram set up of a closed jar solvent vapour annealing chamber.

A liquid solvent is kept in a solvent reservoir and placed inside an airtight chamber. Sufficient time should be given to allow the solvent to vaporise within the chamber and build up the atmosphere. Once adequate time enables a vapour atmosphere, the BCP film can be placed within the chamber. The volume and surface area of solvent in the reservoir, and the volume, temperature, humidity and annealing time in the chamber, determines the vapour pressure inside the chamber. This dictates the morphology of the BCP thin film at its swollen state. For a more controlled study on the effects of the morphology, the chamber could be altered to allow inert gases to flow. This will enable for a more precise control over the chamber environment.

Thus, solvent vapour annealing is an important process for obtaining a functional and stable morphology for the block copolymer thin film. The procedure's main effect is to swell the BCP film and provide mobility to the polymer chains in order to form well-organised structure [30].

### 7.4.2 **Block Copolymer Thin Film Methodology**

The methodology consists of two distinct steps; the material preparation and the film preparation.

#### 7.4.2.1 **Materials and Sample Preparation**

The development and preparation for the materials and sample are an important initial step. They form the backbone for developing a BCP film with metallic features by providing the necessary building blocks.

**Block Copolymer Solution**

The diblock copolymer in powder form was purchased from Polymer Source Inc. The obtained BCP was a poly(styrene-*block*-ethylene oxide) with a molecular mass distribution of PS(480k)-*b*-PEO(227k). The BCP powder of 1%wt was dissolved within toluene. The solution was placed on a magnetic stirrer for 12hr+ at room temperature to fully dissolve the polymers within the solution.

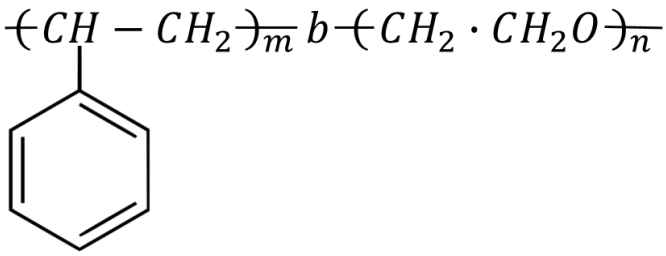

**Figure 7.17.** PS-*b*-PEO DiBlock Copolymer structure.

**Metallic Nanoparticles**

Silver nitrate salt ($AgNO_3$), polyvinylpyrrolidone (PVP) and Industrial Methylated spirits (IMS) were purchased from Sigma Aldrich and used without further purification. The preparation of silver nanoparticles (AgNPs) was carried out following the methods previously reported by Ayyappan et al [45]. The $AgNO_3$ was added to a stirred solution of PVP in IMS with a weight ratio of 1:5:80 ($AgNO_3$:PVP:IMS). IMS has been used as a substitute to Ethanol. The solution was heated to reflux for 3 hours, before cooling and storing. Upon full dissolution, the solution turned to yellow colouration. The presence of the PVP is to act as a surface stabiliser, growth modifier, nanoparticle dispersant, and reducing agent. The ratio of $AgNO_3$ and PVP can be altered in order to obtain different size nanoparticles. The distribution of size is dependent on the length of time for reflux.

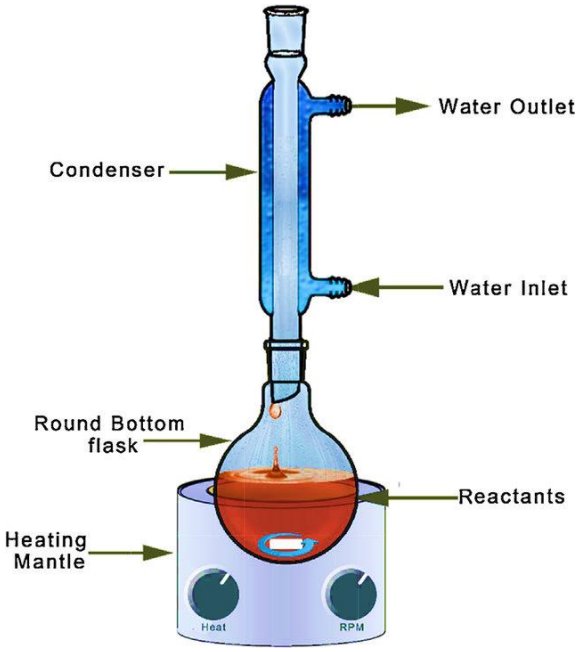


**Figure 7.18.** Schematic diagram of reflux setup [46].

**Substrate Cleaning**

Numerous glass substrates were used throughout the experimental aspects. It is important to consider contamination when using substrates for application purposes, as any contaminant on the substrate could render the results invalid. A contaminant on the substrate could act as a confinement artefact that would result in a distinct variation of the block copolymer from sample to sample and alter the morphology. Considering this, cleaning of the substrate is a significant aspect and arguably one of the most important steps for establishing consistent and quality results. To overcome these issues, the samples were submerged in acetone and sonicated for 20 minutes. Once removed, the samples were dried with a pressured nitrogen gun and rinsed in toluene. Following this, the samples were submerged in toluene and sonicated for a further 20 minutes. Again, followed by drying the substrate with nitrogen. The toluene wash alters the substrate's surface chemistry and surface energy, which is an important factor concerning the BCP features and orientation.

#### 7.4.2.2 **Development Process**

The development process brings together the essential components to make the optical metamaterial notch filter.

Note that previous chapters within this theiss have focused on the laser wavelength 532 nm, this chapter focuses of 405 nm due to the ease of fabrication and availability of materials that are allowed within Bangor Universities E-beam evaporator. Due to the lack of sulphides and

fluorides available, shifting the resonant wavelength to 532 nm is not possible; thus, the BCP will act as the surrounding medium to focus of blue laser light.

### Block Copolymer Films

The BCP film was prepared by spin coating the BCP solution at 3000rpm for 30 seconds, providing a film thickness of ~60 nm. The polymer film spreads over the substrate surface through centrifugal forces, allowing the volatile toluene solution to be driven off the substrate surface. This technique enables the BCP film to distribute over a large area. Controlling the film thickness is achieved via spin speed and acceleration, the concentration of the BCP solution and the volatility of the solvent [47].

Once the BCP film has completed the spin coating operation, the sample is immediately placed within the solvent vapour chamber and place in a preheated oven at 50°C for one hour.

The equipment used for the BCP thin film developed was an Ossila L2001A3 spin coater and a Binder ED-S 056 scientific oven.

### Nanoparticle Encapsulation

Upon obtaining the BCP desired template, with verification through AFM imaging, the colloidal nanoparticles can be added. This is achieved by drop casting the nanoparticle solution onto the BCP film. The colloid should remain on the film for a short period of time to allow for the BCP to swell with the presence of ethanol. Spin coating can be applied at a slow rate of 100rpm for a set amount of time. This time depends on the time required for swelling and the concentration of the nanoparticles in solution. The attendance of the nanoparticle reacts with the PEO polymer, where the nanoparticles bond with the PEO cylinders, and are guided into place with the assistance of the PS swelling and exposing the PEO.

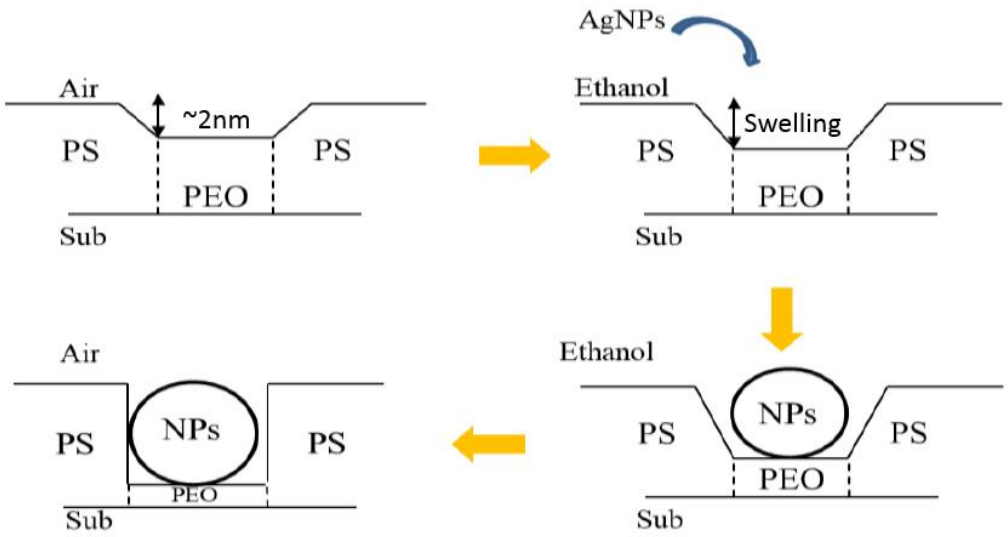


**Figure 7.19.** Schematic representation of selective impregnation of nanoparticles.

Other techniques are available such as selectively etching one of the polymers with E-beam deposition of the metals [48], or pre-swelling in exclusively ethanol and spin coating a dissolved metallic salt on the BCP template where the salt solution enables a reduction of ion exchanges with the PEO polymer to develop the metallic nanoparticles [49]. When using the ion exchange approach an additional SVA is required with a Hydrazine Hydrate atmosphere to start the reduction process.

### Multilayer Assembly

Multi-layer BCP coatings with the presence of plasmonic nanoparticles are important for achieving increased attenuation to the transmission, which in turn increases the optical density. The fabrication process for developing a double layered BCP metafilm for this experiment is presented in figure 7.20. The process involves cross-linking a PDMS spacer layer between the two BCP layers so that they do not interact with one another.

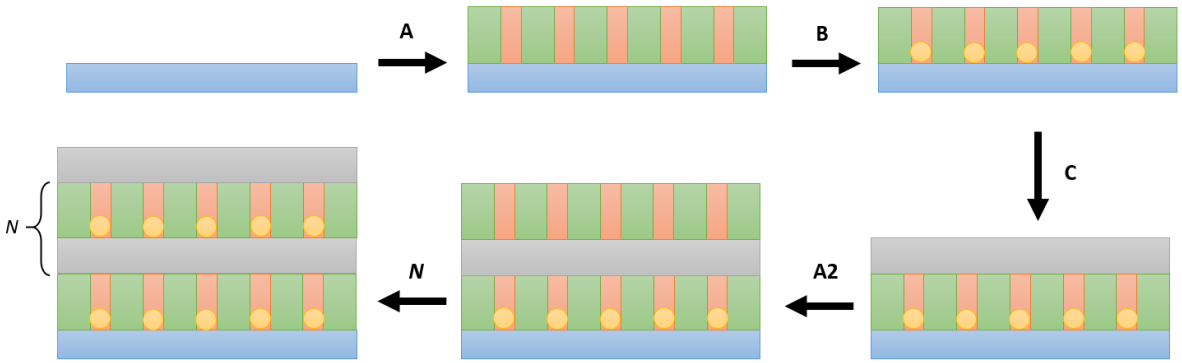


**Figure 7.20.** Schematic representation of the multi-layer fabrication process. (A) self-assembly of the BCP into cylinder patterns, (B) deposition of the silver nanoparticles, (C) spin coat PDMS layer and cross-link through heating, (A2) deposit the second BCP layer. The process continues *N* times.

In an ideal case, and to cater for additional target wavelengths, the BCP film would act solely as a sacrificial layer that could be etched away with $O_2$ reactive ion etching treatments to leave behind the plasmonic nanoparticles within the desired array. Without the attendance of the BCP film, an alternative dielectric with the required refractive index could be applied. As discussed in previous chapters, the change in refractive index surrounding the nanoparticles will alter the plasmonic resonance wavelength. The process could be repeated to build up multiple layers, figure 7.21.

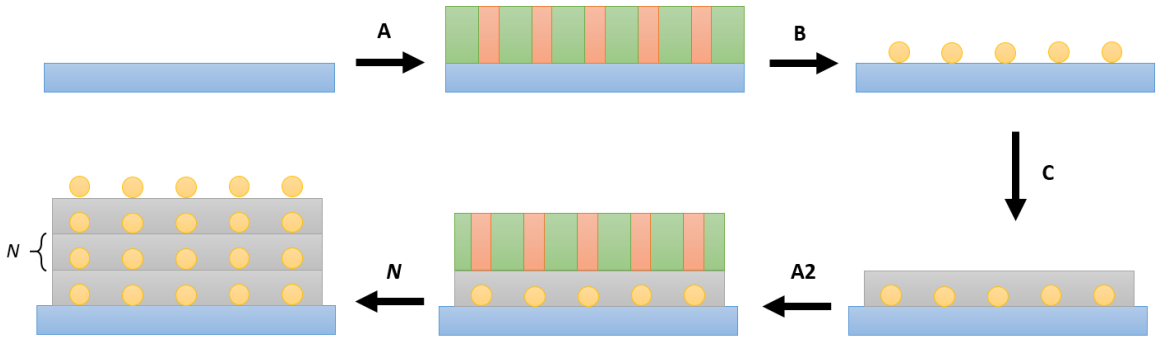


**Figure 7.21.** Schematic representation of the multi-layer fabrication process. (A) self-assembly of the BCP into cylinder patterns and add the desired plasmonic nanoparticles, (B) $O_2$ RIE treatment to obtain the nanoparticle array, (C) deposit a dielectric film to surround the nanoparticles, (A2) deposit the second BCP film. The process continues *N* times until the desired number of layers is obtained.

### 7.4.3 **Surface Morphology Characterisation**

The surface morphology of the BCP thin film was characterised by a Veeco Dimension 3100/V atomic force microscope (AFM). The AFM was used to image the top surface morphology of the BCP sample in tapping mode.

The morphology of the block copolymer film successfully assembled into the cylindrical phase and presents a pentagonal lattice, figure 7.22. However, the template displays defeats in the lattice configuration. The defects can occur from a number of sources, including surface chemistry, time of annealing, temperature of annealing, inexact molecular composition, etc. The PS intersectional distance between the PEO pores is ~43 nm with the PEO pore diameters ~22 nm. Figure 7.22b highlights four areas on the AFM image of the BCP template, figure 7.22a, and demonstrates that the dimensions are near uniform when compared with one another, despite the template defects. The percentage of defects calculated for a given 1 $\mu m^2$ area is 68.3% with a ±3 nm tolerance. This has been calculated using standard AFM software tools coupled with MATLAB image analysis tools. The defect percentage is extremely high and could be mitigated through a number of BCP experimental improvements. This would

drastically improve the metamaterial's optical performance, particularly the bandwidth due to the interspatial distance effecting the near field coupling of neighbouring particles.

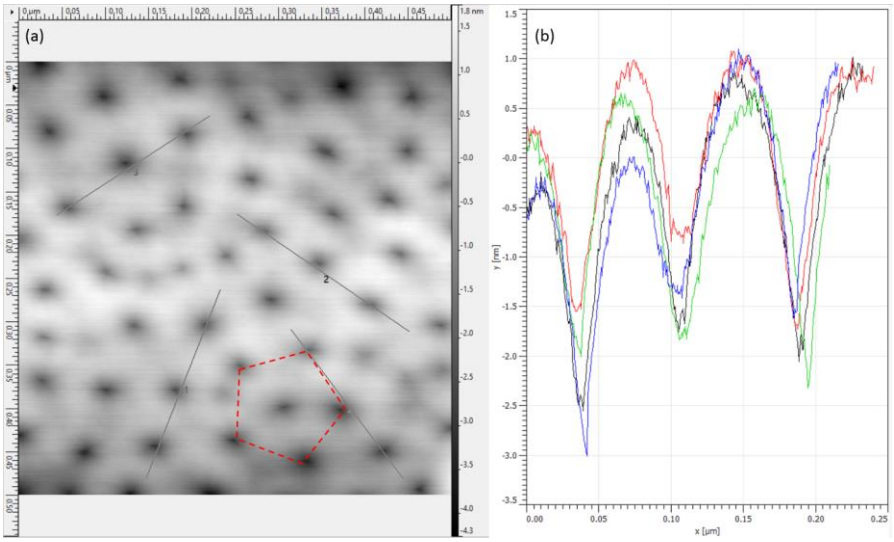


**Figure 7.22.** (a) AFM image and (b) topographical profile.

The assembly stages of the multi-layer approach, figure 7.20, are shown in the AFM images found in figure 7.23. The phase separation of the BCP thin film can be clearly identified on the initial substrate glass (figure 7.23a) and on PDMS spacer layer (figure 7.23d). The dielectric PDMS layer presents a flat surface without distinct topological features (figure 7.23c). The silver nanoparticles have successfully been captured by the block copolymer thin film to a degree. However, not all the PEO features were successfully impregnated and the size of the nanoparticles greatly vary (figure 7.23b). The consequences to having a deviating particle size range results in a broadening of the absorption peak. Furthermore, the interspatial distances between the particles also greatly vary and can also lead to a broader absorption peak. Regardless of the lack of distinct uniformity in the nanoparticle array, they do still interact with the electromagnetic spectrum and validate the concepts presented within this thesis, with a particular focus on the wide-angle blocking capabilities.

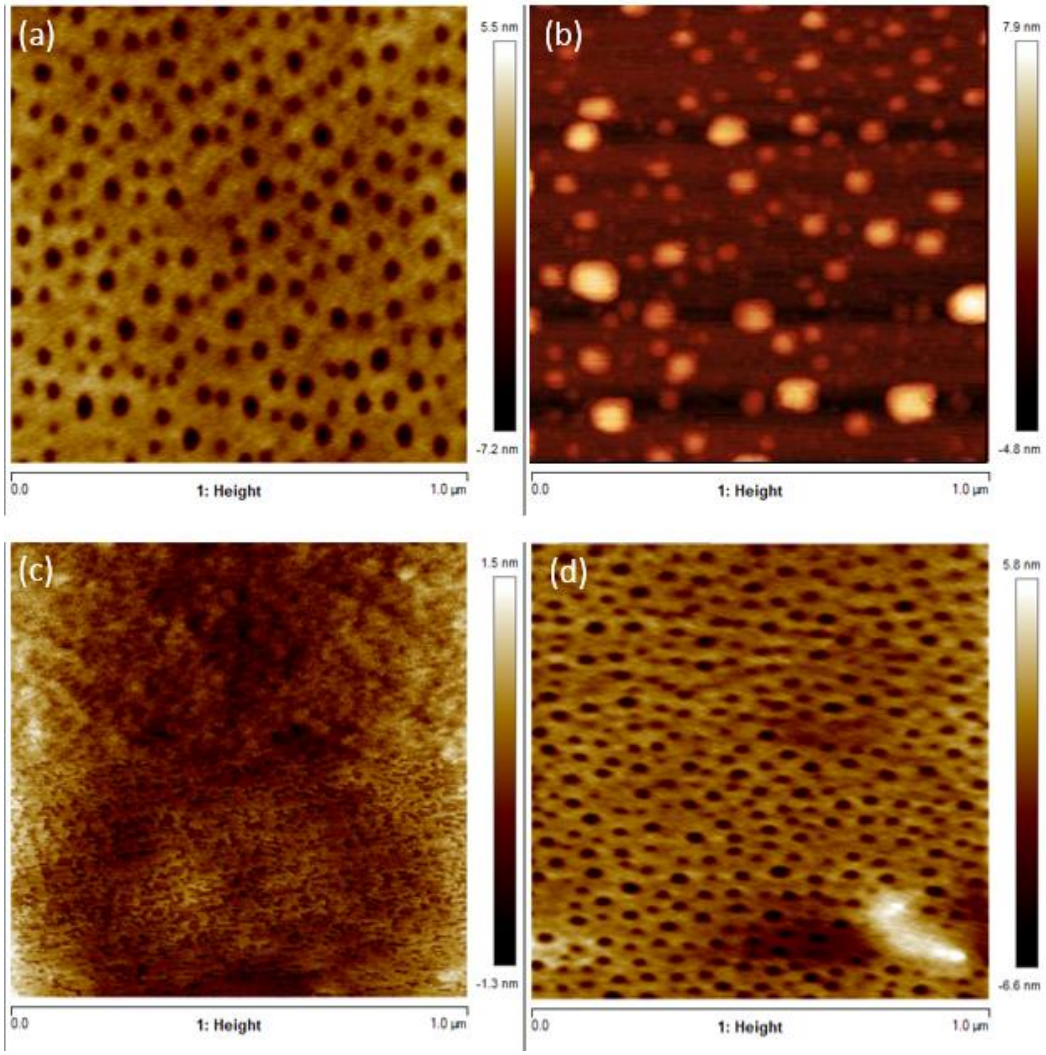


**Figure 7.23.** AFM topographical images at different steps of the fabrication process. (a) after casting first layer, (b) selectively impregnation of silver nanoparticles, (c) crosslinked PDMS layer and (d) casting of the second BCP layer.

### 7.4.4 **Optical Performance**

The optical responses of the colloidal silver nanoparticles were measure using a Unicam UV4 UV/Vis spectrometer. The optical responses for fabricated devices were characterised by a Perkin Elmer Lambda 19 and a Cary 7000 UV-VIS-NIR spectrometer. The Perkin Elmer model was used to compare the single- and double-layer filters at normal incidence, and the Cary model was used for studying the angles of incidence and the polarisation.

The synthesised silver nanoparticles contained in denatured alcohol provide an absorption peak at ~403 nm with a bandwidth of 60 nm, as shown in figure 7.24. This provides a moderate prediction to the performance of the optical metamaterial filter when the nanoparticles are 'trapped' within the block copolymer template because absorption spectrum in proportional to the transmission spectrum through the Beer-Lambert's law [50].

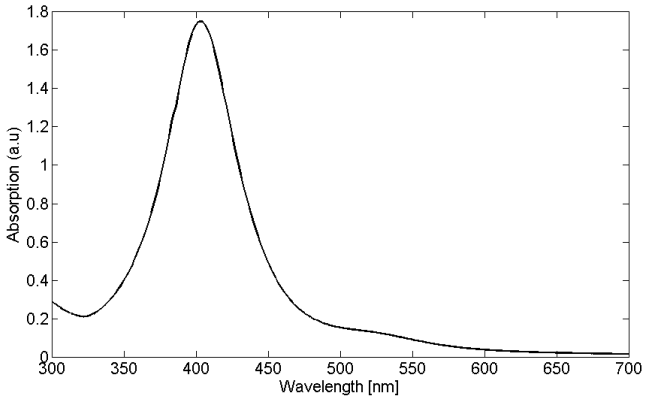


**Figure 7.24.** The absorption spectrum of the fabricated colloidal silver nanoparticles in IMS solution.

Figure 7.25 shows the key experimental results for single layer metafilm and a double layer metafilm, against their simulation counterparts. The presence of the surrounding block copolymer layer redshifts the resonance position from 403 nm (colloidal) to ~412 nm for single layer and 413 nm for the double layer. The average transmission between 400 nm and 700 nm for the single layer is 78% with an IVPT of 86%, and the double layer is 64% with an IVPT of 77%. The bandwidth of the single layer is 105 nm and of the double layer is 112 nm. Comparing to the simulation study, the single layer has a bandwidth of 98 nm, and the double layer has a bandwidth of 104 nm. The reduction in transmission for the experimental data at around ~340 nm is due to the transmission spectrum of the glass substrate.

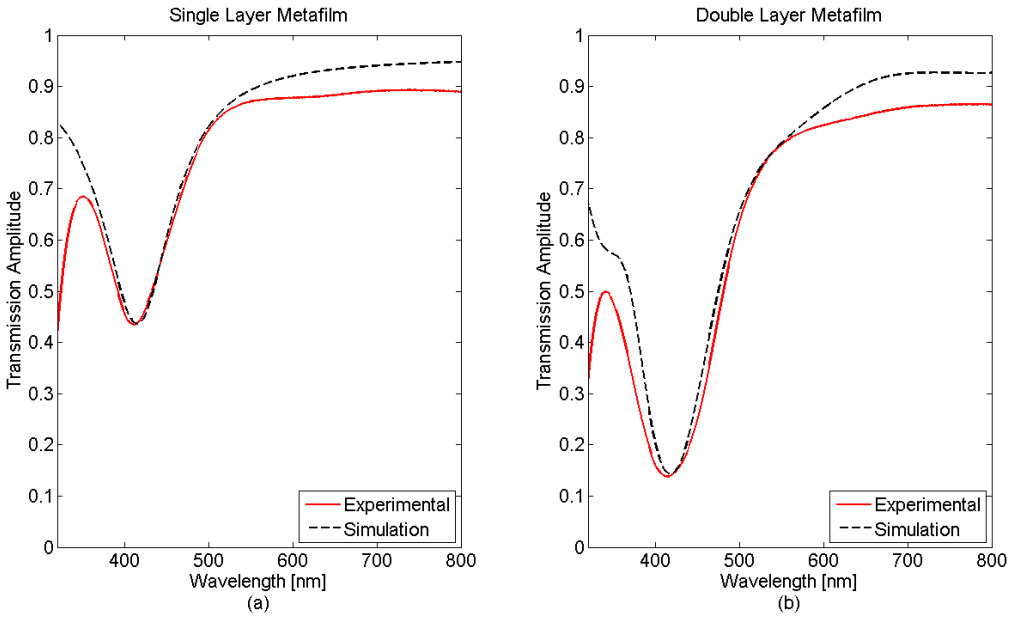


**Figure 7.25.** Transmission amplitudes of (a) single layer and (b) double layer for experimental work against simulation study. Layers consist of BCP with encapsulated silver nanoparticles.

The angle of incidence study demonstrates the close relationship between the simulation and experimental work. Figure 7.26 highlights this similarity with a slight variation in the out of

resonance band (+500 nm). It is evident from the transmission spectra that the optical metamaterial filter does not experience any blue shifting behaviour and is able to provide protection for large angles of incoming laser light at the resonant wavelengths.

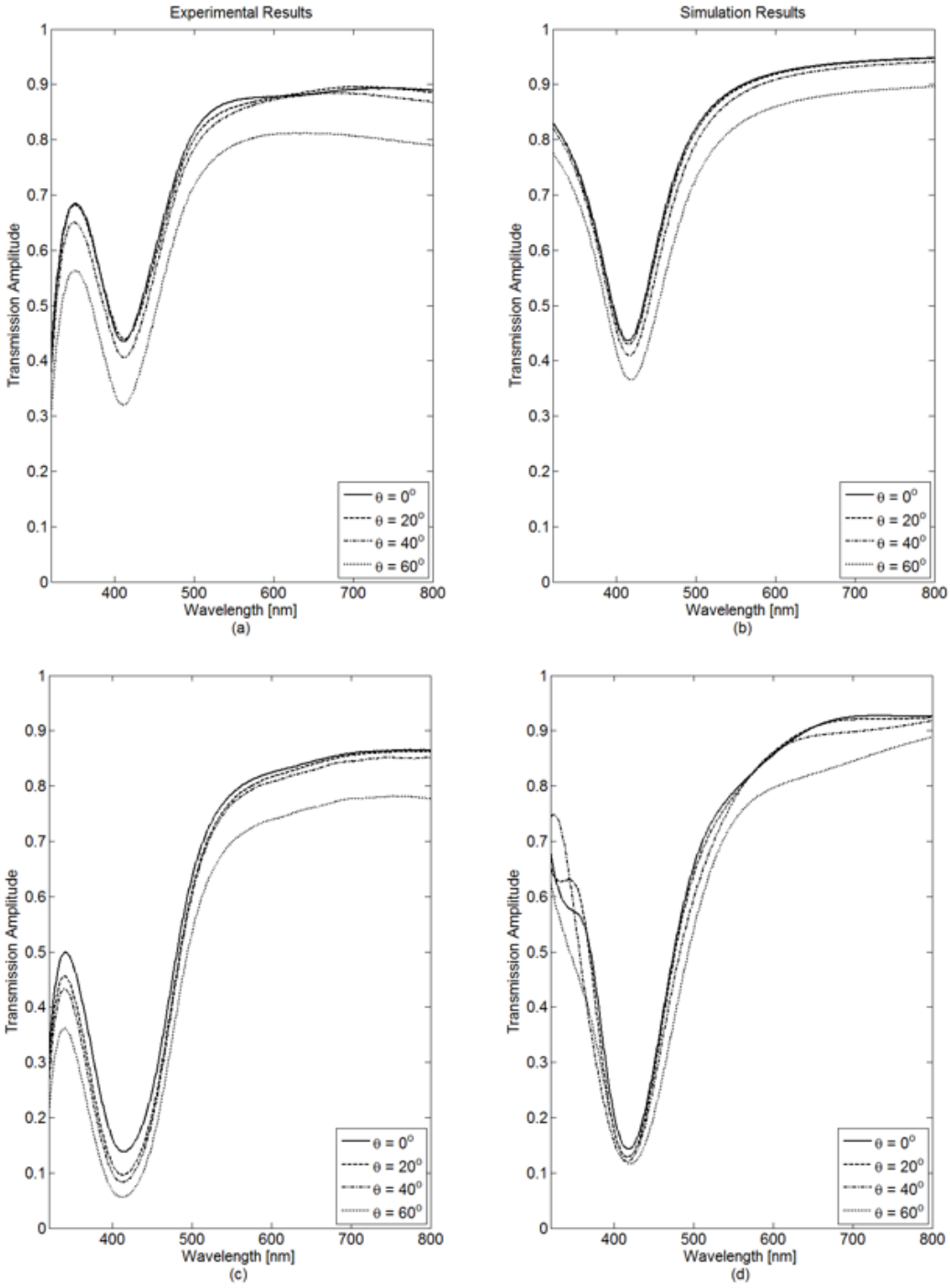


**Figure 7.26.** Transmission amplitudes of angular performance. (a) Single layer experiment, (b) single layer simulations, (c) double layer experiment and (d) double layer simulation.

The optical density (OD) for the single layer remains above 0.33OD and the double layer remains above 0.80OD, across all measured angles for both TE and TM polarisation. Both the

single and double layers provide some variation of OD between TE and TM. This could be due to the defects within the metamaterial lattice where they do not present as a completely uniform hexagonal array.

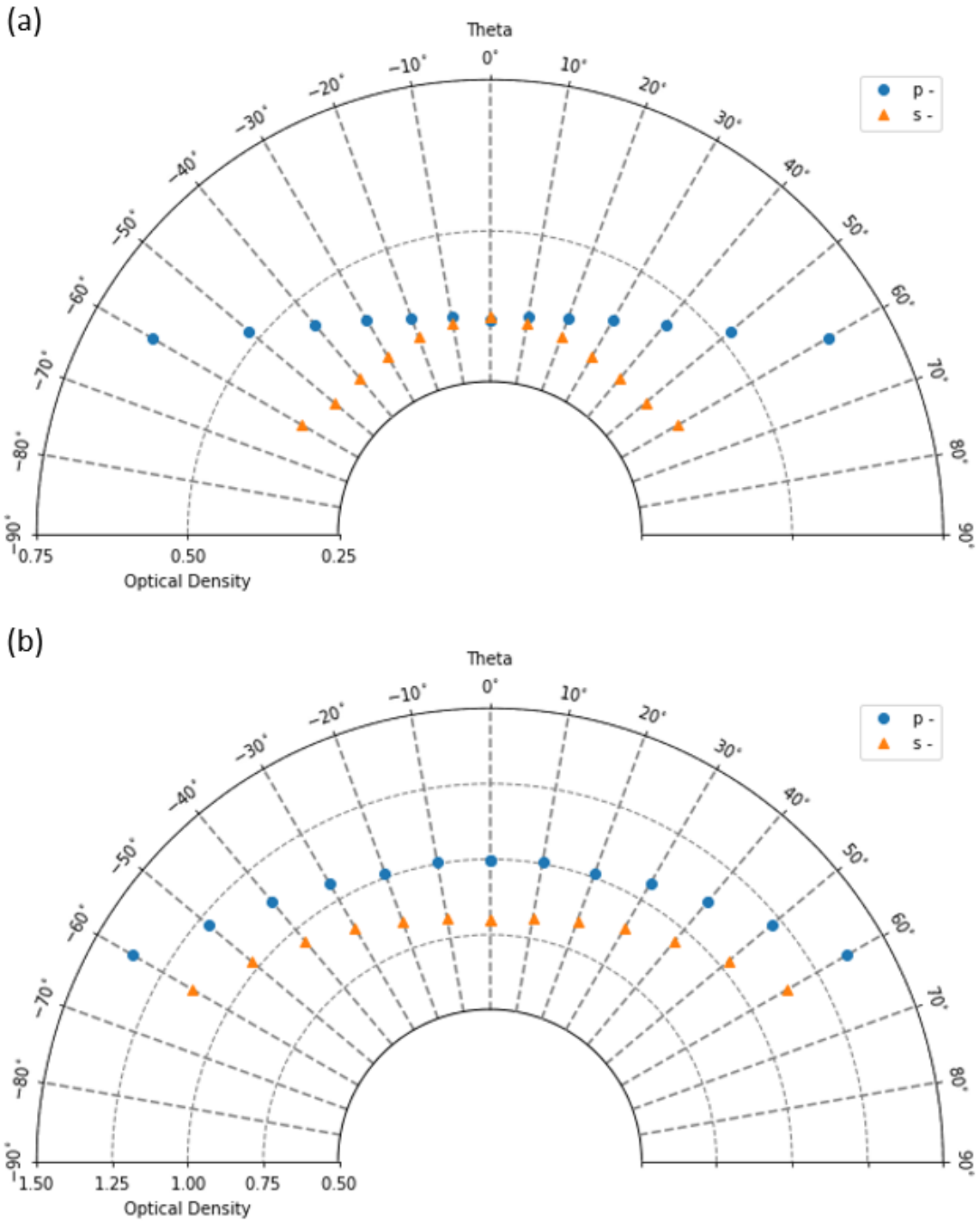


**Figure 7.27.** Optical density of (a) single layer and (b) double layer for experimental work at $\lambda = 410\ nm$.

The colouration of the filter offers a distinct yellowish hue. The picture (figure 7.28) demonstrates the natural world and that with the added filter present. Natural colours can be

selected with the presence of the metamaterial filter; however, if the layers were to increase so would the colouration of the filter. A method for balancing this could be with select blue dyes to counterbalance to a neutral colour.

**Figure 7.28.** Image of the developed metamaterial filter sample in front of natural world.

The transmission colouration response can be calculated accordingly and presented on the standard CIE 1931 colour map. The coordinates for the single layer are ($x = 0.37$ and $y = 0.4$) and the double layer are ($x = 0.4$ and $y = 0.43$). This demonstrates that as the metamaterial layers increase, so does the strength of colouration.

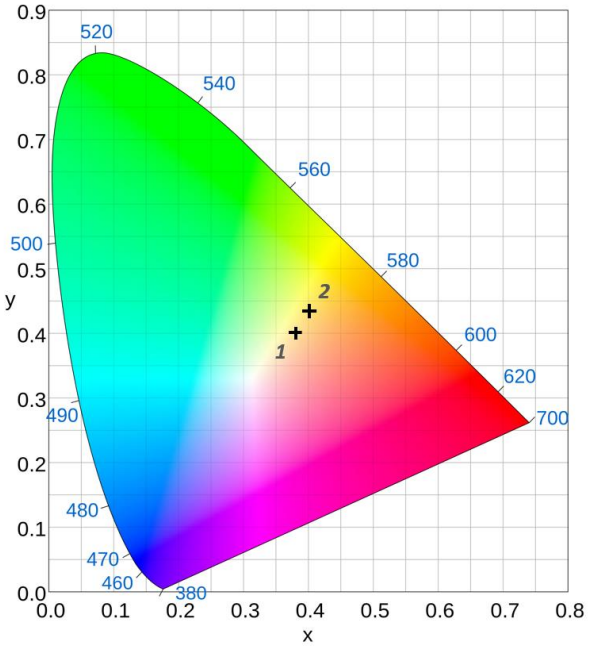


**Figure 7.29.** CIE 1931 colour map for the transmission of single layer (*marked 1*) and (b) double layer (*marked 2*).

### Anti-Reflection Contribution

Anti-reflection (AR) coatings can be added to the filter to improve the overall transmission by creating destructive interference. The AR coating used for this experiment was a four-layer wideband coating consisting of interchanging layers of $MgF_2$ and $ZrO_2$. The AR coating was placed on the backside of the filter to mitigate a portion of the 4% loss on the back interface.

| Air | $MM_{410}$ | Glass | AR | Air |
|---|---|---|---|---|
| 1.00 | $1.51_{Ag}$ | 1.52 | 1.38-2.01 | 1.00 |

The description for that coating is described below;

| Glass | $ZrO_2$ | $MgF_2$ | $ZrO_2$ | $MgF_2$ | Air |
|---|---|---|---|---|---|
| 1.52 | 2.01 | 1.38 | 2.01 | 1.38 | 1.00 |
| | 16.54 nm | 30.31 nm | 131.7 nm | 92.66 nm | |

Figure 7.30 presents the reflection percentage when considering just the anti-reflection contribution. The highest transmission point is at 510 nm with a considerable reflection percentage displayed below 400 nm.

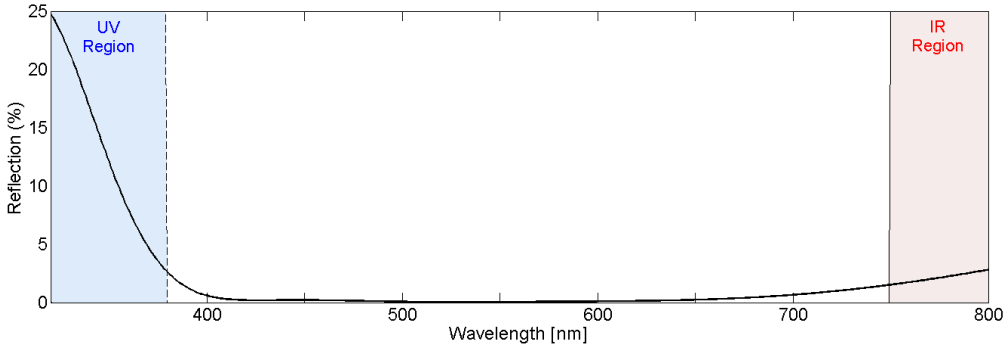


**Figure 7.30.** Reflection of the AR coating.

Comparing the experimental data for the metamaterial coating with and without the AR coating can be found in figure 7.31. As predicted, the transmission increases with a near 4% improvement for the out of band resonant wavelengths, 3.2% for single layer and 3.4% for the double layer. Furthermore, the high reflection peak in the AR coating below 400 nm results in an attenuation of the transmission within the described wavelength range. Additionally, the peak transmission wavelength has shifted from 510 nm to ~670 nm. However, the addition of the back-interface AR does show that with the contribution of an AR coating, the transmission can be increased for the out of resonant bands.

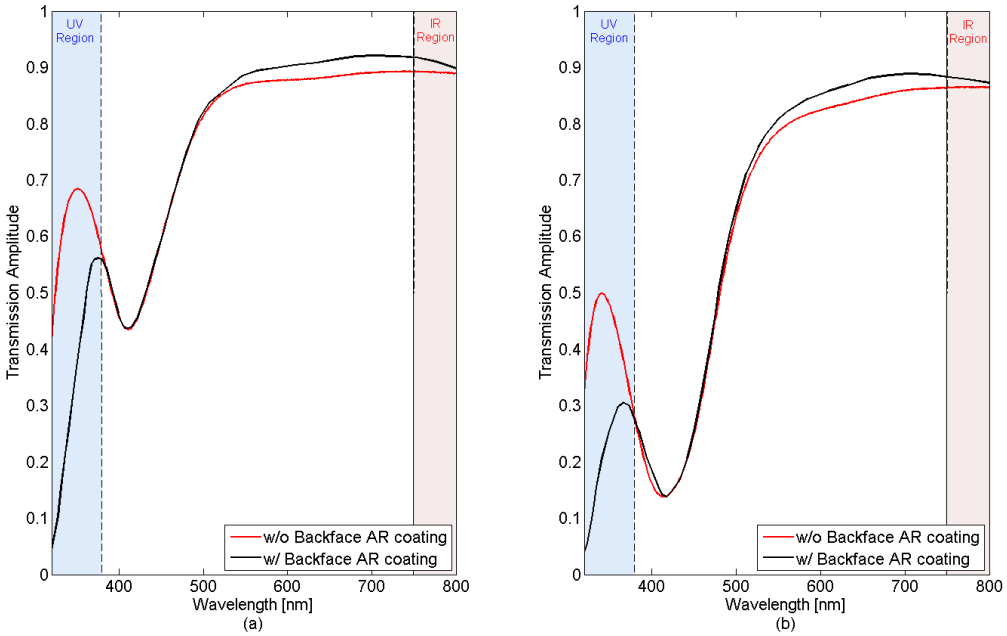


**Figure 7.31.** Transmission amplitudes of (a) single layer and (b) double layer with the addition of an anti-reflection coating on the opposite substrate interface.

Acknowledging the contribution from the AR coating situated on the back interface of the optical metamaterial filter, a simulation has been conducted to examine the contribution of the presence of an AR coating positioned on both the front and back interfaces. The simulation was

performed using Essential Macleod thin film software. The AR coating on the front and back are identical in structure, materials and thickness.

| Air | AR | $MM_{410}$ | Glass | AR | Air |
|---|---|---|---|---|---|
| 1.00 | 1.38-2.01 | $1.51_{Ag}$ | 1.52 | 1.38-2.01 | 1.00 |

Similar to the experimental data, the simulation with an anti-reflection coating on both interfaces results in a loss of transmission at wavelengths below 400 nm. Though, with the addition of the AR between the air-metamaterial interfaces, the transmission is greatly increased at wavelengths greater than 500 nm.

A refined anti-reflection coating so that the wideband response covers the near-UV region would result in a much more defined notch feature in the transmission spectrum. However, the AR discussed in this experimental chapter has been designed to limit the near-UV response as in reality, this does not play a role in the human vision.

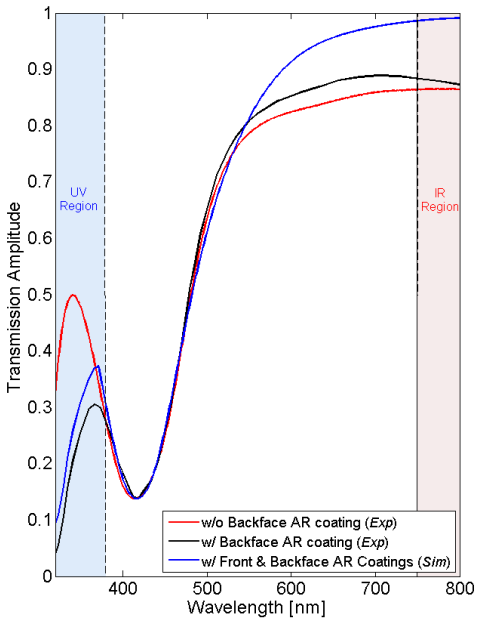


**Figure 7.32.** Simulated transmission amplitudes of double layer with AR coating on both back and front interfaces.

## 7.5 **Summary**

The experimental results presented within this chapter provide a proof-of-concept optical metamaterial filter for blue light, 410 nm. The filter is capable of blocking large angle of incoming light at a particular wavelength without experiencing any blue-shifting behaviour. The method for fabricating the samples took advantage of self-assembly methods through the use of block copolymers. The block copolymers are able to form into a desired arrangement to

act as a template that can selectively impregnate prefabricated silver nanoparticles. The simulation studies in this chapter, performed alongside the experimental work matched up with great accuracy and provide assurance for the previous simulation studies in preceding chapters. A single layer and double layer film were presented to illustrate the effects that an additional layer can have on the performance of the filter. The second layer enabled an increase in optical density from 0.33OD to 0.8OD. Furthermore, the experimental work also demonstrated that combined with an anti-reflection coating, the out of resonant wavelength band for the optical filter experiences an increased transmission performance. Moreover, further work is required to establish a perfect lattice arrangement with a uniformly distributed size of nanoparticles, which would improve the bandwidth of the optical notch. Nonetheless, the work undertaken in this chapter experimentally verifies the theoretical work throughout this thesis and demonstrates that shift-free optical filters are achievable with optical metamaterials.

## 7.6 **References**


[1] W. Arnold, "CMOS device fabrication and the evolution of optical lithographic exposure tools", *Microelectronic Engineering*, vol. 46, no. 1-4, pp. 7-9, 1999. Available: 10.1016/s0167-9317(99)00005-2.

[2] X. Tong, *Functional metamaterials and metadevices*. Springer, 2017.

[3] "Beyond the diffraction limit", *Nature Photonics*, vol. 3, no. 7, pp. 361-361, 2009. Available: 10.1038/nphoton.2009.100.

[4] M. Totzeck, W. Ulrich, A. Göhnermeier and W. Kaiser, "Pushing deep ultraviolet lithography to its limits", *Nature Photonics*, vol. 1, no. 11, pp. 629-631, 2007. Available: 10.1038/nphoton.2007.218.

[5] C. Mack, *Fundamental principles of optical lithography*. Chichester: Wiley, 2012.

[6] A. Gangnaik, Y. Georgiev and J. Holmes, "New Generation Electron Beam Resists: A Review", *Chemistry of Materials*, vol. 29, no. 5, pp. 1898-1917, 2017. Available: 10.1021/acs.chemmater.6b03483.

[7] Z. Wang, B. Ai, H. Möhwald and G. Zhang, "Colloidal Lithography Meets Plasmonic Nanochemistry", *Advanced Optical Materials*, vol. 6, no. 18, p. 1800402, 2018. Available: 10.1002/adom.201800402.

[8] Y. Wang, M. Zhang, Y. Lai and L. Chi, "Advanced colloidal lithography: From patterning to applications", *Nano Today*, vol. 22, pp. 36-61, 2018. Available: 10.1016/j.nantod.2018.08.010.

[9] A. Heifetz, S. Kong, A. Sahakian, A. Taflove and V. Backman, "Photonic Nanojets", *Journal of Computational and Theoretical Nanoscience*, vol. 6, no. 9, pp. 1979-1992, 2009. Available: 10.1166/jctn.2009.1254.

[10] G. Huszka and M. Gijs, "Super-resolution optical imaging: A comparison", *Micro and Nano Engineering*, vol. 2, pp. 7-28, 2019. Available: 10.1016/j.mne.2018.11.005.

[11] A. Emplit, J. Lian, I. Huynen, A. Vlad and M. Sarrazin, "Colloidal pattern replication through contact photolithography operated in a 'Talbot–Fabry–Perot' regime", *Nanotechnology*, vol. 25, no. 14, p. 145303, 2014. Available: 10.1088/0957-4484/25/14/145303.

[12] A. Leontiev et al., "Tuning the Optical Properties of Hyperbolic Metamaterials by Controlling the Volume Fraction of Metallic Nanorods", *Nanomaterials*, vol. 9, no. 5, p. 739, 2019. Available: 10.3390/nano9050739.

[13] J. Yao et al., "Design, fabrication and characterization of indefinite metamaterials of nanowires", *Philosophical Transactions of the Royal Society A: Mathematical, Physical and Engineering Sciences*, vol. 369, no. 1950, pp. 3434-3446, 2011. Available: 10.1098/rsta.2011.0159.

[14] M. Kim et al., "Accordion-like plasmonic silver nanorod array exhibiting multiple electromagnetic responses", *NPG Asia Materials*, vol. 10, no. 4, pp. 190-196, 2018. Available: 10.1038/s41427-018-0033-6.

[15] W. Lee et al., "Individually addressable epitaxial ferroelectric nanocapacitor arrays with near Tb inch−2 density", *Nature Nanotechnology*, vol. 3, no. 7, pp. 402-407, 2008. Available: 10.1038/nnano.2008.161.

[16] R. Yang, C. Sui, J. Gong and L. Qu, "Silver nanowires prepared by modified AAO template method", *Materials Letters*, vol. 61, no. 3, pp. 900-903, 2007. Available: 10.1016/j.matlet.2006.06.009.
[17] K. Tsui et al., "Low-Cost, Flexible, and Self-Cleaning 3D Nanocone Anti-Reflection Films for High-Efficiency Photovoltaics", *Advanced Materials*, vol. 26, no. 18, pp. 2805-2811, 2014. Available: 10.1002/adma.201304938.
[18] A. Goszczak and P. Cielecki, "A Review on Anodic Aluminum Oxide Methods for Fabrication of Nanostructures for Organic Solar Cells", *Current Nanoscience*, vol. 15, no. 1, pp. 64-75, 2018. Available: 10.2174/1573413714666180228152018.
[19] H. Robatjazi, S. Bahauddin, L. Macfarlan, S. Fu and I. Thomann, "Ultrathin AAO Membrane as a Generic Template for Sub-100 nm Nanostructure Fabrication", *Chemistry of Materials*, vol. 28, no. 13, pp. 4546-4553, 2016. Available: 10.1021/acs.chemmater.6b00722.
[20] Y. Lei and W. Chim, "Shape and Size Control of Regularly Arrayed Nanodots Fabricated Using Ultrathin Alumina Masks", *Chemistry of Materials*, vol. 17, no. 3, pp. 580-585, 2005. Available: 10.1021/cm048609c.
[21] C. Lu and R. Lipson, "Interference lithography: a powerful tool for fabricating periodic structures", *Laser & Photonics Reviews*, vol. 4, no. 4, pp. 568-580, 2009. Available: 10.1002/lpor.200810061.
[22] D. Bernard and H. Urbach, "Thin-film interference effects in photolithography for finite numerical apertures", *Journal of the Optical Society of America A*, vol. 8, no. 1, p. 123, 1991. Available: 10.1364/josaa.8.000123.
[23] R. Rumpf, "21st Century Electromagnetics. Lacture 6: Holographic Lithography", University of Texas at El Paso.
[24] L. Cai, X. Yang and Y. Wang, "All fourteen Bravais lattices can be formed by interference of four noncoplanar beams", *Optics Letters*, vol. 27, no. 11, p. 900, 2002. Available: 10.1364/ol.27.000900.
[25] M. Vala and J. Homola, "Flexible method based on four-beam interference lithography for fabrication of large areas of perfectly periodic plasmonic arrays", *Optics Express*, vol. 22, no. 15, p. 18778, 2014. Available: 10.1364/oe.22.018778.
[26] "Crystal Lattice and Unit Cell: Meaning, Types, Videos, Solved Examples", *Toppr-guides*, 2019. [Online]. Available: https://www.toppr.com/guides/chemistry/the-solid-state/space-lattice-or-crystal-lattice-and-unit-cell/..
[27] S. Yang and Y. Wu, "EUV/Soft X-Ray Interference Lithography", 2018 .
[28] H. Kim, S. Park and W. Hinsberg, "Block Copolymer Based Nanostructures: Materials, Processes, and Applications to Electronics", *Chemical Reviews*, vol. 110, no. 1, pp. 146-177, 2010. Available: 10.1021/cr900159v.
[29] V. Castelletto and I. Hamley, "Morphologies of block copolymer melts", *Current Opinion in Solid State and Materials Science*, vol. 8, no. 6, pp. 426-438, 2004. Available: 10.1016/j.cossms.2005.06.001.
[30] X. Gu, "Self-assembly of block copolymers by solvent vapour annealing, mechanisms and lithographic applications", PhD, University of Massachusetts, 2014.

[31] C. Hawker and T. Russell, "Block Copolymer Lithography: Merging “Bottom-Up” with “Top-Down” Processes", *MRS Bulletin*, vol. 30, no. 12, pp. 952-966, 2005. Available: 10.1557/mrs2005.249.
[32] J. Bang, U. Jeong, D. Ryu, T. Russell and C. Hawker, "Block Copolymer Nanolithography: Translation of Molecular Level Control to Nanoscale Patterns", *Advanced Materials*, vol. 21, no. 47, pp. 4769-4792, 2009. Available: 10.1002/adma.200803302.
[33] P. Mansky, "Controlling Polymer-Surface Interactions with Random Copolymer Brushes", *Science*, vol. 275, no. 5305, pp. 1458-1460, 1997. Available: 10.1126/science.275.5305.1458.
[34] D. Borah, S. Rasappa, R. Senthamaraikannan, J. Holmes and M. Morris, "Tuning PDMS Brush Chemistry by UV–O3 Exposure for PS-b-PDMS Microphase Separation and Directed Self-assembly", *Langmuir*, vol. 29, no. 28, pp. 8959-8968, 2013. Available: 10.1021/la401561k.
[35] Y. Kim, J. Mun, G. Yu and K. Char, "Phase transition of block copolymer/homopolymer binary blends under 2D confinement", *Macromolecular Research*, vol. 25, no. 6, pp. 656-661, 2017. Available: 10.1007/s13233-017-5128-3.
[36] M. Wu, D. Wang and L. Wan, "Directed block copolymer self-assembly implemented via surface-embedded electrets", *Nature Communications*, vol. 7, no. 1, 2016. Available: 10.1038/ncomms10752.
[37] Z. Qiang, Y. Zhang, J. Groff, K. Cavicchi and B. Vogt, "A generalized method for alignment of block copolymer films: solvent vapor annealing with soft shear", *Soft Matter*, vol. 10, no. 32, pp. 6068-6076, 2014. Available: 10.1039/c4sm00875h.
[38] PSim, *Txcorp.com*, 2019. [Online]. Available: https://www.txcorp.com/psim.
[39] E. Brini, E. Algaer, P. Ganguly, C. Li, F. Rodríguez-Ropero and N. van der Vegt, "Systematic coarse-graining methods for soft matter simulations – a review", *Soft Matter*, vol. 9, no. 7, pp. 2108-2119, 2013. Available: 10.1039/c2sm27201f.
[40] "PSim Reference Manual — PSim v1.7.0 documentation", *Txcorp.com*, 2019. [Online]. Available: https://www.txcorp.com/images/docs/psim/latest/reference_manual/PSimReferenceManual.html.
[41] M. Matsen, "The standard Gaussian model for block copolymer melts", *Journal of Physics: Condensed Matter*, vol. 14, no. 2, pp. R21-R47, 2001. Available: 10.1088/0953-8984/14/2/201.
[42] M. Mohy Eldin, M. Abu-Saied, T. Tamer, M. Youssef, A. Hashem and M. Sabet, "Development of polystyrene based nanoparticles ions exchange resin for water purification applications", *Desalination and Water Treatment*, vol. 57, no. 32, pp. 14810-14823, 2015. Available: 10.1080/19443994.2015.1080192.
[43] X. Gu, I. Gunkel and T. Russell, "Pattern transfer using block copolymers", *Philosophical Transactions of the Royal Society A: Mathematical, Physical and Engineering Sciences*, vol. 371, no. 2000, p. 20120306, 2013. Available: 10.1098/rsta.2012.0306.
[44] C. Sinturel, M. Vayer, M. Morris and M. Hillmyer, "Solvent Vapor Annealing of Block Polymer Thin Films", *Macromolecules*, vol. 46, no. 14, pp. 5399-5415, 2013. Available: 10.1021/ma400735a.

[45] S. Ayyappan, R. Gopalan, G. Subbanna and C. Rao, "Nanoparticles of Ag, Au, Pd, and Cu produced by alcohol reduction of the salts", *Journal of Materials Research*, vol. 12, no. 2, pp. 398-401, 1997. Available: 10.1557/jmr.1997.0057.
[46] S. Aditha, A. Kurdekar, L. Chunduri, S. Patnaik and V. Kamisetti, "Aqueous based reflux method for green synthesis of nanostructures: Application in CZTS synthesis", *MethodsX*, vol. 3, pp. 35-42, 2016. Available: 10.1016/j.mex.2015.12.003.
[47] Q. Yang and K. Loos, "Perpendicular Structure Formation of Block Copolymer Thin Films during Thermal Solvent Vapor Annealing: Solvent and Thickness Effects", *Polymers*, vol. 9, no. 12, p. 525, 2017. Available: 10.3390/polym9100525.
[48] J. Kim et al., "Highly tunable refractive index visible-light metasurface from block copolymer self-assembly", *Nature Communications*, vol. 7, no. 1, 2016. Available: 10.1038/ncomms12911.
[49] L. Connal et al., "Mesostructured Block Copolymer Nanoparticles: Versatile Templates for Hybrid Inorganic/Organic Nanostructures", *Chemistry of Materials*, vol. 24, no. 21, pp. 4036-4042, 2012. Available: 10.1021/cm3011524.
[50] D. Swinehart, "The Beer-Lambert Law", *Journal of Chemical Education*, vol. 39, no. 7, p. 333, 1962. Available: 10.1021/ed039p333.

# CHAPTER VIII. CONCLUSION AND SUGGESTIONS FOR FURTHER WORKS

A review of the most important new and novel developments described in this thesis, include:

- Merged plasmonics and thin film theory to develop the design principles for an optical metamaterial notch filter with high transmission and a plasmonic resonance rejection band.
- Developed a flexible inverse design software tool to aid the design process.
- Combined traditional optical thin film filters with a metamaterial layer to improve the performance of single notch optical filters.
- Designed a single and multi-notch optical metamaterial filter for visible laser wavelengths.
- Experimentally verified a shift-free wide-angle optical metamaterial notch filter for blue light.

This thesis focused on the fundamentals for establishing shift-free wide-angle optical notch filters to protect against visible laser wavelengths. The importance of developing such device will transform visible laser protection systems for the aerospace and defence industry by rendering visible laser pointers ineffective in the event of an attack.

## 8.1 **Conclusion**

As thoroughly discussed in *Chapter II*, laser attacks from laser pointers have increased significantly year-on-year on a global scale according to the data presented from avionic agencies across the world. The limitations of current narrowband filters for anti-laser striking lie solely with the thin film coating technology. Thin film filters exceed the technological barrier presented with traditional absorbing filters which block off a significant proportion of the visible spectrum. Resulting in monochromatic colouration and low transmission. The ability to design and manufacture thin film coating devices are well-established, particularly thanks to the theoretical work conducted by Herpin, Epstein and Macleod. Thin film laser protection coatings still provide solutions to many modern-day problems and demand a huge amount of appreciation. They are still considered the top-tier optical filter technology. However, the current and vastly demanding requirements for laser protection devices are increase rapidly due to the readily available commercial lasers and military application including weapons, targeting and aiming. As such, the development of laser protection has somewhat been left behind as researchers have almost purely focused on developing the “latest and greatest” lasers. The modern necessities for any laser protection demand a highly transmissive optic with narrow rejection band that can cater for wide-angles with minimal colouration disturbance. This is just

not possible or practical with standard thin film technology. The main reason is down to the fact that the thin film filters' fixed-line spectrum shifts as the angle of incident increases. This is due to a decreasing effective change in the thin film stacks refractive index whilst the film thickness remains unchanged. As such, the rejection band undergoes a shift to shorter wavelengths, restricting the angular performance and blocking potential for a discrete laser wavelength. There is significant demand within the optical and aerospace communities for a notch filter with reduced angular sensitivity. Consequently, BAE systems and MTI are working on solving these matters with a degree of success, particularly with MTI's MetaAir product. The modern day laser protection devices are very much restricted by the periodic table; though overcoming these constraints through metamaterials will enable a whole new capability for optical devices. This is where metamaterials present the greatest opportunities for modern day laser protection devices. However, metamaterials are difficult to design and often use brute force methods. Translating the eventual design into something which can be fabricated, with particular focus on optical metamaterials, presents a whole new set of problems. Little is known about what technology BAE Systems is currently developing, but MTI's MetaAir product is attracting huge crowds and investment. Unfortunately, MTI have opted for an all-dielectric approach; which, in practice could bring narrow reject bands with high optical densities and a unique solution but, as suggested from the literature, the company are not able to solve the angular issues.

The work presented in this thesis is a comprehensive examination of metamaterial science and technology for the application of wide-angle optical notch filters. The objectives are to develop an inverse design strategy, demonstrate the design principles by designing laser protection devices through computational electromagnetic solvers, and offer a fabrication process that can provide a proof-of-concept device to support the theoretical developments presented throughout this thesis, with a particular focus on the angular performance.

The inverse design principles, *Chapter III* and *Chapter IV*, focus of the use of Mie theory to develop the ability to tune the plasmonic resonance according to the surrounding dielectric of a metallic nanoparticle. A minor extension to the linear dependency for localised plasmonic resonances was proposed and used to more accurately describe the resonance wavelength for a periodic array of nanoparticles. A homogenised solution, a metafilm, through an effective Drude-Lorentz model, enables the periodic meta-atoms to be labelled as a thin film equivalent with a dispersive refractive index. The design methodologies for optical thin films have been long established, and by merging the homogenised metafilm into the conventional thin film

design process allows industry driven software, such as Essential Macleod, to compute the solution effectively and with ease, without the need for time costly full-wave electromagnetic solvers.

The design strategy enabled an application approach for this thesis in the form of laser protection devices. Two applications were proposed, a combinational filter, *Chapter V*, and a full three-dimensional metamaterial filter, *Chapter VI*. The combination filter was produced to act as a transition technology for the expansion of metamaterials within industry, by combining standard thin film technology with a metafilm to enhance the optical performance and improve the angular sensitivity. The three-dimensional metamaterial filter is a long term industry development technology that provides the best angle performance. Each of the applications presented demonstrate the inherent ability to block low power handheld lasers, which are often used to dazzle airline pilots over a wide range of incidence angles.

Optical metamaterials contain meta-atoms considerably smaller than the wavelength of interest. Optical lithography and E-beam lithography are incapable of meeting the manufacturing demands for this next generation of optical devices. A techniques that is on the rise for large area nano patterning is the use of block copolymers (BCPs). This thesis has been able to take advantage of this emerging field to produce a prototype device with repeatable nanoscale features. The experimental component of this thesis, *Chapter VII*, utilises the pentagonal self-assembly of diBCPs to selectively impregnate prefabricated silver nanoparticles. Single and multi-layered devices were successfully fabricated as a proof-of-concept to provide evidence for shift-free wide-angle metamaterial filters. The fabricated devices show that the design principles developed within this investigation provide an effective method for realising angularly insensitive metamaterial-based notch filters.

The results from this research have also identified some limitations of the approach. One fundamental limitation is the ability to match the optical density of current thin film technology. This is important for high power CW or pulsed lasers, which require a considerably high optical density. Furthermore, both theoretically and experimentally, the ability to produce ultra-narrow (FWHM <40 nm) bands proves to be a difficult task. As number of layers in the filter increases to improve the optical density, the bandwidth also begins to increase. Additionally, the ability to achieve sharp vertical edges of the notch is restricted by the Fano-resonant behaviour, where the scattering features from the nanoparticles give rise to an asymmetric line-shape due to the interference between the surrounding dielectric and the resonant process. Moreover, and

predictably, the experimental fabrication provided some key challenges including, developing uniformed size nanoparticles and a defect free BCP lattice template.

Nonetheless, despite the limitations, this thesis presents a new approach to solve a current real-world problem which continues to increase in significance. Figure 8.1 grants an overview of the current fixed-line laser protection technology together with the breakthrough that metamaterials has introduced. The research offers a promising avenue for future high-performance laser protection systems that could be used in a wide variety of industries.

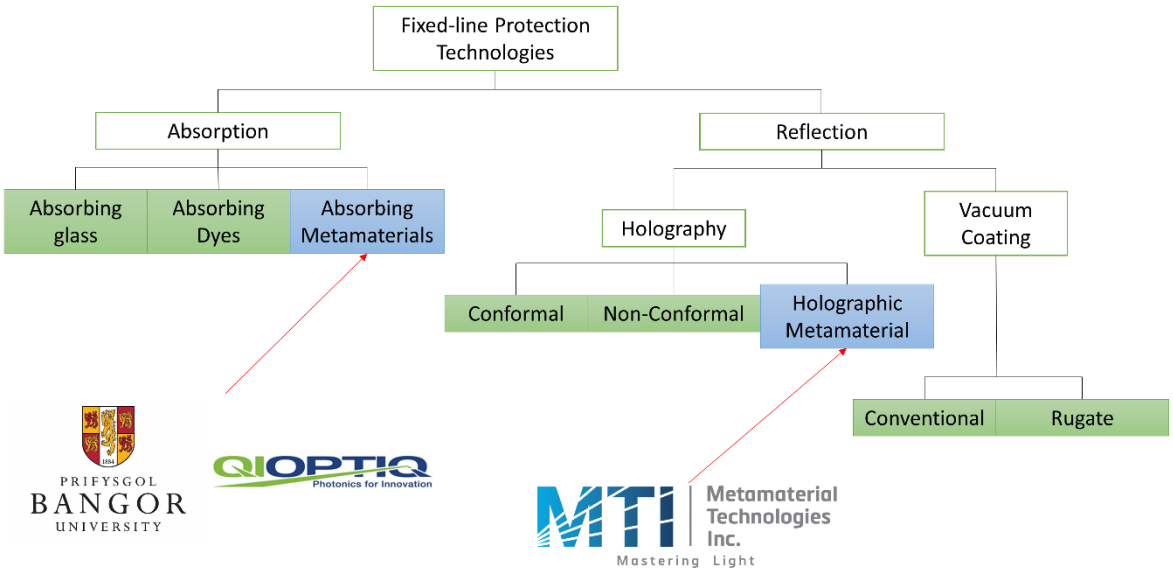


**Figure 8.1.** Fixed-line laser protection technology with the developing research of MTI and the joint efforts of Bangor University and Qioptiq Ltd.

## 8.2 **Recommendations**

As a result of this research, several key areas are recommended for continuous development immediately following the findings presented throughout this thesis.

- Synthesis of nanoparticles with the FWHM <50 nm. This can be achieved through re-dispersing silver nanoparticles, purchased from Sigma Aldrich, into an ethanol solution.
- Synthesis of alternative plasmonic materials and particle shapes to test the optical response.
- Develop and test the silver nanoparticles within a Zinc Sulphide dielectric to shift the resonance to 532 nm.
- Fabricate a multi-layer device to attenuate the rejection band to achieve an optical density of +2OD.

## 8.3 **Commercial Value**

As discussed in the introductory chapter, the commercial value of producing a shift-free wide-angle laser protection filter could be huge. With the laser protection eyewear market predicted to be worth £260mil by 2021 and the metamaterial market predicted to be work £3,728mil in 2025, the product is of this specification would draw a large proportion of the laser protection market and a healthy amount of the metamaterial market. There is still a considerable number of challenges that require a solution before a product of this standard goes to market; even if the optical performance is perfected, the environmental and product robustness would need to be examined. This thesis has highlighted not only the desire and need for a laser protection device with wide-angle coverage, but also demonstrates that it is possible to achieve what Herpin and Epstein (*two greats of thin film optical physics*) thought to be impossible.

## 8.4 **Suggestions for Future Work**

The research conducted for this thesis has explored the development of the next generation of optical notch filters. The addition of the shift-free wide-angle behaviour is in its infancy of research, and has more recently been aided with the introduction of metamaterials and the development of nanofabrication techniques. Although this thesis has been extensive in developing the foundations, there is still much room for growth and expansion before the field is anywhere near exhausted. The future work discussed herein provides an introduction to several areas of development, including alternative design principles, alternative materials and academic interests; some of which have been developed during this doctoral research but were not brought to fruition.

### 8.4.1 **Adjoint Sensitivity Analysis**

Due to the demanding nature of designing metamaterials, especially ones that can be fabricated with modern day lithography limitations, it can quickly become practically impossible to measure the exact true physical quantity values (i.e. materials, shapes, configuration, etc.). A method that has been used successfully within the nuclear sector [1] to predict the system behaviour with a large number of parameters is ‘adjoint sensitivity analysis procedure’ (ASAP) [2]. This technique is a mathematical predictive model where the sensitivities are obtained by calculating the Gateaux-differential of the system’s response at the nominal value of the system’s dependent variables and parameters. There has been some initial research into sensitivity analysis for metamaterial design [3-5], and coupled with the research presented in this thesis, ASAP could be a valid method for mathematically predicting metamaterial designs

by considering aspects including optical behaviour, metamaterial construction and lithographic capabilities.

### 8.4.2 **Phase Engineered Super-Cell Metasurfaces**

Phase engineering deals with manipulating the waveform cycle at a point in time. Metasurfaces reduce three dimensional metamaterials into a near two dimensional form. Traditionally, metasurfaces consist of a single unit-cell. However, a super-cell presents a cluster of unit-cells that are able to individually control and manipulate the input wave [6]. Figure 8.2 demonstrates a simple super-cell with a modulated surface refractive index to control the TE and TM resonant wavelengths, figure 8.3.

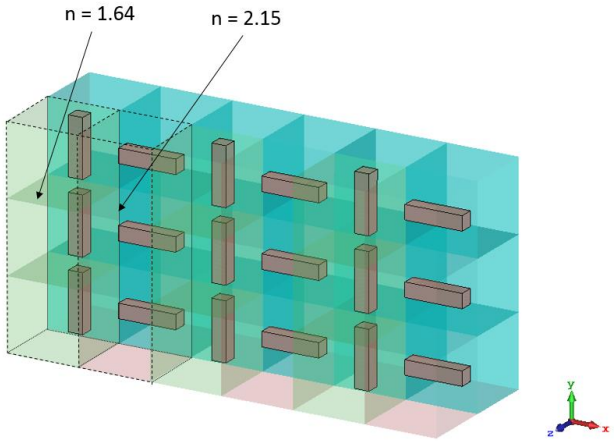


**Figure 8.2.** Simple super-cell metasurface with modulated surface refractive index.

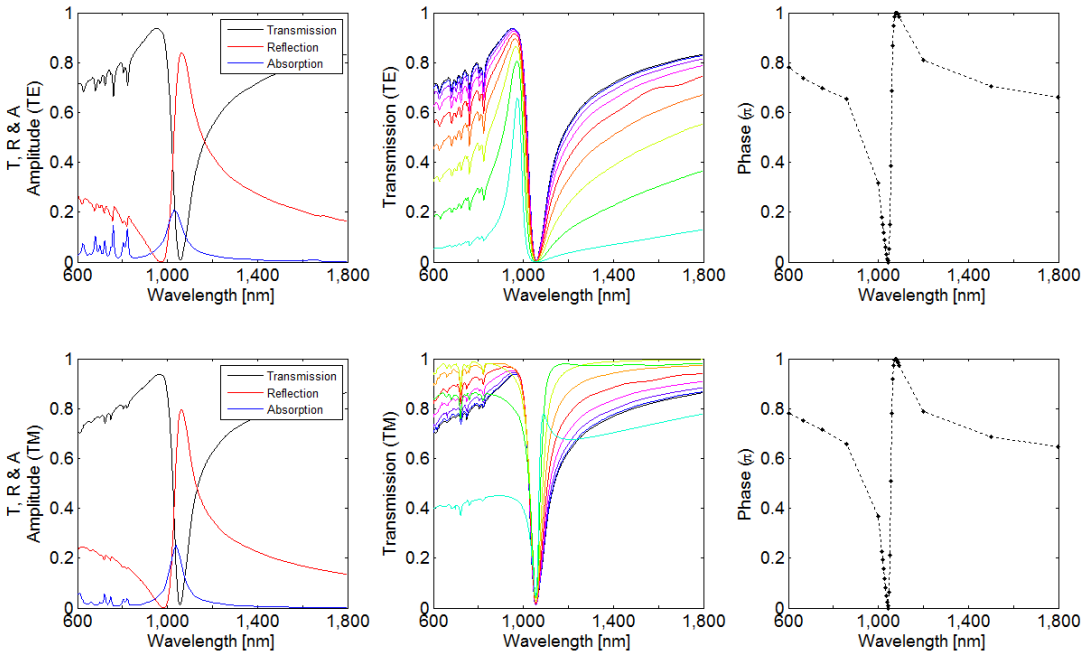


**Figure 8.3.** Transmission and phase response for the metasurface.

A feature of super-cell metasurfaces is the ability to create multi notch resonance with a near two dimensional thickness, where the components of the super-cell engineer the phase waveform.

### 8.4.3 **All-Dielectric Metamaterials**

All-dielectric metamaterials through the use of high index materials are on the rise providing some promising research [7]. Several researchers have demonstrated the ability to create coloured windows through high index metamaterials [8,9]. However, the angular performance has not been discussed. Research throughout this doctoral period has touched on all-dielectric as a potential material but has not found a suitable configuration that could solve for any blue-shift behaviour. The resonant position of a spherical dielectric particle can be found through (Eq. 8.2.1).

$$\lambda_{ref} \approx 2nr \tag{8.2.1}$$

Where $\lambda_{ref}$ is the resonant wavelength, $n$ is the refractive index and $r$ is the radius.

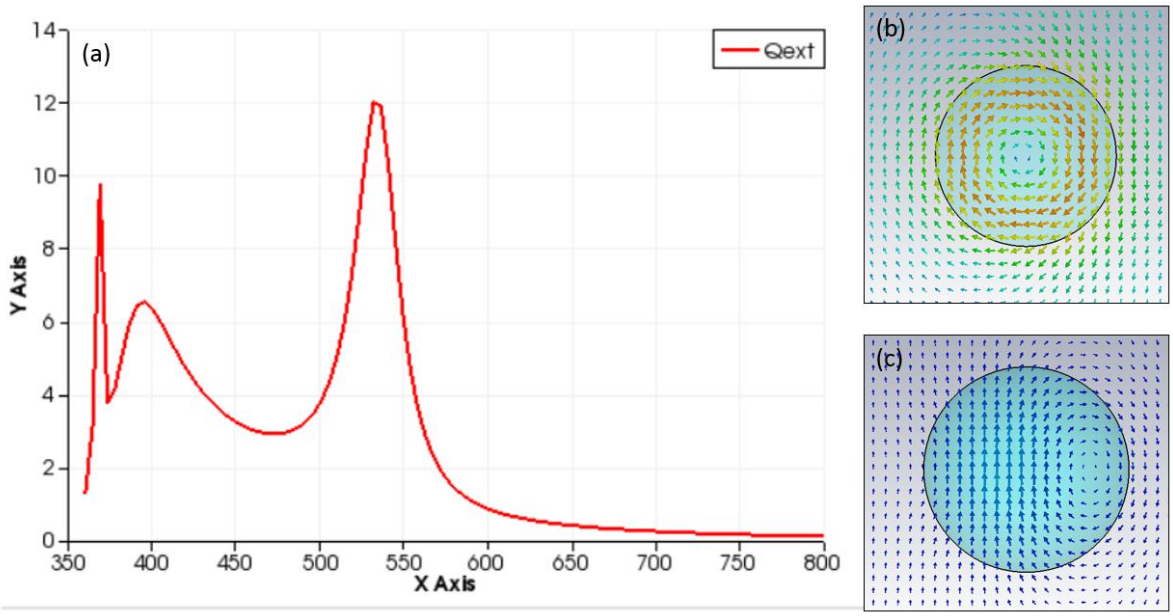


**Figure 8.4.** (a) Extinction cross-section efficiency establish by Mie theory. *X axis denotes the wavelength range and the Y axis signifies the efficiency.* (b) TE polarisation near-field interactions at 532 nm. (c) TM polarisation near-field interactions at 532 nm.

Certain shapes and configurations for the metamaterials may offer improved angular performance with further investigation. An additional aspect that has been known to advance the angular performance of all-dielectric metamaterials is to alter the period of the grating across a curved surface, with a compensated curved design, so that it is always resonant no matter of the angle of incidence [10].

### 8.4.4 *PT* Symmetric Systems

A team at Yale University led by theorist Douglas Stone, observed the Feynman diagrams for a laser and notices that if time was reversed [11], then an opposite effect could take place where light is perfectly absorbed at a single wavelength, known as coherent perfect absorbers (CPAs) or anti-lasers.

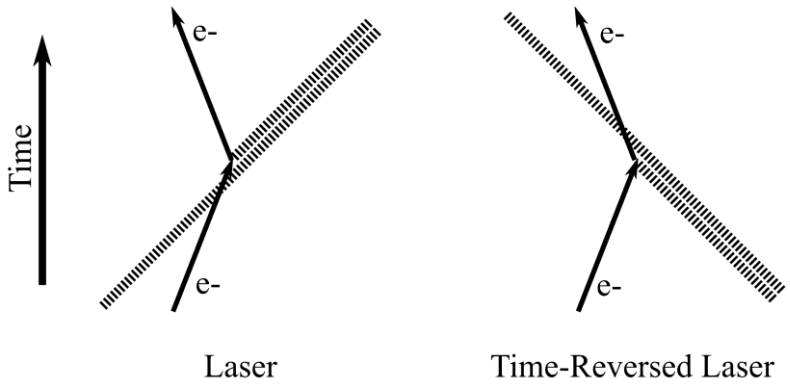


**Figure 8.5.** Feynman diagram for an electron-photon interaction and its time reversed counterpart.

First proposed in 1998 by Bender and Boettcher [12], space-time reflection symmetry, otherwise known as *PT* symmetry, become an expansive research area for fundamental physics. Deriving from the conventional quantum mechanical model, *PT* symmetry has extended the quantum field through the introduction of the complex domain. Continuing on from work conducted with fundamental symmetry principles, the *PT* symmetry theory concluded the existence of non-Hermitian Hamiltonian systems. In more recent years, the topic has been explored, both theoretically and experimentally, in the world of optics and photonic research [13]. The emergence of *PT* symmetry within optics has led to the experimental exploration in the areas of optical wave guides [14], lasers [15], optical resonators [16] and metamaterials [17].

Connecting *PT* symmetric quantum mechanics to optics can be achieved by replacing Schrodinger's equation (Eq. 8.2.2) with the Paraxial equation (Eq. 8.2.3). Where $z$ replaced time and the potential $V$ is replaced by the refractive index of the optical material.

$$i\hbar\frac{\partial\Psi}{\partial t} = -\frac{\hbar^2}{2m}\frac{\partial^2\Psi}{\partial x^2} + V(x)\Psi \tag{8.2.2}$$

$$i\frac{\partial E}{\partial z}+\frac{1}{2k}\frac{\partial^2 E}{\partial x^2}+k_0 n(x)E=0 \qquad (8.2.3)$$

The main feature of *PT* symmetry is the coexistence of gain and loss materials, which are able to switch the activation to achieve some interesting solutions. Early research into the designs of an anti-laser system have been conducted within this doctoral research period, which consider conjectural *PT* symmetry breaking for switchable lasing to anti-lasing of a two dimensional arrange nanoparticle system. The research describes a loss-gain system where the loss naturally originates due to silver nanoparticles and a conjectural gain medium derived from the Drude formula, with the size of the particles at 40 nm in diameter. The hypothetical gain material presents a negative Fermi velocity, resulting in a negative dampening constant. This enables a switch in the denominator sign for Drude's equation. The Fermi energy in the described gain medium can be considered as having non-interacting fermions occupying a higher state being inversely related to that of the silver nanoparticles.

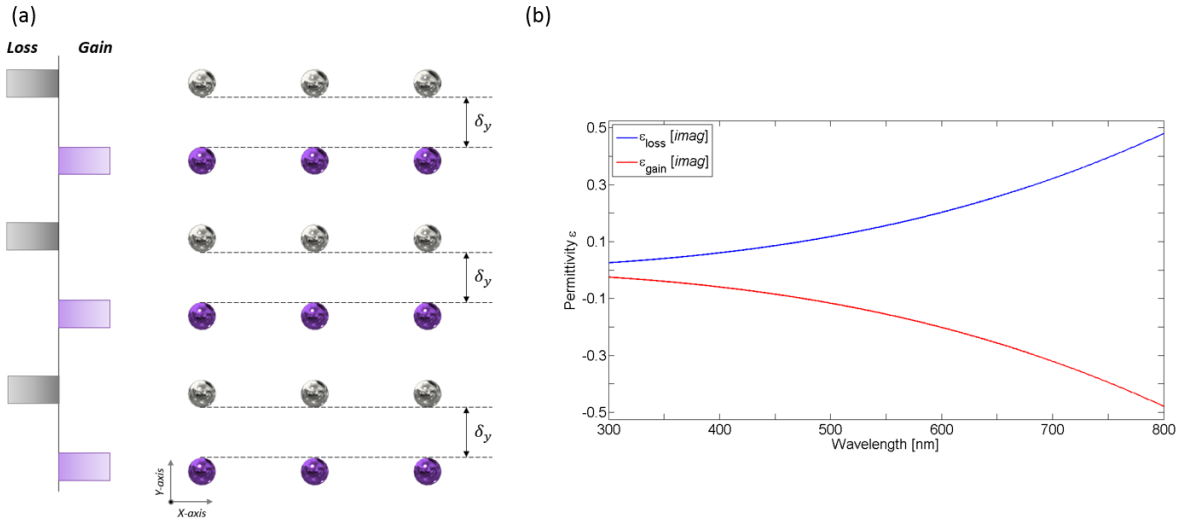


**Figure 8.6.** (a) A schematic diagram of the loss-gain two dimensional arrayed particle system, with the *k*-vector propagating along the *z-axis*. (b) Shows the imaginary component of the permittivity for the silver and gain material respectively.

Figure 8.6a shows the structure design with parity along the *x*- and *z*- *axis* remaining at equilibrium. Adjusting $\Delta\delta_y$ switches the states from a physical equilibrium, a state of unbroken *PT* symmetry, to non-equilibrium, a state of broken *PT* symmetry. The direction of parity breaking along the *y-axis* of the loss-gain two dimensional arrayed particle system, results in a switch from a lasing state to an anti-lasing state and can be described by phase transition to non-equilibrium. The role of time reversal within an optical system can be replaced by the switching of loss and gain, and have a relation to the refractive index of the loss-gain materials. Figure 8.7 demonstrates the unbroken and broken symmetric states. During the broken state,

the lasing and anti-lasing presents a spectral peak and trough within the ultraviolet region (UVA), emitting and absorbing respectively at ~350 nm. The input of the system was 0.5W.

$$P_{xy}: \begin{pmatrix} x \\ z \end{pmatrix} \mapsto \begin{pmatrix} -x \\ -z \end{pmatrix} \tag{8.2.4}$$

$$PT_{\pm\Delta\delta_y}: \begin{pmatrix} y \\ RI_{loss} \end{pmatrix} \neq\mapsto \begin{pmatrix} -y \\ -RI_{gain} \end{pmatrix} \tag{8.2.5}$$

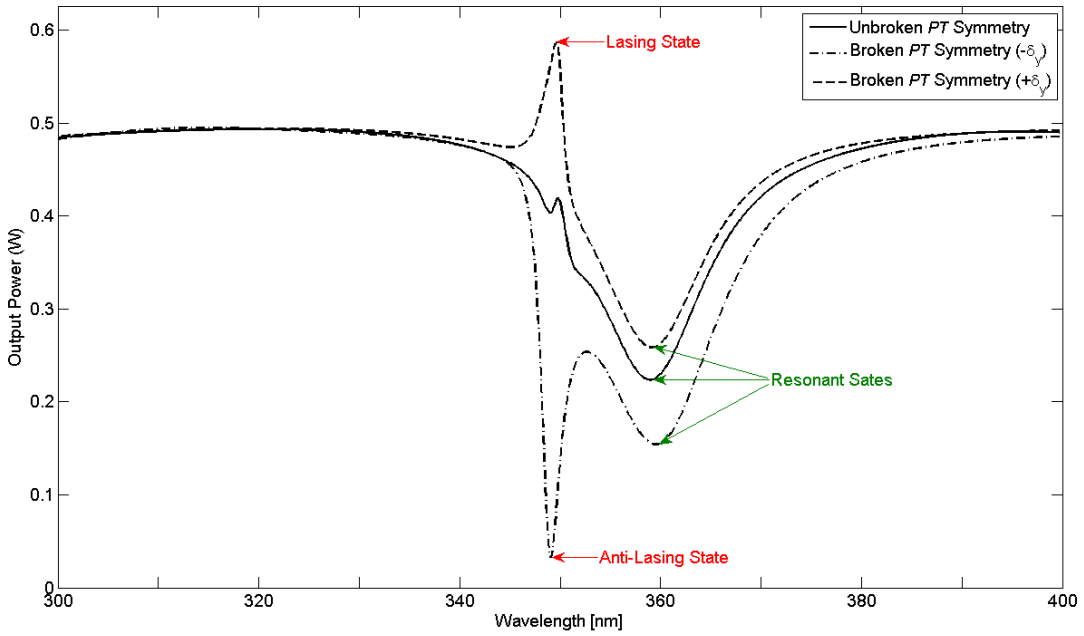


**Figure 8.7.** Power output of the system with relation to wavelength, expressing the broken and unbroken states.

Figure 8.8 highlights the contribution of the loss and gain materials, during equilibrium and non-equilibrium, through isoline amplitudes of the near-field response at 350 nm. At equilibrium the loss and gain particles are separately excited. As expected, during the lasing state, only the gain particles are excited. However, during the anti-lasing state, the loss-gain particles become highly coupled, forcing the activation of both particles.

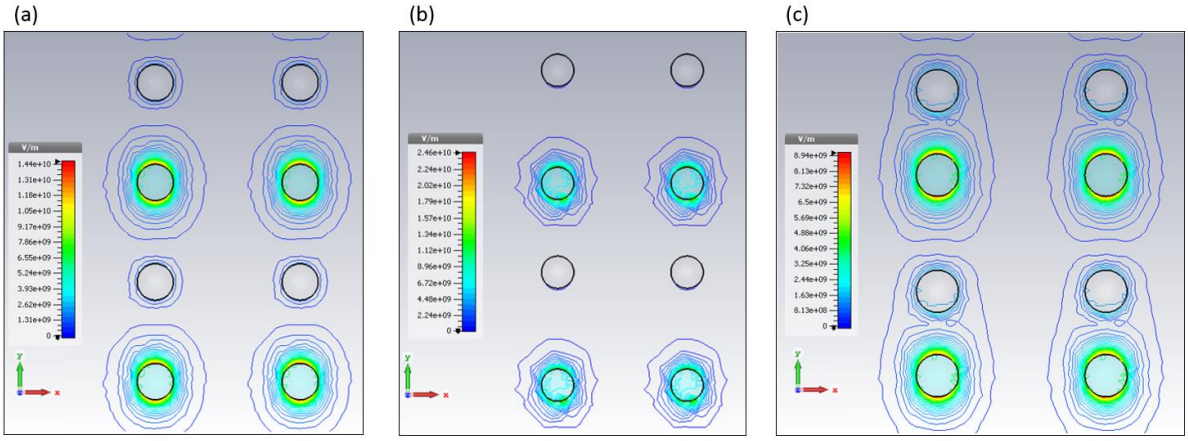

**Figure 8.8.** Near-field response at 350 nm wavelength. (a) State of unbroken *PT* symmetry [equilibrium]. (b) State of broken *PT* symmetry with $\Delta\delta_y = +15\ nm$ [non-equilibrium]. (b) State of broken *PT* symmetry with $\Delta\delta_y = -15\ nm$ [non-equilibrium].

A key attribute to the presence of *PT* symmetry lies with a non-Hermitian Hamiltonian, a complex number. Figure 8.9 shows the calculated modulus of the S matrix eigenvalues ($|s|$) for the broken *PT* states, plotted against the wavelength-particle size parameter ($a/\lambda$).

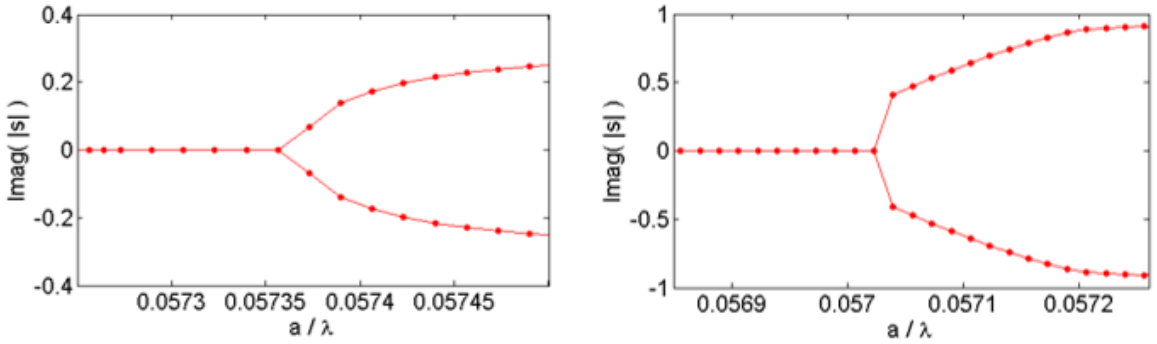


**Figure 8.9.** The modulus of the S matric eigenvalues for the broken *PT* states. (a) State of broken *PT* symmetry with $\Delta\delta_y = +15\ nm$. (b) State of broken *PT* symmetry with $\Delta\delta_y = -15\ nm$.

This short study demonstrates the possibility of obtaining a narrow optical notch filter through the use of breaking the parity time-reversal symmetry of a nanoparticle array consisting of loss and gain materials. The described system has been designed and studied using a full-wave FEM solver, where the arrangement has been subjected to a 0.5 Watt broadband plane wave, propagating along the *z-axis* with the electric field existing along the *y-axis*. Directional adjustment to $\delta_y$ results in lasing or anti-lasing depending on the chosen direction. The proposed system, although conceptual, could be potentially realised using naturally lossy materials (silver, gold) and rare-earth ions such as Cerium ($Ce^{3+}$) or Erbium ($Er^{3+}$). With further investigation, an anti-laser system could be realised at other wavelengths including 532 nm.

8.5 **References**

[1] D. Cacuci, *The second-order adjoint sensitivity analysis methodology*, 1st ed. Chapman and Hall/CRC Press, 2016.

[2] M. Bakr, A. Elsherbeni and V. Demir, *Adjoint Sensitivity Analysis of High Frequency Structures with MATLAB*. SciTech Publishing Inc, 2017.

[3] C. Audet, J. Dennis and S. Le Digabel, "Trade-off studies in blackbox optimization", *Optimization Methods and Software*, vol. 27, no. 4-5, pp. 613-624, 2012. Available: 10.1080/10556788.2011.571687.

[4] G. Allaire, F. Jouve and A. Toader, "Structural optimization using sensitivity analysis and a level-set method", *Journal of Computational Physics*, vol. 194, no. 1, pp. 363-393, 2004. Available: 10.1016/j.jcp.2003.09.032.

[5] J. Sokołowski and J. Zolésio, *Introduction to shape optimization*. Berlin: Springer-Verlag, 1992.

[6] F. Ding, Z. Wang, S. He, V. Shalaev and A. Kildishev, "Broadband High-Efficiency Half-Wave Plate: A Supercell-Based Plasmonic Metasurface Approach", *ACS Nano*, vol. 9, no. 4, pp. 4111-4119, 2015. Available: 10.1021/acsnano.5b00218.

[7] A. Krasnok, S. Makarov, M. Petrov, R. Savelev, P. Belov and Y. Kivshar, "Towards all-dielectric metamaterials and nanophotonics", *Metamaterials X*, 2015. Available: 10.1117/12.2176880.

[8] V. Babicheva and J. Moloney, "Lattice effect influence on the electric and magnetic dipole resonance overlap in a disk array", *Nanophotonics*, vol. 7, no. 10, pp. 1663-1668, 2018. Available: 10.1515/nanoph-2018-0107.

[9] C. Park et al., "Structural Color Filters Enabled by a Dielectric Metasurface Incorporating Hydrogenated Amorphous Silicon Nanodisks", *Scientific Reports*, vol. 7, no. 1, 2017. Available: 10.1038/s41598-017-02911-w.

[10] R. Rumpf, M. Gates, C. Kozikowski and W. Davis, "Guided-mode resonance filter compensated to operate on a curved surface", *Progress In Electromagnetics Research C*, vol. 40, pp. 93-103, 2013. Available: 10.2528/pierc13041209.

[11] Y. Chong, L. Ge, H. Cao and A. Stone, "Coherent Perfect Absorbers: Time-Reversed Lasers", *Physical Review Letters*, vol. 105, no. 5, 2010. Available: 10.1103/physrevlett.105.053901.

[12] C. Bender and S. Boettcher, "Real Spectra in Non-Hermitian Hamiltonians HavingPTSymmetry", *Physical Review Letters*, vol. 80, no. 24, pp. 5243-5246, 1998. Available: 10.1103/physrevlett.80.5243.

[13] C. Huang, F. Ye, Y. Kartashov, B. Malomed and X. Chen, "PT symmetry in optics beyond the paraxial approximation", *Optics Letters*, vol. 39, no. 18, p. 5443, 2014. Available: 10.1364/ol.39.005443.

[14] P. Kalozoumis, C. Morfonios, F. Diakonos and P. Schmelcher, "PT-symmetry breaking in waveguides with competing loss-gain pairs", *Physical Review A*, vol. 93, no. 6, 2016. Available: 10.1103/physreva.93.063831.

[15] H. Zhao and L. Feng, "Parity–time symmetric photonics", *National Science Review*, vol. 5, no. 2, pp. 183-199, 2018. Available: 10.1093/nsr/nwy011.

[16] J. Wen, X. Jiang, L. Jiang and M. Xiao, "Parity-time symmetry in optical microcavity systems", *Journal of Physics B: Atomic, Molecular and Optical Physics*, vol. 51, no. 22, p. 222001, 2018. Available: 10.1088/1361-6455/aae42f.
[17] S. Droulias, I. Katsantonis, M. Kafesaki, C. Soukoulis and E. Economou, "Chiral Metamaterials with PT Symmetry and Beyond", *Physical Review Letters*, vol. 122, no. 21, 2019. Available: 10.1103/physrevlett.122.213201.

# Appendix A **SOFTWARE – OPTICAL META ANALYSIS TOOL**

The design process presented in this thesis, *Chapter III* and *Chapter IV*, have involved the ability to predict the location of the plasmonic resonance wavelength with dependence on the surrounding refractive index. This has been established as an extension to the linear dependency of localised surface plasmonic resonance by considering particles in two- and three-dimensional arrays. Utilising an effective medium theory, the metamaterial can be considered as a single homogenous film, known as a metafilm. Using an effective Drude-Lorentz model to describe the metafilm allows the homogenous material to be defined by four independent constants;

- Effective offset constant – Describes all high frequency pertinent transitions above the resonance wavelength.
- Effective plasma frequency – Describes the frequency that the electron interacts with.
- Effective resonant frequency – Describes the restoring natural frequency.
- Dampening frequency – Describes the "frictional" force.

The Maxwell-Garnett theory cannot limit the effective material into defined constants.

The advantage of considering the metamaterial as an effective homogenous material allows it to be treated identically to a standard thin film. The optical thin film design principles are well established; as such, using the knowledge discussed in *Chapters III* and *Chapters IV*, an inverse design tool has be generated.

Two software tools have been developed throughout this thesis to aid industry optical design engineers in the pursuit for designing metamaterials.

1. A simplistic tool.
2. A complex tool.

Unlike previously discussed metamaterial software that rely on computation algorithms to provide a solution, these tools are underpinned purely by the mathematics described in the thesis. The software has been written in the MATLAB scripting language.

**Inverse Design Tool – Simplistic Approach**

The simplistic tool requires no prior knowledge and simply involves the input of the target wavelength. The background code calculates the unit cell parameters, the material required, the complex refractive index of that metamaterial design, and the effective Drude-Lorentz constants. The provided data can be exported for the use in other software, either as an effective thin film or a 3D unit cell design. For the given task in hand, this provides a *near* instantaneous inverse solution for the metamaterial properties.

Figure A.1 demonstrates the GUI for the simplistic tool with a working example for 520 nm laser wavelength.

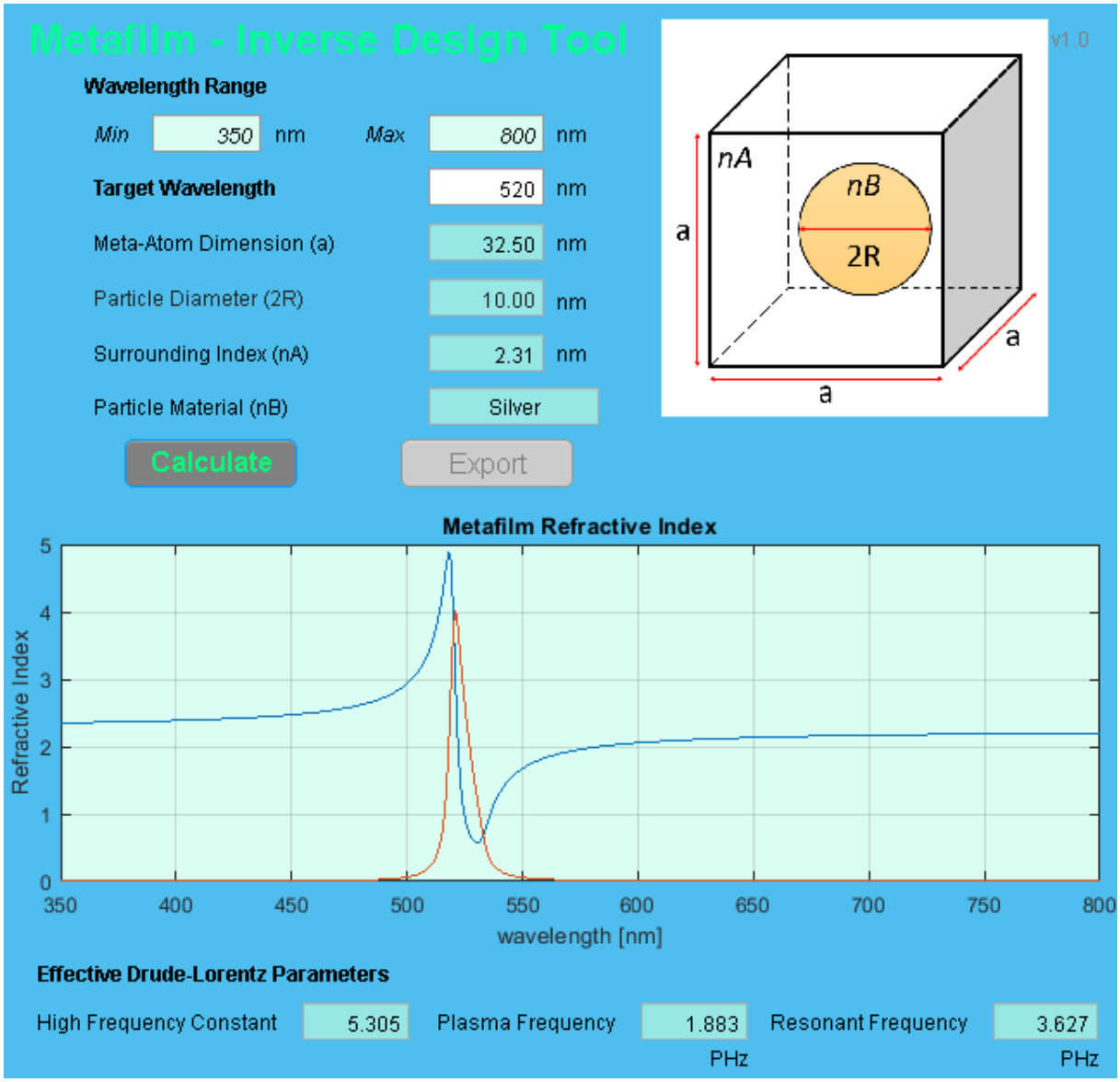


**Figure A.1.** Inverse metamaterial design tool considering just the target wavelength.

### Inverse Design Tool – Complex Approach

The more complex tool contains more features than the simplistic tool and allows for much more control over the design, material and shape of the metamaterial. The transmission, reflection, absorption and optical density of the metamaterial can be analysed, either as an individual film or considered as a full metamaterial design. Furthermore, this software package supports Mie theory (*Chapter III*), equivalent circuit approximations (*Chapter IV*) and hyperbolic metamaterials.

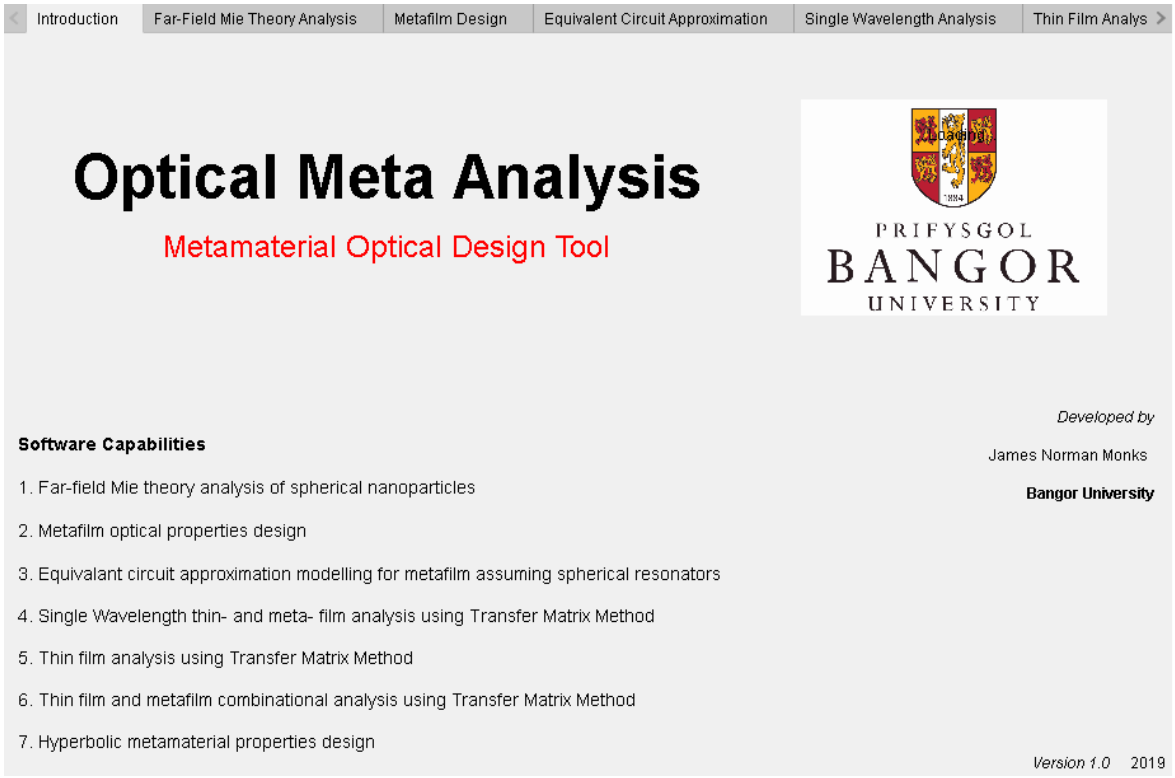


**Figure A.2.** The introduction GUI for the metamaterial optical design tool.

The metafilm design process through this software does not involve selecting the target wavelength, instead it relies on prior knowledge (*discussed throughout this thesis*) to establish a design. Figure A.3 shows the 'Metafilm Design' tab. There are a number of entries required before calculation can take place.

1. Enter the working wavelength range (280 nm – 3000 nm)
2. Select resonator material. If 'custom' is selected, the user will have to input the Drude model constants for their given material.
3. Select resonator shape. The Depolarisation factor determines the shape (2 for a spherical resonator).
4. Enter the volume of the resonator and the unit-cell.
5. Determine the refractive index of the resonator surrounding medium that makes up the unit-cell.

Once the entries have been successfully filled, the metafilm's optical properties can be calculated and exported, or analysed with the software itself. An example can be found in figure A.3b. These parameters have been selected to match the response found in figure A.1.

A real-time demo of the metafilm design software tool can be found in reference [1].

(a)

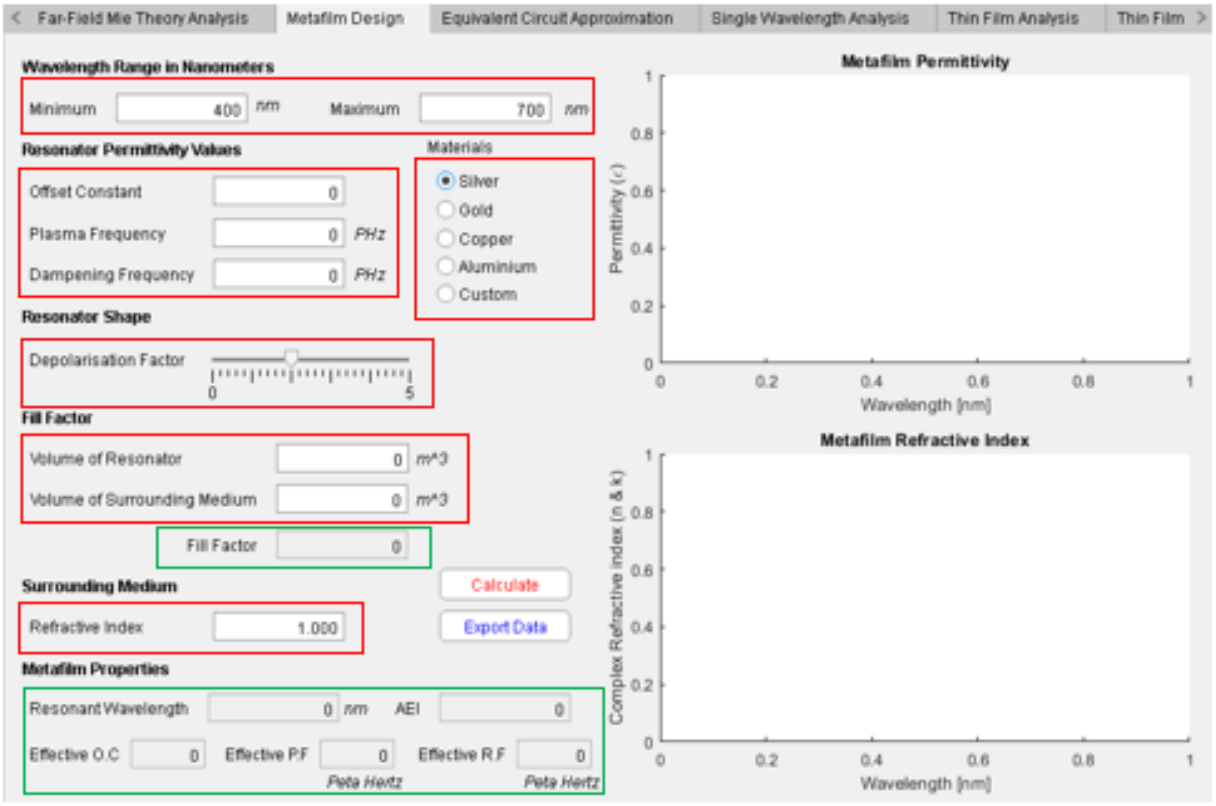


(b)

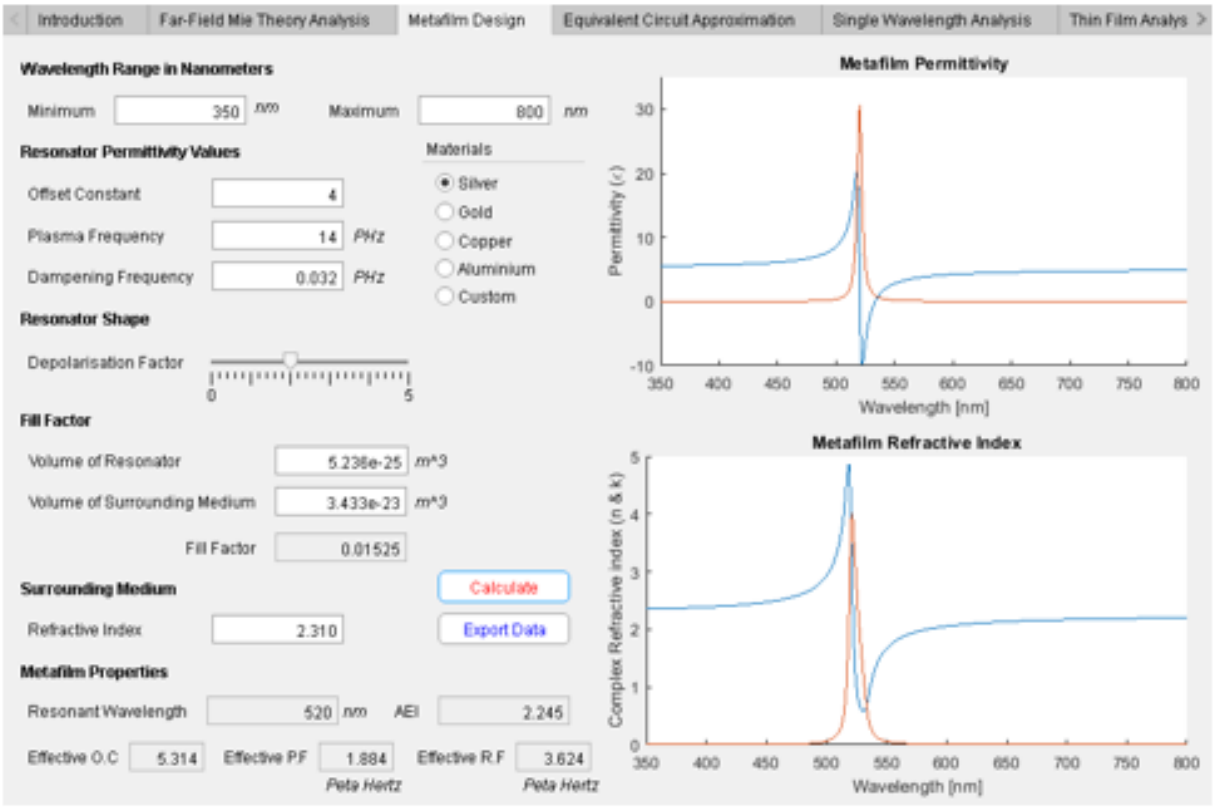


**Figure A.3.** Metafilm design tool. (a) Entries into the 'red' highlighted areas are needed. Data in the 'green' areas will appear upon calculation. (b) Demonstrates the output with completed entry fields.

The ‘Optical Meta Analysis’ tool has several features to aid the design process. The aim is develop a complete in-house design software that does not require expensive industry software. Figure A.4 demonstrates each tab of the software tool, which is shown in figure A.2.

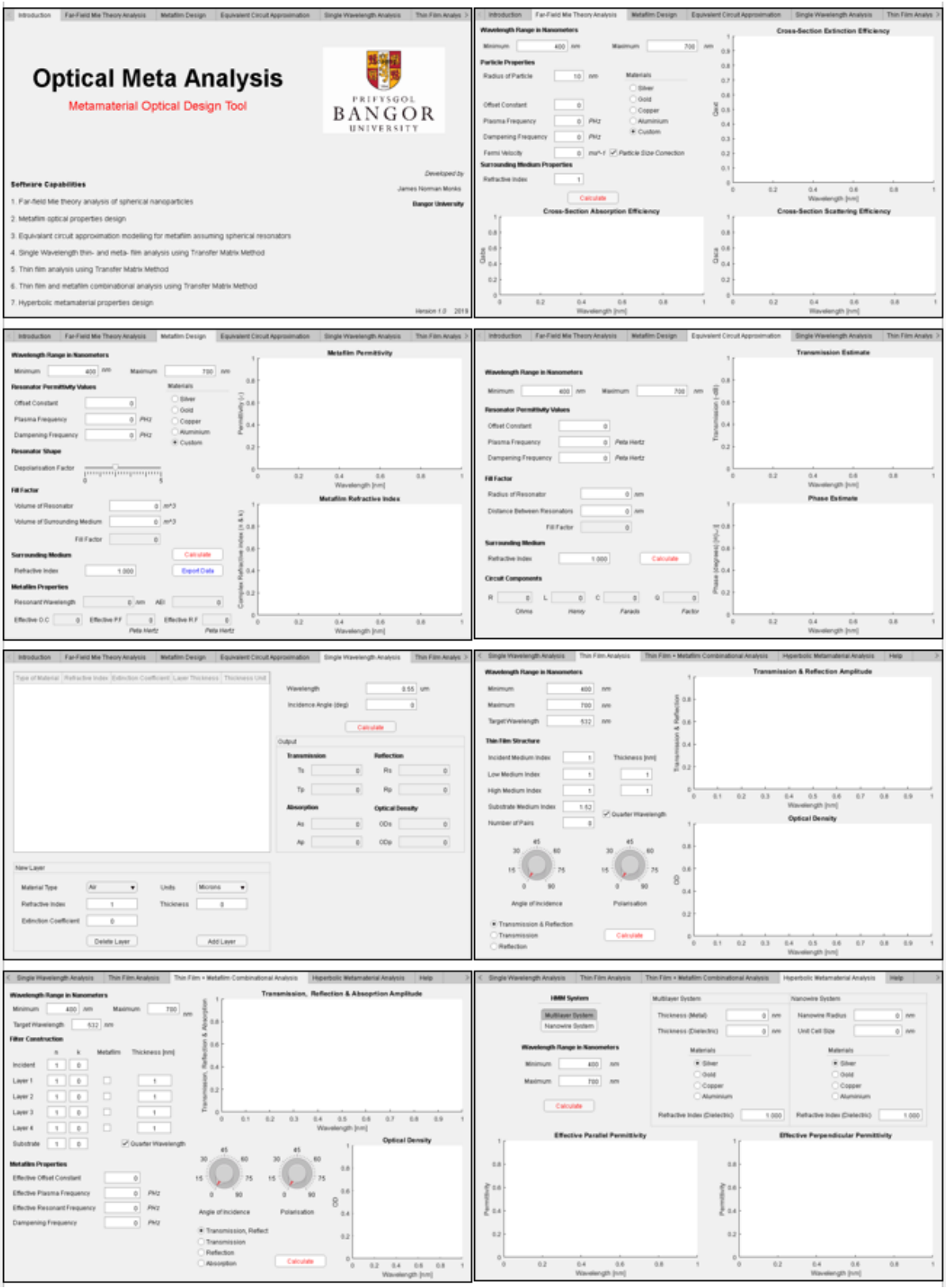


**Figure A.4.** Metafilm design tool.

**Summary**

The inverse design tools presented here contain the mathematical principles discussed in *Chapter III* and *Chapter IV*. The solutions presented in *Chapter V* and *Chapter VI* have been solved through the development of the 'metamaterial optical design tool' with the aid of Essential Macleod and a full-wave simulator CST Studios. The simplistic tool enabled a quick solution without the need of exploring different material parameters, where the more complex inverse design tool requires a more in-depth understanding of materials and metamaterials. The inverse design tools still requires some modifications; however, they do demonstrate the ability produce the optical properties and meta-atom components (material and size) for a metamaterial for a notch filter application. Furthermore, the fabrication of the optical notch filter, *Chapter VII*, provides further evidence that the inverse design tools delivers an accurate solution.

**References**

[1] J. Monks, *METAFILM Software Demo*, 2019. Available: https://youtu.be/aQxjuMkCuYA.